Radiation effects in structural steels for nuclear applications: an atomistic study

Alexander Bakaev

Supervisor: Prof. Dr. Dimitri Van Neck
Co-supervisor: Prof. Dr. Ir. Guido Van Oost
Co-supervisor (SCK): Dr. Dmitry Terentyev

Dissertation submitted in fulfillment of the requirements
for the degree of Doctor (Ph.D.) in Sciences: Physics

Faculty of Sciences
Department of Physics and Astronomy
Ghent University
Academic year 2013-2014

ISBN xxx-xx-xxxx-xxx-x
NUR xxx
Wettelijk depot: x/2009/xx.xxx/xx

Dit werk werd uitgevoerd aan de onderzoeksinstelling
This research was performed at

SCK•CEN
Institute for Nuclear Materials Science
Structural Materials Group
Boeretang 200
B-2400 Mol
Belgium

In samenwerking met
In collaboration with

Universiteit Gent
Faculteit Wetenschappen
Vakgroep Fysica en Sterrenkunde
Center for Molecular Modeling
Technologiepark 903
B-9052 Gent
Belgium

Leden van de examencommissie
- Members of the examining board -

Voorzitter - Chairman -

prof. dr. Freddy Callens
Universiteit Gent
Vakgroep Vaste-Stofwetenschappen - WE04

Secretaris - Secretary -

prof dr. Dimitri Van Neck
Universiteit Gent
Vakgroep Fysica en Sterrenkunde - WE05

Leescommissie - Reading committee -

dr. Lorenzo Malerba
SCK•CEN
Instituut voor Wetenschappen Nucleair Materiaal

prof. dr. Pär Olsson
KTH Koninklijk Instituut voor Technologie
Divisie van Reactor Fysica

dr. Peter Klaver
TU Delft
Materiaalkunde en Techniek

prof dr. Dimitri Van Neck
Universiteit Gent
Vakgroep Fysica en Sterrenkunde - WE05

Overige leden - Other members -

prof. dr. Guido Van Oost
Universiteit Gent
Vakgroep Toegepaste Fysica - EA17

dr. Dmitry Terentyev
SCK•CEN
Instituut voor Wetenschappen Nucleair Materiaal

prof. dr. Stefaan Cottenier
Universiteit Gent
Vakgroep Fysica en Sterrenkunde - WE05

prof. dr. Veronique Van Speybroeck
Universiteit Gent
Vakgroep Toegepaste Fysica - EA17

prof. dr. Jean-Marie Noterdame
Universiteit Gent
Vakgroep Toegepaste Fysica - EA17

Contents

Acknowledgements

The four years of work on this PhD thesis have passed so (too?) quickly, like in one second. It was a really wonderful experience to conduct a collaborative scientific research in the foreign country. Below, I would like to name the people who made possible that now you, dear reader, can turn these pages.

I would like first to express my special appreciation and thanks to my advisor Dmitry Terentyev, you have been a tremendous mentor for me, always ready to help me with any complicated topic. I would like to thank you for encouraging my research and for allowing me to grow as a research scientist. Your advice on both research as well as on my career have been really priceless. I would also like to thank my promoters Prof. Dimitri Van Neck and Prof. Guido Van Oost for kindly assisting me during these four years, for approving all missions abroad to international conferences and summer schools, which I requested. I am very grateful to the management of SCK•CEN: Prof. Dr. Eric van Walle, Dr. Leo Sannen, Dr. Marc Scibbeta, Dr. Rachid Chaouadi, Dr. Milan Konstantinović and our simulation group leader Dr. Lorenzo Malerba for allowing me to perform this PhD in the splendid scientific center — SCK•CEN. This place is superb in the sense that it represents an efficient integration of theoretical investigations and industrial application of nuclear materials.

I am very grateful to Fund of Scientific Research - Flanders (Fond voor Wetenschappelijk Onderzoek — FWO), PERFORM-60, Erasmus Mundus FUSION-EP projects and EFDA programme for the financial support of this PhD thesis. I would also like to thank the support teams of supercomputer clusters in SCK•CEN, UGent, Jülich, Archer (UK) and Helios (Japan) for ensuring almost non-interruptible operation.

I would like to thank cordially Prof. E.E. Zhurkin for introducing me into the world of molecular dynamics modelling during the university studies in Saint-Petersburg. Your wise advice to continue the research in this field in Belgium was really determinative in my final decision to come to SCK•CEN.

I owe a great deal to my dear collaborators from Netherlands and Sweden: Peter Klaver and Pär Olsson. I do appreciate your efficient introductory courses into the practice of electronic structure calculations using DFT, given to me, and your constant readiness to answer to a pile of my questions.

The work on this thesis was done in a tight cooperation with all my dear colleagues from our simulation group and LHMA building: Giovanni, Boris, Peter, Nicolas, Andrei, Monica, Ville, Konstanza, Tautvydas, Frédéric, Amélie... We had thousands of fruitful scientific discussions and you were always making my days happier.

I would like to say a special thanks to my family. Words cannot express how grateful I am to my mother and father for all of the sacrifices that you have made on my behalf. I would also like to thank all of my friends in Belgium and Russia who supported me in writing, and who were always confident that I will reach everything what I plan. At the end I would like express a gratitude to my beloved wife Anastasia who shared all joys and difficulties with me during these four years and was always my support in the moments when there was no one to answer my queries.

Alexander Bakaev
September 2014, Mol.

Samenvatting
-Dutch Summary-

De veilige uitbating van huidige en toekomstige nucleaire fissie- en fusiereactoren zijn onmogelijk zonder een gedetailleerde kennis van de processen die leiden tot de veroudering van structuur- en reactorkuipstalen onder bestraling. In deze doctoraatsthesis onderzoeken we de effecten van stralingsschade in drie materiaalgroepen: austenitische roestvaste stalen die gebruikt worden voor de interne onderdelen in druk water reactoren (DWR); laag activerende ferritisch-martenitische (LFM) stalen dat als structuurmateriaal voor de volgende generatie fissie- en toekomstige fusiereactoren gebruikt zal worden; en reactorkuipstalen die momenteel gebruikt worden in DWR.

De degradatie van al deze materialen door bestraling start op een gelijkaardige manier. In eerste instantie veroorzaakt de neutronenstraling atomaire botsingscascades, die tot de creatie van puntdefecten zoals vacatures en interstitiële atomen leiden. Uiteindelijk vormen deze defecten holtes en dislocatielussen, die beide obstakels zijn voor de mobiliteit van dislocaties tijdens plastische vervorming. Het is dit effect dat de verharding veroorzaakt, wat betekent dat de vloeigrens van het materiaal toeneemt die afgeleid wordt uit trekproeven. Daarenboven kunnen dislocaties deze stralingsdefecten ook absorberen wat kan leiden tot de vorming van zogenaamde 'vrije kanalen' — zones die vrij zijn van stralingsschade. Onder externe spanning kunnen deze leiden tot plaatselijke plastische vervorming, die vervolgens tot spanningsconcentraties leidt en uiteindelijk de start van een scheur. Ten tweede zorgen de gegenereerde puntdefecten voor een verhoogde massaflux in het materiaal die legeringselementen naar vallen (bv. dislocaties en korrelgrenzen) kunnen transporteren. De segregatie van die elementen naar dislocatieslussen kan leiden tot precipitatie, wat de dislocatielussen sterkere obstakels maakt en leidt tot snellere verharding.

Deze thesis is gewijd aan de studie van de interactie tussen dislocaties en stra-

lingsdefecten op de nanoschaal. Deze interacties zijn verantwoordelijk voor de verharding op atomaire schaal en kunnen mogelijks een verklaring geven voor de vorming van vrije kanalen. De atomaire berekeningen worden ook gebruikt om de vorming van nanometrische clusters van legeringselementen onder bestraling te onderzoeken en hun bijdrage tot de verharding van de materialen.

Deze thesis bestaat uit vijf hoofdstukken. Het eerste hoofdstuk geeft een algemeen overzicht over de toepassing van nucleaire fissie en fusie in de elektriciteitsproductie, een inleiding tot de theorie van stralingsschade in vaste stoffen en een inleiding tot experimentele technieken voor de karakterisering en kwantificering van stralingsschade. De motivering voor de geselecteerde materialen en toegepaste methodes wordt ook besproken.

In hoofdstuk 2 wordt een overzicht gegeven van de recente data met betrekking tot de veroudering van stalen door bestraling. Hierbij ligt het zwaartepunt bij austenitische stalen, welke een kubisch vlakken gecentreerde (kvc) kristalstructuur hebben. Het toepassingsgebied en chemische samenstelling van de stalen worden in detail beschreven. Voor de austenitische stalen wordt een overzicht van de data over de microstructuur na bestraling gegeven voor verschillende temperaturen. De macroscopische effecten in de vorm van verharding en verbrossing door de vorming van vrije kanalen wordt besproken. Verklaringen naar de oorsprong van deze effecten in kvc materialen uit de literatuur en gebaseerd op moleculaire dynamica (MD) simulaties worden besproken. Met betrekking tot LFM en kuipstalen, welke de kubisch ruimtelijk gecentreerd (krc) structuur hebben, kan de stralingsschade opgesplitst worden in matrix schade (vorming van dislocatielussen) en de vorming van precipitaten van de legeringselementen. Er wordt ook een overzicht gegeven van de huidige verklaringen van de evolutie van de nanostructuur en resultaten uit de literatuur over de dislocatie-defect interacties in krc metalen.

Hoofdstuk 3 is gewijd aan de beschrijving van de twee simulatiemethodes toegepast in deze thesis, namelijk: *ab initio* berekeningen door middel van dichtheidsfunctionaal theorie (DFT) en klassieke MD simulaties. Voor de eerstgenoemde wordt de DFT code VASP gebruikt om de stabiliteit en de energieën van verschillende legeringselement-defect configuraties in krc Fe te berekenen. Deze informatie laat toe om de nucleatiemechanismen van precipitaten te identificeren. De MD methode wordt toegepast om de dislocatie-defect interactie te simuleren, de onderliggende reacties te analyseren en de sterkte van de obstakels voor de dislocatiemobiliteit te bepalen. De parameterizaties van de toegepaste methodes in dit werk en het algemene algoritme van de berekeningen worden besproken.

De belangrijkste resultaten van dit doctoraat worden samengevat in hoofdstuk

4. De plastische vervorming door dislocaties van austenitische roestvaste stalen werd gemodelleerd met behulp van de binaire FeNi en recent ontwikkelde ternaire FeNiCr modellegeringen. Deze werden geïmplementeerd in een multiprocessor klassieke MD code om de interactie tussen dislocaties en typisch experimenteel geobserveerde stralingsdefecten — Frank lussen — te bestuderen. De simulaties hebben aangetoond dat een afname van de stacking fault energie (SFE) leidt tot een onderdrukking van de absorptie van de lus door een schroefdislocatie en dus kan dit de kans op kanaalvorming verminderen. Wetende dat de absorptie van een lus door een schroefdislocatie leidt tot het sterkste obstakel, leidt een afname in SFE ook tot een afname in de door lussen geïnduceerde verharding. Het verharden door het vormen van een vaste oplossing van de legeringselementen leidt tot de onderdrukking van lus absorptie door de verhoging van de frictie spanning in de secundaire glijdvlakken. De verkregen inzichten met betrekking tot de lusverharding en lusabsorptie als een functie van de temperatuur en SFE geven een richtlijn voor het rationaliseren van de stralingsgeïnduceerde verharding bij kamertemperatuur en reactor bedrijfstemperatuur.

De stralingsgeïnduceerde degradatie van LFM stalen werd bestudeerd door middel van DFT en MD. De *ab initio* berekeningen werden uitgevoerd om de thermodynamische mechanismen te bestuderen die leiden tot de nucleatie en precipitatie van legeringselementen, die experimenteel geobserveerd worden in bestraalde hooggelegeerde Cr stalen. De mogelijke mechanismen voor de vorming van MnSi (ook rijk aan Ni) clusters zijn mogelijk veroorzaakt door de binding van een interstitieel Mn atoom met een nabijgelegen Si atoom. Dit complex wordt gekarakteriseerd door een hoge totale bindingsenergie en kan gebruikt worden als een nucleus voor de groei van MnSiNi rijke clusters. De MD methode werd toegepast om de oorzaak van de verharding van hooggelegeerde Cr stalen te achterhalen, die al numeriek bepaald is uit experimenten. We vonden dat kleine ongedecoreerde dislocatielussen zwakke obstakels voor geïsoleerde dislocaties zijn, terwijl gedecoreerde lussen sterke obstakels zijn. Dus het effect van Cr op de sterkte van de lus is een mogelijke verklaring voor de experimenteel geobserveerde grote verharding in hooggelegeerde Cr legeringen in vergelijking met laaggelegeerde Cr legeringen en puur ijzer. De fysische oorsprong van dit effect is gerelateerd aan de verandering van de dislocatie-defect interactie die de sterkte van het obstakel beïnvloedt.

De eigenschappen van de stralingsdefecten reactorkuipstalen werden bestudeerd door middel van *ab initio* en MD methodes. We hebben een nieuw mechanisme voorgesteld dat de nucleatie van MnNi rijke clusters in bestraalde kuipstalen kan verklaren. De vorming van zulke clusters, die altijd gevonden worden bij atom-probe studies op reactor kuipstalen, kan geïnitieerd worden

door de nucleatie van Mn en Ni clusters bij vacature-koolstof complexen. De vele en thermodynamisch stabiele MnNi-koolstof-vacature complexen zullen frequent interageren met glijdende lussen die onmiddellijk uit botsingscascades kunnen ontstaan. Zulke reacties resulteren in de decoratie van de lussen door koolstof en Mn/Ni atomen. Door middel van MD simulaties konden we vaststellen dat de decoratie van de lussen door Mn/Ni/C atomen leidt tot een uitgesproken toename van de obstakelsterkte in vergelijking met ongedecoreerde lussen. Bovendien leiden de C-gedecoreerde lussen tot een verandering van het interactiemechanisme van de absorptie van <100> lussen tot hun transformatie naar $1/2$<111> lussen. Dus, de koolstof segregatie op dislocatielussen resulteert niet enkel in de verharding maar ook in de verandering van de microstructuur onder langdurige plastische vervorming.

Een overzicht van de verkregen resultaten en een blik naar de toekomst worden gepresenteerd in hoofdstuk 5. Dit werk verduidelijkt de nucleatie mechanismen bij de precipitatie van legeringselementen in LFM en kuipstalen en draagt bij tot de numerieke evaluatie van de verharding door de aanwezigheid van een combinatie van precipitatie en dislocatielussen. De dislocatie-defect interactie mechanismen leiden tot de verharding en creatie van vrije kanalen, gerelateerd met de verbrossing van austenitische stalen. De verkregen resultaten zullen gebruikt worden in simulaties op een hogere schaal, zoals dislocatiedynamica, om spannings-rek relaties te berekenen die verder vergeleken kunnen worden met experimenten en voor de studie en vorming van vrije kanalen in austenitische stalen met verschillende SFE. De nucleatie mechanismen voor clusters van legeringselementen samen met de data base van de corresponderende bindingsenergieën kunnen gebruikt worden als input voor kinetische Monte Carlo of 'mean field theorie' methoden om de evolutie van legeringselementen en stralingsdefecten in LFM en kuipstalen onder bestraling te bestuderen.

Summary

The safe exploitation of current and future fission nuclear reactors and construction of future thermonuclear fusion reactors requires a deep understanding of the processes leading to the radiation-induced degradation of the structural reactor materials. In this PhD thesis we consider radiation damage in three groups of materials: austenitic stainless steels used in pressurized water reactor (PWR) internals, ferritic-martensitic (FM) steels to be used in next generation fission and in future fusion reactors, and reactor pressure vessel (RPV) steels currently used in PWRs.

The radiation-induced degradation of these materials initiates in a similar way. Firstly, the neutron radiation causes the generation of atomic displacement cascades, which lead to the creation of lattice point defects such as vacancies and interstitials. Eventually, these defects agglomerate in the form of dislocation loops and voids which act as obstacles for dislocation movement during plastic deformation. This effect causes hardening, which is the increase of the yield stress usually measured experimentally in the mechanical tests. Also, the dislocations can absorb the radiation defects and this process can lead to the formation of the so called 'dislocation channels' — zones free from radiation defects, which under stress can lead to localized plastic deformation and, consequently, to stress concentration and initiation of a crack. Secondly, the point defects created due to neutron radiation are responsible for the increased mass transport of the solute atoms which start diffusing faster and migrate to sinks, namely the grain boundaries and dislocations. The segregation of the solute atoms to the dislocation lines in the form of loops may lead to the formation of solute clusters, possibly making the loops stronger obstacles for the dislocation motion, leading to enhanced hardening.

This PhD thesis is devoted to the study of the nano-scale dislocation-defect interaction mechanisms, at the origin of the hardening at the atomic scale, which may also provide an explanation for the formation of dislocation channels. The atomistic calculations are also applied to identify the mechanisms

of nucleation of nanometer-scale solute-rich clusters under irradiation in the above mentioned structural and RPV steels, and to explore their contribution to hardening.

The thesis consists of five chapters. Chapter 1 provides a general overview of the application of nuclear and fusion energy for electricity production, and an introduction to the theory of radiation damage in solids and the experimental practice of its characterization and measurement. The motivation for the selection of the materials to study and the applied methods is also discussed.

In chapter 2, a summary of the currently available results on radiation-induced degradation of the steels is presented. The main focus is on austenitic steels which have a face-centered cubic (fcc) crystallographic structure. Detailed information about the application and chemical composition of the steels is provided. For the austenitic steels the available data about the radiation-induced microstructure at different temperatures are summarized. The data about the macroscopic effect of the presence of radiation-induced defects in the form of hardening and embrittlement due to the formation of dislocation channels is also discussed. To this regard, the previously published nanoscale explanations of the origin of these effects in fcc materials, obtained with the molecular dynamics (MD) method using the dislocation-defect interaction modelling, are reviewed. Concerning the FM and RPV steels, that have a body-centered cubic (bcc) lattice, radiation damage can be decomposed into a matrix damage (formation of dislocation loops) and nucleation of solute-rich precipitates. The current explanations of the nanostructural evolution in both steels leading to hardening, and previous results on the dislocation-defect interaction in bcc metals, are summarized.

Chapter 3 is devoted to the description of the two main methods applied in this thesis, namely: electronic structure calculations using density functional theory (DFT) and classical MD simulations. The DFT calculations are performed using the code VASP, in order to determine the stability and energetics of different solute-defect configurations in bcc Fe. This information allows one to identify the nucleation mechanisms of the solute-rich clusters. The MD method is applied to simulate the dislocation-defect interaction, to analyze the undergoing reactions and calculate the strength of the defects hindering the movement of dislocations. The parameterization of the methods applied in this work and the general algorithm for the calculations are provided.

The main results obtained during the work on this PhD thesis are summarized in chapter 4. Dislocation-mediated plastic flow in austenitic stainless steels was simulated using interatomic potentials for binary FeNi and (newly developed) ternary FeNiCr model alloys. They were incorporated into the multiprocessor

classical molecular dynamics code in order to study the interaction of dislocations with the typical experimentally observed radiation defects — Frank loops. The simulations have shown that the decrease of the stacking fault energy (SFE) leads to the suppression of loop absorption and thus reduces the probability for channeling initiation by dislocation glide. Given that the reaction of the loop absorption on a screw dislocation results in the highest unpinning stress, in general the decrease of SFE also leads to a reduction of the loop-induced hardening. Solute alloying leads to the suppression of loop absorption due to the increase of the friction stress in the secondary glide planes. The obtained information on the loop hardening and loop absorption as a function of temperature and SFE provides a guidance for the rationalization of the radiation-induced hardening at room and at reactor operational temperature, as observed in experiments.

The radiation-induced degradation of the FM steels was studied using both DFT and MD methods. Electronic structure calculations using DFT were performed to study the thermodynamic mechanisms leading to the nucleation of solute-rich clusters, observed experimentally in irradiated high-Cr steels. The possible formation mechanisms for Mn-Si (also rich in Ni) clusters in high-Cr alloys may be attributed to the configuration of Fe-Mn mixed dumbbells and a Si atom in the compression site next to the Fe atom in the dumbbell. This atomic system is characterized by a high total binding energy and can serve as a nucleus for the growth of Mn-Si-Ni-rich complexes. The MD modelling method was applied to identify the source of hardening in high-Cr steels, which has already been numerically evaluated experimentally. We have established that small dislocation loops in the undecorated state are essentially weak obstacles for the dislocation motion, whereas the decoration by Cr increases their strength significantly. Thus, the effect of Cr-loop decoration is one of the possible explanations of the enhanced hardening in high-Cr alloys as compared to the low-Cr alloys and pure Fe that is observed in experiments. The physical origin of this effect of loop solute enrichment is related to the change of the dislocation-defect interaction mechanism which affects the unpinning stress.

The properties of radiation defects in RPV steels were also investigated by means of both electronic structure calculations using DFT and MD method. We have proposed a new mechanism explaining the nucleation of Mn-Ni-rich clusters observed in the irradiated RPV steels. The formation of such clusters always observed in atom-probe studies of RPV steels may be initiated by the nucleation of Mn and Ni clusters at vacancy-carbon pairs. The numerous and thermally stable solute-carbon-vacancy complexes will frequently interact with glissile dislocation loops, directly produced in the collision cascades.

Such interaction should result in the subsequent decoration of the loops by carbon and Mn-Ni solutes. By performing dedicated MD simulations, we have established that decoration of dislocation loops by Mn-Ni or carbon atoms leads to a pronounced increase of the unpinning stress as compared to the results obtained for undecorated loops. In addition, the decoration by carbon leads to the modification of the interaction mechanism from the absorption of <100> loops to their transformation into 1/2<111> loops. Hence, the carbon segregation at dislocation loops changes not only the resulting hardening but also the microstructural evolution under prolonged plastic deformation.

A summary of the results obtained and an outlook are presented in chapter 5. The performed work clarifies the nucleation mechanisms of solute-rich clusters in the FM and RPV steels, and contributes to the numerical evaluation of the hardening due to their presence in association with the agglomeration of self-interstitial atom (SIA)-clusters — dislocation loops. The dislocation-defect interaction mechanisms leading to hardening and dislocation channel - related embrittlement in austenitic steels have been also investigated. The results obtained are planned to be incorporated in upper scale models, such as dislocation dynamics, in order to obtain the stress-strain relationships for a further comparison with the experimental data and to study the formation and the pattern of dislocation channels in the austenitic steels with different stacking fault energy. The nucleation mechanisms of the solute-rich clusters together with the database of the corresponding binding energies can be used as input for kinetic Monte Carlo or mean field rate theory methods, in order to model the evolution of the solute-rich defects in FM and RPV steels under irradiation.

List of abbreviations

AGR	Advanced Gas-Cooled Reactor
APT	Atom Probe Tomography
bcc	Body-Centered Cubic
BR1	First Belgian Reactor
BV	Burgers Vector
BWR	Boiling Water Reactor
CANDU	Canada Deuterium Uranium Reactor
CRSS	Critical Resolved Shear Stress
CW	Cold Worked
DFT	Density Functional Theory
dpa	Displacement Per Atom
EAM	Embedded Atom Method
fcc	Face-Centered Cubic
FM	Ferritic-Martensitic
GEN	Generation
GFR	Gas-cooled Fast Reactor
HSFE	High Stacking Fault Energy
ITER	International Thermonuclear Experimental Reactor
JET	Joint European Torus
LFR	Lead-Cooled Reactor
LSFE	Low Stacking Fault Energy
LWR	Light Water Reactor
MAE	Minor Alloying Element
MD	Molecular Dynamics
MMC	Metropolis Monte Carlo
MSR	Molten Salt Reactor
NPP	Nuclear Power Plant
PD	Point Defect
PKA	Primary Knock-on Atom
PWR	Pressurized Water Reactor

RAFM	Reduced Activation Ferritic-Martensitic
RID	Radiation-Induced Defect
RMBK	High Power Channel Type Reactor
RPV	Reactor Pressure Vessel
SA	Solution Annealed
SANS	Small-Angle Neutron Scattering
SCK•CEN	StudieCentrum voor Kernenergie• Centre d'étude de l'Energy Nucleaire
SCWR	Super Critical Water Reactor
SFE	Stacking Fault Energy
SFR	Sodium-Cooled Fast Reactor
SFT	Stacking Fault Tetrahedron
TEM	Transmission Electron Microscopy
VASP	Vienna *Ab initio* Simulation Package
VHTR	Very High Temperature Reactor
VVER	Water-Water Energetic Reactor

1 Introduction

1.1 History of application of nuclear energy for electricity production

All of us cannot imagine the contemporary world without electricity, but only a few people consider the safety of the production technology and its impact on the environment. Nuclear energy is considered to be one of the best sources of electric power due to such advantages as the price of energy, absence of harmful emissions (the emission of isotopes from the nuclear power plant is much below the one of a coal power plant), high ratio of kW·h/(exploitation+fuel expenses) (see Fig. 1.1), possibility of the reusage of fuel, and the high power capacity of a reactor unit (up to 1650 MW).

The history of the nuclear power plants (NPP) goes back to the year 1951 when in the experimental breeder reactor (EBR-1) in Arco (USA) a nuclear fission process gave enough electricity to illuminate four 200-Watt light bulbs and gradually reached an electric power of 0.2 MW. The first commercial nuclear power plant has been built in Obninsk (USSR), producing as much as 6 MW of electricity.

The successive development of nuclear reactors is often conventionally described with generations.

Generation I. These are the first prototype reactors built in the world up to the mid-1960s. The first Belgian reactor (BR1), shown in Fig. 1.2, had been constructed by 1956 and after reaching the criticality level, the output electrical power was 4 MW. It used natural uranium as fuel, graphite as moderator and air as coolant. The chain reaction was maintained via the interaction

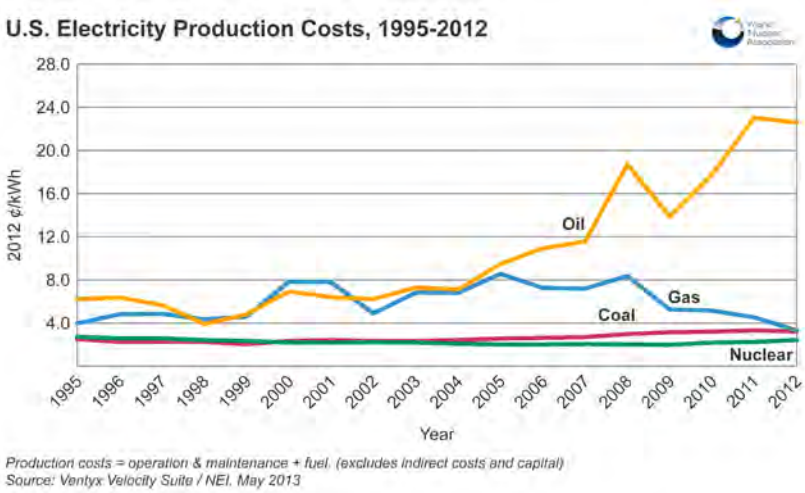

Figure 1.1: U.S. production costs for electricity generated by coal, gas, oil and nuclear. From [1]

Figure 1.2: The first Belgian Reactor BR1 as of December 1956. The sides A and B with lifting platform for charging the reactor. From [2].

of the neutron flux, thermalized by the moderator, with the nuclear fuel. The relatively low neutron fluence in this reactor does not pose very specific requirements for the materials used and no operational lifetime limitation based on the degradation of the structural materials was considered.

Generation II. The reactors built in 1965–1995 are considered to be in this group. As this time in history is famous for the Cold War, competition between the countries and social-political systems led to differences in the types of reactors constructed. The United States and many other Western countries were building two types of reactors which belong to the class of light water reactors (LWR): pressurized water reactors (PWR) and boiling water reactors (BWR). The enrichment of uranium fuel up to about 3% is necessary for their operation.

The *PWR* is the prevalent type (more than 60% of commonly used nuclear reactors) for power production in the world and, in particular, in Belgium. In a PWR (see Fig. 1.3a) ordinary water is used as coolant and moderator. This water in the primary loop is kept under a high pressure of about 160 bar to prevent it from boiling. The operational temperature is about 300 °C. Such reactors are generally considered very safe although in March 1979 it happened the Three Mile Island accident with a partial nuclear meltdown of the reactor.

BWRs (see Fig. 1.3b) also use, as coolant and moderator, water under a pressure of about 75 bar, which exists in the form of water and steam at a temperature of about 300 °C. The advantage of lower pressure is that it allows one to use a single loop system (in contrast to the higher pressure and two-loop design of PWRs), but this is counterbalanced by worse moderation, lower neutron efficiency and consequently lower power density. Reactors of this type were involved in the accident at the NPP in Fukushima, Japan, in March 2011 following the earthquake and tsunami. At present 20% of working NPPs are using this type of reactors.

The former Soviet Union was building two main types of reactors: high power channel type reactors (RMBK as they are abbreviated in Russian translation) and water-water energetic reactors (VVER in Russian). In RMBKs light water is used as a coolant and graphite for moderation so natural uranium in metallic form can be used as nuclear fuel, thereby lowering the price of the kW·h. Unfortunately, the safety of such reactors was disproven in the severe Chernobyl accident in April 1986. As of 2014 only 11 RBMK-type reactors remain in operation in Russia. The construction of new reactors of this type was suspended in 2012. VVER reactors are of the same type as PWR reactors, are widely in operation and are currently planned or being built in China, Hungary, Turkey, Slovakia, India, Finland and Russia.

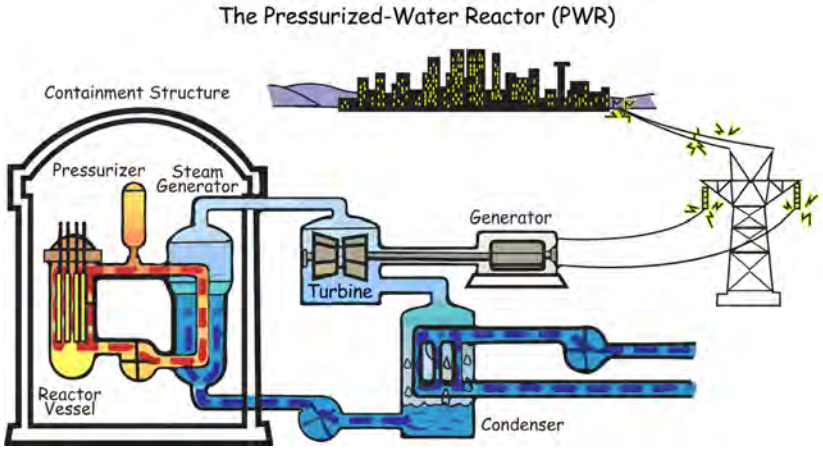

(a) PWR

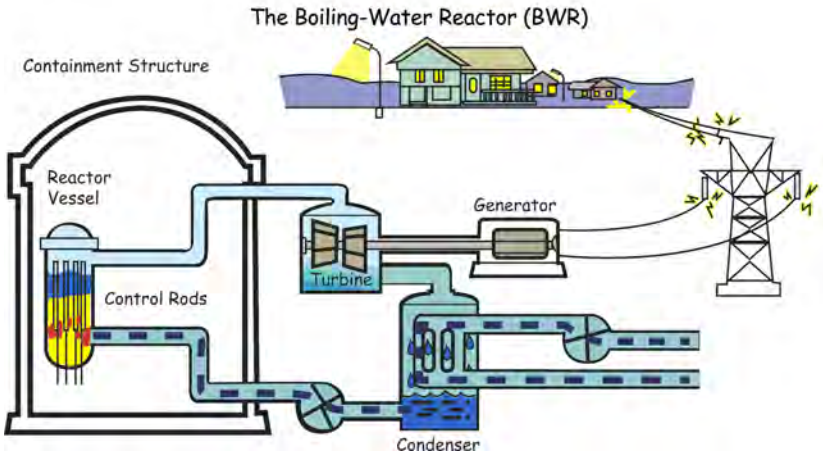

(b) BWR

Figure 1.3: The light water reactors: BWR and PWR. From [3].

CANDU stands for 'CANada Deuterium Uranium' reactor. It utilizes pressurized heavy water as coolant and moderator, and runs on natural uranium fuel. Unlike PWRs, a CANDU reactor is of the channel type setup, with the possibility of online-refuelling. At present 19 CANDU reactors are in use in Canada and 12 in the rest of the world.

AGR is an acronym for advanced gas-cooled reactors developed in Great Britain. Here, the graphite is used as moderator for the neutrons, and carbon dioxide serves as coolant. An improved thermal efficiency is ensured by the elevated gas temperature (up to 640 °C at a pressure of ~40 bars) which in turn requires the ability of stainless-steel cladding to withstand the higher temperature. This cladding is characterized by a high neutron capture cross section, thereby causing the necessity of using enriched uranium fuel. Currently, the United Kingdom possesses seven nuclear power plants of this type. All of them are in operation with two reactor units per power plant.

There are much higher neutron fluences and an elevated temperature regime in such reactors, compared with the GEN I reactors. These issues lead to special requirements for the construction materials in terms of improved mechanical properties and susceptibility to the harsh radiation, while keeping reasonable and affordable price. Nevertheless, the inevitable degradation of such materials under exploitation limits the operational lifespan of a reactor in NPPs. Special surveillance procedures using capsules inserted in the reactor pressure vessel are applied, in order to study the impact of the radiation on the degradation of material's properties. The results of these evaluations are accounted for in the NPP licensing inspections. The US originally licensed the nuclear reactors for 40 years, whereas in 2001, 8 units renewed the license (i.e. the allowance to be in operational use) up to 60 years. In Belgium the planned lifetime is 40 years with an inspection every 10 years.

Generation III. The first reactor of this generation has been built in 1996 in Kashiwazaki, Japan. Within this generation the reactors of the types PWR, BWR and CANDU undergo improvements in terms of advanced fuel technology, superior thermal efficiency, passive safety systems and standardized design for reduced maintenance and capital costs. Such reactors are planned to be in operation for a longer time than the ones of the previous generation (60 years of operation, with a possible extension up to 120+ years prior to complete overhaul and reactor pressure vessel replacement). Generation III reactors are being planned or are under construction in France, United Kingdom, Finland, USA, India and Russia. The EPR — European Pressurized Reactor is a follow-up of the third generation kind akin to the pressurized water reactor (PWR) design with an electrical power output of 1650 MW (net). It is often denoted as GenIII+.

The longer operational period imposed in the generation III creates a challenge in the selection procedure of appropriate structural materials. No specimens have been irradiated for a duration approaching that of the operational lifetime of generation III reactors, so we have no experimental proof that the currently considered materials can preserve acceptable properties over the planned operational period. The irradiation conditions in the material test reactors (MTRs) in principle can imitate the radiation dose accumulated up to long terms [4], although the effect of the increased dose rate on the radiation-induced microstructure of new materials should be studied. Also deeper, more intensive surveillance studies should be performed during the second (i.e. prolonged) part of the planned operational lifetime.

Generation IV. The reactors of this generation are still at the stage of concept and design development, and are not expected to be available for commercial use before 2030. The planned advantages of the GEN IV reactors are the following: reduced period of the highly radioactive stage of nuclear waste, a superior energy yield for the same amount of nuclear fuel, and the possibility to use existing nuclear waste to produce electricity as well as to produce more fuel than the amount used, in a closed fuel cycle perspective. Nevertheless such new technology, along with bringing improvements in safety, will initially pose new risks as reactor operators will have little experience with the new design. Within this generation six main concepts are proposed. Three of them are thermal reactors (where in the reactor core almost all neutrons have low energy) and the other three are fast reactors (where the neutron energy is higher, enabling to burn actinides to reduce the long-life waste and to breed more fuel).

The group of thermal reactors consists of the following concepts:

1. The *VHTR, very high temperature reactor*, uses graphite as moderator with helium or molten salt as coolant. The outlet temperature of 1000 °C increases the thermal efficiency and can be used for hydrogen production or co-generation.

2. The *MSR, molten salt reactor*, operates on either (a) nuclear fuel which is dissolved as uranium tetrafluoride (UF4) in the molten fluoride salt coolant, the fluid reaching criticality in a graphite core which serves as moderator, or (b) nuclear fuel dispersed in the graphite matrix, with the salts efficiently removing heat from the core. The low operation pressure reduces the reactor size.

3. The *SCWR, super critical water reactor* (see Fig, 1.4a), uses supercritical water (at temperature and pressure above the critical point, where it

has both gas and liquid properties) as moderator and coolant. It is essentially a light water reactor (as PWR and BWR) working at a high temperature and pressure. The reactor has high thermal efficiency and ensures considerable plant simplification.

The fast reactor concepts which do not use a moderator are:

1. The *GFR, gas-cooled fast reactor* (see Fig. 1.4b), uses helium as coolant: being an inert gas, it rarely reacts with any material and does not become radioactive while being exposed to radiation. The outlet temperature of 850 °C ensures very high thermal efficiency. The closed fuel cycle is established via the ability to breed new nuclear fuel by transmutation of fertile nuclides to fissile ones (for example, U^{238} to Pu^{239}). The reactor can operate on other types of nuclear fuels such as thorium or minor actinides.

2. The *SFR, sodium-cooled fast reactor*, follows the closed fuel cycle concept with good efficiency due to the high outlet temperature (> 500 °C). Passive safety is ensured, for if the reactor overheats the fuel expands, stopping the chain reaction. Sodium, being heavier than oxygen and hydrogen atoms, is better than water, when a moderator is not needed, since neutrons loose less energy in collisions with sodium atoms. There is no need for high pressure, as the boiling point of sodium is much higher than the operational temperature. Sodium also does not corrode steel reactor parts. A disadvantage of sodium is its chemical reactivity, which requires special measures to prevent and suppress fires. In contact with water and air, sodium explodes and burns, respectively.

3. The *LFR, lead-cooled reactor*, operates with lead or lead/bismuth eutectic liquid metal as a coolant. Unlike sodium, lead does not react significantly with water or air. While lead is cheap and abundant, bismuth, unfortunately, is expensive and quite rare. The LFR has a closed fuel cycle. The reactor is cooled by natural convection with a reactor outlet temperature of 550 °C, possibly ranging up to 800 °C with advanced materials. The reactor follows a turnkey design: the small power plant uses cassette cores running on a close fuel cycle with a 15 to 20 years' refuelling interval, or entirely replaceable reactor modules.

The structural materials for GEN IV type reactors are required to sustain an elevated temperature (up to 600–1000 °C), at which corrosion and diffusion-controlled processes are enhanced as compared to those expected under GEN II and GEN III conditions. The challenge to reduce nuclear waste can be

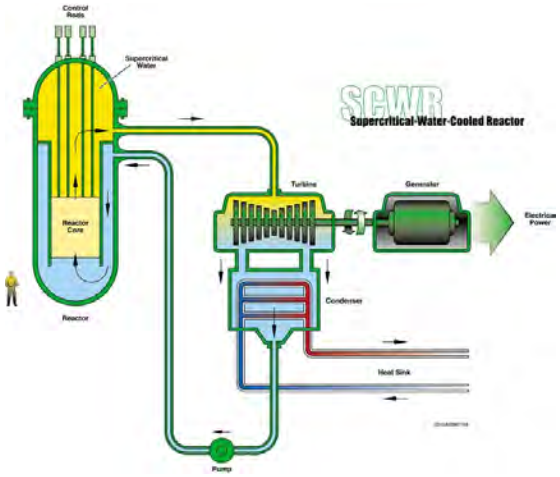

(a) The super critical water reactor (SCWR)

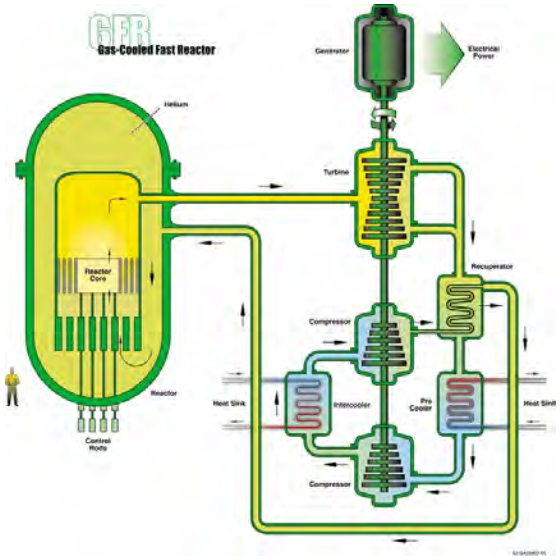

(b) The gas cooled fast reactor (GFR)

Figure 1.4: The examples of generation IV concepts. From [5, 6].

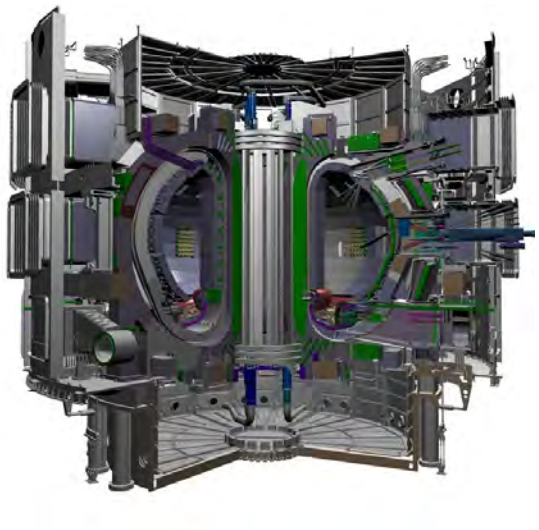

Figure 1.5: Cross-section of the ITER tokamak. From [7].

solved by a substitution of highly activated solute inclusions (minor alloying elements) with less activated equivalents. For instance, molybdenum can be replaced by tungsten and niobium by tantalum in the composition of typical high-Cr ferritic-martensitic steels. The further development and testing of new so-called reduced activation steels is necessary to ensure the exploitation safety by considering the introduction of the low activated substitutes.

Fusion reactors are based on a controlled nuclear fusion process and so far no reactor of this kind has been built for commercial operation. The advantages of such reactors will be the availability of fuel, financial profitability, security, reliability and the relief of the environment. The major problems in this technology are the confinement and the self-sustainment of the reaction. Currently, magnetic confinement is considered to be the most likely approach. The common fusion reaction is when light atoms like deuterium and tritium interact, producing a helium nucleus (an alpha particle) and a high-energy neutron.

The main facilities built or planned for the observable future are:

1. *JET*, which was constructed in 1984 in Oxfordshire (UK). It is the first tokamak in the world and still the world's largest. In 1997 it achieved 16 MW of power production, consuming 25 MW. It is worth noting that

the self-sustaining burning plasma requires at least 5 times more energy release over the input heating power, since the alpha particles carry one fifth of the fusion energy. A fusion power plant requires an excess of at least 10 times;

2. *ITER*, which is the large scale international fusion experiment (see Fig. 1.5) to be based in Cadarache (France), exploring the possibility of 10 times energy out-to-in excess while producing 500 MW of fusion power. The initial plasma experiments are planned to start in 2020, but it is not expected to begin with full deuterium-tritium fusion until 2027;

3. *DEMO* is the first commercial DEMOnstration fusion power plant, where it is planned to produce at least four times the fusion power of ITER, on a continual basis. The energy excess out-to-in is expected to be 25 times. The first construction phase is to last from 2024 to 2033.

1.2 Current nuclear power installations

As of mid-2013, a total of 31 countries were operating nuclear fission reactors for energy purposes. Nuclear power plants generated 2,346 terawatt-hours (TWh or billion kilowatt-hours) of electricity in 2012, less than in 1999 and a 172 TWh or 6.8 percent decrease compared to 2011, as well as 11.8 percent below the historic maximum of nuclear power generation in 2006 [8]. The maximum relative contribution of nuclear power to commercial electricity generation worldwide was reached in 1993, with 17 percent (see Fig. 1.6). It has dropped to 10.4 percent in 2012, a level last seen in the 1980s [8].

Figures for 2013 show that in France (73.28%), Slovak Republic (48.32%) and Belgium (47.92%) [10] a large part of the total energy supply is obtained with nuclear reactors The most popular types (>30 power plants) of nuclear reactors currently working in commercial NPPs are PWR (271), BWR (84) and CANDU (48) out of 436 in total as of 2012 [11]. At the moment seven PWR nuclear reactors allocated in two nuclear power plants are working in Belgium with a total power capacity of 5927 MW [12].

1.3 Materials issues in nuclear reactors

The exploitation of a nuclear reactor is a very challenging and difficult problem. Many thousands of quality assurance procedures must be followed

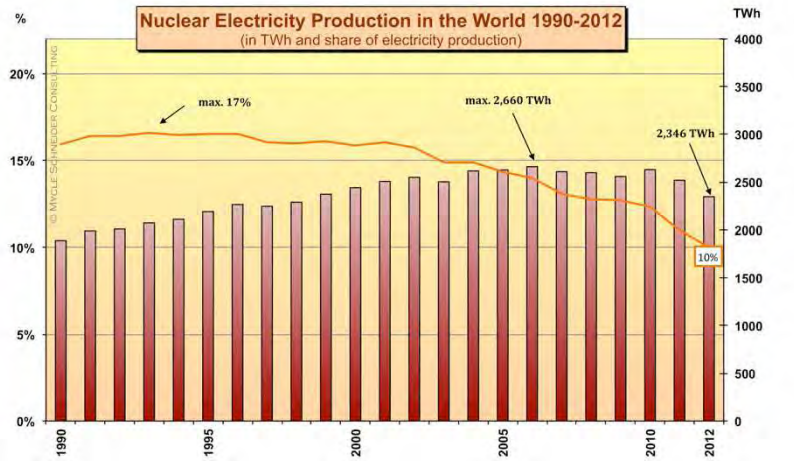

Figure 1.6: Nuclear electricity generation in the world. From [8].

Figure 1.7: Irradiation-assisted stress corrosion cracking has resulted in cracking at the head of a baffle bolt. From [9].

to ensure the safe operation of a nuclear reactor, starting from the high reliability of construction materials up to waste management. One of the main concerns in nuclear energy is the selection of proper materials for a nuclear reactor. At present steels of different brands are used in the reactor and all of them undergo degradation (in terms of mechanical, or chemical or physical properties) being exposed to harsh radiation while in operation. Some of the reactor components can be replaced, for instance, compact elements such as bolts made of austenitic stainless steels, whereas others, like the large reactor pressure vessel, are almost impossible to replace due to the complexity of this procedure and the enormous cost. To get an idea of how the failure of the components takes place, one can consider (see Fig. 1.7) the cracked bolt made of austenitic stainless steel where degradation has happened due to exposure to radiation, accompanied by an applied stress and corrosion, originating from the contact with water.

To rationalize the global impact of irradiation on nuclear steels we have to scale-down and consider the processes occurring at the femto-second time and nano-meter space scales (see Fig. 1.8). High kinetic energy neutrons bump into the atoms of the material, causing their displacement from equilibrium sites. Such atoms are called primary knock-on atoms (PKA). PKAs generate consequently displacements of neighbour atoms resulting in a process called 'displacement cascade' or 'collision cascade'. After the spontaneous recombination a fraction of the cascade-affected volume does not return to its perfect crystallographic structure, which results in the appearance of lattice defects. The most typical point defects (PDs) are self-interstitial atoms (atoms located between the equilibrium sites, expanding the lattice) and a vacancy (absence of an atom in the equilibrium position). For a group of multiple vacancies or self-interstitials it is energetically favourable to gather, forming spherical clusters of vacancies and platelets of self-interstitials (see Fig. 1.9a), which are referred to as voids and dislocation loops, respectively. Dislocation loops of vacancy nature (see Fig. 1.9b) are also observed in different metals under irradiation. A fraction of the in-cascade generated defects recombines, but a certain part contributes to the growth of the already existing clusters, whereas the remaining PDs diffuse and incorporate (i.e. disappear) at extended lattice defects such as dislocations and grain boundaries. As a consequence of point defect diffusion, the mass transfer may result in a significant rearrangement of solutes and interstitial impurities, naturally present in commercial steels, leading to the formation of precipitates and zones with local enrichment or depletion. Correspondingly, the usual sinks for point defects, such as dislocations and grain boundaries, are the most segregation susceptible zones.

The presence of radiation defects causes a directly observable modification of

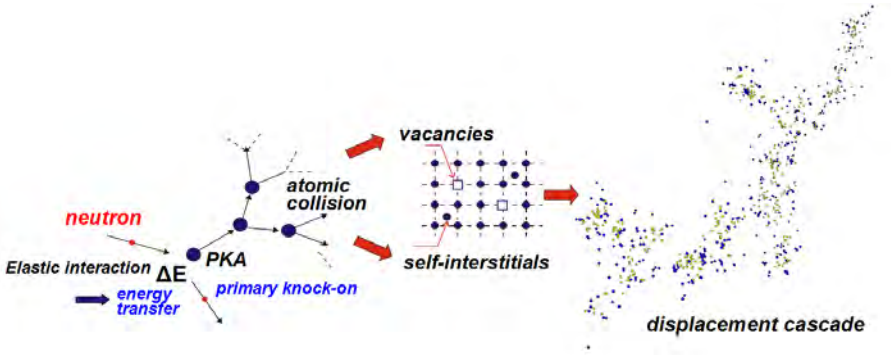

Figure 1.8: The scheme of the primary neutron damage.

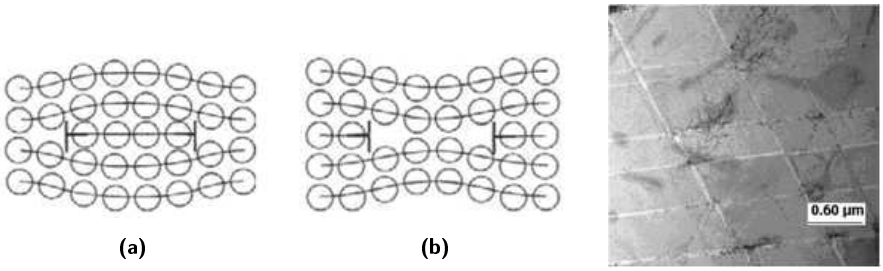

(a) (b) (c)

Figure 1.9: The radiation effects in the material: a) dislocation loop of interstitial nature, from [13]; b) dislocation loop of vacancy nature, from [13]; c) transmission electron microscopy (TEM) micrograph of the clear bands appeared after the plastic deformation of the irradiated austenitic stainless steel, from [14].

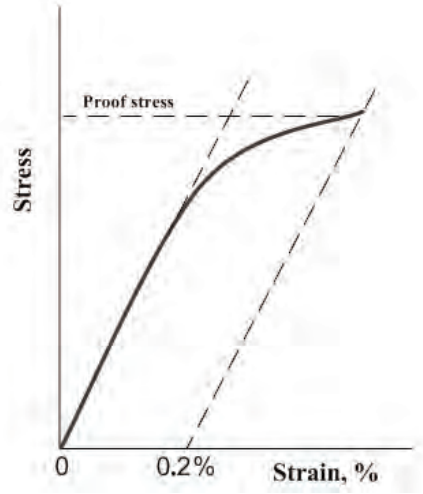

Figure 1.10: The determination of the yield stress. From [16].

the material, for instance the intensive growth of voids, called swelling, is seen as an increase of specimen dimension. The actual voids, however, can not be seen without special equipment for microstructural characterization. Swelling, however, does occur at the high irradiation doses expected for GEN IV and fusion structural materials. In the case of moderate doses (i.e. 0.1 displacements per atom (dpa) for the vessel of PWR [15]), the irradiation-induced microstructure consists of nano-metric radiation-induced precipitates and dislocation loops. Accumulation and growth of the latter defects has a far more complicated effect on the mechanical properties of structural steels. Generally, the presence of numerous nano-sized lattice imperfections leads to an increase of the yield stress (this effect is called hardening (see Fig. 1.11b)), but at the same time is expressed in the reduction of ductility (or total elongation before fracture, see Fig. 1.11b) and shift of ductile-to-brittle transition temperature (i.e. embrittlement, see Fig. 1.11c). The hardening is generally measured as the difference of yield stress at 0.2% plastic strain (see Fig. 1.10) of irradiated and unirradiated materials.

The origin of these changes is rationalized as the suppression of plastic deformation caused by radiation damage. Plastic deformation in structural steels is ensured by dislocation movement, and the radiation-induced defects (RID) act as obstacles for mobile dislocations. Hence, dislocation-RID interaction causes hardening, which is usually quantified by mechanical tensile tests reporting

the stress-strain response under uni-axial loading. Such tests provide both the yield stress and total uniform elongation – one of the most important parameters for the engineering design codes. The measurement of the ductile to brittle transition temperature (DBTT), which is another measure of post-irradiation embrittlement, is realized by the impact Charpy method (see Fig. 1.11a), at which the deformation loading rate is much faster than in the standard tensile tests.

Since the principal mechanisms of embrittlement are the same in both experimental conditions (i.e. Charpy and tensile tests), the hardening is linearly related to DBTT shift. However, the concept of the DBTT is strictly applicable to steels with body centered cubic (bcc) structure such as ferritic, martensitic, bainitic ones. The sharp transition from ductile to brittle behaviour in bcc metals and alloys originates from the relatively high activation energy for dislocations (~1–2 eV [13]). In austenitic steels, which have face-centered cubic (fcc) lattices, the activation of dislocation movement requires much lower energy ($\leq$ 0.2 eV [13]) because of the splitting of dislocations (as will be described later). The embrittlement in austenitic steels is therefore measured by the reduction of the total elongation to fracture. A limiting case for the latter is its absence i.e. as soon as the yield point is reached the specimen reveals a catastrophic failure. This phenomenon is called plastic instability and its occurrence is observed after irradiation below a temperature of $0.2 \cdot T_m$ in both ferritic-martensitic and austenitic steels. The physical understanding of the plastic instability is attributed to the ability of dislocations to remove the RIDs, so that once the yield point is reached the activated dislocations form 'dislocation channels' (or often called 'clear bands'), thereby making the material inhomogeneous. The 'dislocation channels' (see Fig. 1.9c) correspondingly act as 'fast tracks' for the dislocation movement, which results in the formation of dislocation pile-ups at the end of channels (grain boundary). The stress concentration near the zones with highly localized plastic deformation is likely to cause crack nucleation and therefore the initiation of a brittle failure. We are not aware of a direct experimental observation of the formation of dislocation channels in commercial steels, as the process of in-situ TEM deformation is extremely complicated and so far has been performed only for soft materials (i.e. fcc metals and pure bcc iron). The proper quantitative explanation of the hardening, related embrittlement and plastic instability phenomena therefore requires an alternative way to obtain detailed information on the interaction of dislocations with the microstructural features induced by irradiation. Since the RIDs observed in technologically important irradiation conditions are typically of nano-meter size, the consideration of their interaction with dislocations cannot be completely accounted for by classical elasticity theory and requires a fine-scale atomistic approach. The application of the latter to the problem of

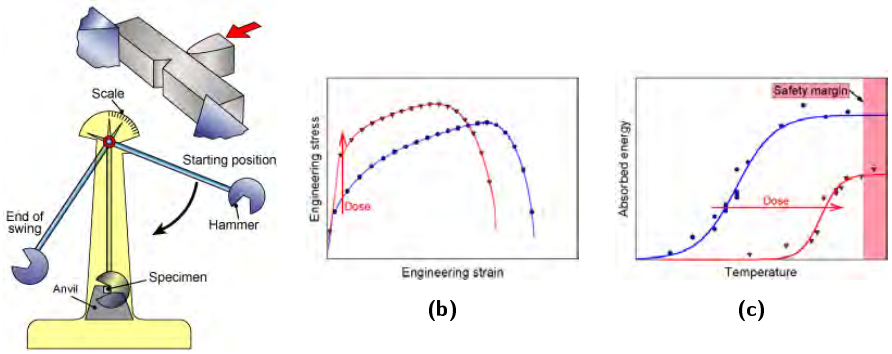

Figure 1.11: Macroscopic effects of radiation in stainless steels. a). Charpy impact test device. From [17], b). The stress-curve showing hardening effect. From [4], c). The DBTT shift as illustration of radiation-induced embrittlement. From [4].

hardening and plastic instability in commercial steels for nuclear applications is the subject of the present thesis.

1.4 Objectives of the thesis

The aim of this thesis is to study the radiation-induced degradation of mechanical properties by means of modelling of the interaction of relevant RIDs with dislocations at the atomic level, taking into consideration the following types of commercial steels:

1. the austenitic stainless steels of the 316 and 304 series used for internal structural components such as formers, baffle plates, bolts;
2. the reduced activation ferritic-martensitic steels of 9Cr type which are the primary candidates for the GEN IV and fusion reactors;
3. the RPV bainitic low copper steels which are used for the reactor pressure vessel in GEN II reactors.

The motivation of the present work comes from the fact that experimental studies of the deformation mechanisms in neutron irradiated samples are either very expensive (as the investigation of the activated materials requires hot-cell protection and remote handling) or even technically impossible. The

computational materials science methods offer a cheaper and elegant way to address the problem at its origin — an atomistic description of the dislocation-RID interaction. The information obtained through atomistic simulations should then be properly used in the up-scale coarse-grain models to derive the properties of materials at the macro-scale.

As mentioned earlier, the change of macroscopic mechanical properties is attributed to the presence of the RIDs which may be irresolvable to TEM techniques. The computer simulation approach does not have such a limitation, and allows one to obtain information on the contribution to plastic deformation defined by 'invisible' damage.

The accumulation of the dose relevant for the future nuclear setups (e.g. GEN IV) in the currently operating research reactors can take a very long time. For example, the Belgian material test reactor BR2 can deliver a dose of up to 0.5 dpa per cycle. While one cycle is 21 days [18], the accumulation of several tens of dpa would take several years making the cost of such irradiation experiments enormously high.

Using a combination of several computational techniques forming the multi-scale chain one solves the problem of time, dose rate, temperature and others, by the application of thoroughly validated tools. Real commercial steels are metallic alloys with rich chemical composition and complex microstructure, hence the explicit treatment of such materials at atomic level is impossible. By considering model alloys, i.e. Fe-based alloys including the key chemical elements, appropriate lattice structure and properties mimicking that of the real steel, a clear advantage of the computer simulation is its ability to identify prevailing factors controlling the processes/mechanisms of radiation-induced embrittlement.

The general structure of the thesis is the following: in this introduction (chapter 1) a general overview of the application of nuclear and fusion energy for electricity production has been given, together with an introduction to the theory of radiation damage in solids, as well as the experimental practice of its characterization and measurement. The motivation for the selection of materials to study and the applied methods are also discussed.

In chapter 2 a summary of the currently available results on the radiation-induced degradation of steels is presented. The main focus is on the austenitic stainless steels which have a face-centered cubic (fcc) crystallographic structure. Detailed information about the application and chemical composition of the steels is also provided. The available data about the radiation-induced microstructure in austenitic steels at different temperatures are summarized. The results of the studies on the macroscopic effects of the presence of

radiation-induced defects in the form of hardening and embrittlement due to the formation of dislocation channels, are also discussed. To this regard previously published nanoscale explanations of the origin of these effects in fcc materials, obtained with the molecular dynamics (MD) method using the dislocation-defect interaction modelling, are reviewed. Concerning the FM and RPV steels, that have a body-centered cubic (bcc) lattice, radiation damage can be decomposed into a matrix damage (formation of dislocation loops) and the nucleation of solute-rich precipitates. The current explanations of the nanostructural evolution in both steels leading to hardening and previous results on the dislocation-defect interaction in bcc metals are summarized.

The main methods applied in this thesis are the electronic structure calculations using density functional theory (DFT) and classical molecular dynamics simulations, whose basics are described in chapter 3. The general scheme of application of each of the methods is given as well.

Chapter 4 provides a short summary of the results obtained, and is subdivided according to the types of steels considered. In the austenitic stainless steels the radiation-induced degradation is addressed by modelling the dislocation-defect interactions in the Fe-Ni and Fe-Ni-Cr model alloys. The effect of temperature, SFE, defect size and interaction geometry on the hardening and absorption of the defects (leading to the formation of dislocation channels) is studied. In the case of FM and RPV steels we address the thermodynamic mechanisms leading to the formation of nanometric solute-rich clusters invisible to TEM observations, and estimate their contribution to radiation-induced hardening.

In chapter 5 we present conclusions and an outlook to future developments in the modelling of the impact of radiation damage on plasticity mechanisms.

The **papers I–XII**, on which this thesis is largely based, are added as appendices.

2 Radiation damage in nuclear steels

Radiation damage in structural steels is a very complex problem (as shown in the Introduction section 1.3), which differs significantly depending on the crystallographic structure of the material considered. In this thesis three grades of structural steels are addressed, where radiation-induced hardening has been observed experimentally. They will be grouped according to the lattice type: fcc-structured austenitic stainless steels, which are the main focus of this work, and the bcc-based FM and RPV steels.

The structure of this chapter is the following: firstly, for each group of steels general information about their application and main properties is summarized. Then the chemical composition and the role of alloying elements are considered. Next, the irradiation-induced microstructure is described: the formation of precipitates and matrix damage. Neutron irradiation affects the mechanical properties of steels leading to hardening, plastic instability (in austenitic steels), swelling, creep, and enhanced corrosion. In this thesis the focus is on radiation-induced hardening and plastic instability due to dislocation channeling. The effects of ambient factors (temperature, dose) are discussed regarding both the microstructure damage and the mechanical properties.

2.1 Fcc materials: austenitic stainless steels

2.1.1 Application and properties

Austenitic stainless steels are used as a material for the internal structures of pressurized water reactors, which are located close to the reactor core. They are also considered as cladding and core reactor materials in GEN IV systems. Such steels are applied to support the fuel assemblies, to maintain the alignment between assemblies and the control bars and to canalize the primary water. In general these internal structures consist of baffle plates made of solution annealed (SA) 304 stainless steel and baffle bolts made of cold worked (CW) 316 stainless steel [19].

In a nuclear reactor these steels experience a large neutron flux at temperatures between 280 °C and 380 °C. They are exposed to a radiation dose up to 80 dpa assuming a 40-year life cycle and depending on fuel management [20].

The main advantages of this class of steels are [14]:

- *superior corrosion resistance* in comparison to ferritic and martensitic steels: corrosion performance may be varied to suit a wide range of service environments by careful alloy composition adjustment, for example, by varying the carbon or molybdenum content;
- *excellent formability*: the response of austenitic steels to deformation can be controlled by chemical composition;
- *no impact property/response transition* at low temperatures and high toughness up to cryogenic temperatures;
- *weldability*.

Unfortunately, such steels are characterized by a greater thermal expansion and heat capacity, with lower thermal conductivity than other stainless or conventional steels. Also note that austenitic stainless steels can not be hardened by heat treatment and are therefore strengthened by cold working.

2.1.2 Chemical composition and its metallurgical effects

The chemical composition of the austenitic stainless steels of 304 and 316 type according to AISI standard [21] and the one of SA304 and CW316 from [19] are shown in Table 2.1. According to the AISI classification, the stainless steels

Table 2.1: The chemical composition (in wt%) of the 304 and 316 austenitic steels.

Steel	C	S	P	Si	Mn	Ni
304 [21]	0.08	0.030	0.045	1.00	2.00	8.00–10.50
304L [21]	0.03	0.030	0.045	1.00	2.00	8.00–12.00
SA304 [19]	0.022	0.0007	0.032	0.36	1.79	9.86
316 [19]	0.054	0.0220	0.027	0.68	1.12	10.60
316 [21]	0.08	0.030	0.045	1.00	2.00	10.00–14.00
316L [21]	0.03	0.030	0.045	1.00	2.00	10.00–14.00

	Cr	N	Mo	Cu	Co	B
304 [21]	18.00–20.00	–	–	–	–	–
304L [21]	18.00–20.00	–	–	–	–	–
SA304 [19]	18.61	0.061	–	0.25	0.064	0.0005
316 [19]	16.60	0.023	2.25	0.24	0.120	0.0005
316 [21]	16.00–18.00	–	2.00–3.00	–	–	–
316L [21]	16.00–18.00	–	2.00–3.00	–	–	–

of a 3XX type are the austenitic ones with, as major alloying elements, nickel (6–12%) and chromium (16–26%). Among them, the steels of 304 type have a lower carbon content to avoid its precipitation. In the 316 steel molybdenum is added for better corrosion resistance. The steels 304L and 316L have a lower carbon content for welding applications. The standard 304L steel is solution annealed. Its microstructure consists of recrystallized grains (~40 μm) which contain few dislocations and a small amount of ferrite (< 1%) [19]. The standard 316 steel is 15% cold worked. It is fully austenitic containing more Ni and Mo and less Cr than the SA 304L steel [19]. The grain size is also about 40 μm.

Chromium forms [14] a protective oxide layer on the steel surface starting from the concentration of 10.5%. The strength of this protective (passive) layer increases with further addition of chromium. It prompts the formation of ferrite within the alloy structure and is described as ferrite stabiliser. Nickel improves [14] general corrosion resistance and prompts the formation of austenite (i.e. it is an austenite stabiliser). Stainless steels with 8–9% nickel have a fully austenitic structure and exhibit superior welding and working characteristic compared to ferritic stainless steels. Increasing nickel content beyond 8–9% further improves both corrosion resistance (especially in acid environments) and workability.

Minor alloying elements (MAE) can be added to improve the properties of the fabricated steels. Among them the most important are the following [14, 22]:

1. *carbon* enhances the strength of the steel but it may have an adverse affect on corrosion resistance by the formation of chromium carbides on grain boundaries;
2. *molybdenum* increases resistance to both local (pitting, crevice corrosion, etc.) and general corrosion, while improving strength and hardenability;
3. *silicon* improves resistance to oxidation, strength;
4. *manganese* increases the solubility of nitrogen in the steel and may be used to replace nickel in nitrogen-bearing grades;
5. *nitrogen* increases strength and enhances resistance to localized corrosion;
6. *sulfur* is an impurity, which is added to improve the machinability of stainless steels;
7. *phosphorus* is an unwanted impurity which increases hardness and strength, but decreases ductility.

Among the listed MAE the austenite former elements are Mn, C and N, whilst the ferrite-stabilizing elements are Si and Mo.

2.1.3 Radiation-induced microstructure

An extensive summary of the effects of neutron irradiation on the microstucture of austenitic stainless steels at different temperatures and accumulated doses has been written by Zinkle et al. [23]. The lack of systematic data at low temperatures (< 350 °C) and low doses (< 10 dpa) in this work was filled by the studies of Pokor et al. [19, 24] where radiation damage in austenitic stainless steels including SA 304L and CW316 was investigated both experimentally and theoretically. In the latter work, the density and sizes of Frank loops after irradiation at 320 °C and 375 °C in material test reactors EBR II, BOR-60 and OSIRIS to doses up to 40 dpa are characterized using the TEM techniques.

2.1.3.1 Precipitates

According to Zinkle et al. [23] several different precipitate phases (like carbides and intermetallics) are normally formed in 316-type austenitic steels during thermal aging at 550 °C to 900 °C even in the absence of irradiation. Neutron irradiation causes the formation of new or composition-modified phases which are not observed during thermal aging. Fig. 2.1 shows the experimental dose

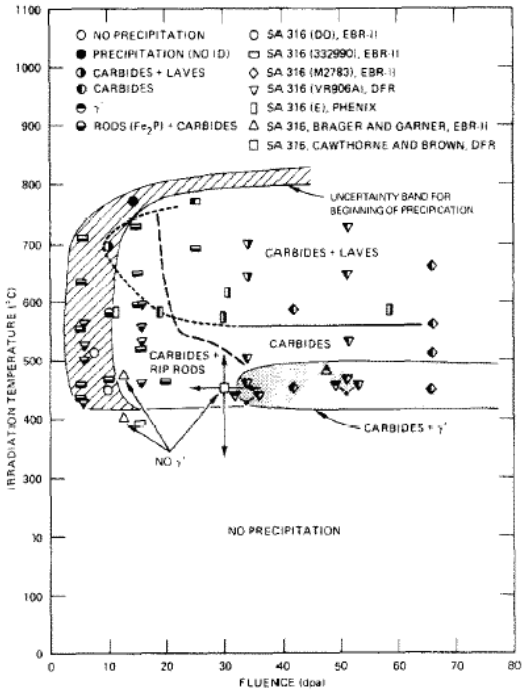

Figure 2.1: Temperature and dose regimes where the precipitation is observed in SA 316 stainless steel irradiated in fast neutron fission reactors. From [23].

and temperature regimes in which precipitation has been observed in SA 316 austenitic steel following the fast reactor irradiation.

In general precipitation occurs only in the temperature range of about 400–800 °C for both mixed-spectrum and fast reactor irradiations [25, 26]. Pronounced precipitation typically does not occur below 1–10 dpa. The 'steady-state' precipitate microstructure is reached starting from the dose of 50 dpa. No precipitation at low doses and temperature below 375 °C has been reported in [19]. Hence, at moderate doses and temperature below ~375 °C the degradation of mechanical properties of austenitic steels is mainly driven by the accumulation of radiation-induced lattice defects.

2.1.3.2 Matrix damage

The typical radiation-induced defects in fcc materials are: Frank dislocation loops with Burgers vector **b**=1/3<111> (with stacking fault inside the loop), perfect dislocation loops with **b**=1/2<110> (without stacking fault), stacking fault tetrahedra (SFT), which are tetrahedron-shaped defects with the sides in the 111 planes, and voids. The computer modelling visualizations of these objects are shown in Fig. 2.2 (see figure caption for explanation).

According to [22, 23] the microstructural damage can be conventionally divided into the three temperature regimes (see Fig. 2.3).

Low temperature regime (below about 300 °C). The typical microstructural features observed in this regime are small defect clusters (so called 'black spots'), faulted Frank dislocation loops, and network dislocations [25, 29]. Their observable densities are nearly independent of irradiation temperature in this low-temperature regime (see Fig. 2.3). The 'black spot' density starts to decrease above ~250 °C. The saturation density of the loop and defect clusters is generally achieved at doses of the order of 1 dpa in this regime.

In the low temperature regime the dominant microstructural feature is a high density of small 'black spot' defect clusters. The average size of the small defect clusters is about 2 nm [29–33]. Numerous studies performed on Fe-Ni-Cr alloys and pure fcc metals indicate that much of the 'black spot' cluster density is created directly in the displacement cascades [33, 34]. The total density of the small defect clusters in austenitic steel is comparable to the densities observed in pure fcc metals of similar mass, such as Ni or Cu. However, it is interesting to note that the fraction of defect clusters that are resolvable as stacking fault tetrahedra in stainless steel is < 1% [31–33], which is much less than the corresponding fraction of 2.5 to 50% observed in Ni or Cu following irradiation at comparable conditions [35]. This points to the fact that the solutes in stainless steels somehow modify the displacement cascade evolution behavior and inhibit SFT formation in it. As a result, the primary defects seen in the austenitic steels are Frank loops, unlike in the pure fcc metals.

High temperature regime (~300 °C to 700 °C). The effect of irradiation consists in the formation of cavities (helium bubbles and/or voids), precipitates, loops and network dislocations. The steady-state microstructure is approached at doses in excess of 10 dpa. Due to complex interactions between the various microstructural components that form during irradiation, a transient regime is typically observed in commercial stainless steels during irradiation at elevated temperatures. This slowly evolving transient may extend to damage levels in excess of 50 dpa in typical 300-series stainless steels, and to > 100 dpa in radiation-resistant developmental steels. The detailed evolution of any

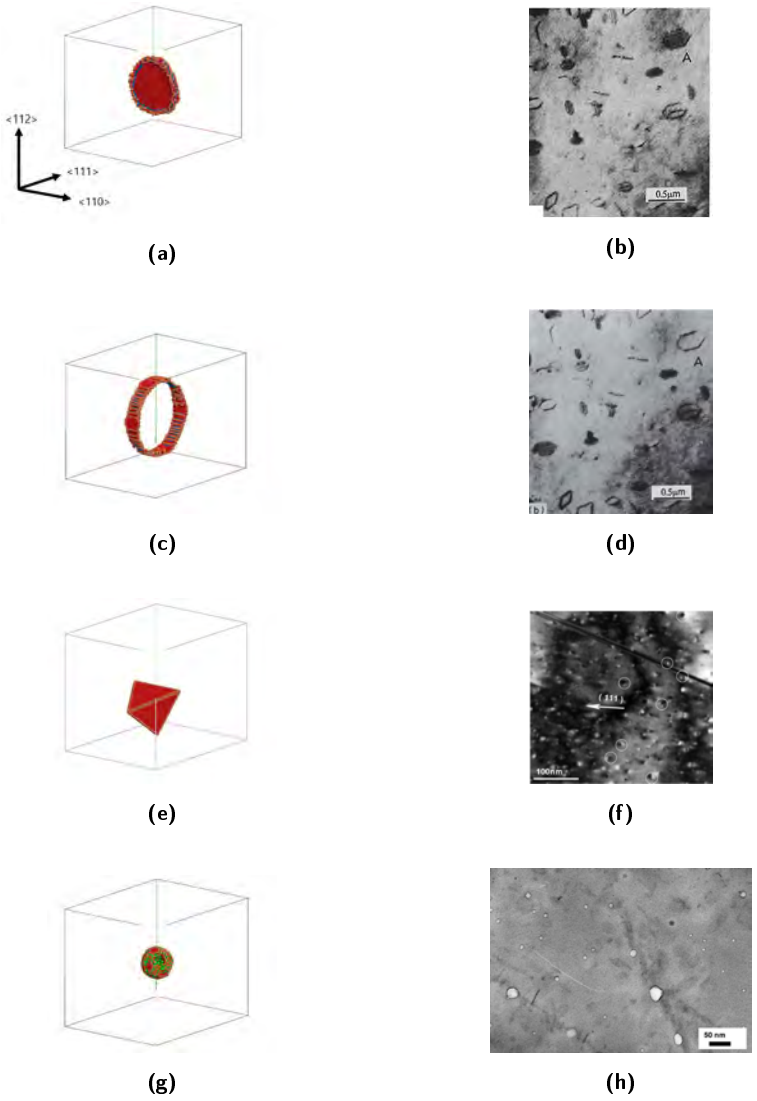

Figure 2.2: The atomistic visualizations of the typical radiation defects in fcc materials a). Frank loop; c). perfect loop; e). SFT; g). void. The orientation of the crystal is the same in all figures (a,c,e,g). The showed atoms were selected using the coordinate number and local neighbourhood analysis (see section 3.2.1 for details). Figures b),d),f) and h) are the TEM micrographs of Frank loops (marked with A) in fcc aluminium 3.5% magnesium alloy, perfect loops (marked with A) in fcc aluminium 3.5% magnesium alloy, SFT and voids in austenitic steels, respectively. The images are from [14, 27, 28].

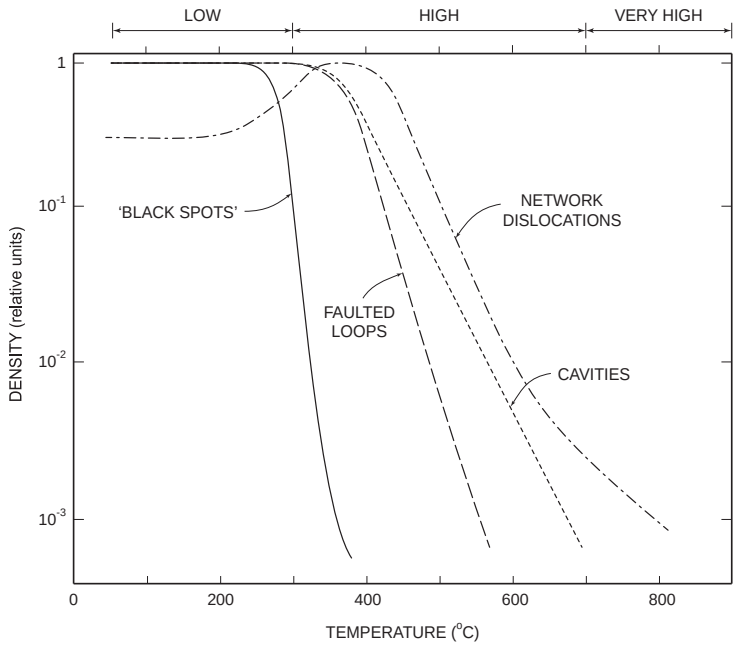

Figure 2.3: Temperature dependence of the experimentally observed 'saturation' densities of the various components in neutron-irradiated austenitic stainless steel. The explanation of the low/high/very high temperature regimes is given in the text. From [23].

given microstructural component in the high-temperature regime is sensitive to slight variations in numerous experimental variables, including the neutron spectrum.

In the study of Pokor et al. [19] two different austenitic alloys (SA 304 and CW 316) irradiated at 330 °C were found to have a similar microstructure. For doses up to 3.4 dpa, it consisted of interstitial Frank loops located in the 111 planes with Burgers vector 1/3<111> and of black dots. In the Fig. 2.4a and 2.4c one can see the TEM micrographs of Frank loops and black dots in SA 304 irradiated up to a dose of 0.8 dpa. Neither irradiation-induced precipitation nor cavity formation were observed.

In the same paper [19] an attempt to explain the nature of black dots has been made. At low dose (0.8 dpa), when both Frank loops and black dots can be observed simultaneously, it was possible to obtain the size distribution of the

Table 2.2: Quantitative analysis of Frank loops at 330 °C for the two alloys indicated. From [19].

Alloy	Dose (dpa)	Frank loop diameter (nm) ±2 nm	Frank loop density (m^{-3})
SA 304	0.8	4.7	$45 \cdot 10^{21}$
	2	5.9	$74 \cdot 10^{21}$
	3.4	7.4	$63 \cdot 10^{21}$
	20	7.3	$62 \cdot 10^{21}$
	40	7.0	$77 \cdot 10^{21}$
CW 316	0.8	9.3	$28 \cdot 10^{21}$
	2	7.7	$28.8 \cdot 10^{21}$
	3.4	10	$31 \cdot 10^{21}$
	10	7.5	$60 \cdot 10^{21}$
	20	7.4	$44 \cdot 10^{21}$
	40	7.3	$62 \cdot 10^{21}$

two types of defects. The black dots were imaged in the so-called 'bright field' mode and the Frank loops in the 'dark field' mode. As the average size, the density and the size distributions of the two families were identical (see Fig. 2.4b), Pokor et al. [19] claimed that black dots and small Frank loops are one single defect seen under different contrast conditions. When the dose increases (up to 40 dpa, accumulated by irradiation in BOR-60 reactor), the size and density of Frank loops increase too. The quantitative results for the average loop size and the loop density for the two steels considered and the various doses are summarized in Table 2.2.

As can be deduced from Table 2.2, the microstructure evolution [19] is rapid for doses under 10 dpa, and tends to saturate for larger doses. The loop sizes in the SA 304 and CW 316 steels are similar. The loop density is higher in the 304 steel than in the 316 one.

In a recent study performed at SCK-CEN [14] three austenitic alloys were considered: a reference austenitic steel (below referred to as Ref SFE) and two austenitic alloys with lower and higher SFE (below referred to as LSFE and HSFE alloys, respectively), both with chemical composition based on the reference alloy of the 304 type. These steels were irradiated at T=300 °C in the reactor BR2 (Belgium) up to the dose of 0.9 dpa. The SFE values of the materials were 11, 30 and 45 mJ/m^2 for the LSFE, reference and HSFE alloys, respectively.

The study pointed to a strong effect of the SFE on the radiation-induced defect

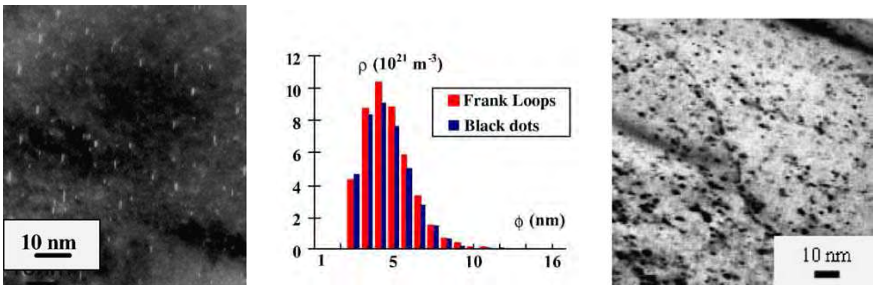

Figure 2.4: a) Imaging of Frank loops, b) size histogram and (c) black dots in SA 304 irradiated at 330 °C to a dose of 0.8 dpa. From [19].

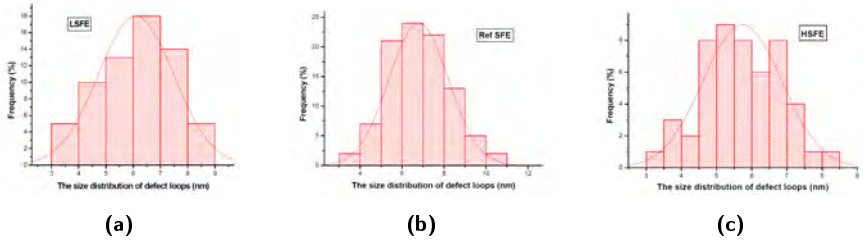

Figure 2.5: Size distribution of small defect clusters observed in three investigated alloys with different SFE in [14]. The lines represent the fitted Gaussian distributions for each alloy.

accumulation behavior. While a high density of Frank dislocation loops and black dots were observed in all three alloys (similar to what was observed earlier by Pokor et al. [19]) a low density of SFTs was found in LSFE and Ref SFE alloys. The mean size of the SFTs and Frank loops was almost the same, but the Frank loop density decreases in the alloys with a higher SFE. In the LSFE alloy, about 17% of the observed defect clusters were SFTs, while they were only about 8% in the reference austenitic steel. Loops of both interstitial and vacancy nature were observed in all three alloys: however, the density of the vacancy loops decreases as the SFE raises. In addition, the total density of the small defect clusters increases when the SFE increases: however, the average size of the clusters was almost the same (see Fig. 2.5 and 2.6).

Very high-temperature regime (above 700 °C). In this regime all radiation-induced defect clusters except for gas-pressurized bubbles are thermally unstable. Thus, the microstructure in this regime is identical to the one found in

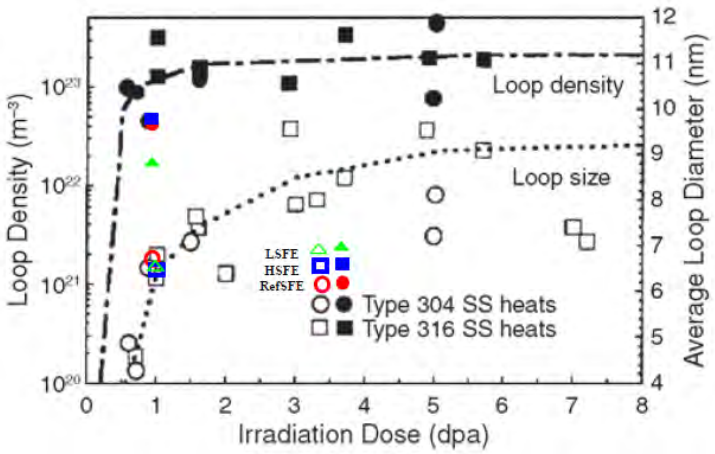

Figure 2.6: Density and size distribution of the three alloys with different SFEs [14] compared with the results on 300-series stainless steels irradiated at 270–290 °C [36]. From [14].

unirradiated steels aged at the same temperature. No significant concentrations of dislocation loops or radiation-produced voids are observed, and the precipitate and network dislocation behavior is equivalent to that observed under thermal annealing. Helium bubble formation can still happen in this temperature regime, but its behavior is determined primarily by the thermal equilibrium vacancy concentration and He concentration.

2.1.4 Macroscopic effects of radiation damage

2.1.4.1 Radiation-induced hardening

The studies of the hardening of austenitic stainless steels completed the investigation of the microstructure in the above mentioned works of Pokor et al. [19, 37] and Li [14]. It was established that hardening is a complex problem which depends on different factors, as is summarized below:

- *Damage dose*. The hardening increases rapidly at low doses saturating above 5 dpa independently of the materials (SA304L or CW316) and the irradiation conditions [37]. The value of saturation of hardening depends on chemical composition and initial metallurgical state.

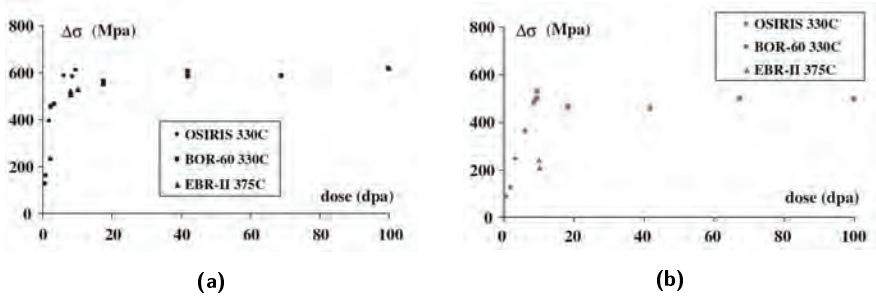

Figure 2.7: Hardening in different materials as a function of radiation damage dose: a) SA 304, b) CW 316. From [37].

- *Neutron irradiation parameters (flux, spectrum, temperature).* No obvious effect of the neutron spectrum and dose rate on the hardening of austenitic steels irradiated in different fission test reactors was found [37]. As shown in Fig. 2.7, for equivalent doses, the hardening is similar in materials irradiated in a reactor with fast spectrum (BOR-60) and in a reactor with mixed spectrum (OSIRIS). For all materials, the hardening is significantly higher after irradiation at 330 °C than after irradiation at 375 °C (BOR-60 and OSIRIS compared to EBR II).

- *Metallurgical state.* It was established [37] that the saturated value of hardening is higher for the solution annealed 304 material (about 620 MPa) than for the CW 316 (about 500 MPa) meaning that the composition may play an effect contributing to hardening. Pokor et al. [37] suggest that the irradiation defect accumulation is mainly dependent on the initial dislocation density [19] and that a cold worked material will harden less than a solution annealed material because a well developed dislocation network acts as absorber for radiation defects.

- *Minor alloying elements.* In the work of Li [14] an attempt has been made to understand the effect of minor alloying elements on hardening. It was however difficult to distinguish the effect related exclusively to solutes and impurities from other consequent effects such as variation of SFE or grain size (inevitably taking place as a result of composition modification). It was found that carbon significantly promoted radiation hardening due to the high density of Frank loops. Carbon atoms might affect the nucleation of the clusters by binding strongly with the radiation defects. The addition of silicon in stainless steels was shown to suppress the radiation hardening because the number of the observed Frank loops was apparently declining with increasing amount of Si.

- *Stacking fault energy*. According to the study of Li [14], the hardening as well as the flow behavior of the investigated steels (with low, reference austenitic steel and high SFE) have been also found to be strongly influenced by the SFE even before irradiation. The SFE value was found to control the main deformation mechanisms of the steels: at room temperature the LSFE alloys deform via twinning and the HSFE alloys via dislocation glide. At T=300 °C the twinning was observed in LSFE alloys. No simple relationship was found between the SFE and the tensile properties of the investigated alloys. Hence, the SFE affects both the mechanism of plastic deformation in un-irradiated materials and dislocation-defect interaction in the irradiated materials.

The classical model for hardening [38] is based on the following dependency:

$$\Delta\sigma = M\alpha_L\mu b\sqrt{\rho_L\psi_L}. \tag{2.1}$$

Here M is the Taylor factor, α_L the obstacle strength of the Frank loop, μ the shear modulus and b the Burgers vector; ρ_L is the density of dislocation loops and ψ_L the average diameter of the loops.

Pokor et al. [37] have modified the model accounting for the fact that Frank loops unfault after reaching a certain size. From elasticity theory considerations, it is known that in materials with a low SFE such as austenitic stainless steels, small faulted Frank loops are more stable than perfect dislocation loops of equivalent size. The reason for this situation is that a partial dislocation has a line energy smaller than that of the perfect dislocation with Burgers vector BV=1/2<110>. For small radii, this difference in line energy can pay for the cost associated with the stacking fault present in the Frank loop. For large radii however, the energy of a faulted loop is higher than the one of a perfect loop, meaning that above a critical radius the faulted loops will tend to unfault forming perfect loops. Under an applied stress, the situation changes. The Peach–Koehler force does work on the partial dislocation required to unfault the Frank loop thus changing the energy balance and reducing the critical radius for Frank loop stability.

The modified model for radiation-induced hardening is expressed by the following equation [37]:

$$\Delta\sigma^* = M\frac{\psi^* - \psi_L}{\psi_L}\left\{\frac{\gamma}{n\sqrt{b_p^2 - b_F^2}}\right\} \text{ where } \psi^* = 2\frac{\mu(b_p^2 - b_F^2)}{\gamma} \tag{2.2}$$

Here γ is the stacking fault energy, b_p and b_F are the Burgers vectors of the perfect loop and Frank loop, respectively, and n is the number of dislocations in

the pile-up, that is the only adjustable parameter not experimentally measured which in principle may be evaluated by measuring the steps size on grain boundaries during in situ deformation [24].

The hardening observed in the work of Pokor et al. [37] is well reproduced by this improved model: when irradiation dose increases, hardening increases, then when mean loop size and density are large enough for the loops to be unfaulted, a saturation of hardening occurs. A criterion for the critical density of the loops (as a function of their size) above which the stress-induced unfaulting will occur has been proposed in [37].

According to this model, the dose from which the hardening starts to saturate (but not the saturated level of hardening itself) depends on the irradiation temperature only. The absolute value of the saturated hardening is mainly determined by the initial dislocation network and possibly by the SFE and loop obstacle strength of the material [37].

2.1.4.2 Radiation-induced dislocation channeling

The formation of dislocation channels (or clear bands) — zones free of radiation defects created as a result of plastic deformation — has been studied in the above mentioned work by Li [14] in the three irradiated austenitic stainless steels with different SFE. The three irradiated alloys were deformed at 300 °C to about 8% with a strain rate $\dot{\epsilon} = 5{\cdot}10^{-7}$ s^{-1}. In the austenitic steel the primary deformation mechanisms are dislocation slip and twinning. The latter is the predominant mechanism at room temperature and at reactor operational temperature in low SFE alloys [39].

Dislocation channels were observed in all three austenitic stainless steels (see Fig 2.8), although their width, spacing, height and density were different in each alloy. The measured average width of dislocation channels observed in the LSFE alloy was about 64.9 nm, in the Ref SFE alloy about 62 nm, in the HSFE alloy 21 nm. The measured average spacing between the dislocation channels observed in LSFE and Ref SFE alloys was about 0.9 µm; in the HSFE alloy about 0.64 µm. In LSFE and Ref SFE alloys dislocation channels heavily intersect with each other, while in the HSFE alloys channels are parallel. In a given area, more dislocation channels were observed in LSFE alloy than in HSFE alloy, so the density of dislocation channels is higher in LSFE than in HSFE alloy.

As was established in [14], at relatively low dose level (0.9 dpa) the irradiation defects are small enough to be cleared out easily by the dislocations (which causes the formation of the channels). Once the clearing process has begun in

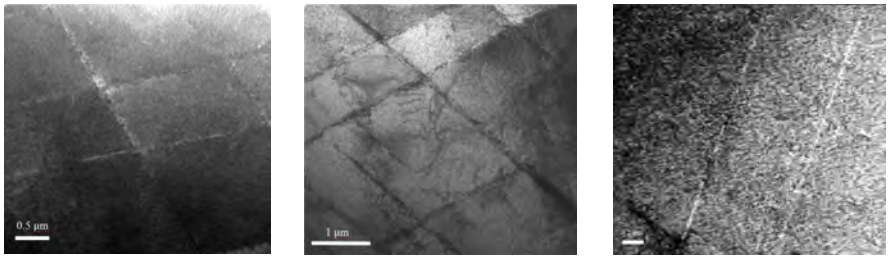

Figure 2.8: a). TEM images of deformed LSFE, Ref SFE and HSFE austenitic alloys, deformed to about 8 % at 300 °C. From [14].

a particular location (dislocation glide plane), further dislocations move more easily in this region. Their faster movement leads to the accumulation of the deformation in the channel.

Although patterns of dislocation debris were observed within channels, the latter were clear of almost all defects of a visible size and no piling up of defects at the side of the channel was found. When the channels intersect one another, dislocation pile-ups occur, causing work hardening. The work hardening process allows higher stress levels, which in turn encourages the clearing of larger radiation defects. As the stress level continues to rise, more clearing of radiation defects in general is promoted, and thus more general dislocation activity in the matrix is possible. The results show that at low dose and low strain the degree of localized deformation in channels follows the order: LSFE alloy > Ref SFE alloy > HSFE alloy. Note that the irradiated LSFE alloy in the experiments of Li [14] was deformed at the reactor relevant temperature of 300 °C not only via dislocation channeling but also via the mechanical twinning, unlike Ref SFE and HSFE alloys, where the deformation was mainly accommodated by the dislocation slip. Thus, the effect of SFE on the initiation of dislocation channels exclusively via the dislocation glide should be explored further. Up to now, the dislocation-defects interaction mechanisms leading to formation of dislocation channels are not fully understood and will be considered in this thesis.

2.1.4.3 Nanoscale explanation of the origin of hardening and dislocation channeling

The origin of radiation-induced hardening and channeling is intimately related to interaction mechanisms of dislocations with the defects. Given the

complexity of in situ TEM straining experiments (see e.g. [40, 41]), molecular dynamics (MD) atomistic simulations offer an efficient complementary tool to investigate the details of dislocation-loop interaction and calculate the stress which an obstacle opposes to the dislocation motion. The key process to be studied by MD is the absorption of defects by dislocations.

The details of the algorithms to simulate the dislocation and dislocation-defect interaction using the MD method are summarized in the chapter 3.2.

It is important to note that the dislocation-defect interaction in bcc and fcc materials differs significantly as the perfect dislocation dissociates into two partials in the fcc material as it is an energetically favorable process. The interaction of an edge dislocation with voids in fcc Cu was considered in [52]. The interaction of dislocations with dislocation-structured obstacles such as SFTs was considered in [53–60].

The application of the model [51] to study the hardening and formation of dislocation channels was done in [55], where the interaction of edge and screw dislocations with SFTs of different sizes at different temperatures and strain rates was studied in pure Cu and Ni. Five possible interaction outcomes were identified, involving either partial absorption, or shearing or restoration of SFTs. The mechanisms that give rise to these processes were described and their dependence on interaction parameters, such as SFT size, dislocation-SFT geometry, temperature and strain rate were determined. Mechanisms that help to explain the formation of defect-free channels cleared by gliding dislocations, as observed experimentally, were summarized.

The reactions with perfect dislocation loops were considered in [61], where the ability of perfect dislocation loops in pure Cu to glide under the influence of the stress of a gliding dislocation were studied. It was shown that a row of loops lying within a few nanometers from the dislocation slip plane can be dragged at a very high speed.

Frank loop (being the dominant radiation defect type of austenitic steels, as discussed above) interaction with dislocation in pure fcc metals (in Cu and Ni) has already been studied by MD simulations in [39, 62, 63]. Rodney [62] performed molecular dynamics simulations of screw dislocations interacting with interstitial Frank loops in pure Ni studying a geometrical configuration favorable to the formation of a helical turn on the dislocation (see Fig. 2.9). Both the interaction mechanism and the pinning stress caused by the defects were analyzed. It was established that the interactions involve athermal cross-slip events and that the Frank loops are strong obstacles with unpinning reactions involving Orowan processes.

Shin et al. [63] applied the molecular dynamics method to simulate in pure

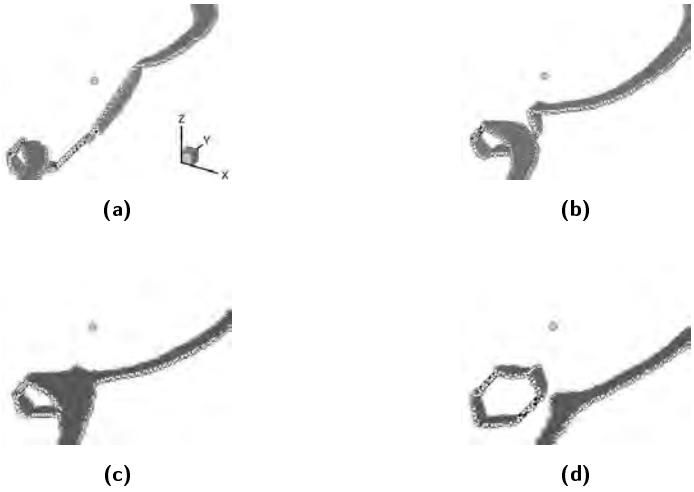

Figure 2.9: The visualization of the unpinning of a screw dislocation from a helical turn at different times (in ps): a) 18, b) 24, c) 25.2 and d) 27 in pure Ni after application of stress τ=600 MPa at T=100 K. From [62].

Cu and pure Ni at T=100 K the interaction between an interstitial Frank loop and gliding dislocations to investigate the mechanism of defect elimination. The interaction with both screw and edge dislocations was considered. It was found that two dislocations in two different parallel slip planes played cooperatively to remove the defect. This finding implies that a group of dislocations might be responsible for a dislocation channel formation, by moving in a group and eliminating the defects.

In the systematic study performed by Nogaret et al. [39], the interaction between edge/screw dislocations with Frank loops in pure Cu was considered. Several interaction mechanisms were revealed depending on the interaction geometry and the impinging dislocation character, namely: (i) loop shear (see Fig. 2.10a); (ii) unfault into glissile configuration (see Fig. 2.10b); (iii) absorption into a glissile superjog (on edge dislocation) (see Fig. 2.10c) or into a sessile helical turn (on a screw dislocation) (see Fig. 2.9a).

Absorption into a helical turn results in especially high unpinning stress and thus is expected to be the main source of hardening. For both screw and edge dislocations the unfaulting mechanism is controlled by the cross-slip process [39, 63]. In general, the number of geometrical configurations leading to loop unfaulting is higher for a screw dislocation [39].

Hence, the interaction with screw dislocations most likely determines both the

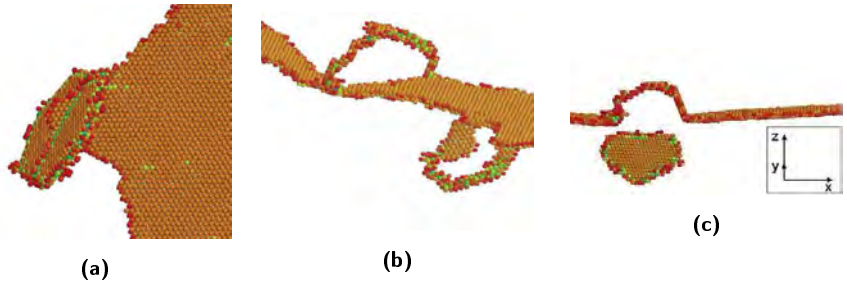

Figure 2.10: The visualization: of a) shear of a Frank loop by an edge dislocation at the stress of 95 MPa; b) glissile configuration after the absorption of the Frank loop by the screw dislocation; c) absorption of half of the Frank loop into the glissile configuration by an edge dislocation. The simulations are done using the pure Cu potential at T=600 K. From [39].

hardening and the formation of free channels.

The main drawback of the simulations made by Nogaret et al. is the use of pure Cu as a model material for austenitic stainless steel. Pure Cu does not reproduce an adequate value of shear modulus (e.g. shear modulus in 111 plane is 41 MPa instead of 75 MPa [39]) while the value of SFE (44 mJ/m^2 at 600 K) is correct. Both SFE and shear modulus values are important for the definition of the interaction mechanism and strength of Frank loops upon plastic deformation mediated by dislocations in fcc metals [13]. It is therefore necessary to investigate the dislocation-defect interaction in the model alloys with the properties mimicking better those of the austenitic stainless steels. In this thesis the new models based on Fe-Ni and Fe-Ni-Cr model alloys will be developed to study the effect of SFE, loop size, ambient temperature on dislocation-defect reaction mechanisms leading to hardening and removal of radiation-induced Frank loops by dislocations.

2.2 Bcc materials

2.2.1 Ferritic-martensitic (FM) steels

2.2.1.1 Application and properties

High-chromium (9–12 wt%) FM (ferritic-martensitic) steels are candidate core reactor materials for GEN IV nuclear systems (e.g. for fuel cladding and

the spallation target in the accelerator driven systems [65]). 9% Cr reduced activation ferritic-martensitic (RAFM) steels are the only possible structural materals suitable for fusion installations (as potential first-wall and breeding blanket structural materials) [66–69]. These steels are expected to operate at high temperature (up to 550 °C, or higher if the steels are strengthened by oxide dispersion) and high neutron flux, consequently high dose rate and accumulated dose (up to 10 dpa per full power year [70]). These experiencing materials should also respect safety standards, being compatible with the coolant used [71], even after the degradation under neutron irradiation or exposure to plasma.

RAFM steels such as EUROFER, F82H and 9Cr-2WVTa were selected for structural applications in fusion systems in Europe, Japan and USA, respectively, using the codes and cross-section libraries for predicting radionuclide inventories of materials exposed to fusion reactor systems. These steels which benefit from favourable cost, availability, exhibit suitable strength, toughness and resistance to radiation damage, especially swelling. They can sustain high temperature, fast change of it (having higher coefficient of thermal conductivity than austenitic steels [72]) and corrosion resistance (in the case of high-chromium FM steels).

The limitation for the use of FM steels are [72–74]:

1. a pronounced tensile strength drop at about 500 °C;
2. a strong reduction in creep strength at T > 600 °C;
3. significant stress softening in low fatigue tests;
4. existance of a DBTT which is between -80 °C and -90 C in the unirradiated state.

2.2.1.2 Chemical composition: reduced activation and effect of chromium concentration

The chemical composition of RAFM steels such as EUROFER, F82H and 9Cr-2WVTa in comparison with the high-chromium steel T91 is given in Table 2.3.

The fabrication of the RAFM steels requires that the radiologically undesirable elements are replaced by other ones which possess similar or equivalent metallurgical functions, but are less activated [75]: Mo is substituted by W which are ferrite formers, increasing tempering temperature, and ensuring a good compromise between DBTT, mechanical strength, ductility and creep

Table 2.3: The composition (wt%) of RAFM steels with favourable combination of properties and of T91 steel.

Country	Alloy	C	Si	Mn	Cr	W	V
Worldwide [76]	T91	0.1	0.32	0.43	8.32	–	0.2
Europe [77]	EUROFER	0.1	0.05	0.5	8–9	1	0.24
Japan [78]	F82H	0.1	0.2	0.5	8	2	0.2
USA [79]	9Cr-2WVTa	0.1	0.3	0.4	9	2	0.25

Country	Alloy	Ta	N	B	Mo	Nb
Worldwide [76]	T91	–	0.03	–	0.96	0.08
Europe [77]	EUROFER	0.06	0.02	0.004	–	–
Japan [78]	F82H	0.04	<0.01	0.003	–	–
USA [79]	9Cr-2WVTa	0.07	–	–	–	–

resistance. Nb is replaced by Ta which are both high temperature carbide formers, stabilizing grain size, increasing resistance to tempering, improving DBTT and strength. Nevertheless, the hands-on levels of post-irradiation activity are not expected, that is why these steels are called only 'reduced activation', and not 'low activation'.

The main alloying element of the FM steels is chromium, in the range 2.5%–18%. The addition of Cr ensures protection from corrosion in the temperature range 300–500 °C [80]. However, the addition of Cr in concentration exceeding 10 wt. % leads to the phase separation resulting in the formation of numerous Cr-rich precipitates (so called α'-phase) [81], which is accelerated under irradiation [82, 83]. This precipitation makes the material brittle (the well-known phenomenon of '475 °C embrittlement' observed in FeCr steels containing more than 13 %Cr is caused by the above mentioned phase separation [84]), consequently an optimum Cr content is defined by the compromise between corrosion resistance and mechanical properties. Cr improves also creep resitance.

In order to understand the effect of alloying with chromium especially on radiation damage, a set of model FeCr alloys has been irradiated and investigated after irradiation by both microstructural examination and mechanical tests in a recent work of Matijasevic et al. [65]. The macroscopic effect of the addition of chromium on the mechanical properties of the unirradiated FeCr alloys is shown in Fig. 2.11. One can see that both the yield stress and the ultimate tensile stress for the model alloys increase linearly with Cr content. Addition of chromium, however, led to a certain reduction of the total elongation. In terms of ductility, low Cr alloys are more ductile than high Cr alloys. Thus,

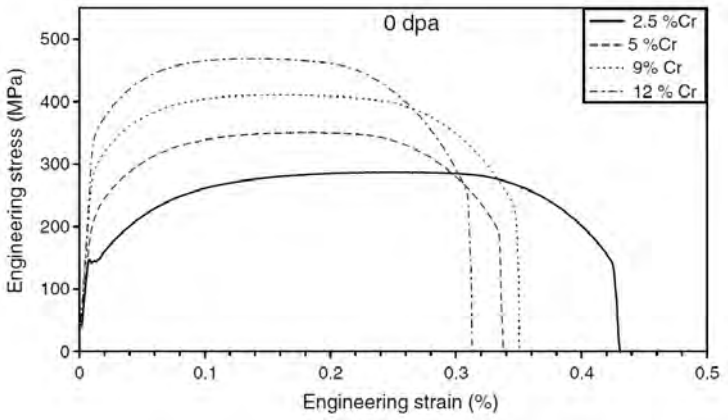

Figure 2.11: Engineering stress and strain curves at room temperature of the model alloys before irradiation. From [65].

low Cr alloys that have larger grain sizes tend to have a lower toughness and larger elongation than high Cr alloys with smaller grains.

One of the most important advantages of the presence of chromium in the iron matrix is the suppression of irradiation swelling [85, 86]. In bcc Fe-based alloys swelling becomes an important problem at relatively high temperature, where hardening due to dislocation loops is no longer playing any important role. The addition of Cr to Fe leads to the decrease of swelling dramatically and this decrease depends on the content of Cr being typically an order of magnitude lower in FeCr alloys compared to pure Fe [87, 88] and stainless steels (1 vol.% per 100 dpa as compared with 1 vol.% per 10 dpa in stainless steels at T>300 °C [74]). Even small quantities of Cr strongly decrease the swelling, which remains low between 1 and 10%Cr and then starts to rise again [88]. At Cr concentration above 10% and high irradiation doses, the swelling has a local maximum and then decreases towards a quasi-asymptotical minimum, in the range of concentration where the precipitation of the Cr-rich α' phase is expected [89, 90]. The lowest irradiation-induced swelling occurs for materials with a Cr content between 5% and 10%. These findings together with the 9%Cr minimum DBTT shift [91] explain the selection of the 9 wt% Cr materials as candidates for the regions of fusion applications which undergo high irradiation doses.

Also it was established that the alloying with chromium increases resistance against thermal creep [92] and influences the extent of radiation-induced

embrittlement [91]. Within this work the latter problem will be addressed by studying the mechanisms leading to hardening due to the interaction of dislocations with radiation-induced defects.

2.2.1.3 Radiation-induced microstructure

The typical radiation defects observed in bcc materials are dislocation loops with Burgers vectors 1/2<111> and <100> and voids. The FM steels are not an exception and also develop this type of nanofeatures. The incubation dose for the appearance of voids is rather large — 10 dpa [93], larger than in austenitic steels. Hence the primary defects seen upon neutron irradiation exposure are dislocation loops [65, 94, 95]. Moreover, solute clusters and precipitates of different kinds are often observed.

Low temperature irradiation regime (T < 350 °C). The formation of dislocation loops is typical for this regime. Under equivalent irradiation conditions, the concentration of loops is generally higher in FeCr alloys than in pure bcc Fe at sufficiently high dose, see for example the results for the Fe-10Cr alloy in Fig. 2.12. The proportion of <100> and 1/2<111> loops also depends on Cr concentration [96, 97]. The mobility of large dislocation loops is decreased in FeCr alloys as compared to pure Fe [95] which leads to the assumption that Cr atoms suppress loop migration, stabilize dislocation loop population in bulk and possibly make them stronger obstacles for dislocation movement [98–100]. This trapping effect of Cr was thus proposed to be responsible for the enhanced hardening induced in the FeCr alloys as compared to pure Fe [98–101].

According to the results of Matijasevic et al. [65] of irradiation of FeCr alloys up to 1.5 dpa at 300 °C in the BR2 reactor (Mol, Belgium), the defect density decreases with increasing Cr concentration as shown in Fig. 2.13. The average size of defects also decreases with alloying by chromium, falling to 6 nm in Fe-12Cr alloy from 13 nm in Fe2.5Cr alloy.

In the recent study of Kuksenko [102] the irradiation-induced formation of α' (enriched up to 55% of Cr) and NiSiCr-enriched (also containing phosphorus) clusters was revealed in Fe-9Cr and Fe-12Cr alloys irradiated up to 0.6 dpa at T=300 °C in BR2. NiSiCr clusters were observed to form also for lower Cr content. Due to their small size these clusters might be associated to defect clusters (small dislocation loops) invisible by TEM. The density of such clusters was about $(2.1\pm0.2)\cdot10^{23}$ m^{-3}, $(2.4\pm0.5)\cdot10^{23}$ m^{-3}, and mean radius (1.1±0.20) nm, (1.65±0.20) nm, respectively.

High temperature irradiation regime (T > 350 °C). While dislocation loops are still produced in this regime (they are stable in Fe-9Cr alloys up to 820 K,

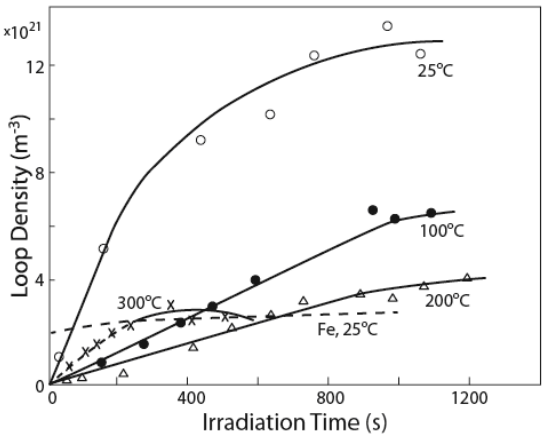

Figure 2.12: Irradiation (by 1 MeV electrons) time dependence of loop density in Fe-10%Cr alloy and in Fe at several temperatures. From [94].

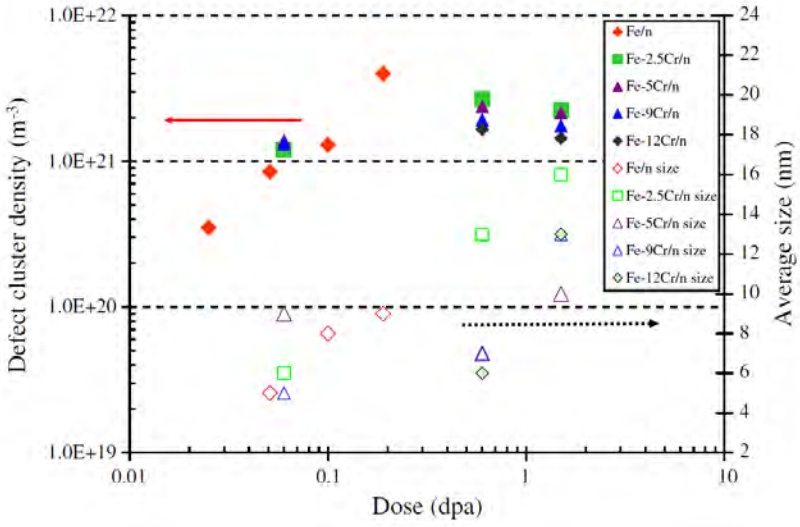

Figure 2.13: Dose dependence of the defect density (open symbols) and size distribution (closed symbols) in Fe and Fe–Cr alloys. From [65].

contrary to pure Fe, where they disappear already at about 620 K [95]), the FM steels are mainly subjected to swelling at this temperature if the dose is high enough to determine the appearance of voids. Two types of swelling exist:

1. *gas bubble swelling*. It is associated with the nucleation of bubbles of gas atoms formed due to transmutation reactions. Bubble swelling is known to occur at relatively high doses (>30 dpa), when sufficient concentration of gaseous atoms is accumulated (this also depends on the irradiation conditions, i.e. for fusion such dose can be significantly lower);

2. *void swelling*. It occurs due to the presence of voids and pores in materials, which are produced by the excess of vacancies in the bulk, forming vacancy clusters. Void swelling occurs faster and in principle can be detected already at 10 dpa.

In the work of Jiao [103] the ferritic–martensitic steels T91, HCM12A, HT-9 and a 9Cr model alloy were irradiated by protons up to 10 dpa at 400 °C and 500 °C and by heavy ions up to 100 dpa at 500 °C. After that the materials were examined using TEM and atom probe tomography (APT) methods. Mn-Si-Ni-rich and Cr-rich precipitates were formed in T91, HCM12A and HT-9 at 400 °C. At higher irradiation temperature of 500 °C the production of Mn-Si-Ni-rich precipitates was substantially larger but in much lower number density compared to irradiation at 400 °C. The Cr-rich precipitates were observed in HCM12A and HT-9 alloys with higher bulk Cr content than the solubility limit of Cr at the irradiation temperature. No difference in size and composition of defects at the same temperature was found between the heavy ion and proton irradiation, except for the lower number density in the case of heavy ion irradiation.

In this thesis the problem of low-temperature (T < 350 °C) embrittlement at the intermediate irradiation dose (up to 30 dpa [104]) will be addressed by means of studying hardening which at these conditions is mainly related to the formation of dislocation loops (possibly decorated by solute atoms) and their interaction with moving dislocations. Also the mechanisms leading to the nucleation of Mn-Si-Ni-rich clusters will be addressed, which may also contribute to the precipitation hardening.

2.2.1.4 Macroscopic effects of radiation damage

2.2.1.4.1 Radiation-induced hardening

As shown in [65], the addition of Cr to Fe strongly influences the radiation hardening with a minimum at 9%Cr. The hardening measured in Fe–Cr alloys irradiated by fast neutrons at T=180 °C is much higher than in pure Fe [100, 105]. After high temperature annealing (at about 500–600 °C) the hardness of un-irradiated materials is almost fully recovered [100]. This means that radiation-produced defects, responsible for strengthening and loss of ductility, are removed by annealing. Also, as during annealing experiments the hardening disappears at lower temperature in Fe than in FeCr alloys, one should assume that the defects, responsible for hardening, are either different in FeCr compared to Fe, or more stable in FeCr than in Fe due to the presence of Cr.

In the computer simulations of dislocation-defect interaction in the FeCr alloys performed in this work the important parameters to vary will be the ambient temperature and dislocation loop size. Here the effects of the former and of the latter in terms of the accumulated dose (which is directly interconnected with the loop size) on the radiation-induced hardening are described:

Effects of dose. Recently, an overview of mechanical properties of 9Cr steels (including EUROFER97), irradiated up to 80 dpa, has been made by Gaganidze [106]. It was shown that the increase of the yield stress is rather steep at doses below 10 dpa at irradiation temperature $T_{irr} \leq 335$ °C which correlates with the rapid increase of the dislocation loop size and density observed in the experiments [65]. The saturation of hardening takes place at about 70 dpa at T_{irr} in the range 300–335 °C (see Fig. 2.14).

Effects of temperature. On the example of the EUROFER97 steel a number of effects attributed to the irradiation temperature was demonstrated in [106]. Overall it was possible to distinguish three temperature regimes, namely:

1. *Low temperature neutron irradiation*. ($T_{irr} \leq 335$ °C) leads to strong hardening and embrittlement of EUROFER97 and other 9Cr RAFM steels. Post irradiation annealing at 550 °C for 3 h leads to a nearly complete recovery of the impact and tensile properties of low temperature ($T_{irr} < 350$ °C) irradiated EUROFER97 indicating substantial healing of radiation defects.

2. *Middle temperature neutron irradiation*. Minor hardening and embrittlement observed at $T_{irr} = 350$ °C indicate considerable healing of radiation damage.

3. *High temperature neutron irradiation*. Neutron irradiation at $T_{irr} \geq 400$ °C has nearly no impact on the post-irradiation mechanical properties.

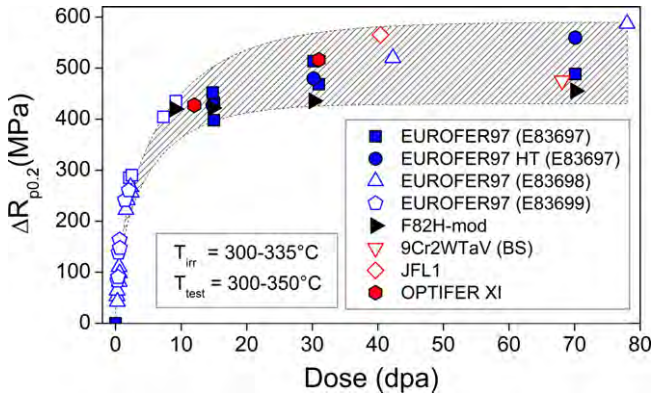

Figure 2.14: Irradiation hardening vs. irradiation dose for EUROFER97 and other RAFM steels for T_{irr} = 300–335 °C and test temperature T_{test} = 300–350 °C from [106]. The hatched area marks the scattering band for high dose results and is guide for the eye.

Given that for GEN IV and fusion applications structural steels are expected to operate in some cases, depending on design, at temperature as low as 250–300 °C, the so-called 'low temperature embrittlement' is one of the key issues in the development of new and assessment of already existing FM steels and, therefore, will be within the focus of this work.

2.2.1.4.2 Nanoscale explanation of the origin of hardening

In the work of Matijasevic et al. [65] an attempt has been made to estimate and compare with the experimental data the hardening mechanisms by correlating microstructural observations from TEM to mechanical property measurements using an Orowan-type mechanism (see formula (2.1) and the corresponding description in the section 2.1.4.1). It was concluded that this mechanism appears to be not appropriate to estimate the hardening from the TEM observed microstructure. This issue was explained [65] by the fact that the important increase of hardening with dose may either be related to the presence of invisible defects or to the modification of loop's strength in synergy with the Cr solution. The former effect can be explained by the existence of a large number of small clusters stabilized by Cr and invisible to TEM, which cannot be present in pure Fe. The latter effect can be the consequence of segregation of Cr at dislocation loops, which modifies the mechanism of loop-dislocation interaction, making loops stronger obstacles.

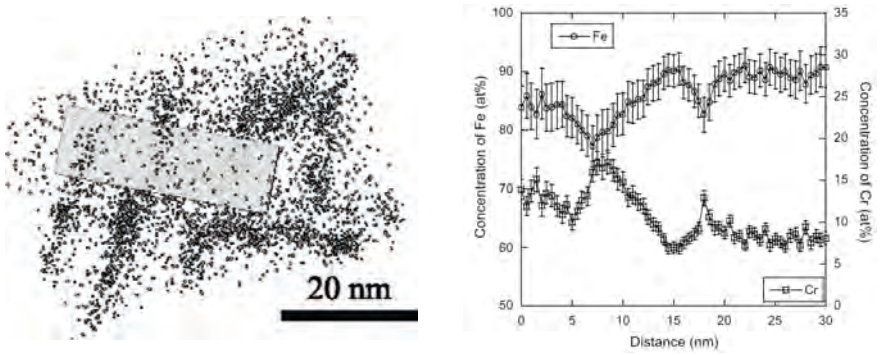

Figure 2.15: Radiation-induced segregation at dislocation lines in T91 steel following irradiation to 7 dpa at 400 °C. The composition profile (b) is along the rectangle in (a). From [107].

Recently, an indisputable proof of the segregation of Cr to dislocation lines and dislocation loops was obtained using the APT technique applied to examine several irradiated FM steels [107] (see Fig. 2.15). Moreover, experimental data from small angle neutron scattering (SANS) technique also point to the existence of numerous population of invisible dislocation loops possibly decorated by Cr [108]. Finally, recent experiments, based on further microstructural analysis of the alloys studied in [65], showed clearly that the solute clusters observed by Kuksenko [102], probably associated with small dislocation loops, may explain the increased hardening [109].

The computer modelling of the microstructure of FeCr alloys under the irradiation was performed using MD and Metropolis Monte Carlo (MMC) methods in the recent study of Malerba et al. [110], where it was summarized that:

1. the stability of point defects is weakly dependent on the presence of Cr in the case of vacancies, but strongly dependent in the case of self-interstitials. Chromium was found to increase the stability of self-interstitial atom (SIA) clusters, especially the small ones, invisible in the electron microscope.

2. the diffusivity of self-interstitials and their clusters is significantly reduced in the presence of Cr and depends non-monotonically on Cr content, as well as on cluster size and temperature. However, this effect

is negligible on the mobility of self-interstitial clusters large enough to become visible dislocation loops.

3. Cr-rich precipitation occurs in the tensile region of edge dislocations, while it appears not to happen at screw dislocations. Prismatic dislocation loops (typically produced under irradiation) tend to be decorated by Cr. Here the term 'decoration' means the presence of high concentrations of interstitial impurities or substitutional solute atoms in the strained region around the loop. Cr accumulates at grain boundaries, while it tends to deplete in the proximity of free surfaces (at least in the absence of oxygen) and voids.

Taking into account the model of the evolution of the microstructure described above and given that standard models of hardening accounting for the pinning of dislocation on the dislocation loops, acting as dispersed barriers, underestimate the hardening measured in the FeCr model alloys [65], the investigation of the effect of Cr decoration at the loops on the hardening mediated by dislocation loops should be elaborated further.

The dislocation-defect interactions, which are directly related to radiation-induced hardening, in bcc materials (mainly α-iron) were extensively investigated using the MD method. The interaction of edge dislocations with BV=1/2<111> with dislocation loops with BV=1/2<111> was studied in [111–114]. The interaction of the same BV loops with screw dislocations was considered in [115]. The interaction mechanisms between <100> loops and edge/screw dislocations were studied in [116–119] and in [120], respectively.

The main reaction mechanisms identified were the following:

1. the obstacle is crossed by the dislocation and both are unchanged (see Fig. 2.16). This reaction was observed in the case of edge dislocations interacting with large 1/2<111> loops that have BV inclined with respect to the glide plane;

2. the obstacle is crossed and modified and the dislocation in unchanged (see Fig. 2.17). Some <100> loops are transformed by edge dislocation into mixed <100> and 1/2<111> loops;

3. the partial absorption of the obstacle by an edge dislocation, that acquires a double superjog, occurs (see Fig. 2.18). This reaction can happen independently on the loop BV (<100> or 1/2<111>).

4. the temporary absorption of the entire obstacle into a helical turn on a screw dislocation occurs (see Fig. 2.19). This reaction was observed in the case of screw dislocations interacting with 1/2<111> loops.

(a) t=1.4 ns. τ=95 MPa **(b)** t=3.7 ns. τ=240 MPa

Figure 2.16: Visualizations of the interaction process for a 331-SIA loop in Fe at T = 100 K and strain rate $\dot{\epsilon} = 5{\cdot}10^6$ s^{-1}. From [112].

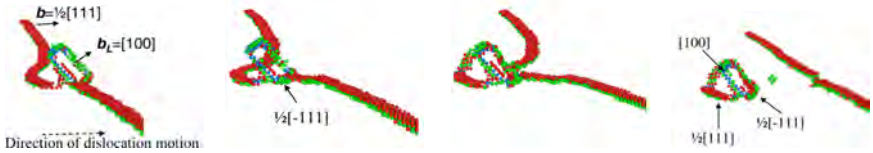

(a) **(b)** **(c)** **(d)**

Figure 2.17: Visualizations of the interaction between 1/2[111] edge dislocation and a [100] loop in Fe at 300 K. From [116].

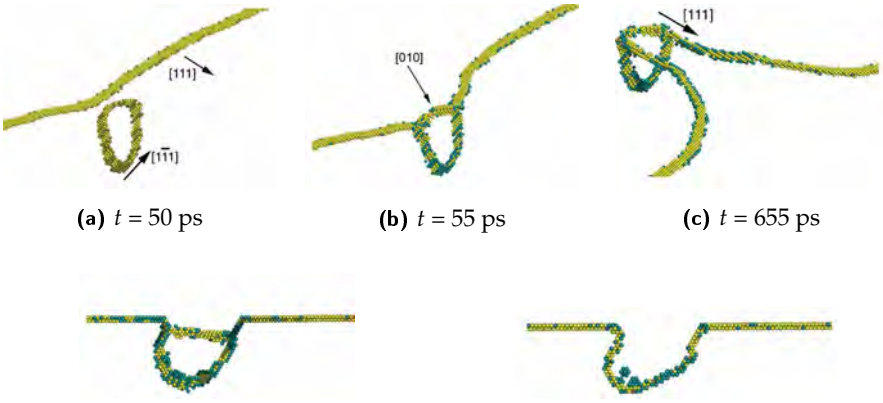

(a) t = 50 ps **(b)** t = 55 ps **(c)** t = 655 ps

(d) t = 655 ps **(e)** t = 765 ps

Figure 2.18: Visualization of the spontaneous glide and transformation process of a 331-SIA loop in Fe at T = 300 K and strain rate $\dot{\epsilon} = 20{\cdot}10^6$ s^{-1}. From [112].

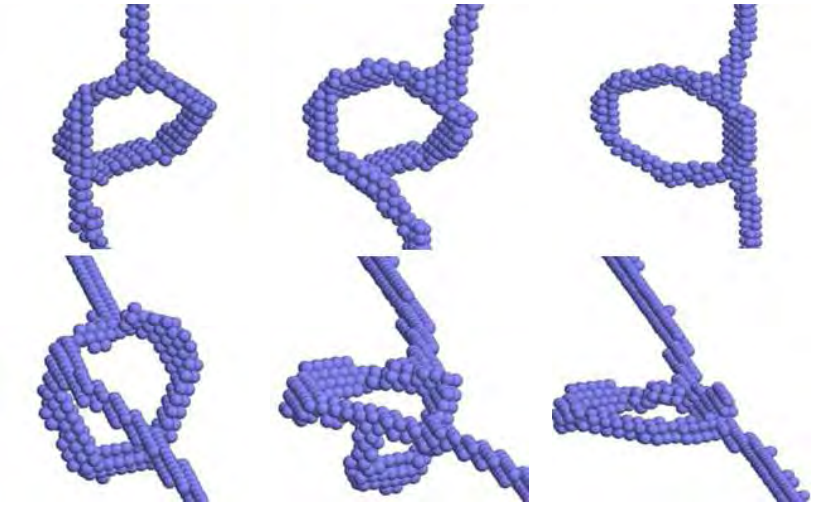

(a) t = 980 ps **(b)** t = 1861 ps **(c)** t = 1880 ps

Figure 2.19: Snapshots from two perspectives of the interaction of a screw dislocation with a 127-SIA loop in Fe at 100 K at the times indicated. From [115].

5. the obstacle is dragged by the dislocation and both remain unchanged. This reaction [121] occurs when a glissile loop has BV parallel to the slip plane of an edge dislocation, but does not intersect it. This process leads to the decrease of the velocity of dislocation.

Thus, the MD studies performed in bcc materials revealed a number of interaction mechanisms resulting in either complete or partial absorption and transformation of dislocation loops — see the reactions 3 and 4 above. The properties of junctions, or reaction segments, that are formed in the direct dislocation–loop interaction, are very important, because they determine the reaction pathway, the unpinning stress and the outcome product [116, 122]. In turn, such environmental variables as temperature and the loading conditions determining the dislocation velocity affect the mobility of the reaction segments and thus indirectly control the interaction mechanism [114, 123]. As summarized in [46], the hardening value, which is given by the difference between the maximum stress realized in the dislocation-defect reaction and the yield stress in the absence of obstacles, strongly depends on the interaction mechanism, usually increases with loop size and decreases with temperature.

Also the Burgers vector of the dislocation loop plays an important role. There

are two populations of the dislocation loops: 1/2<111> and <100> loops. The 1/2<111> interstitial dislocation loops are observed under irradiation at low temperature, while <100> loops are predominantly observed at high temperature [124]. The 1/2<111> loops are known to glide easily and thus under the action of a stress field of moving dislocations they enter direct dislocation reactions [124].

While the interaction of undecorated dislocation loops with dislocation was widely studied, as shown above, the investigation of the influence of loop decoration by chromium on the dislocation-defect interaction and therefore on unpinning stress has not been performed so far. In this work, the two hypothesis about the presence of invisible loops and Cr-segregation on visible loops will be validated by means of atomistic simulations. The obtained parameters of the dislocation- Cr-decorated loops interaction will contribute to the physical understanding of the effect of Cr on radiation-induced hardening. Part of the thesis will also be dedicated to the study of nucleation mechanisms of the other possible source of hardening in FeCr steels, namely the Mn-Si-Ni-rich clusters, whose nucleation at the atomic scale level can not be established experimentally due to their small size.

2.2.2 Reactor pressure vessel (RPV) steels

2.2.2.1 Application and properties

The reactor pressure vessel hosts the reactor core and is one of the principal barriers separating the core from the outside to prevent the release of radioactive substances. The large volume size of this component explains the difficulty of its replacement, which requires a full decommissioning of the reactor. Thus, it is desirable to perform preventive actions to ensure its integrity and to avoid the early closure of the reactor.

The typical operational temperature of light water reactors is in the range 270–330 °C, while the pressure is about 150 bar in a PWR and 70 bar in a BWR. The neutron flux from the reactor core can be estimated between 0.8 to $7{\cdot}10^{11}$ neutrons$\cdot$cm$^{-2}\cdot$s^{-1} [4] which corresponds to a dose less than 10^{-10} dpa/s according to [125]. Considering the 40-years operational lifetime, the neutron fluence can reach $7{\cdot}10^{19}$ n$\cdot$cm^{-2} [4] and the total accumulated dose is about 0.1 dpa [15].

In general, the RPV steels are made of high toughness, quenched and tempered, low-alloyed ferritic steels.

Table 2.4: The composition (wt%) of the typical RPV steels and ASTM norm for RPV steel.

Material	C	N	Si	P	S
ASTM A533-B [129]	$\leq$0.25	–	0.15–0.40	$\leq$0.035	$\leq$0.035
French RPV steel [126]	0.14	0.07	0.195	0.007	0.006
Russian RPV steel [127]	0.16	–	0.30	0.014	0.011

Material	V	Cr	Mn	Ni	Cu
ASTM A533-B [129]	–	–	1.15–1.50	0.40–0.70	–
French RPV steel [126]	–	–	1.30	0.75	0.064
Russian RPV steel [127]	0.26	2.75	0.43	0.16	0.11

Material	Mo
ASTM A533-B [129]	0.45–0.60
French RPV steel [126]	–
Russian RPV steel [127]	0.67

2.2.2.2 Chemical composition

The chemical composition of the RPV steel according to 'ASTM A553-B Class 1' in ASTM norm and 16MND5 in the French AGNOR standard, is given in Table 2.4. The compositions of two RPV steels used in French [126] and Russian [127] GEN II and GEN III reactors are also provided. The dislocation density of the RPV steels is of the order of 10^{14} m^{-2} [128].

While manufacturing several alloying elements are added or purposely kept in the steel to ensure specific qualities, like manganese, which is a powerful solution strengthening element that provides a cheap increase of hardenability. While irradiating the increased solute rearrangement processes driven by diffusion of radiation defects may lead to the formation of precipitates acting as obstacles for dislocation motion. The summary [4] of solubility limits at the operational (300 °C) and tempering (600 °C) temperatures of the minor alloying elements of pure Fe (which serves as a first approximation of the RPV steel) is presented in Table 2.5.

The addition of carbon to iron is the basic feature of a steel. As is known experimentally [135] and from electronic structure calculations using DFT [136], the carbon atom tends to occupy octahedral positions (see Fig. 2.20) in the bcc lattice of α-iron (ferrite).

The content of C (see Table 2.5) exceeds its solubility limit in α-iron at the room and reactor operational temperature (300 °C) thus it tends thermodynamically

Table 2.5: The solubility limits (wt%) of the typical minor alloying elements in α-iron at T=300; 600 °C. From [4].

Temperature	C	N	Si	P	Mn
300 °C	0.001 [130]	0.015 [130]	10 [130]	0.04 [131]	5 [132]
600 °C	0.011 [130]	0.1 [130]	12 [130]	0.48 [131]	3 [130]

Temperature	Ni	Cu
300 °C	4.2 [131]	0.003 [133]
600 °C	5.4 [131]	0.17 [134]

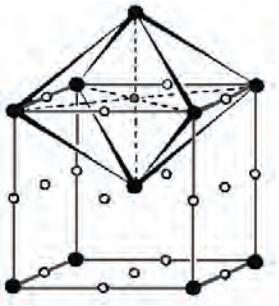

Figure 2.20: The bcc crystallographic structure (black circles) and octahedral positions (white circles). From [137].

to precipitate, forming the additional phase of pearlite, which is a fine two-phased, lamellar structure composed of alternating layers of ferrite and cementite (Fe_3C) [4].

The concentration of copper is also above the solubility limit in many RPV steels. This fact was found after the manufacturing of early pressure vessel as the diffusivity of Cu is very slow and a wrong extrapolation of lower temperature experiments to the high temperatures was used [4]. The concentrations of P, Ni, N, Si and Mn in the RPV steel are below the solubility limit. In the case of P, its content is purposely limited as its intergranular segregation leads to embrittlement under thermal ageing and irradiation [138–140]. N has a low effect on irradiation sensitivity of RPV steels at the temperatures above 250 °C [4]. The effects of Mn, Ni and Si, whose influence on the evolution of radiation damage and its macroscopic effects is predominant, will be discussed below.

2.2.2.3 Radiation-induced microstructure

2.2.2.3.1 Matrix damage

During 40 years of PWR operation (the accumulated dose being about 0.1 dpa [15]) irradiation produces small defects which are very hard to be identified and distinguished. At the moment, there is emerging consensus that matrix damage is roughly associated with point defect clusters [141–143].

The study in [125] reports formation of vacancy cluster-solute complexes (vacancy-Cu /Mn/Ni/Si/... with a size < 1 nm and density < 10^{24} m^{-3}) and nanovoid complexes (vacancy-Cu /Mn/Ni/Si/... with a size < 2 nm and density < 10^{24} m^{-3}). The former are thermally unstable (dissolve) in typical irradiations but would reach a steady state concentration depending on irradiation temperature and flux. The latter are stable (grow) under irradiation and would increase with the square root of fluence, and by lowering irradiation temperature, but would be independent of flux.

2.2.2.3.2 Precipitates

APT studies have revealed the formation of two groups of precipitates in RPV steels (see Fig. 2.21):

1. *Copper-rich precipitates*. Radiation-induced precipitation causes the formation of small Cu precipitates having bcc structure with an average size of 0.5–1.5 nm and typical densities in excess of $(0.1–2)\cdot10^{24}$ m^{-3} [125]. Also, it was established [144] that the rate of copper precipitation is very fast in the early stage of irradiation and is quite independent of copper content. Some experiments suggest that these precipitates can also be decorated by Mn (which delays the copper precipitation [145]), Ni, Si and P [145–149], depending on the initial steel composition and irradiation temperature [150];

2. *Mn/Ni-rich precipitates*. The studies in [125, 145] reveal the formation of Ni-Mn-rich clusters, which also contain limited amount of Si and little or no Cu. The average size and densities are similar to the ones of Cu-rich precipitates. Their formation is favored by high Mn, Ni content and low irradiation temperature. Since they appear mainly at high fluence, they are often denoted as 'late blooming phases'.

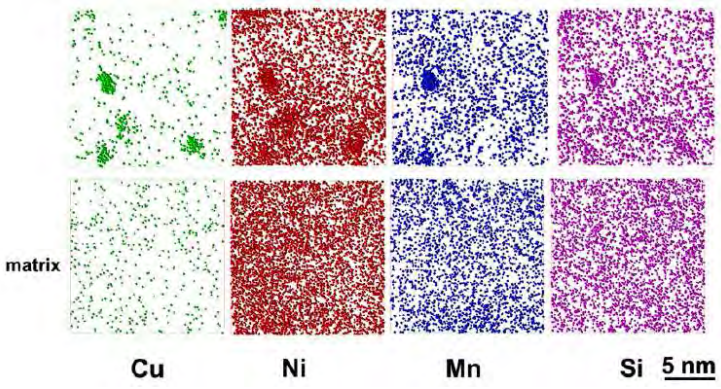

Figure 2.21: Atom maps of submerged arc weld (73 W) revealed the formation of Cu-, Ni-, Mn-, Si-enriched precipitates during irradiation to a fluence of $1.8 \cdot 10^{23}$ m^{-2} (E > 1 MeV), The distribution of the solutes in the matrix is shown in the second row. From [148].

2.2.2.4 Macroscopic effects of radiation damage

2.2.2.4.1 Radiation-induced hardening

The mechanical testing of RPV steels after irradiation in material test reactors shows that at the neutron fluence of $1 \cdot 10^{19}$ $n \cdot cm^{-2}$ there is already considerable hardening [128] (see Fig. 2.22). As the hardening is related to DBTT, the investigation of the former is key to understand embrittlement in RPV steels. There are two major components contributing to radiation-induced hardening: matrix damage and precipitates.

- *Hardening due to matrix damage* The three main characteristics that change the effect of matrix damage on radiation-induced hardening are empirically found to be [128]: the irradiation temperature, the neutron fluence and the Ni-content. The hardening contribution from matrix damage increases when reducing irradiation temperature and increasing the nickel concentration. The matrix damage is raising proportionally to the square root of the neutron fluence (while the one due to Cu-rich precipitates saturates quite rapidly) and therefore is dominating at high neutron exposures. Thus, the consideration of the matrix damage in RPV steels contributes essentially to the understanding of hardening in the long term operation perspective;

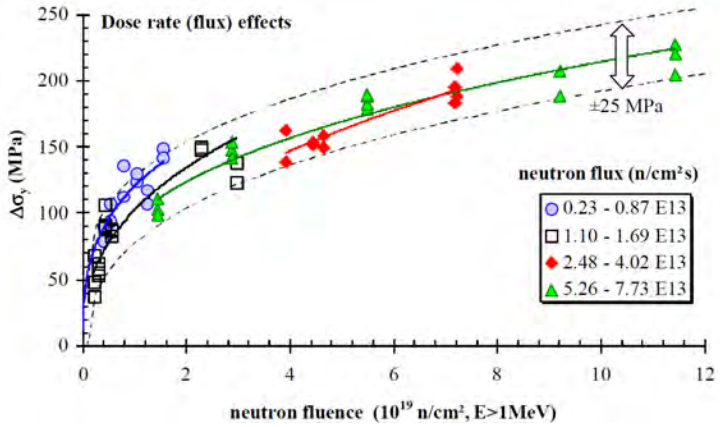

Figure 2.22: The hardening of the irradiated 73W steel depending on the accumulated dose (in terms of neutron fluence). Note that dose rate effects, if any, are small and within the experimental uncertainties. From [128].

- *Hardening due to precipitates*
  - *due to Cu-rich precipitates*. The hardening of RPV steels increases with Cu content up to the maximum at about $1{\cdot}10^{19}$ n·cm^{-2} (E > 1 MeV), in high copper materials [4, 151]. Above this fluence, the hardening does not depend on copper content and is constant: about 10 MPa per 10^{19} n·cm^{-2}. As summarized in [4], the Cu strengthening effect plays a role starting from Cu content of about 0.04% [144] and becomes very strong above 0.1% (i.e. about 50 MPa in comparison to other hardening mechanisms of about 100 MPa at a neutron fluence of about $1{\cdot}10^{20}$ n·cm^{-2}). It was also noted that copper precipitation plays an important, possibly a dominant role in irradiation hardening in steels with Cu content more than 0.1%.
  - *due to Mn-Ni-rich clusters*. The radiation-induced hardening (and consequently the embrittlement) due to the presence of precipitates is expected to saturate at a certain dose. However, the radiation-induced embrittlement increases with the dose: the experiments reporting data for irradiation dose up to 0.1 dpa suggest the onset of the formation of Mn-Ni-rich clusters [150] which would lead to a further progress of embrittlement with irradiation dose. It is possible that their formation contributes to the stability of invisible damage consisting of small dislocation loops as was already dis-

cussed for the of FeCr alloys (see section 2.2.1.4.2).

2.2.2.4.2 Nanoscale explanation of the origin of hardening

No TEM-visible microstructure develops in RPV steels within the technologically relevant range of irradiation doses and temperatures. However, the effects of hardening and loss of ductility are clearly observable and both terms 'matrix damage' and 'precipitate hardening' were found to be important in the construction of the computational models of hardening such as the ones described in [4, 128]. The identification and analysis of the nanometric lattice defects in irradiated RPV steels and their model alloys (such as pure Fe, FeCu, FeMnNi and FeCuMnNi) using methods alternative and complementary to TEM, such as positron annihilation spectroscopy, small angle neutron scattering, internal friction, magnetic after effect and atom probe tomography, are therefore now routinely applied [126, 132, 152, 153]. In the considered materials the radiation-induced defect pattern was different while the initial microstructure (i.e. grain size, density of carbon and of dislocations) was also discrepant. One could have expected that the matrix damage should increase with the reduction of the amount of sinks which happens, for example, if grains become larger and consequently lower density of grain boundaries is present. However, it was established [128] that initial dislocation density and grain size (together with initial microstructure and initial yield strength) have no or negligible effect on radiation-induced hardening. The increase of temperature leads to increased mobility of the radiation defects, such as vacancies and interstitials, leading to the higher probability of their annealing at internal sinks [154, 155], thus reducing the matrix damage and, consequently hardening, as was observed experimentally as reported in [128].

The influence of the Cu-containing precipitates on the hardening is remarkable, especially at low irradiation doses. While the hardening due to their presence saturates with dose, the effect of Mn-Ni-rich clusters, presumably associated with radiation defects of vacancy or self-interstitial type, emerges at higher doses. Currently, it is not clear whether the hardening due to Mn-Ni-rich clusters saturates or not. Understanding the physical origin of these clusters and mechanisms through which they may cause hardening is currently one of the most important issues to be resolved to allow long term operation of GEN II and GEN III reactors.

From the view point of fine-scale atomistic simulations, the thermal stability of the clusters rich in Mn, Ni and Si [156] can not be easily explained as the solute-vacancy interaction is too weak to glue the clusters at the reactor operational temperature. Association of a solute atom with in-cascade created dislocation

loops is possible as it was established in the case of Mn [156]. The simulation of the dislocation-defect interaction performed in pure bcc Fe has shown [112] that 'invisible' dislocation loops (i.e. with size below 2 nm) are weak obstacles and, therefore, do not play any role in hardening. The details of results of the modelling of dislocation-defect interaction in bcc materials can be found in the FM steels section 2.2.1.4.2. Moreover, as the small dislocation loops are known to be extremely mobile, normally they should disappear at internal sinks (i.e. dislocations and grain boundaries) in the course of irradiation [157]. Thus something must be preventing this.

The possible effect of the RPV solutes (i.e. Cu, Mn, Ni) or carbon on the mobility of loops and their interaction with dislocations has so far been unexplored. However, a number of theoretical works suggest that carbon- and/or carbon-vacancy clusters may act as efficient traps especially for the smallest dislocation loops [158–161]. On the other hand, Mn, Cu and Ni atoms have a strong affinity to point defects [156], and therefore potentially can be efficiently transferred by point defects to sinks [162, 163]. If carbon-vacancy defects can indeed significantly suppress the movement of in-cascade created dislocation loops, it is natural to expect enrichment of these loops by Mn, Ni and Cu. Consequently, the enrichment should stabilize the loops and this would enhance the resistance of loops against dislocation glide. The above given scenario, which may potentially explain the mechanisms by which the 'invisible' defects harden RPV steels, will be explored in this work by dedicated atomistic simulations involving both DFT and MD calculations.

2.3 Summary of problems to solve

1. **Austenitic stainless steels.**

   The existing models of dislocation-defect interaction must be refined in a more physically-appropriate way, in terms of correct reproduction of both shear modulus and SFE. Fe-Ni and Fe-Ni-Cr models for fcc solid solution will be developed, verified and applied to study the interaction of dislocations with the radiation-induced defects — Frank loops. The dependency of hardening and absorption of defects (which leads to the formation of dislocation channels) on SFE, defect size, ambient temperature and interaction geometry is to be investigated as well.

2. **FM steels.**

   The possible effect of solute segregation at dislocation loops in FeCr-based alloys on the loop absorption mechanism and related loop pinning

strength should be investigated. The level of Cr segregation, loop size and ambient temperature are the most critical parameters whose effect on the hardening should be studied.

Part of the thesis will also be dedicated to the study of nucleation mechanisms of the other possible sources of hardening in FeCr steels: the Mn-Si-Ni -rich complexes, whose nucleation at the atomic scale level cannot be revealed experimentally due to the small size.

3. **RPV steels.**

   The mechanisms leading to radiation-induced hardening due to 'invisible' damage, presumably originating from the solute-defect clusters of nano-metric size, should be studied. This includes:

   (a) clarification of the mechanisms leading to the formation of solute-defect clusters and their thermal stability, possibly enhanced by carbon atoms;

   (b) calculation of resistance of thermally stable solute-defect clusters (the undecorated dislocation loops invisible to TEM and decorated by Cu/Mn/Ni or C) to dislocation slip.

The output (i.e. critical resolved shear stress, CRSS, i.e. the maximum stress during the dislocation-defect interaction, and reaction mechanisms) obtained for each of the model alloys will serve as means for the development of upper-scale models dealing with an array of obstacles and dislocation networks, such as e.g. dislocation dynamics, thus becoming capable of predicting the mechanical response at the grain-scale. The nucleation mechanisms of the solute-rich clusters together with the database of the corresponding binding energies can be used as input for kinetic Monte Carlo or mean field rate theory methods to model the evolution of the solute-rich defects in FM and RPV steels under irradiation.

3 Computational background

In this chapter we provide the main computational details of the methods used to achieve the goals of this thesis. Electronic structure calculations using DFT are performed to compute the binding and formation energy of the different point defects and solute configurations in bcc iron. Such calculations will complement the fitting database, which, together with experimental data, will allow the development of the interatomic potentials for FM and RPV steels. Secondly, the energetics of the solute-defect interaction allows us to clarify the mechanisms of evolution of the nanostructure, giving for example, an idea about the nucleation of Mn-Ni-rich clusters in RPV steels. The molecular dynamics simulations of dislocation-defect interaction in FeNi, FeNiCr, FeCr, FeC and FeCuNiMn systems are executed to study the increase of the yield stress while the dislocation movement is hindered by the radiation-induced defects, such as, for instance, Frank loops in the austenitic stainless steels. The application of the MD method clarifies the effect of decoration of dislocation loops by Cr, Mn, Ni, Cu, C in the cases of FM and RPV steels, on the hardening. Also the influence of SFE (in the case of austenitic alloys), dislocation loop size, temperature, interaction geometry on the latter is studied.

3.1 Electronic structure calculations (based on the density functional theory)

The method aims at providing the most accurate possible prediction of the basic properties of different materials and energetics of interaction of the crystallographic defects (vacancies, interstitials, solute atoms, grain boundaries,

dislocations) with each other and with chemical elements contained in the alloy.

An electronic structure calculation using DFT is a quantum mechanical approximation to obtain the relaxed atomic and electronic configurations. It is based on two Hohenberg-Kohn theorems. The first one postulates that the ground state properties of a many-electron system are uniquely determined by an electron density that depends on three spatial coordinates only. Thus the many-body problem of N electrons with 3N spatial coordinates is reduced to the three spatial coordinates using the functional of the electron density. In the second Hohenberg-Kohn theorem an energy functional for the system is introduced and it is proven that the correct ground state electron density minimizes this energy functional.

In this method the Born-Oppenheimer approximation [164] is applied, where it is assumed that the speed of electrons is much higher compared to the one of the atoms, so the former always reach their equilibrium structure, no matter how fast the nuclei move with respect to each other. In the framework of Kohn–Sham DFT, the intractable many-body problem of interacting electrons in a static external potential is thus reduced to a tractable problem of non-interacting electrons moving in an effective potential which is applied to solve the Kohn-Sham equation in a self-consistent way [165]. The effective potential takes into account the external potential and the effects of the Coulomb interactions between the electrons: the exchange and correlation interactions. While the kinetic energy functional of such a system is known exactly, the exchange-correlation part of the total-energy functional remains unknown and, thus, is approximated. The simplest approximation is the local-density approximation (LDA), where the functional depends only on the density at the coordinate where the functional is evaluated. A more complex approach is the generalized gradient approximation (GGA) which is still local but also takes into account the gradient of the density at the same coordinate.

3.1.1 General scheme of calculations

In this thesis the DFT calculations were performed using the software and parameterization applied in previous work [166, 167] where the bcc Fe system has been extensively studied. The code named the Vienna *Ab Initio* Simulation Package, VASP [168, 169] with the projector-augmented wave (PAW) potentials [170, 171] has been used. The electron exchange–correlation functional was described within the GGA using PW91 functionals [172], with a Vosko–Wilk–Nusair interpolation [173]. Such parameterization was proven to

accurately describe the properties of transition metals including the magnetic properties.

The ionic relaxation was performed using the conjugate gradient algorithm with a force convergence criterion of 0.03 eV/Å. All the calculations were done keeping the cell shape and volume (equal to the equilibrium volume of bulk iron) constant. Several tests without setting the cell volume/shape constant were done in the case of Mn-Si-rich clusters, thereby proving that the effect on the binding energy was negligible.

The plane-wave cut-off energy was 300 eV which was verified to be large enough to provide converged results. An increased cut-off of 450 eV was used while studying the configurations with carbon atoms. In the bulk iron calculations a 3x3x3 k-point mesh was applied and was sampled by the Monkhorst and Pack scheme for systems with 128 atoms. The lattice parameter of pure ferromagnetic Fe is taken to be 2.831 Å, following previous studies [166, 167].

The general scheme of calculations consisted of the following steps:

1. *verification of the convergence*. Test calculations varying the k-point number and cut-off energy are performed to ensure the convergence of the total energy;

2. *creation of the atomic configurations of the studied systems*. It was important to select carefully the initial magnetic moments for iron and solute atoms. While performing the spin-polarized calculations with Mn, we did a set of calculations varying the initial magnetic moment for Mn within the range (0–4)·μ_B. While in most of the calculations the initial magnetic moment for Mn, which ensures the relaxation to the lowest energy configuration, was $-2\cdot\mu_B$ (the spin is anti-aligned to the spin of the matrix iron atoms), in some of the calculations, like pair interaction Mn-Mn, the initial spin for Mn should have been set to $-4\cdot\mu_B$;

3. *calculation of the total energy*. The comparison of it throughout the configurations with similar amount and types of atoms gives an idea of the thermal stability of the considered system.

To assess the binding energy between the entities in the defect we apply the standard definition conventionally used in many similar DFT works [156]. The binding energy of n defects A_i is defined as [156]:

$$E_B(\{A_i\}) = \sum_{i=1}^{n} E(A_i) - [E(\{A_i\}) - (n-1)E_0]. \tag{3.1}$$

Here $E(A_i)$ is the energy of the configuration containing A_i only, $E(\{A_i\})$ is the energy of the configuration with all the n defects and E_0 refers to a configuration containing no defects or impurities, i.e. bulk bcc iron. Following this notation, a positive value implies an attractive interaction and vice versa.

Considering the defect clusters the term 'total binding energy' refers to the energy which is necessary to separate all the defects away from a cluster. In practice, the dissolution of a complex cluster takes place by consecutive emission of its constitutes and the characterization of the energy barrier for that process requires the introduction of another term. The energy to remove one entity forming a cluster consisting of N objects will be called the *incremental binding energy* of an object #1 to N-1 cluster and will be referred to as E_B^I. If the removal of a single entity (e.g. object #1) from a cluster (containing e.g. three objects) results in the formation of a repulsive configuration (e.g. object #2 repels object #3), the incremental binding energy for object #1 is considered to be equal to the total binding energy of the cluster 1-2-3.

3.2 Molecular dynamics simulations

The classical molecular dynamics method is applied within this work. It is based on the analysis of the evolution of the system of interacting atoms by numerical integration of the Newton equations of motion using finite difference solvers. The general details of the method are fully described in [174]. The difficulty of the model is related to the correct reproduction of interatomic forces which are calculated using a mathematical fitted function — the so called 'interatomic potential'. Within this work we used either previously developed potentials or new potentials are developed.

The simplest model for the atomistic simulation of dislocation is the rigid boundary model [42–46] (see Fig. 3.1a) where the dislocation was inserted in the perfect lattice according to the displacements calculated using elasticity theory. To prevent the relaxation to the perfect crystal state, the atoms located far enough from the dislocation core were fixed. Using this method it is possible to study such dislocation properties as core energy and structure. Although the model allows the simulation of the movement of the dislocation by applying an homogenous shear strain in small increments and relaxation of the positions of the mobile atoms at each increment, the rigid boundaries oppose this movement as their atom positions correspond to the initial position of the dislocation. Thus a configuration force is created on the dislocation, which increases as the dislocation moves closer to the boundary. This causes

the overestimation of the Peierls stress, which is the minimum stress required to displace a dislocation from its equilibrium position.

The flexible boundary model [47–49] (see Fig. 3.1b) is a more sophisticated technique for simulation of dislocations and cracks, which allows the modelling of flexible boundaries according to the elastic and/or lattice properties of the crystal, thus enabling the distortion of the boundaries in response to the dislocation. Within this method the displacement of the dislocation is applied to the whole system; after that the atoms located in the region near to dislocation core are relaxed using the interatomic potentials while the first outer region is the Green's function region and the second outer region is the continuum region. In the latter two regions atoms are fixed during the relaxation of the near-to-core region. This relaxation causes the non-zero forces on the atoms in the first outer region, which are relaxed by displacing the atoms in the first region following the lattice Green's function and via the elastic Green's function in the second region. The displacement at point x due to an infinitesimal force F at point x' is $u{=}G(x{-}x')F$, where G is the Green's function. These iterations are repeated until the forces in the first region reduce below a specific value. In general, this method is a step forward over the simple rigid boundary model as it allows to reduce significantly the minimum size of the inner region keeping the correct core structure and Peierls stress. In addition for the same number of atoms in the inner region the dislocation can move further without interfering with the boundaries. However, the computational efficiency of this method is lower than the one of rigid boundary model, due to complexity of self-consistent convergence with the Green's function boundary conditions.

The above mentioned models are not suitable for dislocation-defect interaction modelling. The flexible boundary model can not be used for modelling dynamic conditions (at non-zero temperature) and in both models the boundaries are not transparent and thus the dislocation can not travel over long distances, which is a requirement in the simulations of the dislocation-defect interaction. These limitations can be overcome using the periodic array model originally proposed by Daw et al. [50]. Within this model the dislocation glide plane is replicated by periodic boundary conditions, thus an indefinite array of infinitely long, parallel dislocation is created. The movement of the dislocation is caused by application of the strain over the block of atoms located above (or below) the glide plane.

Initially, the model for the simulation of the movement (the dynamic behaviour) of edge dislocations in metals having the bcc crystallographic structure was proposed by Osetsky and Bacon in [51]. This model extends an earlier approach of periodic array of dislocations — on an array of edge dislocations

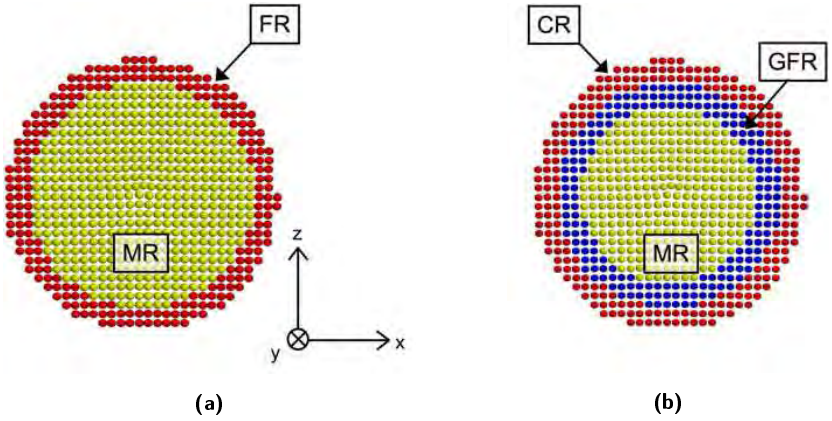

Figure 3.1: (a) Representation of the rigid boundary model, showing regions of fixed (FR) and mobile (MR) atoms. (b) Representation of flexible boundary models showing the continuum (CR), Green's function (GFR) and mobile (MR) atom regions. From [46].

periodic in the Burgers vector direction and allows the external action (either shear strain or resolved shear stress), crystal energy, plastic displacement and dislocation position and velocity to be determined unambiguously. Two versions of the model for either static or dynamic conditions, i.e. zero or non-zero temperature, were described.

To study the dislocation-defect interaction by classical MD we apply the Osetsky and Bacon periodic dislocation model. In this model (see Fig. 3.2) the X and Z axes of the simulated box were oriented along the dislocation line and the direction of the dislocation movement while the slip plane was perpendicular to the Y axis. Periodic boundary conditions were applied along the X and Z axes. The top and bottom planes along the Y axis of the box were free surfaces. The model crystal dimensions were selected in order to reproduce the experimentally observed values of density of dislocations and of the studied defects. The time step of integration of the equations of atomic motion was 2–5 fs.

The external load was applied by the stepwise shift of a few upper atomic planes of the model crystal along the slip direction. In these layers the atoms are rigidly fixed in their positions, and the integration of Newton equations is not performed for them. The external loading rate (applied by shearing) was selected so that the yield stress calculated in the model corresponds to the yield stress of the studied material in the real experiments. Atoms in the lower layers of the crystal were also rigidly fixed in their initial positions, and the

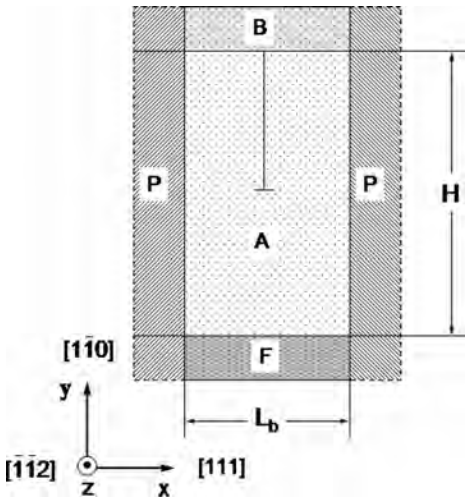

Figure 3.2: The structure of the modelled box in the model of Osetsky and Bacon [51]. From [51].

resulting shear stress caused by the shift of the upper layers of the crystal was determined based on calculation of the force acting on the lower fixed layer of atoms in the direction of the applied load.

For the atomic configurations containing a dislocation and a dislocation loop we carried out a relaxation procedure (crystal energy minimization) at zero temperature, and then the configuration obtained was used as the initial configuration for the MD simulation at the final temperature. The latter was initialized by assigning a velocity to each of the atoms, according to the following procedure. Firstly, momenta were given to all atoms of the system in accordance with the Maxwell distribution for the temperature $2 \cdot T$ (where T is the target temperature), and then the total momentum of the system was calculated, after which all velocities were simultaneously recalculated so that the total momentum of the system was zero. In order to establish the dynamic equilibrium we used the following procedure: during 10000 time steps the equations of motion were integrated and for every 100 steps the momenta of all atoms were recalculated so that the total kinetic energy of the system corresponded to the desired temperature. After this the procedure of external load application was implemented according to the above mentioned algorithm.

3.2.1 General scheme of dislocation-defect interaction modelling

1. **Selection of interatomic potential.** Besides the correct reproduction of the parameters of the modelled steel, it should ensure computational efficiency, so as to be able to model systems of up to 2 mln atoms during a time of several nanoseconds. In this work we will use embedded atom method (EAM)-type [175] interatomic potentials, which are widely used to describe metals and their alloys, except for the Fe-C system where a recently developed covalent bond many-body interatomic potential [176] will be applied. The details of EAM are given in **Paper II**.

2. **Introduction of the crystallographic defects and decoration of the loop.** While the insertion of the edge/screw dislocation and dislocation loop is described in [51], the decoration of the loop by the solutes requires the application of the Metropolis Monte Carlo method [177] to obtain of the exact atomic configurations.

3. **Performing the simulation of dislocation-defect interaction.** This modelling is executed using the in-house molecular dynamics code based on the model of Osetsky and Bacon [51]. There are two versions of the code: for single and parallel-cpu execution. Within this PhD project the author took part in the parallelization of the code applying it to model the binary and ternary systems.

4. **Analysis of dislocation-defect interaction.** The numerical analysis of the strength of defects was done using the stress-strain curves. The maximum values of the applied stress required for the moving dislocation to overcome the defect were obtained from an analysis of the averaged values of the instantaneous stress. The time interval for averaging of the latter was 200–500 fs. To visualize the dislocation defect interaction, we employed the numerical procedure of the linked-cell method, which provides the most effective search for the nearest neighbors of each atom in the model crystal [174]. The atoms of the dislocation core and the stacking fault were analyzed according to several criteria: coordination number, number of nearest neighbors of the atom corresponding to the fcc (in bcc system the analysis is done in a similar way) structure, and the potential energy of each atom. The configuration of the local environment of each atom was compared with the ideal fcc lattice based on the number of neighbors corresponding to the fcc structure. The atoms shown in the figures presented below have less than 12 neighboring atoms whose configuration corresponds to the fcc structure. The atoms of

the dislocation core were identified by the presence of 10 or 11 neighbors; the stacking fault was shown as a double layer of atoms having 9 neighbors.

4 Results of computer simulations

In this section we summarize the main results obtained while working on this PhD thesis. The chapter is subdivided by the three materials studied: austenitic stainless, FM and RPV steels.

4.1 Austenitic stainless steels

The MD modelling of the interaction of a dislocation with typical radiation defects in fcc materials, i.e. Frank loops has already been performed by Nogaret et al. [39] and Rodney [62] using pure Cu and pure Ni interatomic potentials, which were, however, unable to catch the correct combination of SFE and shear modulus relevant for austenitic steels. In this work, we apply the Fe-Ni and the newly developed Fe-Ni-Cr EAM-type interatomic potentials. They are used to investigate the effect of SFE and solid solution on the dislocation-loop interaction, namely corresponding critical resolved shear stress (CRSS) and loop absorption probability. The effect of loop size and temperature on these parameters is also considered.

4.1.1 Dislocation-defect interactions in Fe-Ni model alloys

The Fe-Ni interatomic potential [178] and two pure Ni potentials with low [179] and high SFE [180] have been applied to study the interaction of Frank loops of diameter 4 nm with dislocations. The Fe-50Ni and Fe-70Ni alloys represent the lower and upper bounds of the SFE value for the austenitic steels of 15 and 50 mJ/m^2, while the shear modulus for <110>{111} deformation, which is equal

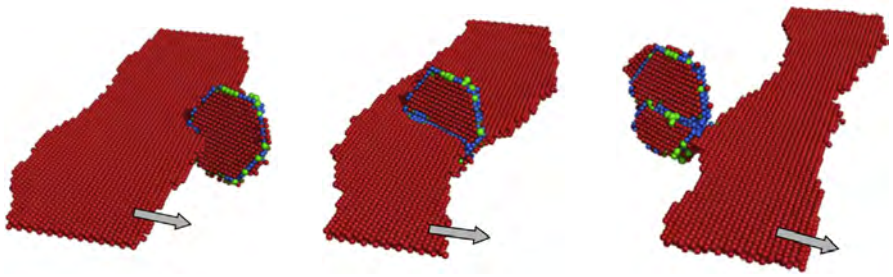

Figure 4.1: Interaction of a 1/2[110] screw dislocation with a 1/3[111] Frank loop in Fe–50Ni at T=300 K. a) Initially, the dislocation is attracted to the loop and moves to interact with the nearest side. b) However, due to the large spacing between the partials, loop shear by the leading partial starts before a constriction can form. c) The two partials consequently shear the loop sequentially, leaving a 1/2[110] step on its surface.

to 75 GPa in austenitic steel [39], was 81 and 94 GPa, respectively. The details of the simulations are fully described in **Paper I**.

We have observed reactions leading to the shear of the loop (see Fig. 4.1), unfaulting prior to interaction, and absorption of the loop in the form of helical turn. While the shear mechanism requires the lowest stress for the dislocation to pass through the obstacle, the formation of the helical turn requires the highest values, which are comparable with the Orowan stress — maximum stress for a dislocation to pass through the unpenetrable obstacle.

We have identified the effect of the loop size: the CRSS is either kept constant or increases up to two times with the increase of the loop size from 4 to 7 nm, if the initial interaction between the leading partial and closest loop segments was repulsive, which is controlled by the BV of the loop and the sense of the dislocation line. No change in dislocation-defect interaction mechanism has been seen, so the increase of loop size does not enhance the absorption probability. The raise of temperature from 300 K to 900 K has no influence on CRSS or leads to its increase in the initially repulsive dislocation-loop configurations. In the low SFE alloy Fe-50Ni the interaction mechanism was unaffected by the temperature, whereas high temperature (900 K) enhanced the complete absorption in the high SFE alloy Fe-70Ni. We have evaluated the effect of SFE: the low SFE alloys are characterized by the large distance between the partial dislocations, while the formation of constrictions on the dislocation is required for the cross-slip mechanism in the case of screw dislocations. The latter process is required for the loop absorption in some of the reactions,

thus the decrease of SFE leads to suppression of this mechanism. The effect of friction stress was remarkable: at low temperature the alloying of the metal leads to suppression of absorption in the case of both edge and screw dislocations due to unfavouring the cross-slip process in the secondary glide planes. This effect disappears with the raise of the temperature up to 900 K.

Thus, beside the loop size and temperature, whose effect on dislocation-defect reaction (and, consequently, on the hardening and formation of clear channels) was known before, we have established the importance of the effect of SFE and alloy composition on both the CRSS and interaction mechanisms leading to absorption of the loops.

4.1.2 Dislocation-defect interactions in Fe-Ni-Cr model alloy

Development of FeNiCr interatomic potential. The importance of taking into account the effect of alloying elements on the dislocation-defect interaction has been proven with the Fe-Ni alloy. While the Fe-50Ni alloy has similar SFE and shear modulus as austenitic stainless steels, the total concentration of alloying elements in the later is about 30%. Moreover, within these 30% among the major alloying elements there is not only nickel (10%) but also chromium (20%). In addition, in the Fe-50Ni alloy there is a large spread (up to 50 mJ/m^2) of the value of SFE around the average of 19 mJ/m^2. This issue may hinder the formation of extended constrictions even at relatively high applied shear stress at the moment when the Frank loop is in contact with the dislocation while the interaction.

Thus, there is a need to refine the current models of interaction of dislocation with radiation defects using better approximation for the austenitic steel, i.e. in the Fe-10Ni-20Cr alloy. Up to now, the main obstacle was the absence of FeNiCr potentials available, which guarantee the austenitic structure of the steel and are suitable to model the plastic behaviour using the Osetsky and Bacon model [51]. During the work on this thesis an Fe-Ni-Cr interatomic potential of the EAM type was developed and validated, which ensures the stability of the fcc phase in the whole range of compositions. The details of the development of the potential and its validation are provided in **Paper II**. In the development of this potential the pure elements (Fe, Ni, Cr) were fitted to reproduce such parameters as the lattice constant, elastic constants, SFE, formation and migration energy of a vacancy, formation energy of different interstitial configurations. The potential was also fitted to reproduce correctly (see Fig. 4.2) the SFE in the whole range of compositions of Ni and Cr while the target value for the elastic constants was optimized for the Fe-10Ni-20Cr alloy.

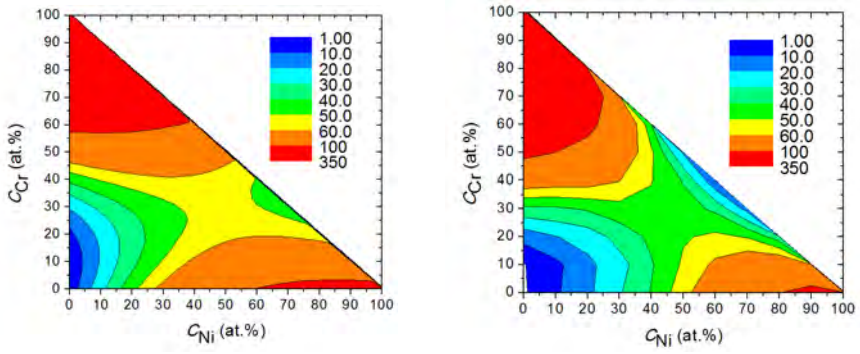

Figure 4.2: The stable SFE (mJ/m^2) as function of composition obtained from thermodynamic calculations [181] (a) and the potential (b).

The properties of the latter were ensured to be close to those of 316L austenitic stainless steel, having a similar composition of alloying elements.

The potential was implemented in the in-house MD code which implements the Osetsky and Bacon model of dislocation-defect interaction. During the work on this thesis the code was parallelized to be able to perform the calculations on the multiprocessor clusters. Interatomic potentials need to be validated against known results to be trusted. In this case we have established that this potential can be applied to model the dislocation movement and verified the thermal stability of the dislocation loops in the temperature range 300–900 K.

The energetics of radiation defects in FeNiCr alloy. Using the Fe-Ni-Cr interatomic potential we have calculated the energetics of the typical defects in the Fe-10Ni-20Cr fcc alloy, such as voids, stacking fault tetrahedra, perfect loops and Frank loops. This was part of the validation of the potential. The results are summarized in **Paper III**. It was verified that the Frank loop has the lowest energy among the defects in the case of interstitial type, while the SFTs are energetically favourable as agglomeration of vacancy type defects, which fits well the experimental observations [19, 23]. The calculation of the formation energy of the defects was found to correspond well with the theoretical predictions based on the elasticity theory [13]. The only discrepancy was identified in the case of hexagonal loops with the sides along <110> and was attributed to the splitting of the sides of the loop into two partials, which is not accounted for in the analytical models.

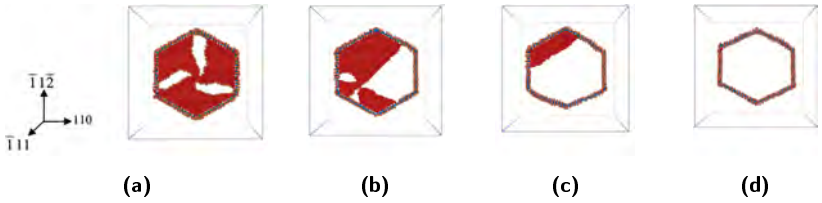

Figure 4.3: Modelling of the interstitial Frank loop of diameter d = 12.1 nm with the sides oriented along <112> directions at T = 300 K at the times (a) 1 ps, (b) 9 ps, (c) 12 ps and (d) 15 ps. The orientation of the crystal is the same in all figures.

The thermal stability of all the defects (see Fig. 4.3) was analyzed in the temperature range 300–1200 K. It was established that all the defects are stable except for the Frank loop with the sides along the <112> directions, which was transformed into a perfect loop at T=300 K and above.

Dislocation-Frank loop interaction modelling. The Fe-10Ni-20Cr alloy was used to model dislocation-defect interaction in austenitic steels in the temperature range T=300–900 K, for loop sizes 2–5 nm and varying interaction geometry. The results were published in **Paper IV**.

We have found that the loop size affects the interaction mechanism. While both small and large loops can follow the 'shear' or 'absorption into a helical turn' (see Fig. 4.4) interaction mechanisms, only the small loops can be absorbed into two glissile superjogs or follow a newly observed mechanism, i.e. the 'absorption and reemission in the other 111 plane'. The temperature effect was also remarkable: the unfaulting reactions were seen more often with the increase of the temperature which is consistent with the thermally-activated mechanism of dislocation movement. The interaction mechanism of the large loops is not affected by the rise of temperature, while in the case of small loops the temperature does have an effect on the process.

We have also evaluated the effect of width of distribution of SFE. The current calculations were done in the Fe-10Ni-20Cr alloy, which is characterized by the lower bound of SFE energy of the austenitic steels, i.e. 20 mJ/m^2. The comparison of the reactions in Fe-10Ni-20Cr and Fe-50Ni (described in the section 4.1.1), having almost equal SFE value but a different width of its distribution, has shown a significantly more frequent formation of constrictions and, consequently, more absorption reactions in the case of Fe-10Ni-20Cr alloy. The average CRSS was also higher in the case of this alloy. Thus, besides the importance of the SFE value itself, as established in section 4.1.1, the width of the distribution of SFE is also an important factor to be accounted for when studying the dislocation-Frank loop interaction.

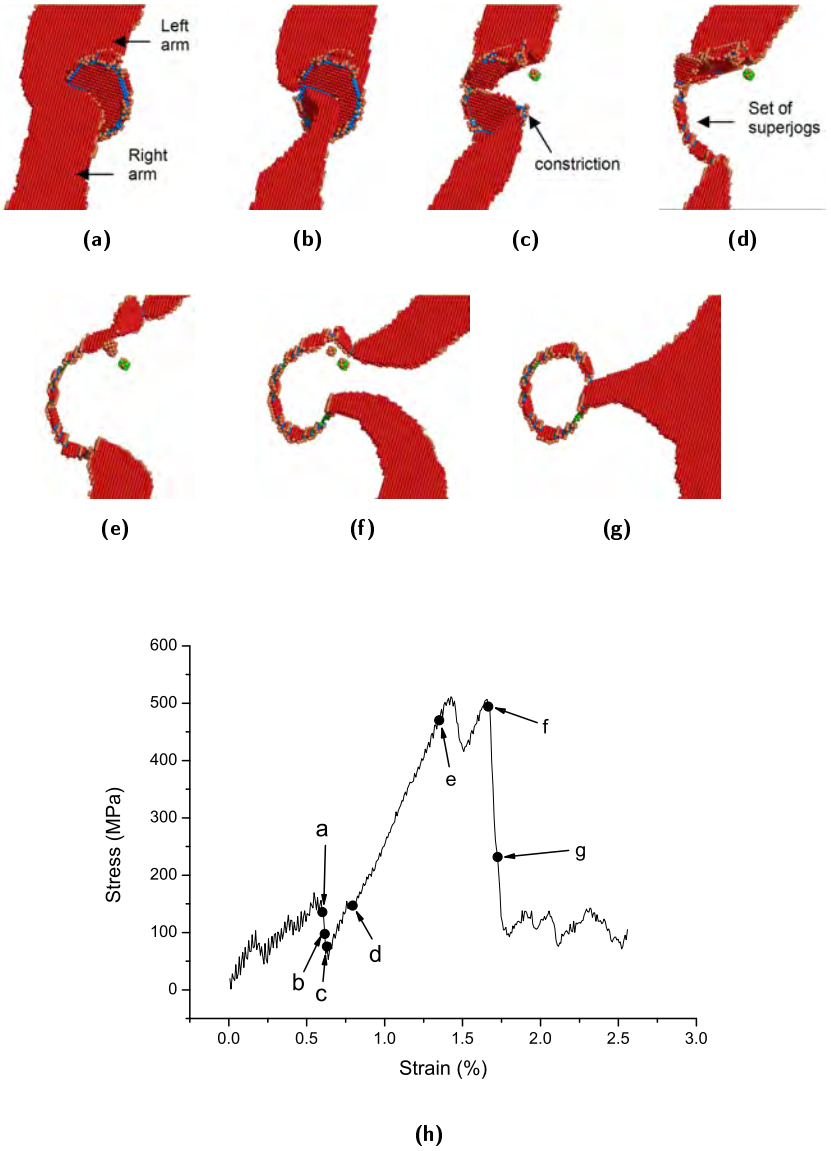

Figure 4.4: Visualizations of the dislocation reaction with the absorption of the loop in the form of helical turn (loop size = 5 nm; BV = 1/3[111]; T = 300 K): snapshots taken at times: (a) 200 ps, (b) 205 ps, (c) 210 ps, (d) 265 ps, (e) 450 ps, (f) 555 ps and (g) 575 ps. The corresponding stress-strain curve is shown in h). The arrows point to the moments shown in a)-g).

4.1.3 Conclusions

We have identified the dislocation-Frank loop interaction mechanisms in austenitic stainless steels using the MD method employed in the Fe-Ni and Fe-Ni-Cr model alloys. The effect of temperature, SFE and alloy composition on the CRSS and absorption of defects, responsible for hardening and formation of the dislocation channels, was also studied. In the preceding experimental work of Li, performed at SCK-CEN, [14] it was established that the increase of SFE decreases the localized deformation level. In that work two deformation modes in the irradiated alloys with different SFE were observed, namely: twinning (in low SFE alloys) and dislocation glide. It was established that the lower SFE enhances channel formation. However, the effect of SFE on the formation of dislocation channels via twinning and via dislocation glide could not be separated. Within the work on this PhD thesis we have investigated the pure effect of SFE on channeling via dislocation glide mechanism. It is found that when this is the only acting mechanism, the lower the SFE, the lower the probability of the formation of constrictions and consequently less frequent absorption of the loops which leads to the formation of dislocation channels and localized plastic deformation. On the basis of this results, we suggest that in low SFE alloys, subject to radiation, twinning deformation mode is the predominant mechanism responsible for channeling. Also, in the work of Li the relationship between SFE and hardening was not established, while here we state that the increase of SFE leads to the increase of loop absorption and consequently to the increase of resulting hardening, because the helical turns on screw dislocations, formed more often in high SFE alloys, are the strongest obstacles.

4.2 FM steels

Within this PhD thesis we have studied the thermodynamic mechanisms leading to the nucleation of solute-rich clusters in FM steels and have verified the hypothesis of enhanced strengthening due to the solutes decorating the dislocation loops, which was proposed in the past by several experimentalists [65]. While the nucleation mechanisms were studied using the electronic structure calculations (based on DFT), the hardening due to the solute-decorated loops was studied by MD simulations applying the so called two-band EAM potential for Fe-Cr [182].

4.2.1 Identification of the nucleation mechanisms of solute-rich clusters

Interaction of minor alloying elements (single solute atom) with lattice defects. In **Paper V** we apply the DFT calculations to study the interaction of minor alloying elements of high-Cr ferritic steels, such as Mo, W, Nb, Ta, V, Mn and Si, with the typical lattice defects, namely: vacancies, interstitials, grain boundaries and free surfaces. Also the effect of solute atoms on the drag of atoms along the close-packed <111> direction and on the modification of the screw dislocation core is considered. It is established that the refractory metals (Mo, W, Nb, Ta) and V — group #1 — all follow the same trend interacting with lattice defects, while the anti-ferromagnetic Mn and diamagnetic Si (group #2) stand out from the trend. It was seen that Mn and Si attract the vacancy in both 1nn (nearest neighbour) and 2nn positions, while the group #1 only in 1nn. Mn is the only element which forms the <110> Fe-Mn dumbbell (see Fig. 4.5) with a very high interaction energy of -0.59 eV and is weakly attracted to an interstitial carbon. Mn, Si and Nb were found to exhibit a considerable affinity to a free surface and, excluding Nb, facilitate the <111> row movement. Only Si was found to cause strong distortion of the screw dislocation core.

Synergy of Mn and Si interacting with the lattice defects. As Mn and Si atoms exhibit peculiar behaviour interacting with lattice defects unlike other solute atoms, we have investigated if there is a synergy between the Mn, Si and Cr (as major alloying element) interacting simultaneously with a vacancy, Fe-Fe, Fe-Cr and mixed solute-Cr <110> dumbbells. The results are summarized in **Paper VI**. In this work we focus on cross-pair solute interaction and among Mn, Si and Cr atoms only the Mn and Si atoms attract each other at 1nn with the energy about 0.09 eV.

We have calculated all the non-equivalent atomic configurations for Mn and Si atoms next to the point defects and found out the lowest energy ones. The interaction energy between Mn-Si pair and a point defect laid in the range 0.1–0.8 eV. The highest attraction between Mn-Si pair and a Fe-Fe dumbbell (Fe-Mn dumbbell and a Si atom nearby) was found to be 0.78 eV. Values of 0.40 eV were found between Mn-Si and Fe-Cr dumbbell and ~0.30 eV between Mn-Si and a vacancy. The pronounced increase of total binding energy (0.2 eV) while inserting the Si atom next to the Fe-Mn dumbbell was rationalized on the basis of change of magnetic moments distribution of neighbour Fe atoms (see Fig. 4.6).

Thus, the enhanced binding energy between Mn and Si next to the point defects in bcc Fe may lead to nucleation of radiation-induced Mn-Si-Ni-rich clusters possibly associated with growing clusters of point defects. As the Cr atoms do

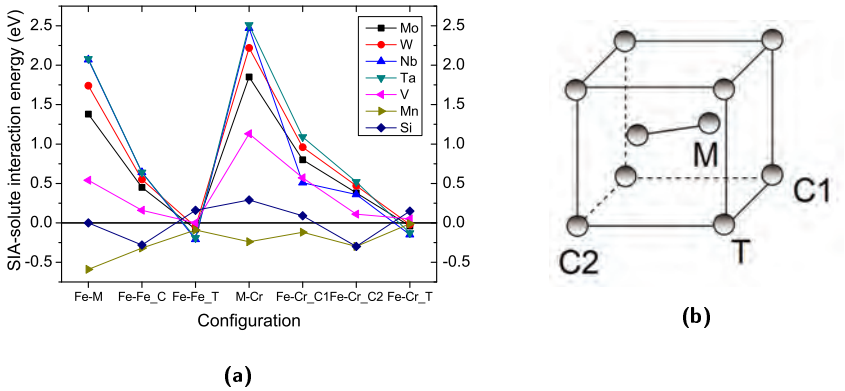

Figure 4.5: (a) SIA-solute interaction energy as a function of local arrangement. (b) Schematic figure explaining the considered configurations. M: Fe-solute mixed dumbbell; C1 and C2 are the sites located in the compressive region of the dumbbell strain field; T is the site located in the tensile region of the dumbbell strain field. Configurations denoted on the figure as Fe–Cr_C/T correspond to the interaction of the mixed Fe–Cr dumbbell with another solute atom placed in either tensile or compressive site. Note that there are two non-equivalent compressive sites. M–Cr configuration corresponds to the case when the dumbbell is formed by Cr and another solute atom. In the case of the configurations involving Cr atom in the dumbbell, the interaction energy between the Fe–Cr dumbbell and another solute atom is calculated.

not play any significant role in this effect, this study is also applicable for RPV steels.

4.2.2 Effect of decoration of dislocation loops by Cr on CRSS and loop absorption

We compared the interaction of undecorated and Cr-enriched dislocation loops with Burgers vectors 1/2<111> and <100> with an edge dislocation at T=(150–800) K. The results are presented in **Paper VII**. The edge dislocation was selected as it is known to be more efficient in terms of loop absorption and its removal compared to screw dislocation. Moreover, the contribution to the plastic flow is comparable for edge and screw dislocations at room temperature and above.

The chromium atoms being oversized in the iron lattice are occupying the tensile positions nearby the dislocation loop line — the outer edges of the loop.

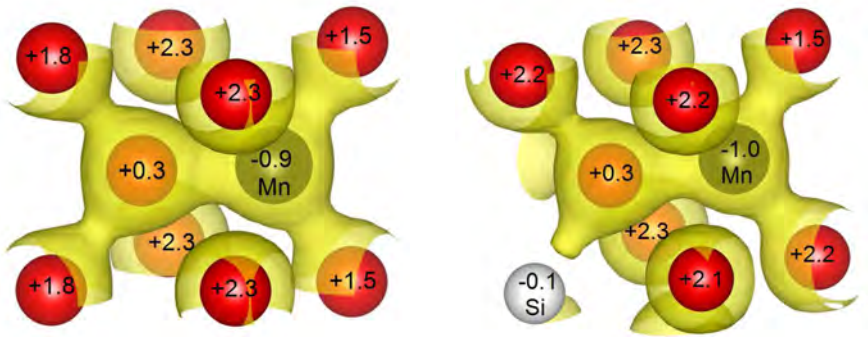

Figure 4.6: Distribution of charge density around a <110> split dumbbell in a eight atom bcc cell. Isosurfaces of 0.55 $e^-/Å^3$ are shown. The numbers denote the magnetic moment on each atom (in units of the Bohr magneton μ_B). The color of the atom refers to its type: red — Fe, black — Mn, white — Si. (a) and (b) figures correspond to FeMn (<110> dumbbell) and FeMn (<110> dumbbell) + Si(C2) complexes, respectively.

The atomic configurations with the decorated loops were obtained using the MMC method [183, 184].

We have found that the Cr enrichment affects the CRSS especially in the case of small loops with BV=1/2<111> with the size 2 nm and less which are invisible to TEM, while the same loops make almost no resistance to dislocation movement in pure Fe. The impact of Cr enrichment diminishes with increasing test temperature, which points to the thermally activated nature of this effect.

The additional CRSS increases with the increase of strain rate (which is interconnected with the dislocation velocity). This issue originates from the fact, that similarly to the suppression of propagation of the reaction segment (which leads to loop absorption and, consequently, to enhancement of CRSS), the latter will not move or move slower as the screw arms will develop more efficiently so no absorption occurs.

Thus, the Cr enrichment of the dislocation loop (see Fig. 4.7) may lead to substantial modifications of the dislocation-defect interaction mechanism depending on loading conditions: suppression of cross-slip, propagation of the reaction segment on the loop surface and dynamic drag. In general, this process unfavours the absorption of the radiation-induced dislocation loops and, consequently, increases the CRSS.

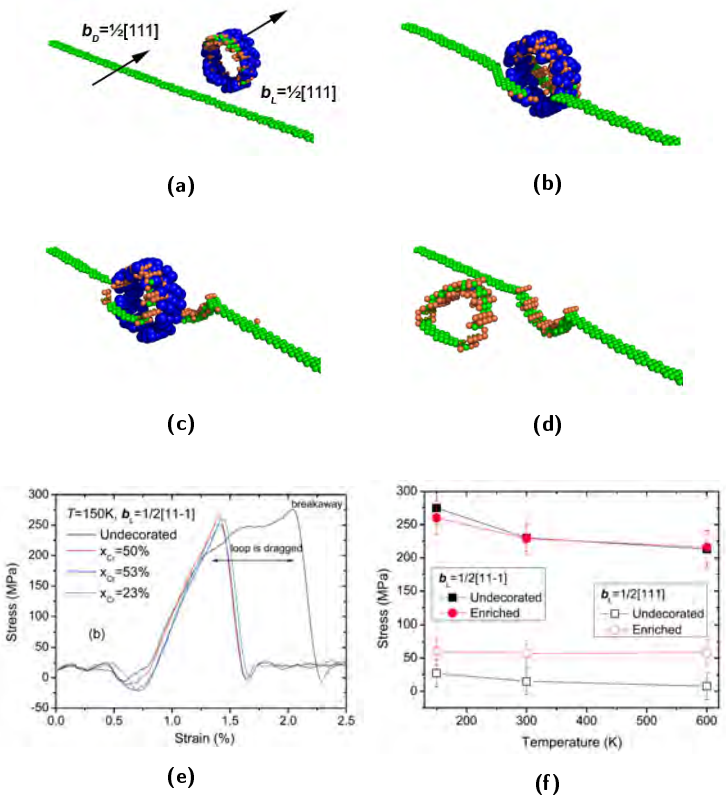

Figure 4.7: The atom-core visualization of the interaction of the enriched 1/2<111> loop with the dislocation at 150 K and dislocation velocity v_D = 10 m·s^{-1}. Blue balls show Cr atoms which are located in the loop core. (a) The model before load is applied; (b) the dislocation approaches the immobilized loop; (c) the segment substitution has occurred; (d) view of the dislocation-core atoms, showing the half-absorbed loop. The examples of the stress-strain curve in the case of 1/2<111> loops at T=150 K and the average unpinning stress calculated in the reactions with 1/2<111> loops of diameter 3.5 nm depending on ambient temperature are shown in e) and f), respectively.

4.2.3 Conclusions

Following the analysis sketched above, the nucleation of Mn-Si-Ni clusters, experimentally found by the APT method in high-Cr steels, may be attributed to the association of Fe-Mn mixed dumbbells with substitutional Si atoms. Such a configuration is characterized by high binding energy and can grow

further by adding Si and Mn atoms dragged by vacancies and self-interstitials.

The effect of Cr enrichment in the core of the dislocation loops consists in a significant increase of their resistance to dislocation movement. The enhanced hardening, attributed to Cr segregation, can explain the discrepancy of the hardening measured in the experiments of Matijasevic et al. [65] and the predictions according to the dispersed barrier model [185] based on the observed microstructure of the irradiated Fe-Cr samples. The physical origin of this effect is related to the change of the interaction mechanism, namely: the segregation suppresses the propagation of the reaction segment preventing the loops absorption and dynamic loop drag. Consequently, the resulting unpinning stress increases.

4.3 RPV steels

Within this PhD thesis we have investigated the thermodynamic mechanisms leading to the nucleation of Mn-Ni-rich clusters, experimentally found in RPV steels by APT [148]. Using the DFT method we have studied the stability of a vacancy-carbon pair and the possibility of its association with solute atoms (typical minor alloying elements, including Mn and Ni). If such solute-vacancy-carbon complexes are stable, they can serve as traps for nanometric interstitial dislocation loops, directly produced in displacement cascades. This interaction can lead to the formation of solute/carbon-enriched dislocation loops. Here, the effect of the solute/carbon segregation on the strengthening of invisible and visible in TEM dislocation loops is verified by MD simulations. Trapped loops become sinks for solute atoms (Ni, Mn, Si, Cu) transported by point defects, thereby getting decorated by them. This might be the mechanism of nucleation of Mn-Ni clusters, observed by APT. Here, therefore, we also study the interaction of dislocations with Mn-Ni-Cu-enriched loops, using a suitable potential, expressly developed for this purpose.

4.3.1 Identification of the nucleation mechanisms of solute-rich clusters

Thermal stability of vacancy-carbon pairs. We have compiled the published DFT data on the vacancy–carbon interaction in bcc iron and performed additional calculations to fill up some gaps. The results are summarized in **Paper VIII**. According to the published results of the electronic structure calculations [136, 186–188] and our calculations, the vacancy-carbon (V-C)

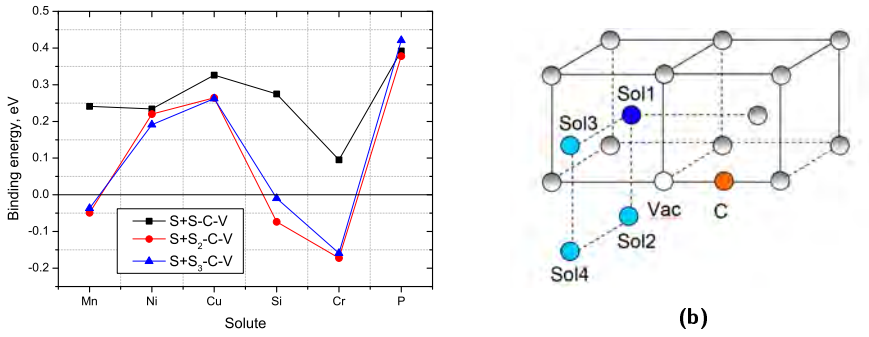

Figure 4.8: a). The incremental binding energy of the nth solute to S$_{(n-1)}$–C–V cluster. b). The schematic picture of larger solute–vacancy–clusters considered.

attraction is within the range 0.47–0.74 eV. Using the available DFT database, object kinetic Monte Carlo (OKMC) modelling was performed to simulate the isochronal annealing experiments in Fe-based alloys where the evolution of V-C complexes has been studied. The best explanation of the experiments was provided using the V-C binding energy of 0.65 eV. The stable configurations of the V-C complexes that remain stable up to 650 K were identified. Thus, the mobility of carbon and vacancy is mutually mitigated.

Interaction of vacancy-carbon pair with minor alloying elements of ferritic steels. As the V-C pair is a stable defect in the iron matrix, we have investigated whether solute atoms can gather at this complex. For this we have identified the stability of clusters consisting of one or several solute atoms of one kind, namely Mn, Ni, Cu, Si, Cr and P, and a vacancy-carbon pair. The summary of results is published in **paper IX**. We have established that all the considered solutes may form stable S-V-C (solute-vacancy-carbon) clusters having the same structure irrespective of the solute type. Also we have estimated the thermal stability of these defects by analyzing the sum of binding and migration energy, i.e. the dissociation energy.

We have found (see Fig. 4.8) that the S-C-V complexes can grow up to S$_4$-C-V clusters in the case of Ni, Cu and P-containing clusters. Further addition of Mn-, Cr- and Si-rich atoms to S$_2$-C-V is not energetically favourable due to the repulsive interaction between solutes or solute-carbon. The dissociation barrier for S-C-V clusters is by about 0.2–0.3 eV higher than the one of V-C pair which points to the fact that the association of vacancies with any kind of the studied

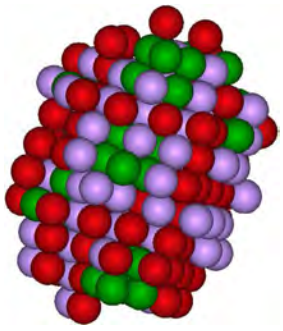

Figure 4.9: The ternary CuMnNi-rich precipitate. It has a nearly spherical shape and consists of a mixture of ~20% Cu, ~40% Ni and ~40% Mn. The red (dark) atoms denote Ni, the purple (light) atoms denote Mn and the green (grey) atoms denote Cu.

solutes leads to a stronger pinning of both freely migrating interstitial carbon and vacancies. It is worth to note that the enhanced binding of a Mn-Si pair in presence of points defects (for instance, vacancies) may be also responsible for the nucleation of Mn-Ni-rich solute clusters at a vacancy-carbon pair.

4.3.2 Interatomic potential for the FeCuNiMn system

In order to be able to study the effect of Cu, Ni, Mn on hardening, an EAM-type potential for the FeCuNiMn alloy was fitted on the basis of the available experimental and newly calculated DFT data. The details of the fitting process are presented in **Paper X**. The FeCuNi potential was developed in [189], while part of the work of this thesis was devoted to contribute to the fitting of the Fe-Mn, Fe-Mn-Cu and Fe-Mn-Ni potentials. The developed potential was applied to model the atomic structure of the CuMnNi precipitates using the MMC method (see Fig. 4.9).

4.3.3 Radiation-induced hardening due to solute-enriched dislocation loops

In this PhD we studied whether there is any contribution to hardening from the dislocation loops enriched by carbon or manganese-nickel-copper solutes.

Effect of C decoration on loop absorption and CRSS. In **Paper XI** we have applied the molecular dynamics method to study the effect of carbon decoration on the absorption of <100> dislocation loops by dislocations in iron.

This article complements the study of interaction of dislocation with 1/2<111> dislocation loops where strong suppression of the drag of carbon-decorated loops by dislocations was found [190]. Also in the case of direct interaction between dislocation and carbon-decorated loops, invisible loops are found to act as obstacles whose strength is at least twice as high as compared to that of undecorated ones. Additional strengthening due to the carbon decoration on the visible loops was also regularly observed.

The atomic configurations of the solute enriched loops were obtained using the MMC method. Later on the interaction between the edge dislocation and the undecorated and solute-enriched dislocation loop with BV <100> in the temperature range T=(150–800) K (see Fig. 4.10) was studied. We have determined that carbon decoration leads to the modification of the interaction mechanism in the intermediate temperature range (T=300–600 K) which consists in suppression of complete absorption of <100> loops in favour of transformation into 1/2<111> loops. This process is accompanied by the increase of CRSS. The strongest effect of carbon decoration on CRSS was observed in the case of loops which are athermally absorbed on dislocation lines at T=300 K and above.

Effect of Mn segregation on loop absorption and CRSS. In **Paper XII** we have considered the effect of Mn segregation on the strength of dislocation loops during the passage of a dislocation. In the Fe-Mn binary, Fe-Mn-Ni ternary and Fe-Mn-Ni-Cu quaternary alloys the segregation of Mn to the core of 1/2<111> dislocation loops occurs at equilibrium at 600 K.

When analyzing the regions close to the dislocation loop core, Mn appears to be the most strongly segregating element, while Cu is the weakest one. Mn and Ni occupy competing positions in the loop core, so the segregation level of Mn in the ternary alloy is lower than in the binary. At the same time, the addition of Cu suppresses the segregation of Ni, so that Mn concentration in the loop core recovers back, as a result. Hence, the interplay between all three chemical elements may contribute to the final chemical arrangement (without accounting for kinetic effects). In any case, Mn seems to always prevail, its content being about 2–3 and 5 times higher than that of Ni and Cu, respectively. Mn is therefore expected to play the major role on the properties of loops upon plastic deformation in the quaternary Fe-Mn-Ni-Cu alloys. The separate effect of the other elements, however, still needs to be assessed.

The study of the interaction with edge dislocations of small, 1.5 nm diameter 1/2<111> dislocation loops (see Fig. 4.11a) enriched with Mn, Mn-Ni and Mn-Ni-Cu reveals that the main effect of the enrichment is the significant increase of the unpinning stress. By increasing Mn content in the core of the loops, the unpinning stress increases too. This effect has obviously direct

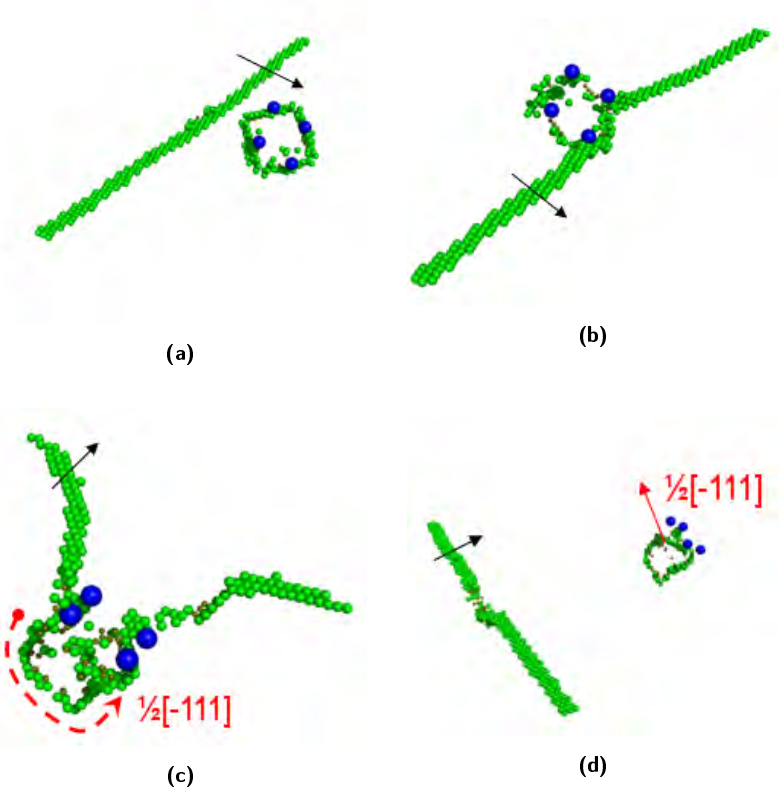

Figure 4.10: Visualization of different stages of the reaction involving a [100] loop decorated by four C atoms (blue spheres) at T=300 K. A black arrow shows the direction of dislocation movement. On (d), the dislocation got unpinned and transmitted to the left part of simulation box via periodic boundary conditions. A red dashed line shows the position of the 1/2[111] segment formed after the flip of the upper part of the pre-existing [100] loop.

consequences on increasing the radiation hardening attributed to the so-called matrix damage. The study of the interaction with edge dislocation of larger (3.5 and 5 nm diameter) 1/2<111> loops (see Fig. 4.11b) reveals that the enrichment suppresses mainly the absorption and dynamic drag of loops i.e. reactions involving instantaneous removal of loops by the dislocation front. Instead of being absorbed, the loops remain essentially intact after interaction with the dislocation, except being partially absorbed and sheared. This effect, too, may have consequences regarding the strain hardening evolution and in

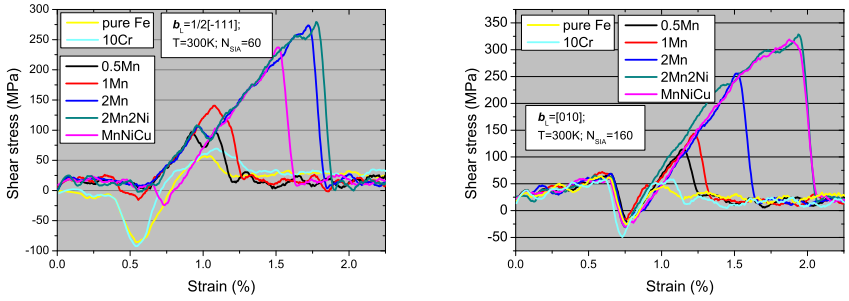

Figure 4.11: Stress-strain relationship corresponding to the interaction of (a) $1/2[\bar{1}11]$ dislocation loops of size 1.5 nm and (b) [010] dislocation loops of size 3.5 nm, whose configurations were obtained by MMC simulations in several alloys. The composition of the alloys is reported in the figure inset, as well the concentration of Mn in the loop core.

particular, the formation of defect-free channels, expected to be prevented or at least delayed. Note, however, that at the doses relevant for RPV steels no TEM-visible defects were observed and, consequently, no channels can be distinguished after deformation.

4.3.4 Conclusions

The nucleation of the Mn-Ni rich clusters in RPV steels may be caused by the association of Mn and Ni solutes with vacancy-carbon pairs (available in the matrix upon irradiation). The numerous formation of Mn-vacancy-carbon- and Ni-vacancy-carbon-rich clusters will produce 'traps' for glissile dislocation loops, directly produced in cascades. The interaction of the loops with the solute-rich clusters may result in the annihilation of vacancies and accommodation of solutes and carbon in the core of the dislocation loops.

In order to evaluate the effect of dislocation loops enriched by carbon or substitutional solutes on the dislocation-defect interaction process we have performed MD simulations. Carbon decoration leads to the modification of the interaction mechanism in the intermediate temperature range (T=300–600 K) which consists in suppression of complete absorption of <100> loops in favour of transformation into $1/2$<111> loops. This process is accompanied by the increase of CRSS. The strongest effect of carbon decoration on CRSS was

observed in the case of loops which are athermally absorbed on dislocation lines at T=300 K and above. The main effect of the Mn enrichment is the significant increase of the unpinning stress. By increasing Mn content in the core of the loops, the unpinning stress increases too.

The above mentioned effects of C and Mn may explain the contribution of invisible matrix damage (i.e. small dislocation loops non-resolvable by TEM) to the net hardening.

5 Conclusions and outlook

5.1 Conclusions

The main objectives of this thesis were to study the nanoscale dislocation-defect interaction mechanisms leading to hardening and the formation of dislocation channels in austenitic steels, to find out the nucleation mechanisms of solute-rich clusters in the FM and RPV steels, and to estimate their contribution (in association with dislocation loops) to the radiation-induced hardening.

We have used binary FeNi and ternary FeNiCr interatomic potentials to model austenitic stainless steels, by simulating the interaction of dislocations with typical radiation defects, i.e. Frank loops, by means of classical molecular dynamics. It was found that:

1. a decrease of SFE leads to suppression of loop absorption and thus reduces the probability for channel initiation by dislocation glide. Given that the reaction of the loop absorption on a screw dislocation results in the highest unpinning stress, in general a decrease of SFE also leads to a reduction of the loop-induced hardening;

2. solute alloying leads to further suppression of loop absorption due to the increase of the friction stress in the secondary glide planes.

The obtained information on the loop hardening and loop absorption as a function of temperature and SFE provides a guidance for the rationalization of the radiation-induced hardening and plastic instability at room and reactor

operational temperature reported in [14], where the highest localized deformation was observed in the austenitic alloys with low SFE. While two deformation modes, namely dislocation glide and twinning, were observed in the considered alloys, by our work we clarify the specific effect of the deformation via the dislocation glide to the formation of the dislocation channels. Confronting our results (i.e. that higher SFE enhances channeling) with experimental observations in [14], we suggest that in low SFE alloys, subject to radiation, twinning deformation mode is the predominant mechanism responsible for channeling. Also, the above mentioned results of this work propose the trend for the hardening depending on the SFE which was not clearly established in the experimental work [14].

We have applied the DFT method to study the thermodynamic mechanisms leading to the nucleation of solute-rich clusters, observed experimentally in irradiated high-Cr steels [102, 107, 191, 192]. The possible formation mechanism for Mn-Si-Ni-rich clusters in high-Cr alloys may be attributed to the formation of Fe-Mn mixed dumbbells and a Si atom in the compression site next to the Fe atom. This configuration is characterized by a high total binding energy and may serve as a nucleus for growing Mn-Si-Ni-rich complexes.

The molecular dynamics modelling method was applied to identify the source of hardening in the FeCr alloys experimentally studied in [65]. We have established that small dislocation loops in the undecorated state are essentially weak obstacles for the dislocation motion, while the decoration of loops by Cr atoms increases their strength significantly. Thus, the effect of Cr-loop decoration is one of the possible explanations of the enhanced hardening in high-Cr alloys, as compared to low-Cr alloys and pure Fe, studied in [65]. The physical origin of this effect is related to a change of the interaction mechanism which influenced the unpinning stress.

We have also proposed a new mechanism explaining the nucleation of nano-sized Mn-Ni-rich clusters observed in irradiated RPV steels. The formation of such clusters can be initiated by the nucleation of Mn and Ni clusters at vacancy-carbon pairs.

Numerous and thermally stable solute-carbon-vacancy complexes will frequently interact with glissile dislocation loops, directly produced in collision cascades. Such interactions should result in the subsequent decoration of the loops by carbon and Mn-Ni solutes. By performing dedicated MD simulations, we have established that the Mn-Ni and carbon decoration leads to a pronounced increase of the unpinning stress attributed to the decorated loops, as compared to the undecorated ones. In addition, the carbon decoration leads to a modification of the interaction mechanism in the intermediate temperature range (T=300–600 K) which consists in a suppression of the

absorption of <100> loops in favour of transformation into 1/2<111> loops. Hence, carbon segregation at dislocation loops changes not only the resulting hardening (in terms of raise of the CRSS) but also the microstructural evolution under prolonged plastic deformation.

5.2 Outlook

In the future we foresee to further improve the models of nucleation of the solute-rich clusters and dislocation-defect interaction in austenitic stainless, FM and RPV steels.

We plan to study the interaction of edge dislocations with Frank loops and screw/edge dislocation with SFTs and perfect dislocation loops. The latter were found to be created as an outcome of several reactions with Frank loops at different temperatures.

Dislocation pile-up was not considered within this work, while this effect might have an influence on dislocation-defect interaction mechanisms according to [39] and may possibly affect the increase of unpinning stress, enhancing the reactions with formation of a helical turn and, consequently, hardening.

Twinning deformation is another important mode of slip in austenitic alloys. The effect of SFE and temperature on the interaction of a twin band with the Frank loops should be investigated.

While only the basic interactions of dislocations and dislocation loops were considered within this PhD thesis, this data can be crucially useful for the parameterization of dislocation dynamics methods, which allow the evolution of the crystal to be studied at a significantly higher scale (about micrometer scale). This method is foreseen to be applied to obtain the stress-strain curves that can then be compared with experimental data. Also, such modelling may reveal the formation of dislocation channels and explain the pattern of dislocation channels which are parallel or intersect depending on SFE [14].

While the basic atomic configurations of Mn-Si-rich clusters were considered, the mechanisms of growth of such complexes to Mn-Si-Ni-rich clusters, observed by APT, are still to be elucidated. The analysis of the lifetime of stable Mn-Si(-Ni)-rich clusters with and without carbon atoms is also an important aspect in view of the validation of the DFT data by experiments.

The interaction of a screw dislocation with <100> and 1/2<111> loops, being enriched with either Cr or Mn-Ni solutes, is still to be done in order to complete models for binary interactions between dislocations and dislocation loops in

Fe-Cr and Fe-Mn-Ni alloys, which are the model systems to study the plasticity in FM and low-Cu RPV steels, respectively.

Bibliography

[1] http://www.world-nuclear.org/info/Economic-Aspects/Economics-of-Nuclear-Power/

[2] http://www.sckcen.be/br1/images/historyphotos/index.htm

[3] http://www.nrc.gov/reading-rm/basic-ref/students/reactors.html

[4] M. Lambrecht, *PhD thesis*, University of Ghent, 2008.

[5] https://www.gen-4.org/gif/jcms/c_9360/scwr

[6] https://www.gen-4.org/gif/jcms/c_9357/gfr

[7] https://www.iter.org/mach

[8] http://www.worldnuclearreport.org/IMG/pdf/20130716msc-worldnuclearreport2013-lr-v4.pdf

[9] http://www.ornl.gov/science-discovery/nuclear-science/research-areas/reactor-technology/light-water-reactor-sustainability

[10] http://www.iaea.org/pris/CountryStatistics/

[11] http://www.world-nuclear.org/info/Nuclear-Fuel-Cycle/Power-Reactors/Nuclear-Power-Reactors/

[12] http://www.iaea.org/pris/CountryStatistics/CountryDetails.aspx?current=BE

[13] D. Hull and D.J. Bacon, Introduction to Dislocations, Elsevier Science, 2011. Pictures are reprinted with permission from Elsevier.

[14] X. Li, *PhD thesis*, University of Ghent, 2009.

[15] V. Jansson, *PhD thesis*, University of Helsinki, Finland: 2013.

[16] http://www.substech.com/dokuwiki/doku.php?id=tensile_test_and_-strain-stress_diagram

[17] http://www.twi-global.com/technical-knowledge/faqs/material-faqs/faq-what-is-charpy-testing/

[18] http://publications.sckcen.be/dspace/bitstream/10038/447/1/er_-25.pdf

[19] C. Pokor, Y. Brechet, P. Dubuisson, J.P. Massoud and A. Barbu, J. Nucl. Mater. 326 (2004) 19–29. Pictures and tables are reprinted with permission from Elsevier.

[20] http://www-pub.iaea.org/MTCD/publications/PDF/P1522_web.pdf

[21] H. Chandler, *Heat Treater's Guide: Practices and Procedures for Irons and Steels*, ASM International, 1994.

[22] A. Volgin, *PhD thesis*, Universite de Rouen, 2012.

[23] S.J. Zinkle, P.J. Maziasz and R.E. Stoller, J. Nucl. Mater. 206 (1993) 266–286. Pictures are reprinted with permission from Elsevier.

[24] C. Pokor, *PhD thesis*, CEA SACLAY, 2002.

[25] P.J. Maziasz and C.J. McHargue, Int. Mater. Rev. 32 (1987) 190.

[26] P. Maziasz, J. Nucl. Mater. 169 (1989) 95–115.

[27] K.H. Westmacott, R.S. Barnes, D. Hull and R.E. Smallman, Philos. Mag. 6 (1961) 929–935. Pictures are reprinted with permission from Taylor & Francis.

[28] S.I. Porollo, A.M. Dvoriashin, Y.V. Konobeev, A.A. Ivanov, S.V. Shulepin and F.A. Garner, J. Nucl. Mater. 359 (2006) 41–49. Pictures are reprinted with permission from Elsevier.

[29] P.J. Maziasz, J. Nucl. Mater. 191–194, Part B (1992) 701-705.

[30] P.J. Maziasz, Trans. ANS 39 (1981) 433.

[31] T. Muroga, Y. Miyamoto, H. Watanabe and N. Yoshida, J. Nucl. Mater. 155–157, Part 2 (1988) 810–814.

[32] S.J. Zinkle and R.L. Sindelar, J. Nucl. Mater. 155–157, Part 2 (1988) 1196–1200.

[33] N. Yoshida, J. Nucl. Mater. 174 (1990) 220–228.

[34] T.M. Robinson and M.L. Jenkins, Philosophical Magazine A 43 (1981) 999–1015.

[35] B.N. Singh and S.J. Zinkle, J. Nucl. Mater. 206 (1993) 212–229.

[36] G.S. Was and P.L. Andresen, Corrosion 63 (2007) 19–45.

[37] C. Pokor, Y. Brechet, P. Dubuisson, J.P. Massoud and X. Averty, J. Nucl. Mater. 326 (2004) 30–37. Pictures are reprinted with permission from Elsevier.

[38] J. Friedel, *Dislocations*, Pergamon Press, 1964.

[39] T. Nogaret, C. Robertson and D. Rodney, Philos. Mag. 87 (2007) 945–966. Pictures are reprinted with permission from Taylor & Francis.

[40] I.M. Robertson, A. Beaudoin, K. Al-Fadhalah, L. Chun-Ming, J. Robach, B.D. Wirth, A. Arsenlis, D. Ahn and P. Sofronis 2004 *Dislocation-obstacle interactions: Dynamic experiments to continuum modeling* Intenational Conference on Fundamentals of Plastic Deformation La Colle sur Loup, FRANCE pp. 245–250.

[41] J. Robach, I. Robertson, H. Lee and B. Wirth, Acta Materialia 54 (2006) 1679–1690.

[42] H.B. Huntington, J.E. Dickey and R. Thomson, Physical Review 100 (1955) 1117–1128.

[43] R.M.J. Cotterill and M. Doyama, Physical Review 145 (1966) 465–478.

[44] R. Chang and L.J. Graham, physica status solidi (b) 18 (1966) 99–103.

[45] V. Vitek, R.C. Perrin and D.K. Bowen, Philos. Mag. 21 (1970) 1049–1073.

[46] J.P. Hirth and L. Kubin, *Dislocations in Solids*, Elsevier Science, 2009.

[47] S. Rao, C. Hernandez, J. Simmons, T. Parthasarathy and C. Woodward, Philosophical Magazine A 77 (1998) 231–256.

[48] J.E. Sinclair, P.C. Gehlen, R.G. Hoagland and J.P. Hirth, Journal of Applied Physics 49 (1978) 3890–3897.

[49] R. Thomson, S.J. Zhou, A.E. Carlsson and V.K. Tewary, Phys. Rev. B 46 (1992) 10613–10622.

[50] M.S. Daw, S.M. Foiles and M.I. Baskes, Materials Science Reports 9 (1993) 251–310.

[51] Y.N. Osetsky and D.J. Bacon, Model. Simul. Mater. Sci. Eng. 11 (2003) 427–446. Pictures are reprinted with permission from IOP Publishing.

[52] D.J. Bacon and Y.N. Osetsky, Materials Science and Engineering: A 400–401 (2005) 353–361.

[53] B. Wirth, V. Bulatov and T. Diaz de la Rubia, Journal of Engineering Materials and Technology 124 (2002) 329.

[54] D.J. Bacon and Y.N. Osetsky, JOM 59 (2007) 40–45.

[55] Y.N. Osetsky, D. Rodney and D.J. Bacon, Philos. Mag. 86 (2006) 2295–2313.

[56] Y. Osetsky, D. Bacon, B. Singh and B. Wirth, J. Nucl. Mater. 307-311 (2002) 852–861.

[57] Y.N. Osetsky, R.E. Stoller and Y. Matsukawa, J. Nucl. Mater. 329–333, Part B (2004) 1228–1232.

[58] Y.N. Osetsky, R.E. Stoller, D. Rodney and D.J. Bacon, Materials Science and Engineering: A 400–401 (2005) 370–373.

[59] P. Szelestey, M. Patriarca and K. Kaski, Model. Simul. Mater. Sci. Eng. 13 (2005) 541.

[60] Y.N. Osetsky, Y. Matsukawa, R.E. Stoller and S.J. Zinkle, Philos. Mag. Lett. 86 (2006) 511–519.

[61] Z. Rong, Y.N. Osetsky and D.J. Bacon, Philos. Mag. 85 (2005) 1473–1493.

[62] D. Rodney, Acta Materialia 52 (2004) 607–614. Pictures are reprinted with permission from Elsevier.

[63] C. Shin, H.-H. Jin, J.H. Kwon, J.-H. Shim and T.S. Byun, Journal of the Korean Physical Society 52 (2008) 1250–1254.

[64] T. Nogaret, D. Rodney, M. Fivel and C. Robertson, J. Nucl. Mater. 380 (2008) 22–29.

[65] M. Matijasevic and A. Almazouzi, J. Nucl. Mater. 377 (2008) 147–154. Pictures are reprinted with permission from Elsevier.

[66] K. Shiba, M. Enoeda and S. Jitsukawa, J. Nucl. Mater. 329–333, Part A (2004) 243–247.

[67] L.V. Boccaccini, L. Giancarli, G. Janeschitz, S. Hermsmeyer, Y. Poitevin, A. Cardella and E. Diegele, J. Nucl. Mater. 329–333, Part A (2004) 148–155.

[68] S. Jitsukawa, A. Kimura, A. Kohyama, R.L. Klueh, A.A. Tavassoli, B. van der Schaaf, G.R. Odette, J.W. Rensman, M. Victoria and C. Petersen, J. Nucl. Mater. 329–333, Part A (2004) 39–46.

[69] R.L. Klueh and D.R. Harries, *High-Chromium Ferritic and Martensitic Steels for Nuclear Applications*, ASTM, 2001.

[70] http://indico.cern.ch/event/229108/contribution/16/material/slides/0.pdf

[71] J. Van den Bosch, D. Sapundjiev and A. Almazouzi, J. Nucl. Mater. 356 (2006) 237–246.

[72] A.A.F. Tavassoli, J. Nucl. Mater. 302 (2002) 73–88.

[73] P. Marmy and B.M. Oliver, J. Nucl. Mater. 318 (2003) 132–142.

[74] N. Baluc, R. Schaublin, P. Spatig and M. Victoria, Nuclear Fusion 44 (2004) 56–61.

[75] http://192.107.58.30/presentationsWorkshop/VanDenBosch1.pdf

[76] ASTM A213 Standard Specification, Annual Book of ASTM Standards, Section 01.01, 112-118.

[77] D. Dulieu, K.W. Tupholme and G.J. Butterworth, J. Nucl. Mater. 141–143, Part 2 (1986) 1097–1101.

[78] N. Yamanouchi, M. Tamura, H. Hayakawa, A. Hishinuma and T. Kondo, J. Nucl. Mater. 191–194, Part B (1992) 822–826.

[79] R.L. Klueh and P.J. Maziasz, MTA 20 (1989) 373–382.

[80] D. Sapundjiev, S. Van Dyck and W. Bogaerts, Corrosion Science 48 (2006) 577–594.

[81] R. Fisher, E. Dulis and K. Carroll, Journal of metals (1953) 690–695.

[82] P. Dubuisson, D. Gilbon and J. Seran, J. Nucl. Mater. 205 (1993) 178–189.

[83] M. Mathon, Y. Carlan de , G. Geoffroy, X. Averty, A. Alamo and C. Novion de, J. Nucl. Mater. 312 (2003) 236–248.

[84] R. Williams and H. Paxton, Journal of The Iron and Steel Institute 185 (1957) 358–372.

[85] E.A. Little and D.A. Stow, J. Nucl. Mater. 87 (1979) 25–39.

[86] S.I. Porollo, A.M. Dvoriashin, A.N. Vorobyev and Y.V. Konobeev, J. Nucl. Mater. 256 (1998) 247–253.

[87] E. Little and D. Stow, J. Nucl. Mater. 87 (1979) 25–39.

[88] F.A. Garner, M.B. Toloczko and B.H. Sencer, J. Nucl. Mater. 276 (2000) 123–142.

[89] P. Grobner, Metallurgical Transactions 4 (1973) 251.

[90] V. Sagaradze, I. Kositsyna, V. Arbuzov, V. Shabashov and Y. Fillippov, The physics of metals and metallography 92 (2001) 508–517.

[91] A. Kohyama, A. Hishinuma, D.S. Gelles, R.L. Klueh, W. Dietz and K. Ehrlich, J. Nucl. Mater. 233v237, Part 1 (1996) 138–147.

[92] K.-H. Mayer and F. Masuyama, *The development of creep-resistant steels, in: Creep-resistant steels*, Woodhead Publishing Ltd., Cambridge, England: 2008.

[93] S.J. Zinkle and J.T. Busby, Materials Today 12 (2009) 12–19.

[94] N. Yoshida, A. Yamaguchi, T. Muroga, Y. Miyamoto and K. Kitajia, J. Nucl. Mater. 155–157 (1988) 1232–1236. Pictures are reprinted with permission from Elsevier.

[95] K. Arakawa, M. Hatanaka, H. Mori and K. Ono, J. Nucl. Mater. 329–333 (2004) 1194–1198.

[96] E. Little and D. Stow, Metal science 14 (1980) 89–94.

[97] D.S. Gelles, J. Nucl. Mater. 108–109 (1982) 515–526.

[98] E.A. Little, Int. Metal Rev. 204 (1976) 25–60.

[99] K. Suganuma and H. Kayano, radiation effects 54 (1981) 81–86.

[100] K. Suganuma and H. Kayano, J. Nucl. Mater. 118 (1983) 234–241.

[101] L. Malerba, A. Caro and J. Wallenius, J. Nucl. Mater. 382 (2008) 112–125.

[102] V. Kuksenko, C. Pareige and P. Pareige, J. Nucl. Mater. 432 (2013) 160–165.

[103] Z. Jiao, V. Shankar and G.S. Was, J. Nucl. Mater. 419 (2011) 52–62.

[104] http://www.efda.org/wpcms/wp-content/uploads/2014/06/JG12.356-web.pdf

[105] F. Hammad, M. Matta and K. Mohammed, J. Nucl. Mater. 108–109 (1982) 428–435.

[106] E. Gaganidze and J. Aktaa, Fusion Engineering and Design 88 (2013) 118–128. Pictures are reprinted with permission from Elsevier.

[107] Z. Jiao and G.S. Was, Acta Materialia 59 (2011) 4467–4481. Pictures are reprinted with permission from Elsevier.

[108] C. Heintze, F. Bergner, A. Ulbricht and H. Eckerlebe, J. Nucl. Mater. 409 (2011) 106–111.

[109] F. Bergner, C. Pareige, M. Hernandez-Mayoral, L. Malerba and C. Heintze, J. Nucl. Mater. 448 (2014) 96–102.

[110] L. Malerba, G. Bonny, D. Terentyev, E.E. Zhurkin, M. Hou, K. Vortler and K. Nordlund, J. Nucl. Mater. 442 (2013) 486–498.

[111] Y.N. Osetsky, D.J. Bacon, Z. Rong and B.N. Singh, Philos. Mag. Lett. 84 (2004) 745–754.

[112] D. Bacon, Y. Osetsky and Z. Rong, Philos. Mag. 86 (2006) 3921–3936. Pictures are reprinted with permission from Taylor & Francis.

[113] A. Nomoto, N. Soneda, A. Takahashi and S. Ishino, Materials Transactions 46 (2005) 463–468.

[114] D. Terentyev, L. Malerba, D. Bacon and Y. Osetsky, Journal of Physics: Condensed Matter 19 (2007) 456211.

[115] X.Y. Liu and S.B. Biner, Scripta Materialia 59 (2008) 51–54. Pictures are reprinted with permission from Elsevier.

[116] D. Terentyev, P. Grammatikopoulos, D. Bacon and Y. Osetsky, Acta Materialia 56 (2008) 5034–5046. Pictures are reprinted with permission from Elsevier.

[117] J. Marian, B. Wirth and J. Perlado, Physical Review Letters 88 (2002) 255507.

[118] Y. Osetsky, A. Serra and V. Priego, J. Nucl. Mater. 276 (2000) 202–212.

[119] D. Terentyev, L. Malerba, T. Klaver and P. Olsson, J. Nucl. Mater. 382 (2008) 126–133.

[120] J. Marian, B. Wirth, R. Schaeublin, G. Odette and J. Perlado, J. Nucl. Mater. 323 (2003) 181–191.

[121] Z. Rong, D. Bacon and Y. Osetsky, Materials Science and Engineering: A 400–401 (2005) 378–381.

[122] D. Terentyev, Y.N. Osetsky and D.J. Bacon, Scripta Materialia 62 (2010) 697–700.

[123] D.A. Terentyev, Y.N. Osetsky and D.J. Bacon, Acta Materialia 58 (2010) 2477–2482.

[124] M.L. Jenkins, Z. Yao, M. Hernandez-Mayoral and M.A. Kirk, J. Nucl. Mater. 389 (2009) 197–202.

[125] G. Odette and B. Wirth, J. Nucl. Mater. 251 (1997) 157–171.

[126] E. Meslin, M. Lambrecht, M. Hernandez-Mayoral, F. Bergner, L. Malerba, P. Pareige, B. Radiguet, A. Barbu, D. Gomez-Briceno, A. Ulbricht and A. Almazouzi, J. Nucl. Mater. 406 (2010) 73–83.

[127] http://www.gruppofrattura.it/ocs/index.php/esis/ECF19/paper/viewFile/9115/5883

[128] R. Chaouadi, *An Engineering Radiation Hardening Model for RPV Materials*, Report SCKvCEN-R-4235, SCK-CEN, Belgium: 2005.

[129] ASTM A533 Standard Specification, Annual Book of ASTM Standards, Section 01.04.

[130] M. Hansen, *Constitution of Binary Alloys, Metallurgy and Metallurgical Engineering Series*, McGraw-Hill Book Company, 1958.

[131] A.D. Romig and J.I. Goldstein, MTA 11 (1980) 1151–1159.

[132] F. Bergner, M. Lambrecht, A. Ulbricht and A. Almazouzi, J. Nucl. Mater. 399 (2010) 129–136.

[133] K. Dohi, T. Onchi, F. Kano, K. Fukuya, M. Narui and H. Kayano, J. Nucl. Mater. 265 (1999) 78–90.

[134] S. Jumel, *PhD thesis*, L'Universite des Sciences et Technologies de Lille, 2005.

[135] K. Tapasa, A. Barashev, D. Bacon and Y. Osetsky, J. Nucl. Mater. 361 (2007) 52–61.

[136] C. Domain, C. Becquart and J. Foct, Phys. Rev. B 69 (2004) 144112.

[137] http://www.techfak.uni-kiel.de/matwis/amat/def_en/kap_1/illustr/h_okta.gif

[138] G.E. Lucas and G.R. Odette, Proc. of the Second International Symposium on Environmental Degradation of Materials in Nuclear Power Systems – Water Reactors (1985) 345–360.

[139] L. Debarberis, B. Acosta, A. Zeman, S. Pirfo, P. Moretto, A. Chernobaeva and Y. Nikolaev, International Journal of Microstructure and Materials Properties 2 (2007) 326–338.

[140] M.K. Miller, R. Jayaram and K.F. Russell, J. Nucl. Mater. 225 (1995) 215–224.

[141] K. Fukoya, H. Nakata, K. Fujii, S. Dumbill, J.M. Hyde, S. Yanagita and K. Hono, Proceedings on an International Symposium on Mechanisms of Material Degradation and Non-Destructive Evaluation of Light Water Reactors (2002) 91–102.

[142] C.A. English, J.M. Hyde and S.R. Ortner, Proceedings on an International Symposium on Mechanisms of Material Degradation and Non-Destructive Evaluation of Light Water Reactors (2002) 53–75.

[143] G.R. Odette and G.E. Lucas, Jom-Journal of the Minerals Metals & Materials Society 53 (2001) 18–22.

[144] R. Chaouadi and R. Gerard, J. Nucl. Mater. 345 (2005) 65–74.

[145] E. Meslin-Chiffon, *PhD thesis*, Universite de Rouen, 2007.

[146] R.G. Carter, N. Soneda, K. Dohi, J.M. Hyde, C.A. English and W.L. Server, J. Nucl. Mater. 298 (2001) 211–224.

[147] J.T. Buswell, P.J.E. Bischler, S.T. Fenton, A.E. Ward and W.J. Phythian, J. Nucl. Mater. 205 (1993) 198–205.

[148] M.K. Miller and K.F. Russell, J. Nucl. Mater. 371 (2007) 145–160. Pictures are reprinted with permission from Elsevier.

[149] N. Soneda, K. Dohi, A. Nomoto, K. Nishida and S. Ishino, Proc. of the International Symposium on Research for Aging Management of Light Water Reactors (2007)

[150] G.R. Odette and G.E. Lucas, Radiation Effects and Defects in Solids 144 (1998) 189–231.

[151] B.D. Wirth, G.R. Odette, W.A. Pavinich, G.E. Lucas and S.E. Spooner, Effects of Radiation on Materials: 18th International Symposium, ASTM STP 1325 (1999) 102–121.

[152] M.J. Konstantinovic and B. Minov, J. Nucl. Mater. 425 (2012) 112–116.

[153] M. Lambrecht and A. Almazouzi, J. Nucl. Mater. 385 (2009) 334–338.

[154] Y. Nagai, Z. Tang, M. Hassegawa, T. Kanai and M. Saneyasu, Phys. Rev. B 63 (2001) 134110.

[155] A. Hempel, M. Saneyasu, Z. Tang, M. Hasegawa, G. Brauer, F. Plazaola, S. Yamaguchi, F. Kano and A. Kawai, Proc. of 19th International Symposium on Effects of Radiation on Materials, American Society for Testing and Materials Science & Engineering (2000) 560–578.

[156] P. Olsson, T.P.C. Klaver and C. Domain, Phys. Rev. B 81 (2010) 054102.

[157] G.S. Was, *Fundamentals of Radiation Materials Science: Metals and Alloys*, Springer, 2007.

[158] V. Jansson, L. Malerba, A. De Backer, C.S. Becquart and C. Domain, J. Nucl. Mater. 442 (2013) 218–226.

[159] Y. Osetsky, D. Bacon, A. Serra, B. Singh and S. Golubov, Philos. Mag. 83 (2003) 61–91.

[160] D. Terentyev, L. Malerba and M. Hou, Phys. Rev. B 74 (2007) 104108.

[161] N. Anento, A. Serra and Y.N. Osetsky, Model. Simul. Mater. Sci. Eng. 18 (2010) 025008.

[162] E. Vincent, C.S. Becquart and C. Domain, Nucl. Instrum. Meth, B 228 (2005) 137–141.

[163] E. Vincent, C.S. Becquart and C. Domain, J. Nucl. Mater. 359 (2006) 227–237.

[164] P. Hohenberg and W. Kohn, Physical Review 136 (1964) B864.

[165] W. Kohn and L. Sham, Physical Review 140 (1965) 1135.

[166] T. Klaver, P. Olsson and M. Finnis, Phys. Rev. B 76 (2007) 214110.

[167] P. Olsson, C. Domain and J. Wallenius, Phys. Rev. B 75 (2007) 014110.

[168] G. Kresse and J. Hafner, Phys. Rev. B 47 (1993) 558–561.

[169] G. Kresse and J. Furthmuller, Phys. Rev. B 54 (1996) 11169–11186.

[170] P.E. Blochl, Phys. Rev. B 50 (1994) 17953–17979.

[171] G. Kresse and D. Joubert, Phys. Rev. B 59 (1999) 1758–1775.

[172] J.P. Perdew, J.A. Chevary, S.H. Vosko, K.A. Jackson, M.R. Pederson, D.J. Singh and C. Fiolhais, Phys. Rev. B 46 (1992) 6671–6687.

[173] S.H. Vosko, L. Wilk and M. Nusair, Canadian Journal of Physics 58 (1980) 1200–1211.

[174] P. Allen and D.J. Tildesley, *Computer simulation of liquids*, Clarendon Press, 1987.

[175] M. Daw and M. Baskes, Phys. Rev. B 29 (1984) 6443.

[176] D. Hepburn and G. Ackland, Phys. Rev. B 78 (2008) 165115.

[177] G. Bonny, D. Terentyev, E.E. Zhurkin and L. Malerba, J. Nucl. Mater. 452 (2014) 486–492.

[178] C. Becquart, Report F16O-CT-2003-508840, PERFECT IP Lille (2005) 22p.

[179] Y. Mishin, D. Farkas, M.J. Mehl and D.A. Papaconstantopoulos, Phys. Rev. B 59 (1999) 3393–3407.

[180] A. Voter and S. Chen, Materials Research Society Symp. Proc. 82 (1987) 175–180.

[181] A.P. Miodownik, Calphad 2 (1978) 207–226.

[182] P. Olsson, J. Wallenius, C. Domain, K. Nordlund and L. Malerba, Phys. Rev. B 72 (2005) 214119.

[183] E.E. Zhurkin, D. Terentyev, M. Hou, L. Malerba and G. Bonny, J. Nucl. Mater. 417 (2011) 1082–1085.

[184] D. Terentyev, X. He, E. Zhurkin and A. Bakaev, J. Nucl. Mater. 408 (2011) 161–170.

[185] R.W. Cahn and P. Haasen, *Physical Metallurgy*, Elsevier Science, 1996.

[186] C.J. Forst, J. Slycke, K.J. Van Vliet and S. Yip, Physical Review Letters 96 (2006) 175501.

[187] C.-C. Fu, J.D. Torre, F. Willaime, J.-L. Bocquet and A. Barbu, Nat Mater 4 (2005) 68–74.

[188] T. Ohnuma, N. Soneda and M. Iwasawa, Acta Materialia 57 (2009) 5947–5955.

[189] G. Bonny, R.C. Pasianot, N. Castin and L. Malerba, Philos. Mag. 89 (2009) 3531–3546.

[190] D. Terentyev, N. Anento and A. Serra, Journal of Physics: Condensed Matter 24 (2012) 455402.

[191] V. Kuksenko, C. Pareige, C. Genevois, F. Cuvilly, M. Roussel and P. Pareige, J. Nucl. Mater. 415 (2011) 61–66.

[192] V. Kuksenko, C. Pareige and P. Pareige, J. Nucl. Mater. 425 (2012) 125–129.

A Paper I

Interaction of dislocations with Frank loops in Fe–Ni alloys and pure Ni: An MD study

D. Terentyev, A. Bakaev, Yu.N. Osetsky

Journal of Nuclear Materials 442 (2013) S628

Journal of Nuclear Materials 442 (2013) S628–S632

Contents lists available at SciVerse ScienceDirect

Journal of Nuclear Materials

journal homepage: www.elsevier.com/locate/jnucmat

Interaction of dislocations with Frank loops in Fe–Ni alloys and pure Ni: An MD study

D. Terentyev [a,*], A. Bakaev [a,b], Yu.N. Osetsky [c]

[a] SCK•CEN, Nuclear Material Science Institute, Boeretang 200, B-2400 Mol, Belgium
[b] Center for Molecular Modeling, Department of Physics and Astronomy, Ghent University, Technologiepark 903, 9052 Zwijnaarde, Belgium
[c] Materials Science and Technology Division, ORNL, Oak Ridge, TN 37831, USA

ARTICLE INFO

Article history:
Available online 1 February 2013

ABSTRACT

Variation of the stacking fault energy in FCC alloys and austenitic steels is well known to influence the evolution of radiation damage and its effect on deformation mechanisms. The primary defects observed in austenitic steels under neutron irradiation are mainly Frank loops. Here, we study the interaction of edge and screw dislocations with Frank loops in low stacking fault energy Fe–Ni alloys. The interatomic potentials employed were specially developed to reproduce a number of properties of real austenitic steels. The influence of temperature and loop morphology on the interaction mechanism and the critical resolved shear stress for dislocations to overcome loops has been investigated. All investigated reactions have been subdivided into three classes depending on temperature, loop size and interaction geometry. It is shown that by decreasing stacking fault energy below a certain value the formation of constrictions on dislocations is suppressed so that loop unfaulting becomes a less favorable mechanism in comparison with loop shear. Additional effect of solid-solution alloying, causing a non-negligible friction stress, is expressed in the impedance of the propagation of dislocations in the secondary glide planes, which is another factor limiting the unfaulting process.

1. Introduction

Plasticity of metals and metallic alloys is known to be controlled by the movement of dislocations [1]. Irradiation of metals, metallic alloys and steels by energetic particles causes modification of the crystal microstructure resulting in the formation of new lattice defects such as precipitates, dislocation loops and voids [2]. These defects act as obstacles to dislocation glide, thereby causing hardening and consequently embrittlement [1,2]. In the case of neutron irradiation (of structural and in-core reactor components at temperature below $0.3T_M$), the matrix damage created is composed mainly of dislocation loops (see e.g. [3]). Interaction of moving dislocations with loops is therefore an important contribution to plastic deformation mechanisms in irradiated crystalline materials, as was directly revealed by transmission electron microscopy studies (for FCC metals see e.g. [4–6]).

In FCC metals, alloys and austenitic stainless steels, which are subject of the present work, both faulted Frank loops (FLs) with Burgers vector (BV) 1/3⟨1 1 1⟩ and perfect unfaulted loops with BV ½⟨1 1 0⟩ form under irradiation [1]. Due to the low stacking fault energy (SFE) of austenitic alloys, FLs are a major component of the microstructure formed under neutron irradiation [7]. The interaction of FLs with dislocations has already been studied by Molecular Dynamics (MD) simulations in pure FCC Ni and Cu. A systematic study performed by Nogaret et al. [8] has revealed several mechanisms depending on the interaction geometry and impinging dislocation character. The following three mechanisms have been identified: (i) loop shearing; (ii) loop unfaulting into glissile configuration; (iii) loop absorption into glissile superjogs (on edge dislocations) or helical turns (on screw dislocations). For both screw and edge dislocations the unfaulting mechanism is controlled by a cross-slip process. In general, the number of geometrical configurations leading to loop unfaulting is higher for a screw dislocation [8].

In the case of a screw dislocation two distinct unfaulting mechanisms have been revealed [8,9]: (i) the formation of a D-Shockley partial dislocation segment, which sweeps the fault. The sweeping is accommodated by cross-slip of the dislocation around the loop. (ii) Cross-slip of the dislocation, formation of a constriction and its re-dissociation in the loop habit plane. Then, two partials remove the fault. Both of these mechanisms require the formation of constrictions and propagation of dislocations in the secondary glide planes. Note that cross-slip dislocation movement, also occurring by means of the constriction formation and being directly related to SFE of a material, plays a crucial role in the process of work-hardening [1].

The previous studies were performed for pure Ni and Cu, due to the lack of reliable interatomic potentials for austenitic steels (i.e.

* Corresponding author. Tel.: +32 014 33 31 97.
E-mail address: dterenty@sckcen.be (D. Terentyev).

0022-3115/$ - see front matter © 2013 Elsevier B.V. All rights reserved.
http://dx.doi.org/10.1016/j.jnucmat.2013.01.328

Cu has relatively low SFE but also too low shear modulus, while Ni has comparable shear modulus but very high SFE). Recently, however, an Fe–Ni interatomic potential set has been developed specifically to reproduce both shear modulus and SFE comparable to those of austenitic stainless steels [10]. In this work, we apply this potential to study the interaction of FLs with dislocations in Fe–Ni solid solutions containing 50 at.% and 70 at.% Ni. The choice of these two compositions was governed by the desired value of SFE (i.e. to be in the range of that relevant for austenitic steels) and full stability of FCC phase. We also perform simulations of pure Ni using two different potentials predicting low and high SFE. In this way, we attempt to make a step further towards understanding the effect of low SFE on dislocation-loop interaction.

The effect of alloying (i.e. variation of SFE, shear modulus and dislocation friction stress) on dislocation-FL interaction mechanisms is also addressed in this work. We show that by decreasing SFE below a certain value the formation of constrictions is suppressed so that unfaulting becomes a less favorable mechanism in comparison with loop shear. Furthermore, the presence of a non-negligible friction stress may also impede the propagation of dislocations in the secondary glide planes, which is an essential factor suppressing the unfaulting process that has not been reported so far.

2. Simulation details

The interaction of dislocations with FLs has been studied for pure Ni and Fe–50Ni and Fe–70Ni random alloys. The Fe–Ni potential was specifically developed to mimic properties of 316 austenitic steels and was parameterized using a wide range of data including some obtained by *ab initio* calculations [10]. The potential has the standard Embedded Atom Method (EAM) form [11], which offers a reasonable compromise between computing speed and reliability. For random alloys, the potential predicts an FCC structure to be more stable than BCC if Ni content exceeds 40 at.% [10]. The stacking fault energy increases smoothly from 0 to 125 mJ/m^2 with increasing Ni content, as shown in Fig. 1. In Fe–50Ni, SFE is about 15 mJ/m^2, which is in the range of the lowest values for austenitic steels [12], while in Fe–70Ni it rises to 50 mJ/m^2, which represents an upper bound.

To perform the simulations of pure Ni, we applied two EAM potentials developed by Mishin [13] (henceforth M-potential) and Voter [14] (henceforth V-potential). The M-potential is the basis of the Fe–Ni potential used here, while the latter was often used in the past to study behaviour of lattice defects in Ni. The basic properties of these potentials are summarized in Table 1. The V-potential predicts SFE = 58 mJ/m^2 which is close to that of the Fe–70Ni. The M-potential provides twice as high value of SFE in pure Ni. The shear modulus of Fe–50Ni and Fe–70Ni alloys is close to that of austenitic steels.

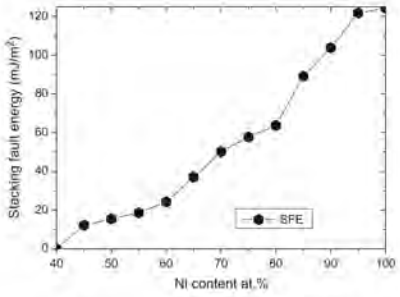

Fig. 1. Evolution of SFE as a function of alloy composition.

The interaction between dislocations and loops was studied using a classical MD approach [15] applying the so-called method of 'periodic array of dislocations' [16]. A pure shear deformation $[1\,1\,0]\,(1\,1\,1)$ with a constant strain rate ($10^6\,s^{-1}$) was used to initiate the movement of a dislocation at a desired velocity, with other relevant details found in Ref. [16]. The model, with axes oriented along $[1\,1\,0]$, $[1\,\bar{1}\,2]$ and $[\bar{1}\,1\,1]$ directions, contained about 1.2 M mobile atoms and dimensions along x, y and z were $84 \times 62 \times 52 * a_0^3$ (where a_0 was chosen appropriately to account for thermal expansion). Periodic boundary conditions were applied along x and y directions, while atoms in a few outer $\pm z$ atomic layers were rigidly fixed in their perfect crystal positions. Screw and edge dislocations with $\boldsymbol{b} = 1/2[1\,1\,0]$ have been introduced and relaxed. Both types of dislocations dissociated in the $(1\,1\,1)$ plane into two Shockley partial dislocations during relaxation.

An FL was introduced 10 nm away from the leading partial dislocation so that its geometrical centre coincided with the dislocation glide plane. The four non-equivalent orientations of BV were inspected. We have considered regular hexagonal FLs with sides oriented along $\langle 1\,1\,2\rangle$ and $\langle 1\,1\,0\rangle$ directions and diameter of 4 nm. Due to the imposed periodic boundary conditions along the dislocation line, the centre-to-centre spacing between the loops was 28 nm.

Integration of Newton's equations was performed using a constant time step equal to 2 fs. Calculations were done in the framework of a microcanonical NVE ensemble (see e.g. [15]), where atom number, N, system volume, V, and total energy, E, are conserved if the work of external forces is taken into account. Most of the simulations were done at 300 K and some additional ones at 600 K and 900 K. The initial temperature was achieved applying the Maxwellian distribution to the atoms in the model, which was equilibrated for 10 ps to prior to applying the constant strain rate deformation. The identification of the dislocation core and stacking fault atoms was realized by applying a combination of methods, namely: central symmetry analysis, common neighbour analysis, potential energy analysis and counting specific number of FCC neighbours.

3. Results

3.1. Interaction mechanisms

Based on the main set of MD simulations performed at 300 K for loops of 4 nm size, we distinguished three basic interaction mechanisms: (i) loop shear, (ii) loop absorption and (iii) loop unfaulting

Table 1
Lattice properties predicted by different interatomic potentials for pure Ni and Fe–50Ni and Fe–70Ni solid solutions. SFE in the Fe–Ni alloys was computed by considering 250 Å^2 as a surface of the stacking fault and by performing 100 relaxation runs sampling the spatial distribution of solutes.

	Pure Ni: potential M	Pure Ni: potential V	Fe–50Ni	Fe–70Ni
a_0 (Å) Lattice unit	3.52	3.52	3.7	3.66
E_c Cohesive energy (eV/atom)	−4.45	−4.45	−4.40	−4.44
E_v^f (vacancy formation energy (eV)	1.60	1.56	1.63	1.62
E_i^f ⟨100⟩-dumbbell formation energy (eV)	4.93	4.70	4.7	4.56
Shear modulus (GPa)	147	71	81.2	93.5
SFE (mJ/m^2)	125	58	15	50

prior to contact with the dislocation line. Fig. 2 summarizes schematically the reaction outcome depending on the material and interatomic potential at 300 K. We see that in low SFE Ni and Fe–50Ni models, the main interaction mechanism is shear. While in high SFE Ni – it is unfaulting and absorption. Hence, a decrease of SFE enhances the shear of loops. In the Fe–50Ni alloy, there is only one configuration where the FL is completely absorbed into the screw dislocation (SD) line (see Fig. 2a). In the following we briefly describe the interaction mechanisms and differences observed in the reactions performed in the Fe–50Ni solid solution and in pure Ni.

As discussed in [8,9], a screw dislocation is more efficient than an edge dislocation at absorbing FLs. Two examples of reactions between a screw dislocation and FLs with sides oriented along ⟨1 1 0⟩ directions and $\boldsymbol{b} = 1/3[1\,1\,\bar{1}]$ and $1/3[1\,1\,1]$ are visualized in Figs. 3 and 4, respectively. A brief description of the interaction mechanisms is provided in the captions. The same reactions were modelled in pure Cu [8] and in Ni [9] and absorption via cross-slip movement was observed. Here, we observed loop absorption only in pure Ni (with both potentials) and Fe–70Ni, while in the low SFE alloy (i.e. Fe–50Ni), the cross-slip movement was suppressed and for $1/3[1\,1\,1]$ loop shear has occurred instead.

Two possible reasons led to the absence of absorption in these two cases. Absorption requires cross-slip, but the absence of a constriction during the interaction (see Fig. 4) does not allow for cross-slip and the corresponding sweeping up of the stacking fault. In contrast, a constriction was formed in the reaction shown in Fig. 3, but the constriction did not propagate across the loop surface, unlike in the reaction modelled in pure Cu or Ni. The mechanism that suppresses such propagation may be attributed to a significant lattice friction arising from the presence of solute atoms.

Finally, the mechanism referred to as 'Unfault before reaction' (see Fig. 2), occurs when the approaching dislocation initiates nucleation and propagation of two Shockley partial dislocation segments on the loop surface. The partials sweep across the extrinsic fault transforming an FL into a perfect loop ($\boldsymbol{b} = \frac{1}{2}\langle 1\,1\,0\rangle$). This unfaulting mechanism was observed for both screw and edge dis-

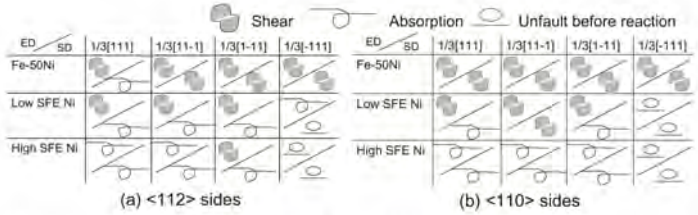

Fig. 2. The outcome of the interaction between a dislocation and Frank loop ($D_L = 4$ nm). The notation for the interaction mechanism is explained on the legend above the tables. ED and SD stand for an edge and screw dislocation, respectively. Data for 'low' and 'high' SFE Ni were obtained using the V and M potentials, respectively. The reactions were modelled at 300 K. Figs. (a and b) report the results obtained for the hexagonal loops with sides oriented along ⟨1 1 2⟩ and ⟨1 1 0⟩ directions, respectively.

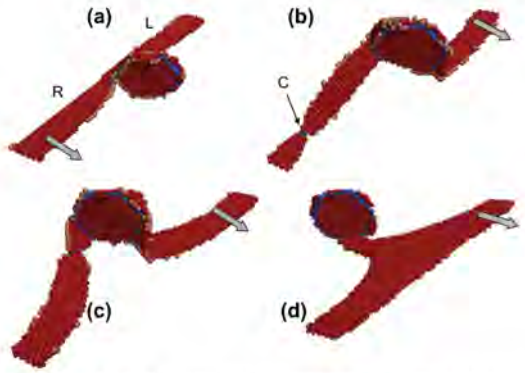

Fig. 3. Interaction of a $1/2[1\,1\,0]$ SD with a $1/3[1\,1\,1]$ FL in Fe–50Ni at 300 K. Initially, the loop attracts the dislocation. On the contact with the loop, the dislocation forms constriction (a) and changes its glide plane from $(1\,1\,\bar{1})$ to $(1\,1\,1)$. Then, the left dislocation arm (labelled L) makes a second cross-slip and returns to the original glide plane (b). Now, the left arm is pinned at the front bottom corner of the loop, while the right arm is attached to the rear middle corner (b). The two arms (dissociated in different planes) are connected by the constriction (labelled C). The right arm is not glissile in the $(1\,1\,1)$ plane and therefore only the left arm bows out under the action of increasing shear stress. This causes movement of the constriction towards the loop, thus reducing the length of the right arm on the cross-slip plane (c). Finally, the remainder of the right arm undergoes a second cross-slip so that the leading partial dislocation is completely restored (d). Now, only the trailing partial is pinned by the lower segment of the loop and final unpinning occurs via formation of a dipole and its closure. As a result, the Frank loop is fully restored, while the glide plane of the screw dislocation has been shifted down.

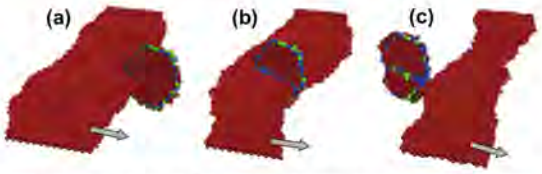

Fig. 4. Interaction of a 1/2[1 1 0] SD with a 1/3[1 1 1] FL in Fe–50Ni at 300 K. Initially, the dislocation is attracted to the loop and moves to interact with the nearest side (a). However, due to the large spacing between the partials, loop shear by the leading partial starts before a constriction can form (b). The two partials consequently shear the loop sequentially, leaving a 1/2[1 1 0] step on its surface (c).

locations. In the absence of a nearby dislocation line the same loop was observed to be stable against unfaulting at temperature up to 900 K for at least 10 ns. We therefore conclude that the nucleation of partial dislocation segments on the loop surface was induced by the stress field of the approaching dislocation. This effect was not reported in earlier studies [8,9], most probably due to the high dislocation velocity simulated there. However, loop unfaulting due to nucleation of partial dislocation segments was not observed in the reactions modelled in the Fe–50Ni alloy. These examples clearly demonstrate that a decrease of SFE suppresses the nucleation of partials on the extrinsic stacking fault and the presumed enhanced friction stress suppresses the movement of partials that could remove the stacking fault.

3.2. Effect of temperature and loop size on critical stress and interaction mechanism

To investigate the effect of loop size and temperature on loop absorption we performed a set of additional calculations at 600 K and 900 K with FLs of different sizes containing 331 (4.5 nm), 397 (5 nm), 631 (7 nm) SIAs. The goal was to see how an increase of loop size or temperature may enhance the unfaulting reaction over shear. Thus, we considered an edge dislocation and interaction geometries which at 300 K led to shear (see Fig. 2). All simulations were carried out using the V-potential for pure Ni (SFE ≈ 58 mJ/m^2). For the loops of size 4.5 nm containing sides oriented along both ⟨1 1 0⟩ and ⟨1 1 2⟩ directions, we see that increasing temperature up to 900 K does not change the interaction mechanism. The loops were sheared. The same mechanism was observed for all the larger loops studied here. The critical resolved shear stress (CRSS or τ_C) for dislocation breakaway as a function of loop size and temperature is presented in Fig. 5. τ_C is not sensitive to simulation temperature in the case of $\boldsymbol{b}$ = 1/3[1 1 1] (⟨1 1 0⟩ sides) and $\boldsymbol{b}$ = 1/3[1 1 1] (⟨1 1 2⟩ sides). Whereas for other configurations, τ_C decreases with rising temperature and increases with loop size, as one would expect.

The above results also show that by increasing simulation temperature in the Fe–50Ni alloy the loop shear mechanism does not change to loop absorption. In pure metals, on the other hand, e.g. in Cu [8] and in Ni studied here, increasing temperature induced complete absorption of FLs even for an edge dislocation. The absorption occurred in a two-step reaction: (i) emergence of a screw dipole and (ii) formation of constriction on dislocation loop and cross-slip movement of the screw arms unfaulting the loop. Such mechanism has been regularly observed in pure Ni modelled using the high SFE M-potential. In contrast, in the Fe–50Ni, characterized by very low SFE, a constriction was not formed and in all cases loops were sheared before the two partials could form a constriction. This demonstrates that SFE controls the formation of constriction and activation of cross-slip, as expected, nevertheless a possible influence of enhanced friction stress in the alloys should not be forgotten.

Indeed, alloying of Fe with Ni essentially increases the friction stress for both edge and screw dislocations as compared to pure FCC metals (e.g. Ni, studied here). The mean flow stress for an edge dislocation moving in the Fe–50Ni and Fe–70Ni alloys is presented in Fig. 6. The latter was calculated by averaging the resolved shear stress while the dislocation moves with steady-state velocity of 4 m/s. We can see that in the Fe–50Ni alloy, the average flow stress is slightly lower than in Fe–70Ni, but in both cases the mean flow

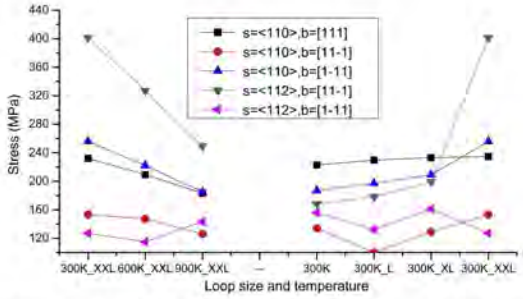

Fig. 5. CRSS in pure Ni (V potential) for an edge dislocation to unpin from Frank loops of different size. Notations L, XL and XXL stand for the loop containing 331, 397 and 631 SIAs, respectively. The orientation of the loop sides (⟨1 1 0⟩ or ⟨1 1 2⟩) and of the BV is summarized in the box.

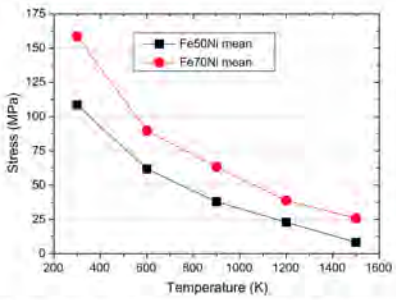

Fig. 6. Average flow stress corresponding to the movement of an edge dislocation at a speed of 4 m/s in the Fe–50Ni and Fe–70Ni alloys.

stress at $T < 1200$ K exceeds 20 MPa, which is the Peierls stress for a screw dislocation in pure Ni calculated with the V-potential at 0 K. The Peierls stress for an edge dislocation in pure Ni (4 MPa) is even lower.

To clarify the role of SFE on loop absorption in the presence of non-negligible friction stress, we have repeated a number of reactions involving an edge dislocation in Fe–70Ni (SFE ≈ 50 mJ/m^2). While at low temperature mainly shear was observed, at high temperature (900 K) the outcome of the interactions was the same as obtained in pure Ni using the V-potential (SFE ≈ 58 mJ/m^2). This result confirms that SFE plays a major role in the interaction process and the enhanced friction stress due to solution alloying has a secondary effect. However, a possible influence of a combination of the enhanced friction stress and variation of SFE, relevant for alloys, needs to be explored further.

4. Summary and conclusions

In this work we have studied the interaction of both edge and screw dislocations with Frank loops in pure Ni and random concentrated Fe–Ni solid solution alloys, which are characterized by low and high values of SFE in the range relevant for austenitic stainless steels. The interaction has been studied using constant strain rate loading conditions corresponding to dislocation velocity of 4 m/s. The main difference between reactions in pure Ni and the Fe–50Ni alloy was in the ability of dislocations to absorb Frank loops. In the Fe–50Ni alloy (SFE = 15 mJ/m^2) no absorption was seen in any cases involving an edge dislocation and for the screw dislocation only one configuration led to absorption. Hexagonal loops with ⟨1 1 0⟩ sides were not absorbed under any conditions and increasing temperature up 900 K in the low SFE alloy did not modify the reaction mechanism, which was a 1/2⟨1 1 0⟩ pure shear of the loop. However, in the Fe–70Ni alloy (SFE = 50 mJ/m^2) some reactions led to complete absorption at 900 K, demonstrating that SFE plays a significant role in the interaction process leading to absorption.

One also has to note that the friction stress, enhanced in the alloys by means of solid solution, suppresses the reconstruction of a sheared Frank loop, which occurs via migration of the 1/2⟨1 1 0⟩ ledge formed in the shear reaction over a loop surface. In pure metals, the migration occurs rather fast, so that the planar loop surface is restored almost immediately after the interaction. However, in the alloys the restoration was seen to depend on the temperature. We therefore expect that loops can be destroyed by consequential shearing much more efficiently in alloys than in pure FCC metals. Hence, both modulation of SFE and friction stress are essential features in the determination of the reaction outcome.

Finally, a number of statements can be made based on the above summarized results:

(i) A decrease of SFE makes the formation of constrictions energetically unfavourable and hence suppresses cross-slip of screw dislocation segments, as long known from plasticity theory of FCC metals [1]. Given that in some reactions cross-slip is an essential pre-requisite for loop absorption, a decrease of SFE reduces the probability for absorption. This has been shown in the earlier studies in Ni and Cu [8,9], as well as here.

(ii) The enhanced friction stress has also been shown to suppress the absorption reaction in the case of both edge and screw dislocations. In pure Ni or Cu bowing dislocation side arms can acquire screw character and cross-slip, whereas in the alloys this process was hindered, presumably due to the friction stress in secondary glide planes. Increasing temperature, which reduces the friction stress, allows cross-slip to occur in the alloys in the same way as in pure metals.

(iii) With regard to the effect of temperature and loops size on the resistance of Frank loops against shearing, we found that some configurations are sensitive to these parameters and some not. In particular, the sensitive configurations are those where the initial interaction is repulsive (i.e. the approaching leading dislocation is repelled by the closest loop segments as determined by the mutual signs of BVs and senses of dislocation lines). In this case, the CRSS increases with loop size and decreases with temperature.

Acknowledgements

This work was performed in the framework of the EC-funded FP7/PERFORM60 project, under grant agreement 232612. Part of calculations has been performed at HPC Julich within the 'SORT' project. Research was partly supported by the Office of Fusion Energy Sciences, US Department of Energy (YNO).

References

[1] D. Hull, D.J. Bacon, Introduction to Dislocations, Butterworth-Heinemann, Oxford, 2001.
[2] S.G. Was, Fundamentals of Radiation Materials Science, Springer, New York, 2007.
[3] B.N. Singh, S.J. Zinkle, J. Nucl. Mater. 206 (1992) 212.
[4] J. Robach, I. Robertson, B. Wirth, A. Arsenlis, Philos. Mag. 83 (2003) 955.
[5] I.M. Robertson, A. Beaudoin, K. Al-Fadhalah, L. Chun-Ming, J. Robach, B.D. Wirth, A. Arsenlis, D. Ahn, P. Soltonis, Mater. Sci. Eng., A 400–401 (2004) 245.
[6] J. Robach, I. Robertson, H. Lee, B. Wirth, Acta Mater. 54 (2006) 1679.
[7] S.J. Zinkle, P.J. Maziasz, R.E. Stoller, J. Nucl. Mater. 206 (1992) 266.
[8] T. Nogaret, C. Robertson, D. Rodney, Phil. Mag. 87 (2007) 945.
[9] D. Rodney, Acta Mater. 52 (2004) 607.
[10] C. Becquart, Report F16O-CT-2003-508840, PERFECT IP Lille (2005) 22p.
[11] M. Daw, M. Baskes, Phys. Rev. B 29 (1984) 6443.
[12] T.S. Byun, Acta Mater. 51 (2003) 3063.
[13] Y. Mishin, D. Farkas, M.J. Mehl, D.A. Papaconstantopoulos, Phys. Rev. B 59 (1999) 3393.
[14] A. Voter, S. Chen, in: Mater. Res. Soc. Symp. Proc. 82, 1987, p. 175.
[15] M. Allen, D. Tildesley, Computer Simulation of Liquids, Clarendon Press, Oxford, 1987.
[16] Y.N. Osetsky, D.J. Bacon, Modell. Simul. Mater. Sci. Eng. 11 (2003) 427.

B Paper II

Interatomic potential to study plasticity in stainless steels: the FeNiCr model alloy

G. Bonny, D. Terentyev, R.C. Pasianot, S. Ponce and A. Bakaev

Modelling and Simulation in Materials Science and Engineering
19 (2011) 085008

IOP PUBLISHING MODELLING AND SIMULATION IN MATERIALS SCIENCE AND ENGINEERING

Modelling Simul. Mater. Sci. Eng. **19** (2011) 085008 (14pp) doi:10.1088/0965-0393/19/8/085008

Interatomic potential to study plasticity in stainless steels: the FeNiCr model alloy

G Bonny[1], D Terentyev[1], R C Pasianot[2,3,4], S Poncé[1,5] and A Bakaev[1,6]

[1] SCK•CEN, Nuclear Materials Science Institute, Boeretang 200, B-2400 Mol, Belgium
[2] CAC-CNEA, Departamento de Materiales, Avda. Gral. Paz 1499, 1650 San Martín, Pcia. Buenos Aires, Argentina
[3] CONICET, Avda. Rivadavia 1917, 1033 Buenos Aires, Argentina
[4] UNSAM/CNEA, Instituto Sabato, Avda. Gral. Paz 1499, 1650 San Martín, Pcia. Buenos Aires, Argentina
[5] Université Catholique de Louvain, Institute of Condensed Matter and Nanosciences, Chemin du cyclotron 2 bte L7.01.07, B-1348 Louvain-la-Neuve, Belgium
[6] Ghent University, Center for Molecular Modeling, Technologiepark 903, B-9052 Zwijnaarde, Belgium

E-mail: gbonny@sckcen.be

Received 15 May 2011, in final form 7 September 2011
Published 3 November 2011
Online at stacks.iop.org/MSMSE/19/085008

Abstract

Austenitic stainless steels are commonly used materials for in-core components of nuclear light water reactors. In service, such components are exposed to harsh conditions: intense neutron irradiation, mechanical and thermal stresses, and aggressive corrosion environment which all contribute to the components' degradation. For a better understanding of the prevailing mechanisms responsible for the materials degradation, large-scale atomistic simulations are desirable. In this framework we developed an embedded atom method type interatomic potential for the ternary FeNiCr system to model movement of dislocations and their interaction with radiation defects. Special attention has been drawn to the Fe–10Ni–20Cr alloy, whose properties were ensured to be close to those of 316L austenitic stainless steel. In particular, the stacking fault energy and elastic constants are well reproduced. The fcc phase for the Fe–10Ni–20Cr random alloy was proven to be stable in the temperature range 0–900 K and under shear strain up to 5%. For the same alloy the stable glide of screw dislocations and stability of Frank loops was confirmed.

(Some figures may appear in colour only in the online journal)

1. Introduction

Austenitic stainless steels are commonly used materials for in-core components of nuclear light water reactors (LWRs) [1, 2]. In service, such components are exposed to harsh conditions:

0965-0393/11/085008+14$33.00

intense neutron irradiation, mechanical and thermal stresses and aggressive corrosion environment. This combination of factors allows the occurrence of irradiation assisted stress corrosion cracking (IASCC), radiation induced creep and swelling, which all limit life time of the in-core components. So far, the available knowledge on degradation of the internal components of LWRs originates mainly from either the analysis of materials extracted from power reactor components, or tests on materials irradiated in test reactors or using accelerator facilities. In order to optimize in-service lifetime and avoid costly replacement campaigns, a deeper fundamental understanding of the above-mentioned degradation mechanisms is desirable, which hopefully could serve as input for engineering- and design-level modelling.

In this framework two work packages within the European project PERFORM60 are dedicated to study the micro-structure and plasticity laws of 316L stainless steels [3]. In this project multi-scale modelling techniques and experiments on FeNiCr model alloys are combined to gain a deeper understanding of the prevalent degradation mechanisms. As a part of the multi-scale modelling effort, atomistic simulations are foreseen to investigate the effects of radiation damage on the alloy's micro-structure and dislocation mobility. For this, ternary FeNiCr interatomic potentials, which can mimic mechanical properties of 316L stainless steels, must be developed. At the same time, the potential should acquire a relatively simple formalism, which allows for million-atom simulations within a reasonable computational time. Hence, the embedded atom method (EAM) [4] formalism was taken as a natural choice. Since the requirements with respect to micro-structure and plasticity are essentially different and not necessarily compatible within a single interatomic potential framework, two sets of potentials will be developed.

Here we focus on the requirements regarding plasticity studies at atomic level. For this purpose the essential materials properties to be fitted in a large concentration range near the target composition of 316L steel (i.e. Fe–10Ni–20Cr), are three, namely, stability of the fcc phase, elastic constants and stable stacking fault energy (SFE). In addition, the potential must provide the stability of the fcc phase under large deformation (up to 5% shear strain), stability of Frank loops (of size at least up to 10 nm) and ensure stable dislocation glide in a wide temperature (0–900 K) and composition range (5–30% Ni and Cr).

In the literature two different EAM FeNiCr (N and H) potentials were developed by Grujicic and Zhou [5] and Smith and Was [6], respectively. However, in these latter works the full parametrization of the potential is not reported. With respect to available potentials for binary alloys, no advantage could be taken either of state-of-the-art FeNi [7, 8] nor FeCr [9, 10] potentials. Namely, at the target composition of 10% Ni and 20% Cr with the latter potentials, it was tested that at finite temperature and under strain the fcc phase is not (meta)stable and a spontaneous transformation to the bcc phase occurs. An alternative for the Fe part of the potentials described in [7–10] could be the bond order potential developed in [11] that reproduces the experimentally observed bcc–fcc–bcc transition with temperature. However, such an approach does not necessarily guarantee fcc stability in the concentration range of interest as in 316L steels both carbon and nitrogen play an important role in stabilizing the fcc phase, which is not considered in the present simplified model alloy. Therefore a new FeNiCr ternary potential is fitted including the pure elements.

2. Methods

2.1. Energy model

The atomic interactions are described using the EAM [4], which is widely used to describe metals and their alloys. In addition to pair interactions, V, this approach includes an embedding

energy, F, dependent on the local electron density, ρ. The latter term approximates the many-body contribution of all nearby atoms. The total energy within EAM is given as

$$E = \frac{1}{2} \sum_{\substack{i,\, j=1 \\ j \neq i}}^{N} V_{t_i t_j}(r_{ij}) + \sum_{i=1}^{N} F_{t_i}(\rho_i), \tag{1}$$

Here N represents the total number of atoms in the system, r_{ij} is the distance between atoms i and j and t_i denotes chemical species (Fe, Ni or Cr in our case). The local electron density around atom i, contributed from its neighbours is given as

$$\rho_i = \sum_{\substack{j=1 \\ j \neq i}}^{N} \phi_{t_j}(r_{ij}), \tag{2}$$

where ϕ denotes the electron density function of the considered element. Thus, for the FeNiCr ternary system twelve functions need to be defined: ϕ_{Fe}, ϕ_{Ni}, ϕ_{Cr}, F_{Fe}, F_{Ni}, F_{Cr}, V_{FeFe}, V_{NiNi}, V_{CrCr}, V_{FeNi}, V_{FeCr} and V_{NiCr}.

In this work, the electron density function ϕ is defined as the product of a Thomas–Fermi screening function and a cut-off,

$$\phi(r) = S \frac{\exp(-\beta r)}{r} \frac{x^4}{1 + x^4}. \tag{3}$$

Here S is a normalization factor, $x = (r - r_{\mathrm{cut}})/h$, with β and h fitting parameters and r_{cut} the cut-off distance. The pair potential V is defined as a linear combination of piecewise cubic splines and the electron density function ϕ,

$$V_{\chi\gamma}(r) = \sum_{k=1}^{N_p} [a_k (r_k - r)^3 \Theta(r_k - r)] - K \phi_\gamma(r) \delta_{\chi\gamma}. \tag{4}$$

Here r_k are the knots, a_k fitting parameters, Θ the Heaviside unit step function and δ Kronecker's delta. The dependence on ϕ stems from the effective gauge transformation [12–15] on the pure potentials from which K is derived. The embedding function F is parametrized as

$$F = A\sqrt{\rho} + B\rho + C\rho^2 + D\rho^4, \tag{5}$$

with A, C and D fitting parameters. The linear term in ρ follows from the same effective gauge transformation from which B is derived. The optimized parameter set for the present potential is given in the appendix.

2.2. Fitting strategy

Prior to the cross interactions, the potentials for the pure elements were fitted. The material properties considered in these fits are the stability of different crystallographic structures (bcc, fcc, fct and hcp), their cohesive energy E_{coh}, and equilibrium lattice (with lattice constants a, b and c), the elastic constants for the equilibrium lattice (in our case cubic) C_{11}, C_{12}, C_{44} [16], vacancy formation and migration energy, formation energy of self-interstitial configurations ($\langle 1\,0\,0 \rangle$, $\langle 1\,1\,0 \rangle$ and $\langle 1\,1\,1 \rangle$ dumbbells, tetrahedral and octahedral sites), stable SFE and Rose's equation [17]. As a first approximation, these properties were expressed using a rigid lattice, so that the resulting formulae are linear in the fitting parameters $\{a_k, A, B, C, D\}$, for given β, h and r_{cut}. The former were optimized by a weighted least square fit to the target properties for each chosen set $\{\beta, h, r_{\mathrm{cut}}\}$. In this way, $\{\beta, h, r_{\mathrm{cut}}\}$ are manually tuned aiming at best

matching the relaxed properties to the target values for each trial potential. This strategy allowed for a satisfactory result in a reasonable number of iterations.

For the alloy, the SFE as a function of composition and the elastic constants for the Fe–10Ni–20Cr target composition were fitted. The latter fits were performed using a variance expansion of the energy for a random alloy [7]. This method allows one to write the energy (and its derivatives) as a linear combination of the fitting parameters $\{a_k\}$, which were optimized following a least square fit to the target values. The average energy per atom in a random alloy is given as

$$\begin{aligned}
\langle E_{\text{alloy}}\rangle &= \sum_X C_X \langle E_X\rangle,\\
\langle E_X\rangle &= \frac{1}{2}\sum_Y \sum_\nu N_\nu C_Y V_{XY}(r_\nu) + F_X(\langle \rho_X\rangle) + \frac{1}{2}\langle \sigma_X^2\rangle F_X''(\langle \rho_X\rangle),\\
\langle \rho_X\rangle &= \sum_Y \sum_\nu N_\nu C_Y \phi_Y(r_\nu),\\
\langle \sigma_X^2\rangle &= \sum_Y \sum_\nu N_\nu C_Y (1-C_Y)\phi_Y(r_\nu)^2 - \sum_{\substack{Y,Z\\ Y\neq Z}} \sum_\nu N_\nu C_Y C_Z \phi_Y(r_\nu)\phi_Z(r_\nu).
\end{aligned} \tag{6}$$

Here the sum over X (Y and Z) runs over all elements in the alloy while ν runs over the neighbour shells, with N_ν the number of atoms in shell ν and C_X the concentration of element X. This expression is derived in a similar way as in [7] by treating the random alloy as a multi-nomial distribution of solutes.

The expressions for the elastic constants, C_{ijkl}, are derived through the method of uniform deformations, where every atomic position, $\vec{r}$, is subject to the transformation, $\vec{r}' = (1-\bar{\bar{\varepsilon}})\vec{r}$, with $\bar{\bar{\varepsilon}}$ the small strain tensor. Thus, by evaluating the change in the above average energy per atom up to 2nd order in the components of the latter, one obtains (see e.g. [5])

$$C_{ijkl} = \frac{1}{\Omega}\frac{\partial^2\langle E_{\text{alloy}}\rangle}{\partial\varepsilon_{ij}\partial\varepsilon_{kl}}, \tag{7}$$

where Ω is the atomic volume. For a cubic crystal, only three of these coefficients remain independent, e.g., $C_{11} = C_{1111}$, $C_{12} = C_{1122}$ and $C_{44} = C_{1212}$.

3. Results

3.1. Pure potentials

The static properties of the pure potentials are summarized in table 1 and compared with the target values selected from DFT data or experiments. As mentioned in the introduction, the purpose of the ternary potential is to describe the elastic and plastic properties of 316L steel in a large concentration range near the target composition. Therefore, we focused primarily on the correct reproduction of the elastic constants, the SFE and stability of the fcc phase (artificially imposed in the case of Fe and Cr). As shown in table 1, the fcc structure for both Fe and Cr was artificially stabilized to avoid possible instabilities observed using bcc Fe and Cr potentials mentioned in the introduction. With respect to the target values, high weight was given only to Ni, since this element has the fcc lattice as a physical ground state. For Ni, the lattice parameter a, cohesive energy E_{coh} and the energy difference relative to other structures ΔE_0 are taken from experiment [18] and density functional theory (DFT) calculations [19]. For Fe and Cr the target values come from DFT calculations [8, 21, 20] and [22], respectively.

Table 1. Static properties of the pure elements. For the cases where two target values are reported we refer to the range. References for the target values are provided in the text.

	Iron		Nickel		Chromium	
	Target	Potential	Target	Potential	Target	Potential
E_{coh} (fcc) (eV/at.)	—	4.12	4.45	4.45	—	3.69
ΔE_{coh} (fcc-bcc) (eV/at.)	−0.16	+0.11	+0.15	+0.19	−0.39	+0.05
ΔE_{coh} (fcc-hcp) (eV/at.)	—	0.00	+0.03	+0.02	—	+0.04
a (fcc) (Å)	3.425[a]	3.499	3.519	3.519	3.610	3.584
a (hcp) (Å)	—	2.474[b]	—	2.488[c]	—	2.523[d]
a (bcc) (Å)	2.867	2.962[e]	2.801	2.801	2.878	3.149[f]
C_{11} (GPa)	141	141	247	247	249	247
C_{12} (GPa)	100	100	147	147	178	183
C_{44} (GPa)	108	108	125	125	143	145
E_{SF} (mJ m^{-2})	4	0	111–128	113	341	272
E_m (Vac) (eV)	0.95–1.05	0.61	1.08–1.30	1.17	2.19	2.25
E_f (Vac) (eV)	1.89–1.95	1.94	1.45–1.79	1.48	2.14	2.11
E_f ($\langle 1\,0\,0\rangle$ SIA) (eV)	3.53–3.65	3.60	4.07–4.11	4.08	—	5.10
E_f ($\langle 1\,1\,0\rangle$ SIA) (eV)	—	3.91	4.99–4.91	4.71	—	5.60
E_f ($\langle 1\,1\,1\rangle$ SIA) (eV)	4.56	4.61	4.69–4.72	4.76	—	5.40
E_f (Octa SIA) (eV)	4.35	3.87	4.25–4.32	4.89	—	5.71
E_f (Tetra SIA) (eV)	4.32	4.58	4.69–4.71	4.99	—	5.56

[a] $c/a = 1.065$.
[b] $c/a = 1.633$.
[c] $c/a = 1.663$.
[d] $c/a = 1.736$.
[e] $c/a = 0.895$.
[f] $c/a = 0.793$.

An excellent agreement with the target values is observed for Ni, while both Fe and Cr show poor agreement.

For Ni, the elastic constants are in excellent agreement with the experimental values [23]. Since both Fe and Cr are unstable in the fcc phase, no data for their elastic constants are available. The reported target values are therefore linear extrapolations of the experimentally measured elastic constants of Ni–Fe and Ni–Cr fcc solid solutions taken from [6, 23], thereby following the same strategy as Grujicic and Zhou [5]. As shown in table 1, the elastic constants resulting from both Fe and Cr potentials are in excellent agreement with the target values.

The target values for the stable fcc stacking fault are based on experiment (128 mJ m^{-2} for Ni) [24] and the extrapolation of low temperature (300 K) thermodynamic calculations (all other values) [25]. The latter calculations are polytope expansions [26] based on Calphad type free energy parametrizations for fcc and hcp phases. The latter have been shown to be in excellent agreement with experimental data for (Fe,Ni,Cr) solid solutions (see [25] and references therein). For both Fe and Ni potentials the SFE is in excellent agreement with the target values. For the Cr potential, however, the target value is underestimated by ∼70 mJ m^{-2}. Given the instability of fcc Cr, this outcome is, however, of minor importance, as long as the correct trend in the order of SFE for the alloy is reproduced (see below).

In figure 1 the $\langle 1\,1\,2\rangle$ $\{1\,1\,1\}$ gamma lines are presented for the pure potentials, from which the unstable stacking fault can be determined. The latter is connected to the mobility of 1/6 $\langle 1\,1\,2\rangle$ Shockley partial dislocations, for which a smooth gamma line is desirable, a characteristic that is reproduced by the potential.

The target vacancy migration and formation energy, reported in table 1 is obtained from DFT calculations and experimental data. In particular, for fcc Fe and Cr these are DFT data

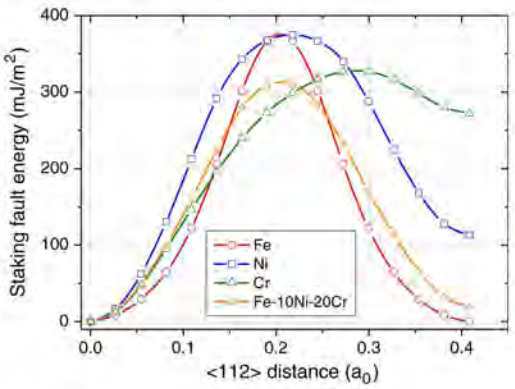

Figure 1. ⟨1 1 2⟩ {1 1 1} gamma cut calculated for the pure elements and Fe–10Ni–20Cr.

from [21, 22], while for fcc Ni we took experimental data from [18] and DFT data from [20]. It must be noted that relaxation of point defects in a fcc Cr matrix cannot be performed due to the instability of the phase and therefore only unrelaxed data are reported. As shown in table 1 the values obtained from the potential are in excellent agreement with the target ones, except for the vacancy migration barrier in Fe, which is largely underestimated. The energy reported for Cr correspond to non-relaxed structures for the sake of comparison with DFT.

The target formation energies of the different SIA configurations in Fe and Ni are obtained from DFT calculations [21–22]. No DFT data for SIAs in fcc Cr are available due to the above-mentioned phase instability. From table 1 it is clear that all potentials predict a ⟨1 0 0⟩ dumbbell to be the ground state, in agreement with the DFT results. The formation energy of a ⟨1 0 0⟩ dumbbell as well as its relative stability against other SIA configurations is in excellent agreement with DFT.

In figure 2 the average lattice energy, $E^* = E/E_{\mathrm{coh}}$, under uniform expansion and contraction (with strain $a^* = 9\Omega B/E_{\mathrm{coh}}(a/a_0 - 1)$, with B the bulk modulus) calculated with the different potentials is compared with Rose's universal equation of state [17]. Both Ni and Cr potentials reproduce well the equation of state. For Fe, there is poor agreement with Rose's equation for both large contraction and expansion. The former is due to the incompatibility with the ⟨1 0 0⟩ dumbbell formation energy while the latter is due to the short interaction range of the potential (4.0 Å compared with 5.6 Å for both Ni and Cr).

3.2. Alloy

3.2.1. Stacking fault energy. The stable SFE maps obtained from the potential and thermodynamic calculations [25] are compared in figure 3. For the potential the SFE was sampled with an interval of 10%. Each data point was obtained by averaging over 30 runs varying the distribution of solutes in the Fe matrix. The crystals containing in total 6000 atoms were fully relaxed. The resulting error on the average was at most 3.5 mJ m^{-2} (the error is defined as the 95% confidence interval around the average value; i.e. 1.96 times the standard error). Around the target composition, Fe–10Ni–20Cr, the thermodynamic calculations are reproduced as well as experimental results for 316L steels—23 mJ m^{-2} [25] and 10–30 mJ m^{-2}

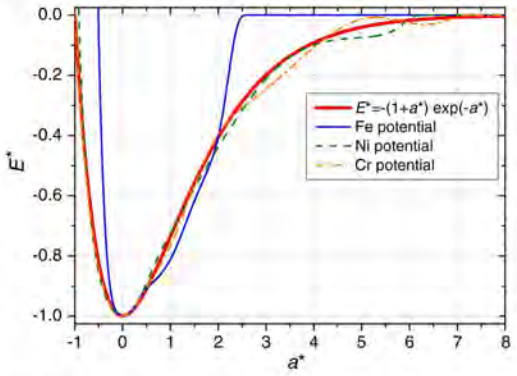

Figure 2. Evaluation of Rose's equation for the different potentials.

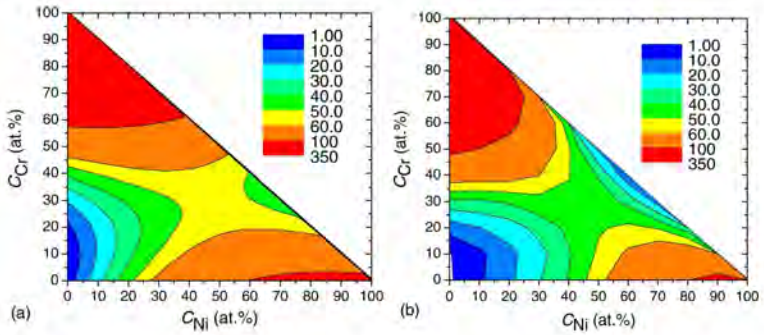

Figure 3. The stable SFE (mJ m^{-2}) as function of composition obtained from thermodynamic calculations [25] (*a*) and the potential (*b*).

[27–29] versus 20 mJ m^{-2} obtained with the potential. The potential also reproduces correct trends in SFE when varying Cr and Ni content. As a matter of fact, the saddle around Fe–45Ni–30Cr is reproduced.

Also worth of noticing is that the ⟨1 1 2⟩ {1 1 1} gamma line for the Fe–10Ni–20Cr alloy, superposed in figure 1, is smooth and exhibits a single hump, as in the case of the pure elements.

3.2.2. Elastic properties. In table 2 the elastic properties of our potential for the Fe–10Ni–20Cr alloy are compared with experimental values obtained in mono-crystals of 316L steels [30–32]. For the experimental data we also report the scattering range. C_{11}, C_{12} and C_{44} are the three independent elastic constants for cubic crystals), $B = (C_{11}+2C_{12})/3$ is the bulk modulus, $C' = (C_{11} - C_{12})/2$ is the tetragonal shear modulus, $G = (3C_{44} + 2C')/5$ is the isotropic shear modulus, $A = C_{44}/C'$ is the anisotropy ratio (dimensionless) and $y = C_{12}/C_{11}$ the relative constancy (dimensionless). The elastic constants for the random alloys were obtained

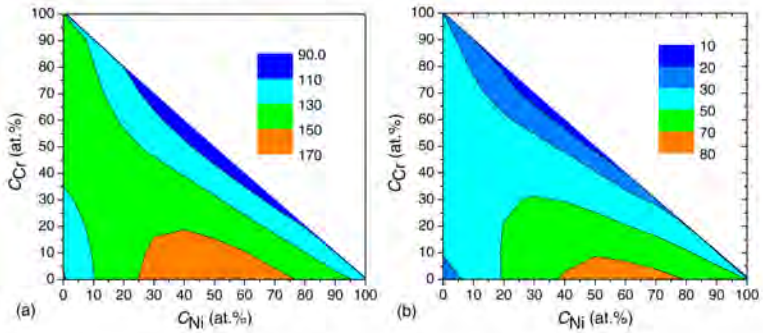

Figure 4. C_{44} (*a*) and C' (*b*) as a function of composition at 0 K.

Table 2. Comparison of the elastic constants (GPa) between the potential for the Fe–10Ni–20Cr alloy and 316L stainless steels [30–32].

	C_{11}	C_{12}	C_{44}	B	C'	G	A	γ
Exp.	204–226	132–134	111–122	157–164	35–46	81–92	2.4–3.5	0.59–0.66
Pot.	214	136	129	162	39	93	3.3	0.64

by the deformation and subsequent relaxation of cubic boxes containing 2048 atoms. The resulting error on the average was less than 1 GPa. Clearly, the obtained values are in excellent agreement (<10%) with the experimental data.

In figure 4 both C_{44} and C' are plotted in the whole composition range. The latter constants define the upper and lower bounds, respectively, for the shear modulus. For our purpose, C' is of particular interest since it defines the stability of the fcc phase with respect to small deformation. For the fcc phase to remain stable under deformations, C' must be strictly larger than zero (in practice $>\sim$10 GPa). As shown in figure 4(*b*), C' exceeds 10 GPa in the whole concentration range and is above 30 GPa for the target composition.

Figure 5 presents the shear modulus obtained by applying a pure shear of $\langle 1\,1\,0\rangle\{\text{-}1\,1\,1\}$ type to crystals containing about 40×10^3 atoms. This is the same type of shear as encountered by dislocations. The modulii were calculated as follows. Perfect crystals with different compositions (Fe–10Ni–20Cr, Fe–15Ni, Fe–15Cr, Fe–5Ni–10Cr and Fe–20Ni–40Cr) were thermalized and subsequently loaded by applying a shear strain at a constant rate of 10^7 s^{-1}. The loading was performed until the strain reached 5%. The simulation temperature was varied from 0 K up to 900 K. In all cases, the crystals kept fcc structure up to the maximum strain and no structural defects (e.g. faults) were found. The latter observation is consistent with figure 4 and confirms the stability of the fcc phase even under large deformation. In figure 5 the temperature effect on the shear modulus is illustrated by the vertical bar attached to the point corresponding to Fe–10Ni–20Cr alloy. Clearly, the effect of temperature is much weaker than the change in SFE due to the variation of composition.

3.2.3. Plastic properties As a validation of the developed potential for the modelling of dislocations we present some results obtained in Fe–10Ni–20Cr, Fe–15Ni and Fe–15Cr random

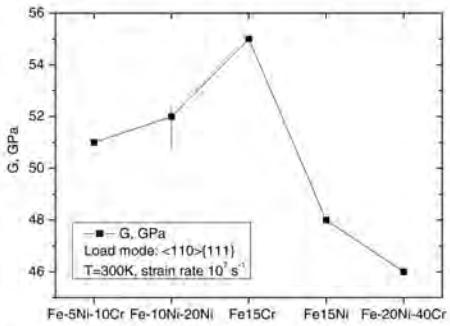

Figure 5. Shear modulus versus composition, measured at 300 K. The vertical bar attached to the point corresponding to Fe–10Ni–20Cr shows the variation of the shear modulus in the temperature range 0–900 K.

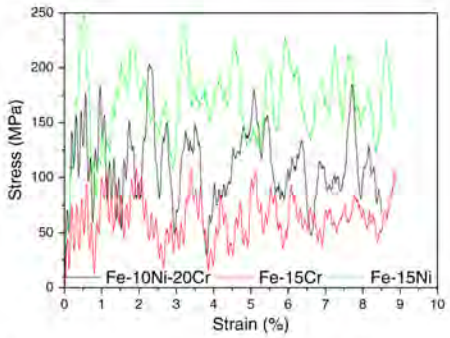

Figure 6. Evolution of the resolved shear stress in Fe–10Ni–20Cr, Fe–15Ni and Fe–15Cr crystals containing a $1/2\langle 1\,1\,0\rangle\{1\,1\,1\}$ screw dislocation. Simulation temperature is 300 K.

alloys. The crystals containing a $1/2\langle 1\,1\,0\rangle\{1\,1\,1\}$ screw dislocation were first relaxed, then thermalized at 300 K and finally loaded, by applying a pure shear at constant strain rate of $10^8\,s^{-1}$. To study the dislocation movement we have applied a model of a periodic array of dislocations developed by Osetsky and Bacon [33]. In this model, the principal axes of the simulation crystal are oriented along the $x = \langle 1\,1\,0\rangle$, $y = \langle 1\,1\,2\rangle$ and $z = \langle 1\,1\,1\rangle$ directions and periodic boundaries are applied along the x- and y-axes, whereas atoms are fixed in the few upper and lower planes normal to the z direction. Shear strain is applied by displacement of the upper block of fixed atoms at constant velocity. The crystal contains about 400k atoms and the corresponding dislocation density and velocity are $0.5 \times 10^{14}\,m^2$ and $45\,m\,s^{-1}$, respectively. The evolution of the resolved shear stress is presented in figure 6. In all the alloys the dislocation was split into two partials with a width of stacking fault ribbon of about 10 nm. The two partial dislocations were seen to execute uniform movement independent of each other. As a consequence, the width of the stacking fault ribbon was seen to vary between 7 and 12 nm. During the simulations no significant curvature on the lines of the partials was observed,

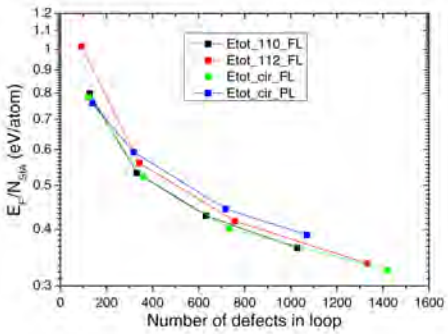

Figure 7. The formation energy of interstitial dislocation loops of different kinds calculated in the Fe–10Ni–20Cr alloy. See text for the explanation of the legend.

irrespective of the alloy composition. The friction stress, however, varies with composition; as follows from figure 6, increasing Ni or Cr content raises the friction stress. It is worth mentioning that the current simulations were performed at a relatively large strain rate—as proper behaviour at high rates ensures the same at lower strain rates—hence we expect that the friction stress will drop significantly when applying typical MD strain rates, i.e., 10^6–10^7 s^{-1}.

3.2.4. Dislocation loops Stability of Frank loops experimentally observed in irradiated austenitic steels is an important aspect with regard to the study of their impact on the pinning of dislocations. Using our potential, four different kinds of interstitial loops have been studied at 0 and 900 K. These are Frank loops of hexagonal shape with sides oriented along the ⟨1 1 0⟩ directions (henceforth 1 1 0_FL) and ⟨1 1 2⟩ directions (henceforth 1 1 2_FL), Frank loops of circular shape (henceforth cir_FL) and perfect loops of circular shape (henceforth cir_PL). The loop diameter was varied from 2 up to 10 nm.

The formation energy normalized by the number of interstitials forming the loop is presented in figure 7. We observe that for all studied sizes the perfect loops have a higher formation energy than any type of Frank loop. The latter observation is consistent with the low SFE reproduced by the potential and the experimental observation of Frank loops in 316L steels [34–36].

Having established that Frank loops are energetically most favourable, we have checked their stability against applied shear stress, as they may unfault under the action of stress of an approaching dislocation. We have observed the latter transformation in pure fcc crystals for relatively large loops [37] (whose self-energy is close to becoming higher than that of a perfect loop).

Relaxed Frank loops of size 10 nm were exposed to a ⟨1 1 0⟩{1 1 1} load by applying a shear strain at a constant rate of 10^7 s^{-1}, up to a total strain of 2.5% at 900 K. The loops were found to be stable and did not unfault up to the maximum strain, corresponding to a shear stress of 1.3 GPa. The configurations of loops, visualized using central symmetry analysis [38], at the beginning and at the end of load are shown in figure 8. We see that the extrinsic stacking fault was not removed under load, although the imposed shear stress caused the splitting of 1/3 ⟨1 1 1⟩ dislocation segments aligned along the ⟨1 1 0⟩ directions (see configurations *d* and *e* in figure 8) in 'cir_FL' and '1 1 0_FL', thus forming stair rod dislocations and additional faults

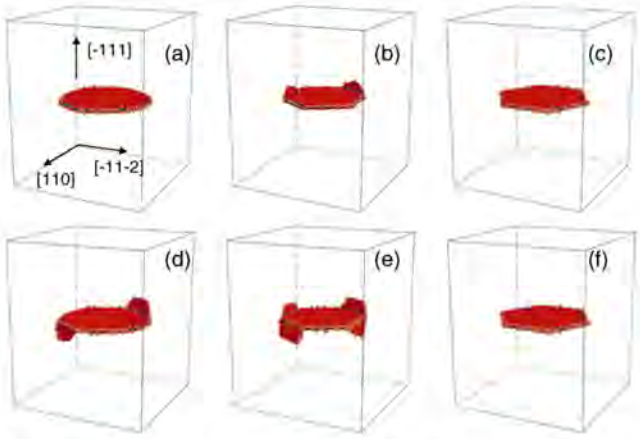

Figure 8. Frank loops (a =cir_FL, b =1 1 0_FL and c =1 1 2_FL) of interstitial type thermalized at 900 K before (upper row) and after (lower row) load. Details regarding the loading conditions are found in the text.

in the inclined $\{1\,1\,1\}$ planes. We attribute this effect to the stress, because no such splitting has been observed in the circular loop under thermal annealing. We can therefore conclude that Frank loops of size 10 nm and below are stable under a shear stress of ~1 GPa in the temperature range 0–900 K in the target composition alloy.

4. Summary and conclusions

We have developed an EAM type interatomic potential for the ternary FeNiCr system to model movement of dislocations and their interaction with radiation defects. Special attention has been drawn to the Fe–10Ni–20Cr alloy, whose properties were ensured to be close to those of 316L austenitic stainless steels. In particular, the SFE and elastic constants are well reproduced.

Given the good reproduction of the latter properties, preliminary simulations were run to test the suitability of the potential for plasticity studies. Based on the zero Kelvin elastic constants (C' in particular) the stability of the fcc phase against small deformations and temperature was confirmed. In addition, the fcc phase for the Fe–10Ni–20Cr random alloy was proven to be stable in the temperature range 0–900 K and under shear strain up to 5%.

Then, the glide of screw dislocations and stability of Frank loops in the target alloy was checked. The glide of a $1/2\langle 1\,1\,0\rangle\{1\,1\,1\}$ screw dislocation in the Fe–10Ni–20Cr alloy was modelled at 300 K using a periodic array of dislocations under constant strain rate conditions. The dislocation was found to split into two partials connected by a stacking fault ribbon of ~10 nm width. During the MD runs, no constriction of the ribbon nor dislocation cross slip was observed. The Frank loops of different shapes and sizes (up to 10 nm) were also found to be stable at finite temperature under substantial load. These results suggest that the developed potential is suitable to study the movement of dislocations and their interaction with Frank loops in an alloy with properties close to 316L austenitic steels.

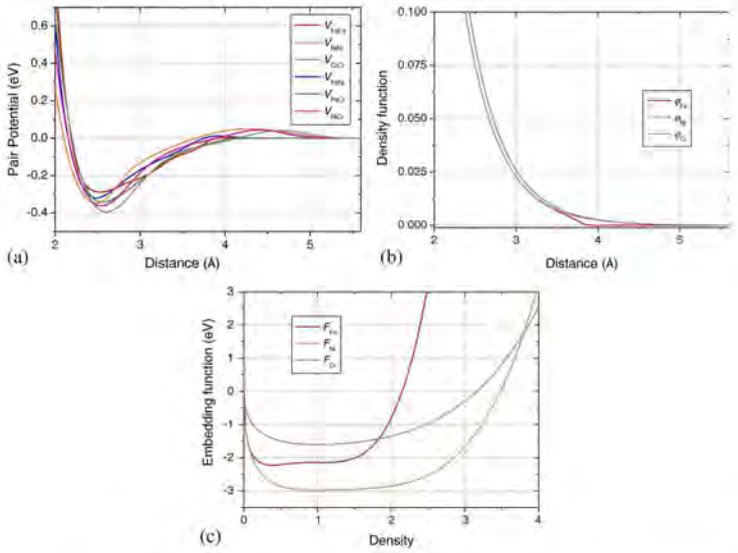

Figure A.1. Plot of the potential functions: pair potentials (*a*), density functions (*b*) and embedding functions (*c*).

Acknowledgments

This work was performed in the framework of the EC-funded FP7/PERFORM60 project, under grant agreement 232612. The work was also partially sponsored by the Belgo-Argentine FWO-MINCYT bilateral cooperation agreement, Project VS.004.10N. Part of the calculations were performed on the HPC cluster Jülich within the APM project. AB acknowledges financial support from FWO-Vlaanderen.

Appendix

The optimized parameter sets used in equations (3)–(5) are summarized in table A.1. A visualization of the potential functions (in effective gauge [11]) is given in figure A.1. These figures illustrate that the potential functions are smooth and that no significant oscillations occur.

Table A.1. Summary of the potential parameters. The energy and distance units are eV and Å, respectively.

k	r_k	a_k		
FeFe				
1	2.5	2.660 526	$A = -8.666\,245\,13$	$r_{\text{cut}} = 4.0$
2	2.8	3.566 762 07	$B = 9.413\,754\,92$	$\beta = 2.0$
3	3.1	−1.272 9965	$C = -3.237\,213\,54$	$h = 0.25$
4	3.4	2.100 276 86	$D = 0.348\,448\,677$	$S = 27.868\,9586$
5	3.7	−0.901 005 963		$K = 18.827\,5098$
6	4.0	0.393 902 864		

Table A.1. Continued

k	r_k	a_k		
7	2.4	12.0		
8	2.0	100.0		
NiNi				
1	2.5	−1.813 934 25	$A = -7.865\,656\,25$	$r_{\text{cut}} = 5.6$
2	2.844 444 44	4.303 289 23	$B = 5.951\,077\,74$	$\beta = 2.0$
3	3.188 888 89	−0.425 690 56	$C = -1.110\,141\,59$	$h = 0.25$
4	3.533 333 33	0.156 449 935	$D = 0.050\,508\,392$	$S = 27.875\,0306$
5	3.877 777 78	0.035 027 069		$K = 11.902\,1555$
6	4.222 222 22	0.149 366 37		
7	4.566 666 67	0.010 832 29		
8	4.911 111 11	−0.019 697 11		
9	5.255 555 56	−0.137 669 014		
10	5.6	0.085 392 233		
11	2.4	4.5		
12	2.0	100.0		
CrCr				
1	2.5	1.731 704 02	$A = -3.625\,808\,68$	$r_{\text{cut}} = 5.6$
2	2.942 857 14	1.841 434 06	$B = 2.266\,361\,49$	$\beta = 2.0$
3	3.385 714 29	0.755 016 121	$C = -0.265\,780\,601$	$h = 0.25$
4	3.828 571 43	−0.468 318 806	$D = 0.019\,526\,015$	$S = 31.261\,3817$
5	4.271 428 57	−0.047 416 719		$K = 4.532\,722\,97$
6	4.714 285 71	0.461 509 957		
7	5.157 142 86	−0.410 733 637		
8	5.6	0.113 373 503		
9	2.0	100.0		
FeNi				
1	2.0	62.418 0774	$K = 0.0$	
2	2.357 142 86	4.442 735 75		
3	2.714 285 71	2.402 634 93		
4	3.071 428 57	0.627 280 711		
5	3.428 571 43	−1.153 962 15		
6	3.785 714 29	1.318 395 61		
7	4.142 857 14	−0.707 8573		
8	4.5	0.099 942 305		
FeCr				
1	2.0	62.393 2019	$K = 0.0$	
2	2.342 857 14	4.649 491 19		
3	2.685 714 29	2.410 933 47		
4	3.028 571 43	0.101 143 751		
5	3.371 428 57	0.439 673 171		
6	3.714 285 71	−0.239 918 132		
7	4.057 142 86	0.218 918 034		
8	4.4	−0.153 852 387		
NiCr				
1	2.0	71.465 182	$K = 0.0$	
2	2.478 571 43	0.686 470 816		
3	2.957 142 86	1.799 965 78		
4	3.435 714 29	0.044 759 399		
5	3.914 285 71	−0.470 971 247		
6	4.392 857 14	0.585 425 288		
7	4.871 428 57	−0.417 474 26		
8	5.35	0.102 0253		

References

[1] Roberts J T A 1981 *Structural Materials in Nuclear Power System* (New York: Plenum)
[2] Ma B M 1983 *Nuclear Reactor Materials and Applications* (Princeton, NJ: Van Nostrand-Reinhold)
[3] Leclercq S, Lidbury D, Van Dyck S, Moinereau D, Alamo A and Al Mazouzi A 2010 *J. Nucl. Mater.* **406** 193
[4] Daw M S and Baskes M I 1984 *Phys. Rev.* B **29** 6443
[5] Grujicic M and Zhou X W 1993 *CALPHAD* **17** 383
[6] Smith R W and Was G S 1989 *Phys. Rev.* B **40** 10322
[7] Bonny G, Pasianot R C and Malerba L 2009 *Modelling Simul. Mater. Sci. Eng.* **17** 025010
[8] Malerba L *et al* 2010 *J. Nucl. Mater.* **406** 7
[9] Olsson P, Wallenius J, Domain C, Nordlund K and Malerba L 2005 *Phys. Rev.* B **72** 214119
[10] Bonny G, Pasianot R C, Terentyev D and Malerba L 2011 *Phil. Mag.* **91** 1724
[11] Müller M, Erhart P and Albe K 2007 *J. Phys.: Condens. Matter.* **19** 326220
[12] Finnis M W and Sinclair J E 1984 *Phil. Mag.* A **50** 45
[13] Ercolessi F, Parrinello M and Tosatti E 1988 *Phil. Mag.* A **58** 213
[14] Johnson R A 1989 *Phys. Rev.* B **39** 12554
[15] Bonny G and Pasianot R C 2010 *Phil. Mag. Lett.* **90** 559
[16] Kittel C 1996 *Introduction to Solid State Physics* (New York: Wiley)
[17] Rose J H, Smith J R, Guinea F and Ferrante J 1984 *Phys. Rev.* B **29** 2963
[18] Ehrhart P 1991 *Atomic Defects in Metals* (New York: Springer) p 88
[19] Mishin Y, Mehl M J and Papaconstantopoulos D A 2005 *Acta Mater.* **53** 4029
[20] Tucker J D, Najafabadi R, Allen T R and Morgan D 2010 *J. Nucl. Mater.* **405** 216
[21] Klaver T P C, Ackland G J and Hepburn D J 2011 The effect of magnetic ordering on defect and solute properties in dilute FeNiCr austenitic steels *Phys. Rev.* B submitted (arXiv:1107.0260)
[22] Olsson P and Domain C 2011 private communication
[23] Simmons G and Wang H 1977 *Single Crystal Elastic Constants and Calculated Aggregate Properties* (Cambridge, MA: MIT Press)
[24] Murr L E 1975 *Interfacial Phenomena in Metals and Alloys* (Reading, MA: Addison-Wesley)
[25] Miodownik A P 1978 *CALPHAD* **2** 207
[26] Denteneer P J H and van Haeringen W 1987 *J. Phys. C: Solid State Phys.* **20** L883
[27] Goodchild D, Roberts W T and Wilson D V 1970 *Acta Metall.* **18** 1137
[28] Kelly A and Groves G W 1970 *Crystallography and Crystal Defects* ed J D Arrowsmith (Harlow: Longmans) p 255 chapter 8
[29] Hertzberg R W 1989 *Deformation and Fracture Mechanics of Engineering Materials* 3rd edn (New York: Wiley) p 67
[30] Silk M G, Lidington B H and Hammond G F 1980 *Br. J. Non-Destr. Test.* **22** 55
[31] Ledbetter H M 1981 *Br. J. Non-Destr. Test.* **34** 286
[32] Ledbetter H M 1985 *Ultrasonics* **23** 9
[33] Osetsky Y N and Bacon D J 2003 *Modelling Simul. Mater. Sci. Eng.* **11** 427
[34] Zinkle S J, Maziasz P J and Stoller R E 1993 *J. Nucl. Mater.* **206** 266
[35] Lee E H, Hunn J D, Hashimoto N and Mansur L K 2000 *J. Nucl. Mater. Mater.* **278** 266
[36] Pokor C, Brechet Y, Dubuisson P, Massoud J-P and Barbu A 2004 *J. Nucl. Mater.* **326** 19
[37] Kadoyoshi T, Kaburaki H, Shimizu F, Kimizuka H, Jitsukawa S and Li J 2007 *Acta Mater.* **55** 3073
[38] Rodney D 2004 *Acta Mater.* **52** 607

C Paper III

Energetics of radiation defects in Fe-based austenitic alloys: Atomic scale study

A. Bakaev, D. Terentyev, X. He, E.E. Zhurkin

Nuclear Instruments and Methods in Physics Research B 303 (2013) 33

Nuclear Instruments and Methods in Physics Research B 303 (2013) 33–36

Contents lists available at SciVerse ScienceDirect

Nuclear Instruments and Methods in Physics Research B

journal homepage: www.elsevier.com/locate/nimb

Energetics of radiation defects in Fe-based austenitic alloys: Atomic scale study

A. Bakaev [a,b,d], D. Terentyev [a,d], X. He [c], E.E. Zhurkin [d,*]

[a] SCK•CEN, Boeretang 200, Mol B2400, Belgium
[b] Center for Molecular Modeling, Department of Physics and Astronomy, Ghent University, Technologie park 903, 9052 Zwijnaarde, Belgium
[c] China Institute of Atomic Energy, 275-51 Xiazhen, Fangshan, Beijing 102413, China
[d] Department of Experimental Nuclear Physics K-89, Faculty of Physics and Mechanics, St. Petersburg State Polytechnical University, 29 Polytekhnicheskaya str., 195251 St. Petersburg, Russia

ARTICLE INFO

Article history:
Received 13 July 2012
Received in revised form 23 December 2012
Accepted 30 December 2012
Available online 21 January 2013

Keywords:
Radiation defects
Austenitic steels
Formation energies
Dislocation loops

ABSTRACT

Energetics of typical radiation defects observed in austenitic stainless steel of 304L type has been characterized in the model $FeNi_{10}Cr_{20}$ alloy by means of atomistic simulations employing a set of interatomic potentials specially derived to reproduce main features of 304L steel. The following defects have been considered: dislocation loops of both interstitial and vacancy nature, stacking fault tetrahedron, perfect loops and voids. The formation energy of these defects has been calculated at 0 K and the obtained results have been compared with the prediction of the elasticity theory. A good agreement has been found in all the cases except for the hexagonal Frank loop, whose sides have splitted into 1/6⟨112⟩ partial dislocations, thus lowering the total formation energy. High temperature annealing, performed using molecular dynamics simulations, has proven that the considered defects are thermally stable in the temperature range 300–1200 K.

1. Introduction

Iron-based materials such as austenitic steels are important for many structural applications requiring high strength and good ductility, such as components in nuclear and fusion setups. With this respect, a good resistance against irradiation is another important requirement for such kind of materials. Neutron irradiation causes a certain degradation of the mechanical properties in these steels due to the production of radiation defects that are mainly dislocation Frank loops of self-interstitial (SIA) kind [1–3]. Free energy of lattice defects depends on its size, morphology and ambient temperature. Thus, the knowledge of the defect formation energy vs. its size allows one to predict the morphology and structure of the defects generated under neutron irradiation.

The aim of the present work is to perform atomistic numerical calculations to compute the formation energy of different radiation defects (such as SIA and vacancy Frank loops, perfect dislocation loops, stacking fault tetrahedron (SFT) and voids) with size up to 12 nm (i.e. well resolvable in transmission electron microscopy) at zero temperature ($T = 0$ K) in the random $FeNi_{10}Cr_{20}$ FCC alloy, which is used as a model for austenitic steel of 304L type. To do that, we employ a classical molecular dynamics (MD) and static (MS) simulations. The latter are performed using a set of recently developed interatomic potentials specifically derived to reproduce main features of 304L steel [4]. A comparison of the obtained formation energy with the prediction according to the elasticity theory [5] for vacancy type defects in FCC materials is also performed. In addition, we also study thermal stability of the examined defects by means of annealing modeled using MD simulations in the temperature range 300–1200 K.

2. Method

We applied atomistic computer simulations in the framework of classical molecular dynamics (see e.g. [6]). The latter allows tracking individual trajectories of each atom by means of integrating Newton's equations of motion. To perform the calculations we applied a standard MD algorithm developed in [7]. The details of the defect identification are described in the same work.

To compute the interaction forces between the atoms we used a recently developed Fe–Ni–Cr potential [4], which is based on the well-known model of the embedded atom [8] and it is optimized for the correct reproduction of the mechanical properties of austenitic steels of 304L and 316L types. This potential can correctly reproduce the values of cohesive energy, lattice constants, elastic constants C_{11}, C_{12}, C_{44}, the energy of formation and migration of a vacancy, the formation energy of various configurations of interstitials (i.e. ⟨100⟩, ⟨110⟩ and ⟨111⟩ dumbbells, interstitials in the octahedral and tetrahedral positions), stacking fault energy (SFE) of pure Fe, Ni, Cr and of the alloy $FeNi_{10}Cr_{20}$. In addition, a good agreement with the previously published experimental data

* Corresponding author. Tel./fax: +7 812 552 7531.
E-mail address: ezhurkin@phmf.spbstu.ru (E.E. Zhurkin).

0168-583X/$ - see front matter © 2013 Elsevier B.V. All rights reserved.
http://dx.doi.org/10.1016/j.nimb.2012.12.086

Table 1
Characteristics of the considered lattice defects.

Defect type	The size d, nm	Number of point defects	Formation energy, eV/(point defect)
Void	0.7	17	0.75
	2.1	444	0.36
	3.5	2109	0.21
Stacking fault tetrahedron (SFT)	1.5	15	0.82
	3.0	54	0.63
	5.2	153	0.50
	7.0	276	0.33
	8.8	435	0.31
	10.7	630	0.27
Circular perfect loop $b = 1/2\langle 110\rangle$ of interstitial/vacancy nature	1.4	36	1.38[a]/1.16[b]
	4.2	316	0.64[a]/0.59[b]
	7.0	887	0.45[a]/0.41[b]
	9.8	1742	0.37[a]/0.34[b]
Circular Frank loop $b = 1/3\langle 111\rangle$ of interstitial/vacancy nature	1.4	31	1.33[a]/1.09[b]
	4.2	253	0.63[a]/0.51[b]
	7.0	733	0.44[a]/0.39[b]
	9.8	1417	0.35[a]/0.30[b]
Hexagonal Frank loop with the sides along $\langle 110\rangle$ directions $b = 1/3\langle 111\rangle$ of interstitial/vacancy nature	1.0	19	1.66[a]/1.08[b]
	3.0	127	0.85[a]/0.63[b]
	5.0	331	0.56[a]/0.44[b]
	7.0	631	0.46[a]/0.35[b]
	9.0	1027	0.39[a]/0.30[b]
Hexagonal Frank loop with the sides along $\langle 112\rangle$ directions $b = 1/3\langle 111\rangle$ of interstitial/vacancy nature	1.7	43	1.42[a]/1.01[b]
	5.2	343	0.64[a]/0.50[b]
	8.6	931	0.49[a]/0.38[b]
	12.1	1807	0.45[a]/0.31[b]

[a] Formation energy of the loop of interstitial nature.
[b] Formation energy of the loop of vacancy nature.

and with results obtained using *ab initio* method (the details of comparisons are given in [4]) is also achieved.

Molecular dynamics calculations were performed at $T = 0$ K for defects of various types, whose characteristics are given in Table 1. The dimensions of the model box were $42.4\ a_0 \times 44.1\ a_0 \times 53.7\ a_0$ (where a_0 is lattice constant equal to 3.51595 Å) and it contained about 400,000 atoms.

Two types of dislocation loops were considered, namely: the interstitial and the vacancy ones. Vacancy and interstitial loops were created by, respectively, the removal or introduction of atomic planes in the form of a disk taking into account the appropriate orientation of the Burgers vector and contours of the edges of extra-half plane along the dislocation line.

Then the relaxed crystals were used as initial configurations for MD calculations at nonzero temperature, whereby we investigated the stability of the defects at finite temperatures T, varied in the range 300–1200 K. The temperature was initialized by assigning velocities to each of the atoms, according to the following procedure: at the beginning the impulses of atoms are given according to the Maxwell distribution to a temperature of $2 \times T$ (where T is the required temperature). Then we calculated the total impulse of the system, and after that we produced a simultaneous conversion of all the velocities so that the zero total impulse of the system is achieved. We used the following procedure for the establishment of dynamic equilibrium: during the first 10000 steps we performed the integration of the equations of motion, whereas every 100 steps the moments of all atoms were renormalized so that the total kinetic energy of the system corresponded to the desired temperature.

3. Results and discussion

By analyzing the final configurations of the relaxed crystals containing the studied defects of interest we found that dislocation segments forming a perfect loop split in $\{111\}$ planes into two partial dislocations (see Fig. 1a) according to the following reaction:

$$\frac{1}{2}\langle 110\rangle \rightarrow \frac{1}{6}\langle 211\rangle + \frac{1}{6}\langle 12\bar{1}\rangle \quad (1)$$

In the case of the hexagonal-shaped Frank loops with the sides oriented along $\langle 110\rangle$ directions, the sides of the loop are splitted into two partials (see Fig. 1b) by the following reaction:

$$\frac{1}{3}\langle 111\rangle \rightarrow \frac{1}{6}\langle 110\rangle + \frac{1}{6}\langle 112\rangle \quad (2)$$

This splitting does not occur in the case of Frank loops with the sides oriented along $\langle 112\rangle$ directions (see Fig. 1c), since the dislocation segments are not contained in any of the crystallographic planes of $\{111\}$ type.

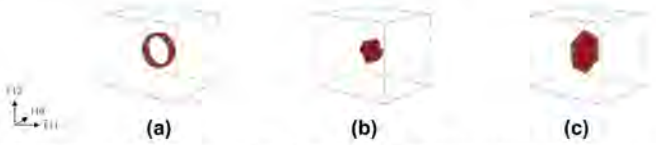

Fig. 1. Visualizations of final configurations of the defects: (a) interstitial circular perfect loop $d = 9.8$ nm; (b) vacancy hexagonal Frank loop $d = 5.0$ nm with the sides along $\langle 110\rangle$ directions; (c) vacancy hexagonal Frank loop $d = 12.1$ nm with the sides along $\langle 112\rangle$ directions. The orientation of the crystal is the same in all figures.

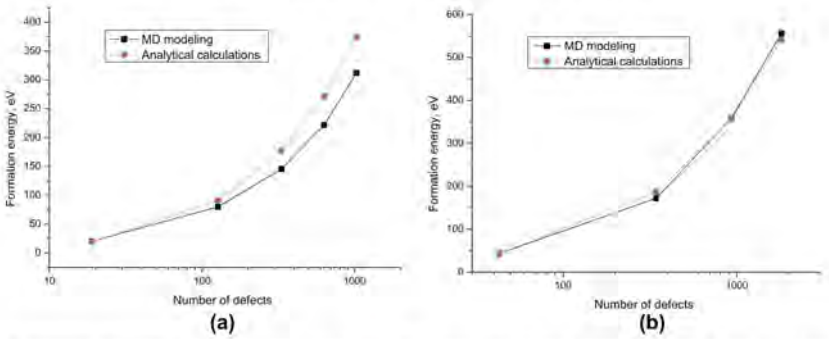

Fig. 2. The dependences of formation energy on the number of point defects in the configurations (a) hexagonal vacancy Frank loop with the sides oriented along ⟨1 1 0⟩ directions; (b) hexagonal vacancy Frank loop with the sides oriented along ⟨1 1 2⟩ directions.

Fig. 3. Modeling of the interstitial Frank loop of diameter $d \approx 12.1$ nm with the sides oriented along ⟨1 1 2⟩ directions at $T = 300$ K at the times (a) 1 ps, (b) 9 ps, (c) 12 ps and (d) 15 ps. The orientation of the crystal is the same in all figures.

The dependence of the formation energy of different defects on defect size and number of point defects (vacancies/interstitial) contained (shown in Table 1) was then analyzed. We found that in the case of interstitial-type defects in the studied range of defect sizes a hexagonal Frank loop with the sides oriented along ⟨1 1 0⟩ directions had the lowest formation energy. Whereas in the case of vacancy-type defects, it was SFT. Note, that both types of these defects were experimentally observed (see e.g. [3]). With this regard, our results suggest that the two above-mentioned defects will be the primarily defects to be formed as a result of the evolution of displacement cascades induced by primary knocked atoms, which are in turn triggered by fast neutrons.

For the case of vacancy defects, we compared the formation energy computed using the MS calculations with the estimates obtained by analytical models, derived on the basis of elasticity theory [5,9], which is shown in Fig. 2. We found that for all types of vacancy defects the results of MS calculations well correspond to the theoretical estimates. The exception is the Frank loop with the sides oriented along ⟨1 1 0⟩ directions (see Fig. 2a), as in this case the split of the dislocation segments lowering their self energy occurs, as mentioned above. This reaction is not accounted for in the theoretical model, which explains the observed disagreement.

Modeling of MD annealing at finite temperature for 100 ps has shown that all types of the considered defects are stable up to the highest temperature studied i.e. 1200 K. The only exception was the interstitial Frank loop with the sides oriented along ⟨1 1 2⟩ directions. In the latter case, the transformation of the loop into the perfect one is observed to occur in a wide temperature range (300–1200 K), and this process is illustrated in Fig. 3. The latter process occurs due to the emergence (nucleation) of three pairs of partial dislocations on the loop's surface (see Fig. 3a). The nucleated dislocations repel each other and progressively eliminate the stacking fault (see Fig. 3b and c), completely sweeping the fault (see Fig. 3d).

4. Conclusions

In the considered range of defect sizes (1–10 nm), the minimal formation energy is found for the hexagonal Frank loop and SFT in the case of interstitial and vacancy types of defects, respectively. We can therefore conclude that these kinds of defects should be primary formed in austenitic steels under irradiation.

Thermal stability of the considered defects by means of MD annealing at different temperatures was also studied. All kinds of the considered defects are found to be stable in the studied temperature range except for the Frank loop with the sides oriented along ⟨1 1 2⟩ directions. In the latter case, the transformation of Frank loop into a perfect dislocation loop was observed at 300 K and above.

For the case of vacancy defects, we compared the results of MS calculations with the estimates of analytical models, derived based on the elasticity theory [5,9]. We found that for all types of vacancy defects the results of MS calculations are in very good agreement with the theoretical estimates, except for the Frank loop with the sides oriented along ⟨1 1 0⟩ directions, as in this case the dislocation segments split into two partials, which is not considered in the analytical treatment.

Acknowledgements

The author thanks FWO-Vlaanderen for their financial support. The research was partially supported by the European seventh Framework Program, under "PERFORM 60" project.

References

[1] C. Pokor, Y. Brechet, J. Nucl. Mater. 326 (2004) 19.
[2] C. Pokor, Y. Brechet, J. Nucl. Mater. 326 (2004) 30.
[3] S.J. Zinkle, P.J. Maziasz, R.E. Stoller, J. Nucl. Mater. 206 (1993) 266.
[4] G. Bonny, D. Terentyev, R.C. Pasianot, S. Ponce, A. Bakaev, Modell. Simul. Mater. Sci. Eng. 19 (2011) 085008.
[5] R.A. Johnson, Philos. Mag. 16 (1967) 553.
[6] M.P. Allen, D.J. Tildesley, Computer Simulation of Liquids, Clarendon Press, Oxford, 1987.
[7] Y.N. Osetsky, D.J. Bacon, Modell. Simul. Mater. Sci. Eng. 11 (2003) 427.
[8] M.S. Daw, M.I. Baskes, Phys. Rev. B 29 (1984) 6443.
[9] J.A. Sigler, D. Kuhlmann-Wilsdorf, Phys. Status Solidi 21 (1967) 545.

D Paper IV

Interaction of a screw dislocation with Frank loops in Fe-10Ni-20Cr alloy

D. Terentyev, A. Bakaev

Journal of Nuclear Materials 442 (2013) 208

Journal of Nuclear Materials 442 (2013) 208–217

Contents lists available at SciVerse ScienceDirect

Journal of Nuclear Materials

journal homepage: www.elsevier.com/locate/jnucmat

Interaction of a screw dislocation with Frank loops in Fe–10Ni–20Cr alloy

D. Terentyev [a,*], A. Bakaev [a,b,c]

[a] SCK CEN, Boeretang 200, Mol B2400, Belgium
[b] Center for Molecular Modeling, Department of Physics and Astronomy, Ghent University, Technologiepark 903, 9052 Zwijnaarde, Belgium
[c] Department of Experimental Nuclear Physics K-89, Faculty of Physics and Mechanics, St. Petersburg State Polytechnical University, 29 Polytekhnicheskaya Str., 195251 St. Petersburg, Russia

ARTICLE INFO

Article history:
Received 4 March 2013
Accepted 26 August 2013
Available online 31 August 2013

ABSTRACT

The interaction of 2 and 5 nm Frank loops with a moving screw dislocation is studied in Fe–10Ni–20Cr alloy (a model of austenitic 304 and 316 steels) employing the newly developed Fe–Ni–Cr interatomic potential in molecular dynamics simulations. The applied potential ensures full stability of FCC phase and smooth evolution of stacking fault energy (SFE) as a function of chemical composition, fitted to be in a close agreement with the CALPHAD database. A model of Fe–10Ni–20Cr random alloy closely reproduces elastic properties and SFE of 316-type austenitic steels. The results reveal a number of interaction mechanisms depending on loop orientation and ambient temperature. Half of the observed reactions lead to loop unfaulting despite a low SFE of the alloy. The unfaulting reactions are enhanced with temperature and the critical stress for the unfaulting is regularly higher in comparison with the loop shear interaction. By comparing present results with a recent study done in a low SFE Fe–50Ni alloy, we reveal that a magnitude of local variation of SFE is an important factor controlling the formation of dislocation constrictions. In the Fe–50Ni alloy, characterized by strong variations of local SFE, the constrictions are almost never observed so that the loop shear interaction prevails, while absorption is rare. In the Fe–10Ni–20Cr alloy, characterized by small variations of local SFE, the constrictions are regularly formed resulting in frequent loop unfaulting.

1. Introduction

Irradiation of structural steels for nuclear applications by neutrons throughout the lifecycle causes modification of the crystal microstructure resulting in the formation of black dots, dislocation loops and voids [1,2]. These defects act as obstacles to dislocation glide, thereby causing hardening and consequently embrittlement [3], thus limiting the functional lifespan of a setup. In the case of neutron irradiation at temperature below $0.3T_M$ (T_M is the melting point) at a dose up to few (~5), DPAs (displacement per atom), the matrix damage created is composed mainly of dislocation loops with Burgers vector (BV) equal to 1/3<111> (i.e. so called Frank loops) with mean size of a few nm [2,4–6]. Upon plastic deformation, the formation of so called 'free channels' has been observed in austenitic steels with different stacking fault energy (SFE) in [5]. Width, spacing, height and density of channels were found to depend on SFE. The effect of SFE on the interaction of moving dislocations with Frank loops (FL) and formation of free channels therefore needs to be understood as it brings an important contribution to plastic deformation mechanisms and phenomena of plastic localization in irradiated austenitic steels. Given the complexity of the in situ TEM straining experiments (see e.g. [7,8]), molecular dynamics (MD) atomistic simulations offer an efficient complementary tool to investigate the details of dislocation-loop interaction.

FL-dislocation interaction in pure FCC metals (in Cu and Ni) has been studied by MD simulations already [9–11]. A systematic study performed by Nogaret et al. [9] has revealed several mechanisms depending on the interaction geometry and an impinging dislocation character, namely: (i) loop shear; (ii) unfault into glissile configuration; (iii) absorption into a glissile superjog (on edge dislocation) or into a sessile helical turn (on a screw dislocation). Absorption into a helical turn results in especially high unpinning stress and thus is expected to be the main source of hardening. For both screw and edge dislocations the unfaulting mechanism is controlled by the cross-slip process [9,12]. In general, the number of geometrical configurations leading to loop unfaulting is higher for a screw dislocation [9]. Hence, the interaction with screw dislocations most likely determines both the hardening and the formation of free channels.

* Corresponding author.
E-mail address: dieterv@sckcen.be (D. Terentyev).

0022-3115/$ - see front matter © 2013 Elsevier B.V. All rights reserved.
http://dx.doi.org/10.1016/j.jnucmat.2013.08.044

In the case of a screw dislocation, two distinct unfaulting mechanisms have been revealed [10,12]; (i) the formation of a D-Shockley partial dislocation segment, which sweeps the fault. The sweeping is accommodated by cross-slip of the dislocation around the loop. (ii) Cross-slip of the dislocation, formation of a constriction and its re-dissociation in the loop habit plane. Then, two partials remove the fault. Both of these mechanisms require the formation of constrictions and propagation of dislocations in the secondary glide planes. The formation of a constriction on the other hand is determined by the value of SFE and elastic constants of material. Importantly to point that the interatomic models of Ni and Cu, employed in [10,12], are not suitable to mimic properties of dislocations in austenitic steels due to essential discrepancy of SFE and shear modulus. Hence, there is a need for an atomistic model emulating low SFE austenitic steels.

This was addressed recently, by performing MD simulations in Fe–Ni random alloy [13], for which the potential was developed by using BCC-Fe potential by Ackland [14] and FCC-Ni potential from Mishin [15], allowing for SFE to vary in a wide range depending on the alloy's composition. SFE as a function of Ni concentration for the applied Fe–Ni potential is shown in Fig. 1(a). Above 40 at.%, SFE becomes definitely positive demonstrating that FCC phase becomes more stable than BCC. It has been shown that in Fe–50Ni with SFE comparable to real austenitic steels (i.e. ~20 mJ/m^2) [13], the formation of constrictions is suppressed so that unfaulting becomes a less favorable mechanism in comparison with loop shear. At the same time, the presence of a non-negligible friction stress caused by solutes was seen to impede the propagation of dislocations in the secondary glide planes, which is another essential factor suppressing the unfaulting process [13]. The overall conclusion was that in the Fe–50Ni alloy, characterized by SFE of 20 mJ/m^2, the major interaction mechanism is loop shear. Hence, the explanation for the experimental observation of free channels, so far based on the results obtained in pure Cu and Ni in [12], needs further clarification [13].

An important drawback of the Fe–Ni model applied in [13] was a strong variation of SFE depending on local atomic arrangement. The spread of SFE for three different Fe–Ni alloys is shown in Fig. 1(b), simulation details are described in figure capture. Even though the average SFE value in Fe–50Ni is 19 mJ/m^2 the width of the distribution is about 50 mJ/m^2. It is therefore possible that the strong local variation of SFE does not allow for the formation of extended constrictions even at relatively high level of applied shear stress while the FL is in contact with dislocation during the interaction process. The origin of the strong SFE variation is related to a tiny balance in the stability of FCC relative to BCC phase. To overcome this problem, a new Fe–Ni–Cr potential has been developed by utilizing FCC phase as a ground state for Fe, Ni and Cr. By doing that the full stability of FCC phase and smooth evolution of SFE, in a close agreement with the CALPHAD database, were ensured in the whole composition range [16]. In addition, the potential was specifically developed to mimic elastic properties of 316 austenitic steels for 'target composition' i.e. Fe–10Ni–20Cr and was parameterized using a wide range of data including some obtained by *ab initio* calculations and from experiments. Here, we study the interaction of 2 and 5 nm Frank loops with a screw dislocation in Fe–10Ni–20Cr alloy (a model of austenitic 316 steel) employing the newly developed Fe–Ni–Cr interatomic potential whose details are described in [16].

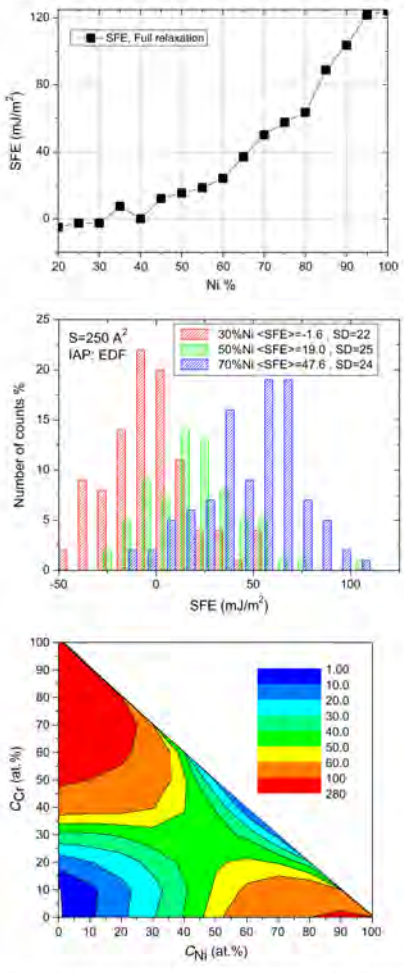

Fig. 1. (a) SFE in the position of stable stacking fault calculated using EDF potential (for the fault surface of ~20.000 A^2) at 0 K. (b) The distribution of the SFE in Fe–xNi alloys, calculated at 0 K using the EDF interatomic potential (IAP) for the surface (S) of fault of about 250 A^2 (i.e. 16$\boldsymbol{b}$ × 2$\boldsymbol{b}$, this would correspond to the constriction of 2$\boldsymbol{b}$ width made on a 4 nm loop). Each distribution is obtained for 500 runs varying initial distribution of Ni atoms. The abbreviation SD stands for standard deviation. (c) SFE (given in mJ/m^2) in the Fe–Ni–Cr as a function of composition [16]. In all the cases, SFE is calculated by generating a crystal containing a fault and using standard molecular static relaxation procedure, for details see [16].

2. Simulation techniques

The general computational methodology is exactly the same as applied in our previous work dealing with simulations in Fe–Ni alloys [13]. The interaction between a screw dislocation (SD) and interstitial FLs was studied using classical MD approach by applying shear deformation of $[-1-10](-111)$ type with a constant strain rate of 3×10^7 s^{-1} (resulting in the steady state velocity of

Table 1
Lattice parameters as a function of temperature.

T (K)	a_0 (Å)
303–306	3.52196
606–610	3.53254
902–908	3.54847

50 m/s). The crystallite, with axes oriented along [1 1 0], [1 −1 2] and [−1 1 1] directions, contained about 1.2M mobile atoms. Its dimensions along x, y and z were $40 \times 40 \times 10$ nm^3. An equilibrium lattice unit, a_0, was chosen appropriately to account for thermal expansion and its value is reported in Table 1. Periodic boundary conditions were applied along x and y directions, while atoms in a few outer $\pm z$ atomic layers were rigidly fixed in their positions. A screw dislocation with BV = 1/2[1 1 0] has been introduced according to the method applied by Rodney [10] and then relaxed using a combination of conjugate gradient and velocity quenching methods [17]. After the relaxation, the dislocation was dissociated in the (−1 1 1) plane into two Shockley partials located at a distance of about 10 nm from each other, which corresponds well to the value expected from the elasticity theory considerations.

An FL was introduced at a distance of ~10 nm away from the leading partial dislocation so that its geometrical center coincided with the dislocation glide plane. The three non-equivalent orientations of BV for each FL were inspected, and the case when BV = 1/3[−1 1 1] was excluded since the probability of the direct interaction with such loops is very low. We have considered circular Frank loops with a diameter of 2 and 5 nm. Due to the imposed periodic boundary conditions along the dislocation line, the center-to-center spacing between the loops was 40 nm, which corresponds to a volumetric density of 1.5×10^{22} m^{-3}. To explore both possibilities for the SD to approach the loop, we have performed simulations by applying positive and negative shear strain.

Integration of Newton's equations was performed using a constant time step equal to 5 fs. Calculations were done in the framework of a microcanonical *NVE* ensemble, where a number of atoms, N, system volume, V, and total energy, E, are conserved if the work of external forces is taken into account. The simulations were performed at 300, 600 and 900 K. The identification of the dislocation core and stacking fault atoms was realized by applying a combination of methods, namely: central symmetry analysis, common neighbor analysis, potential energy analysis and counting specific number of FCC neighbors.

Prior to study the interaction of the dislocation with FLs we have modeled its movement in the defect-free crystal to evaluate the friction stress, τ_f, which the dislocation experiences at the imposed strain rate. A smooth movement of the dislocation was seen at all studied temperatures, the width of the stacking fault ribbon was seen to vary (±25% from the average value) and no constrictions were seen to form on the dislocation line. Following the stress–strain curves, we could observe that increasing temperature reduces the instantaneous friction stress. The apparent friction stress τ_f was calculated by averaging the instantaneous resolved shear stress during the period within which the dislocation moves with the steady-state velocity for a distance of 40 nm (i.e. passes the whole crystal one time). The obtained τ_f are presented in Table 2. To validate the atom-core dislocation analysis we have measured the dislocation velocity in all simulation runs by tracking its position (as determined by the structural analysis) and compared it with the Orowan relationship linking strain rate with dislocation density, its Burgers vector and dislocation velocity i.e. $\dot{\gamma} = \rho b v$. A good agreement between the results is achieved (see Table 2) confirming consistency of geometrical parameters of the model, applied loading conditions and visualization techniques employed.

3. Results

MD simulations have been performed and the resulting stress–strain curves together with the atom-core visualization animations for every interaction mechanisms described below are attached to this paper as electronic supplementary material, which is the group of archived files. Root of each of the archived files contains a folder, whose name corresponds to the reaction type following the described below (see Section 3.1). Every folder contains subfolder, whose name refers to a specific reaction studied for a given BV orientation, loop size and simulation temperature. In this subfolder one finds the file named 'sscurve.gif', which is the stress–strain curve for a given reaction, and folder called 'vis_10video'. The latter contains three movies showing the interaction mechanism viewed along the three principal axes of the crystal i.e. [1 1 0], [1 −1 2] and [−1 1 1] vectors. By checking the evolution of dislocation-loop configurations from the three perspectives, it is easy to identify such important features as formation of constrictions, cross-slip movement and loop unfault, which is necessary in order to rationalize the interaction mechanism. We invite a reader to download the supplementary material offering an access to full details of the interaction mechanism for each simulated reaction, while in the next section several principal mechanisms observed will be described in detail and demonstrated by visualization snapshots.

3.1. Interaction mechanisms

All observed reactions have been subdivided into six groups depending on principal mechanisms involved and outcome products observed. A description of each type of the observed reaction mechanism is given below. Some of the interaction mechanisms have been observed in earlier studies in pure FCC metals [9,10] and in Fe–50Ni [13]. However, some new mechanisms have also been identified. In the following we illustrate a number of the interaction mechanisms as detected by atom-core visualization techniques. The evolution of the stress–strain relationships corresponding to the below described reactions is provided in Fig. 2.

(1) *Unfault with the formation of a 'full' helical turn*: The interaction process involving a 1/3[1 1 1] loop and a screw dislocation is illustrated in Fig. 3. In this configuration the loop is initially attracted to a leading partial (LP) dislocation, which bends towards the loop. Under the action of applied stress, the dislocation moves towards the loop and on the contact it forms the junction, see Fig. 3(a). While, the trailing partial (TP) dislocation reaches the junction, the LP unzips from the junction and cuts the loop, as shown in Fig. 3(b). The TP follows the LP so as the constriction is formed in the opposite side of the loop. At this step, the loop is splitted into upper and lower parts connected to the two dislocation arms, see Fig. 3(c). The lower part, attached to the 'right arm', is immediately reformed as a set of superjogs by the propagation of the D-Shockley dislocation [10] over the loop fault combined with the cross-slip of the constriction, see Fig. 3(d). The constriction on the 'left arm' is not yet formed. Its formation occurs with further increase of the applied stress up to 103 MPa (at

Table 2
Dislocation movement without defects.

T (K)	Yield stress (from MD) (MPa)	Steady-state velocity (from MD) (m/s)	Velocity from Orowan law (m/s)	Shear modulus (GPa)
300	96.8	47.0	43.7	70
600	56.4	49.9	43.8	69
900	37.2	48.9	45.2	61

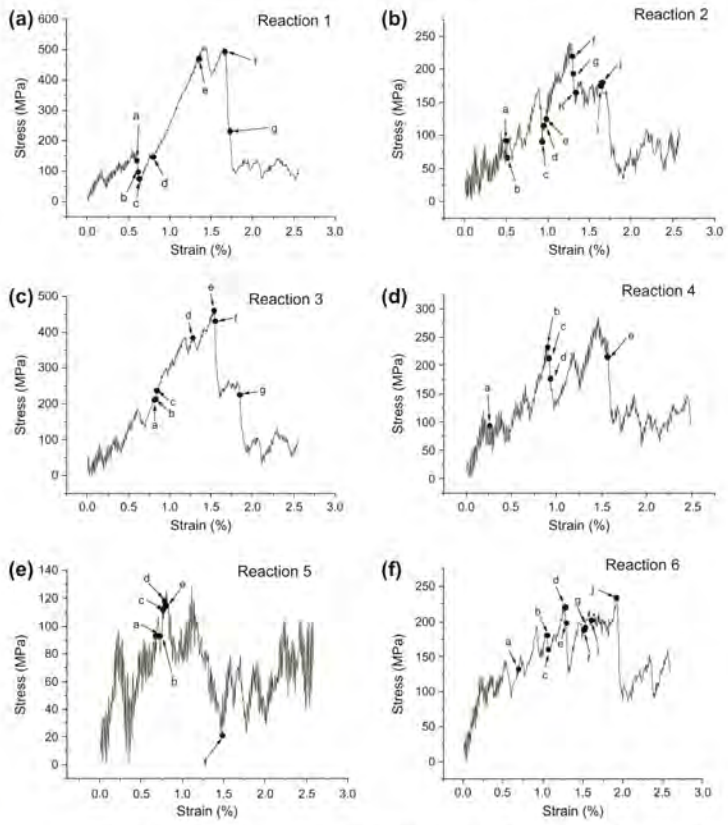

Fig. 2. Stress–strain curves obtained for the interaction according to mechanism (a)#1 (b)#2 (c)#3 (d)#4 (e)#5 (f)#6 (see Section 3.1). The letters refer to moments shown below in Fig. 3–8 for the reactions #1–#6, respectively.

T = 300 K), which triggers the removal of the extrinsic stacking fault in the same manner as for the lower part, see Fig. 3(e). Further increase of shear stress shrinks the set of segments dissociated in different {1 1 1} planes into a confined helical turn, see Fig. 3(e). The helical turn cannot move in the dislocation glide plane and the unpinning of the dislocation proceeds in two steps: (i) firstly, the LP arms form an edge dipole (see Fig. 3(f)) and close (see Fig. 3(g)), forming a straight 1/6<1 1 2> LP which propagates away from the loop increasing the area of the fault; (ii) then, the TP arms close in the same way, thus leaving behind a perfect ½<1 1 0> loop and closing the faulted area created by the LP.

(2) *Unfault with the formation of a 'bridge' segment*: This interaction mechanism was observed only for the small loops with BV = 1/3 [1 1 −1] at 600 K and 900 K. Initially, the LP is attracted to the loop and it moves towards the loop upon action of increasing shear stress. It forms the junction on the contact with the loop, see Fig. 4(a). The junction cross-slips downwards thus forming a 'bridge' connecting the LP with the top segment of the loop, see Fig. 4(b). The 'bridge' is made of several segments, being formed as a result of the dislocation cross-slip and re-dissociation in corresponding {1 1 1} planes. Then, the TP approaches and forms the constriction followed by the unfaulting of the bottom part of the loop, see Fig. 4(c). Eventually, the bridge is transformed into the helical turn, and correspondingly, the fault of the upper part of the loop is swept (thus, the superjog is formed), as shown in Fig. 4(d and e). With the applied stress the dislocation arms start to bow and conjunct via the closure of the dipole, see Fig. 4(f and g). Then two superjogs approach one another, see Fig. 4(h and i), and the TP unpins, see Fig. 4(j), leaving the perfect loop with BV = 1/2[1 1 0] behind the dislocation.

(3) *Shear with the formation of constriction*: The interaction of the screw dislocation with a 1/3[1 1 −1] loop can serve as an exam-

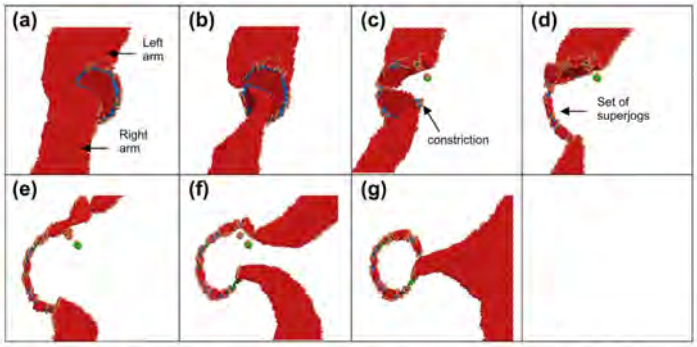

Fig. 3. Visualizations of the dislocation reaction #1 (D_L = 5 nm; BV = 1/3[1 1 1]; T = 300 K): snapshots taken at times: (a) 200 ps, (b) 205 ps, (c) 210 ps, (d) 265 ps, (e) 450 ps, (f) 555 ps and (g) 575 ps.

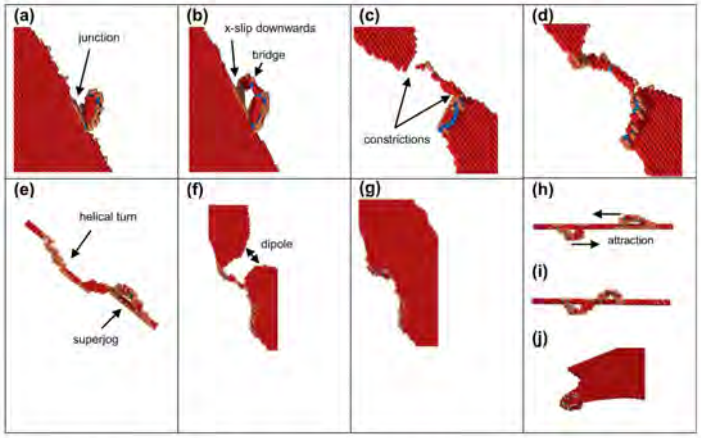

Fig. 4. Visualizations of the dislocation reaction #2 (D_L = 2 nm; BV = 1/3[11–1]; T = 600 K): snapshots taken at times: (a) 165 ps, (b) 170 ps, (c) 310 ps, (d) 315 ps, (e) 325 ps, (f) 430 ps, (g) 435 ps, (h) 445 ps, (i) 545 ps and (j) 550 ps.

ple of this type of interaction. The LP dislocation is attracted to the closest segment of the loop. Further increase of the stress pushes the TP to form a short constriction, see Fig. 5(a). The locally constricted node dissociates in (1 −1 1) plane and glides downwards along the loop side, again gets constricted at the bottom of the loop and re-dissociates in the original glide plane, see Fig. 5(b and c). It thus can be considered that the 'left arm' performed a double cross-slip movement and displaced underneath the loop being attached to the loop via two segments (dissociated in different {1 1 1} planes) connected by a constriction. The connecting configuration being sessile in the (−1 1 1) plane pins the left arm. Under increasing stress, both arms bow out and the 'left arm' eventually makes contact with the back side of the loop at 289 MPa, see Fig. 5(d). Further increase of shear stress results in the formation of an edge dipole (see Fig. 5(e)) and its closure reforming the straight LP, see Fig. 5(f). Finally, sufficiently high shear stress pushes back the double cross-slipped 'left arm' to join with the loop, as shown in Fig. 5(g) and the edge dipole closes leaving the faulted loop.

(3P) *Unfault after shear with formation of constriction*: The mechanism is similar to the one observed in the reaction #3. However, after the unpinning of the LP, the TP dipole is formed and its closure provokes loop unfaulting (see Fig. 5(g)). As a result, a perfect loop with BV = 1/2<1 1 0> is left behind the dislocation.

(3SJ) *Shear with formation of constriction and absorption of half loop*: The initial stage is the same as in reaction #3. Before the closure of the TP dipole the re-dissociated segment (shown in Fig. 5(c)) transforms into superjog on the left dislocation arm. This jog glides away from the preexisting loop as TP unpins leaving

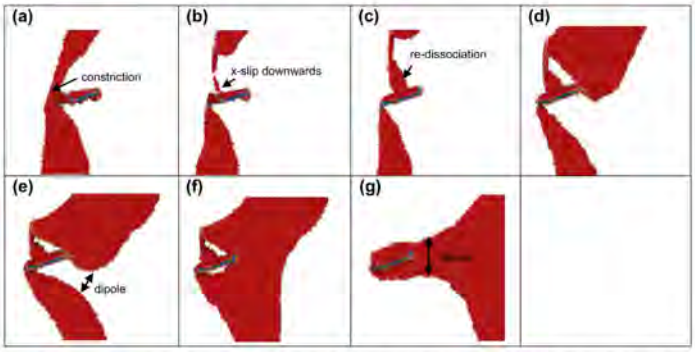

Fig. 5. Visualizations of the dislocation reaction #3 (D_L = 5 nm; BV = 1/3[1 1 −1]; T = 300 K): snapshots taken at times: (a) 270 ps, (b) 275 ps, (c) 280 ps, (d) 425 ps, (e) 510 ps, (f) 515 ps and (g) 615 ps.

half-absorbed faulted loop behind. The superjog has the same structure as the one observed in reaction #5 (see below).

(4) *Simple shear*: The interaction process involving a 1/3[1 −1 1] loop and a screw dislocation is illustrated in Fig. 6. The LP is attracted to the loop surface, see Fig. 6(a), at sufficiently high shear stress it approaches the loop, shears its fault and propagates further, see Fig. 6(b and c). The TP follows the same sequence of the basic steps, see Fig. 6(d). The unpinning of the TP from the loop occurs via the closure of the dipole, as is shown in Fig. 6(e). The sheared faulted loop with a step (a pair of stair-rod dislocations) on its surface is left behind. The step is however quickly removed recovering flat habit plane surface after the unpinning of the dislocation.

(4P) *Shear with unfaulting prior the unpinning of the TP*: The mechanism of the interaction is the same as in reaction #4. Prior to the unpinning of the TP (see Fig. 6(e)), the loop fault is removed by nucleation of the two partials on its surface, which sweep the fault The bottom and upper parts of the loop are disconnected from the left point (i.e. from junction with TP) and reorient in the other two {1 1 1} planes inclined in the (−1 1 1) glide plane. After that the TP unpins leaving a perfect loop with BV = 1/2<1 1 0> behind. Such reaction was observed only at high temperature.

(5) *Absorption into two glissile superjogs*: The interaction of the screw dislocation with a 1/3[1 −1 1] loop at T = 900 K can serve as the only example of this type of interaction. The LP is attracted to the loop and gets pinned on it, see Fig. 7(a). While the TP approaches the loop, the bottom part of the loop is already absorbed via the formation of D-Shockley partial, as is shown Fig. 7(b). At the moment the TP reaches the loop, the upper part of the loop also unfaults via the propagation of the D-Shockley dislocation, see Fig. 7(c–e). The two parts of the loop are now accommodated as glissile superjogs on the TP and LP dislocations. The whole configuration moves as the applied shear stress reaches 91 MPa, see Fig. 7(f). At this, the two superjogs are moving along dislocation line in opposite directions.

(6) *Absorption and reemission in the other {1 1 1} plane*: This reaction was observed only at 300 K for the interaction with a 1/3[1 −1 1] loop at T = 300 K. The LP is attracted by the loop and

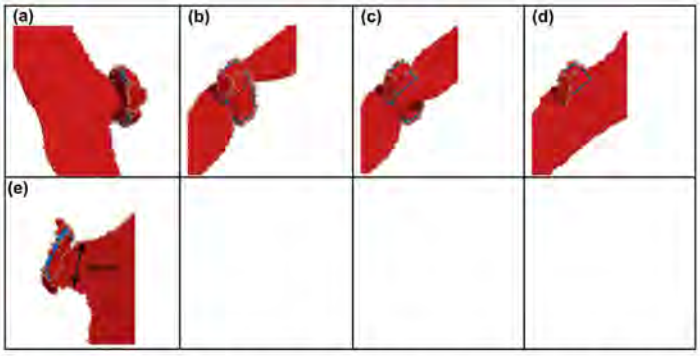

Fig. 6. Visualizations of the dislocation reaction #4 (D_L = 5 nm; BV = 1/3[1 −1 1]; T = 300 K): snapshots taken at times: (a) 85 ps, (b) 300 ps, (c) 305 ps, (d) 310 ps and (e) 520 ps.

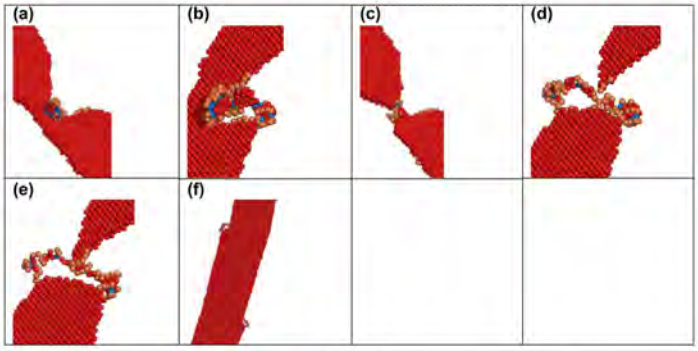

Fig. 7. Visualizations of the dislocation reaction #5 (D_L = 2 nm; BV = 1/3[1 −1 1]; T = 900 K): snapshots taken at times: (a) 225 ps, (b) 240 ps, (c) 255 ps, (d) 260 ps, (e) 265 ps and (f) 495 ps.

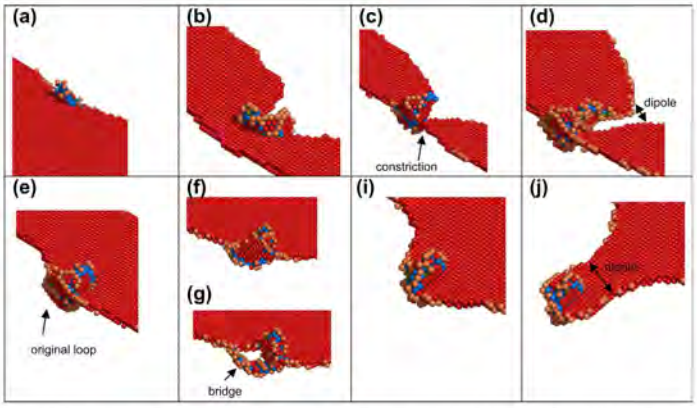

Fig. 8. Visualizations of the dislocation reaction #6 (D_L = 2 nm; BV = 1/3[1 −1 1]; T = 300 K): snapshots taken at times: (a) 230 ps, (b) 350 ps, (c) 355 ps, (d) 425 ps, (e) 430 ps, (f) 505 ps, (g) 510 ps, (h) 535 ps and (i) 640 ps.

moves towards it which results in its pinning, see Fig. 8(a). With increasing shear stress, the TP approaches the loop and forms a constriction across the loop surface, see Fig. 8(b and c). After that the constricted part of the dislocation re-dissociates in the loop habit plane, while the dislocation arms continue to bow, see Fig. R6(c). Then, the TP emerges a dipole which eventually closes, see Fig. 8(d and e). The pre-existing loop is now absorbed into the 'bridge' configuration on the TP, see Fig. 8(f and g). The bridge consists of multiple segments re-dissociated in different {1 1 1} planes, see Fig. 8(g). Then, the TP emerges a dipole, see Fig. 8(i and j), which closes leaving the faulted Frank loop in the (1 1 1) plane.

The type of the interaction mechanisms observed in the simulations referred to each the studied case is presented in Table 3 and the corresponding critical unpinning stress (τ_C) is given in Table 4. The same information is presented graphically in Fig. 9(a) and (b), for 2 and 5 nm FLs, respectively. The figure presents τ_C as a

Table 3
Classification of the interaction mechanisms observed for 2 and 5 nm FLs, referred to in the table as 'S' and 'L', respectively. In the reactions where negative shear strain was applied, a symbol '_m' is added in the coloumn 'FL size'.

Burgers vector of FLs	FL size	Temperature (K)		
		300	**600**	**900**
1/3[1 1 1]	**L**	1	1	1
	L_m	3P	3	3
	S	3	3	3
	S_m	3	3	3
1/3[1 1 −1]	**L**	3	3	3
	L_m	1	1	1
	S	3	3	3SJ
	S_m	1	2	2
1/3[1 −1 1]	**L**	4	4	4
	L_m	4	4	4
	S	4	4	5
	S_m	6	4	4P

Table 4
Critical unpinning stress (after subtraction of yield stress) measured in MPa for 2 and 5 nm FLs, referred to in the table as 'S' and 'L', respectively. In the reactions where negative shear strain was applied, a symbol '_m' is added in the coloumn 'FL size'.

Burgers vector of FLs	FL size	Temperature (K)		
		300	600	900
1/3[1 1 1]	L	415	368	365
	L_m	313	251	231
	S	163	126	104
	S_m	147	116	116
1/3[1 1 −1]	L	364	308	243
	L_m	398	354	290
	S	162	135	135
	S_m	207	183	134
1/3[1 −1 1]	L	189	169	142
	L_m	252	140	121
	S	112	98	91
	S_m	137	120	105

function of Burgers vector of FLs collected in three bars each corresponding to a certain simulation temperature.

First, we discuss the result obtained for the smaller loops. Among the well-established interaction mechanisms we list the following ones: absorption into a helical turn [10], simple shear [9] and absorption into two glissile superjogs [9]. We can see from Fig. 9(a) that in the case of 2 nm FL with BV = 1/3[1 1 1] temperature does not modify the interaction mechanism and the loop is sheared in all the cases (i.e. reaction #3 realizes). The similar interaction mechanism (and similar τ_C) is identified for half of the cases of FLs with BL = 1/3[1 1 −1] at 300 K. Loop unfaulting into a helical turn was observed for the other half of the cases at all the studied temperatures. Finally, FL with BV = 1/3[1 −1 1] interacts with the dislocation mainly via shear mechanism, whose details may vary depending on simulation temperature. This configuration offers the lowest resistance against the dislocation motion. The fact that the loop shear interaction requires rather low unpinning stress is also confirmed in our previous simulations in Fe–50Ni [13].

It is also worth noticing that for 5 nm loop, the unfault into a helical turn occurred in half of the studied cases for DLs with BV = 1/3[1 1 1] and 1/3[1 1 −1] (in the second half of cases reaction #3 (shear with the formation of constriction) – was identified). The simple shear was the only mechanism observed for FLs with BV = 1/3[1 −1 1]. In the case of large loops temperature did not have any essential influence on the interaction mechanism.

3.2. Loop strength

The unpinning stress, expressed in reduced units ($\mu b/L$, μ = 93 GPa, b = 0.7a_0, L = 40 nm-D_L, where D_L is the loop size), is shown in Table 5. Here, we used the isotropic shear modulus, while an anisotropic shear modulus for the <1 1 0>{1 1 1} type of load is ~60 GPa i.e. by a factor 1.5 lower. This means that for the data reported in Table 5, the maximum exerted stress (i.e. Orowan stress) should not exceed 0.65–0.75 μb/L, which is indeed the case. Moreover, we can clearly see that the Orowan stress realizes only in the case of unpinning from a helical turn, which implies loop absorption mechanism. This result is perfectly consistent with the early studies performed in pure Ni and Cu as well as in Fe–50Ni (see introduction for Refs.).

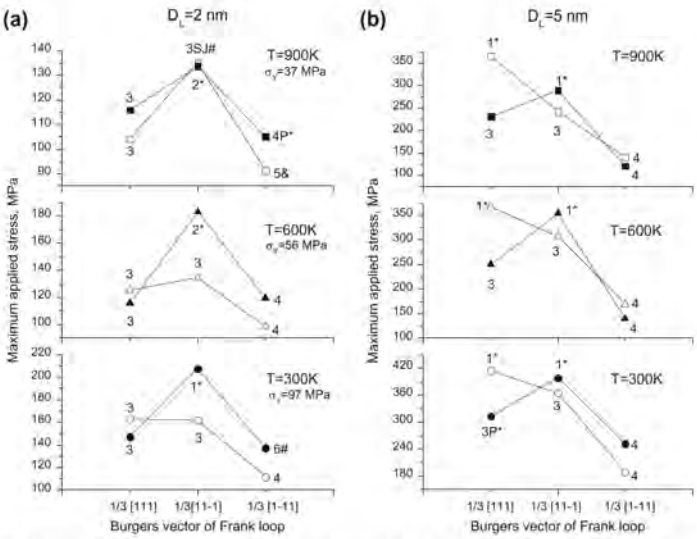

Fig. 9. τ_C as a function of Burgers vector of FL with size (a) 2 and (b) 5 nm. Three bars on each figure show the results obtained at 300, 600 and 900 K from down to top. The numbers next to the symbols on the figures refer to the type of the interaction mechanism (see Section 3.1). The latter one, which is marked with * and # symbols, implies, respectively, that the reaction led to the loop unfault or the loop structure was modified after the interaction but remained faulted. The reaction marked with & symbol led to the full absorption of the loop in the form of two superjogs. Open and filled symbols correspond to the direction of applied strain i.e. ½[1 1 0] and ½[−1 −1 0], respectively.

Table 5
Unpinning stress (subtracting yield stress) expressed in reduced units of $\mu b/L$ ($\mu b/L$, $\mu = 93$ GPa, $b = 0.7a_0$, $L = 40$ nm–D_L, where D_L is the loop size).

Burgers vector of FLs	FL size	Unpinning stress (μb/L)		
		300	600	900
1/3[1 1 1]	L	0.65	0.58	0.58
	L_m	0.49	0.40	0.36
	S	0.27	0.21	0.17
	S_m	0.24	0.19	0.19
1/3[1 1 −1]	L	0.58	0.49	0.39
	L_m	0.64	0.57	0.46
	S	0.27	0.23	0.23
	S_m	0.35	0.31	0.22
1/3[1 −1 1]	L	0.28	0.25	0.21
	L_m	0.38	0.21	0.18
	S	0.18	0.16	0.15
	S_m	0.23	0.20	0.17

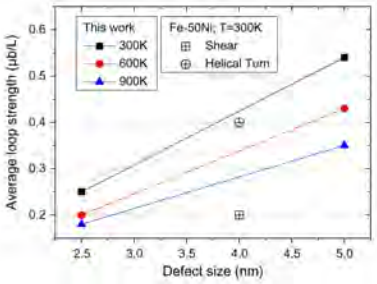

Fig. 10. Average τ_C measured for FLs in this work compared with average τ_C for loop shear and emission of a helical turn measured in Fe–50Ni at 300 K in [13]. The values for μ and L for the results from [13] are 80 GPa and 18 nm, respectively.

Finally, we compare the unpinning stresses measured in this work with the data obtained in Fe–50Ni for 4 nm Frank loops in [13]. Since the spacing of defects was different in the two simulations we compare τ_C using the reduced units. There are two interaction mechanisms which offer upper and lower bounds for the unpinning stress, namely: absorption into helical turn and loop shear. Therefore in Fig. 10, we plot τ_C corresponding to these two reactions in Fe–50Ni (obtained at 300 K) and compare them with the average τ_C measured at each studied temperature. The averaging is performed over τ_C values obtained for different interaction geometries. It clearly follows from Fig. 10 that τ_C for the emission of a helical turn in Fe–50Ni follows well the trend line based on the results obtained in Fe–10Ni–20Cr. While, the loop shear mechanism in Fe–50Ni offers much weaker resistance to dislocation glide. This comparison demonstrates the importance of the variation of the interaction mechanism on the hardening associated to the presence of Frank loops.

4. Summary and discussion

In this work we have studied the interaction of a screw dislocation with Franks loops of size 2 and 5 nm, in the temperature range 300–900 K in Fe–10Ni–20Cr FCC random alloy. The latter alloy is used as a model of 316-type austenitic steels, since the applied ternary interatomic potential has been especially developed to reproduce elastic constants and SFE of that steel. The interaction of a screw dislocation and Frank loops was characterized in terms of reaction mechanism and unpinning stress.

The results reveal six different interaction mechanisms about half of which lead to the unfaulting of a pre-existing loop. The unfaulting reactions are seen more often as temperature increases. This is consistent with temperature activated cross-slip mechanism [18] necessary to ensure the loop absorption. Thus with increasing test temperature the intensity of channel formation should raise. This also implies that the high SFE austenitic steels/alloys, where dislocations are easier to cross-slip, should have a lower resistance against channel formation. Since the unpinning stress in the case of the unfaulting reactions is regularly higher than for loop shear or reconstruction reactions (see the Section 3.1 for details), Frank loops will augment the flow stress more intensively (thus contributing to hardening) with increase of deformation temperature.

Previously, the interaction of dislocations with 4 nm Frank loops was studied in random Fe–50Ni and Fe–70Ni alloys with SFE ~20 and 50 mJ/m^2, respectively [13]. Only one possible interaction geometry leading to absorption into a helical turn was indentified and it was concluded that the absorption of loops is suppressed due to the high formation energy of a constriction. The latter is needed for the cross-slip movement of the dislocation line to promote loop unfaulting. The present calculations are also done in the low SFE alloy, however, much more frequent formation of constrictions and unfault events is observed. Correspondingly, the average strength of loops in Fe–10Ni–20Cr is also found to be higher in the present simulations.

We believe that the difference between the results obtained in Fe–50Ni and Fe–10Ni–20Cr comes from the amplitude of SFE variation as a function of local solute arrangement. As mentioned in introduction (see also Fig. 1), SFE variation is much stronger for the Fe–Ni potential developed in [19]. For such wide dispersion of SFE, the formation of somewhat extended constriction is extremely sensitive to the variation of local chemical arrangement and in practice hardly occurs for a sufficiently long dislocation segment to initiate loop unfaulting process.

5. Conclusions

Based on the above presented and discussed results we can draw the following conclusions:

1. Approximately half of the inspected configurations for dislocation-loop interaction lead to loop unfaulting, despite of rather low stacking fault energy of the alloy. The obstacle strength in reactions causing loop unfault is 0.5–0.65 μb/L, while it is ~0.2 μb/L in case of simple loop shear.
2. A new type of the interaction mechanism leading to the partial unfaulting and reconstruction of the Frank loops (but in a different {1 1 1} plane) was observed. Such reaction occurred only in the case of 2 nm loops. The strength of such interaction mechanism is of the order of 0.25 μb/L.
3. The primary feature controlling absorption in the alloy is the formation of short constrictions allowing for the local cross-slip dislocation movement. Strong local variation of SFE (such as in Fe–50Ni [13]) makes practically impossible the formation of constrictions on relatively large loops, preventing from loop unfault. Thus, magnitude of local variation of SFE is another factor to be accounted for in the consideration of dislocation-Frank loop interaction.

Acknowledgements

This work was performed in the framework of the EC-funded FP7/PERFORM60 project, under grant agreement 232612. Part of calculations has been performed at HPC Julich within the 'SORT' project. The research was partly supported by the FWO grant.

References

[1] G.S. Was. Fundamentals of Radiation Materials Science. Springer, New York, 2007.
[2] S.J. Zinkle, P.J. Maziasz, R.E. Stoller, J. Nucl. Mater. 206 (1993) 266.
[3] D.J. Bacon, Y.N. Osetsky, D. Rodney, Dislocation Obstacle Interactions at the Atomic Level, in: J.P. Hirth, L. Kubin (Eds.), Dislocation in Solids, 2010, p. 1 (Chapter 88).
[4] S.M. Bruemmer, E.P. Simonen, P.M. Scott, P.L. Andresen, G.S. Was, J.L. Nelson, J. Nucl. Mater. 274 (1999) 299.
[5] X.Q. Li, A. Almazouzi, J. Nucl. Mater. 385 (2009) 329.
[6] P.J. Maziasz, J. Nucl. Mater. 205 (1993) 118.
[7] I.M. Robertson, A. Beaudoin, K. Al-Fadhalah, L. Chun-Ming, J. Robach, B.D. Wirth, A. Arsenlis, D. Ahn, P. Sofronis, Mater. Sci. Eng., A 400–401 (2004) 245.
[8] J. Robach, I. Robertson, H. Lee, B. Wirth, Acta Mater. 54 (2006) 1679.
[9] T. Nogaret, C. Robertson, D. Rodney, Phil. Mag. 87 (2007) 945.
[10] D. Rodney, Acta Mater. 52 (2004) 607.
[11] C. Shin, H.H. Jin, J.H. Kwon, J.H. Shim, T.S. Byun, J. Korean Phys. Soc. 52 (2008) 1250.
[12] T. Nogaret, D. Rodney, M. Fivel, C. Robertson, J. Nucl. Mater. 380 (2008) 22.
[13] D. Terentyev, A. Bakaev, Y.N. Osetsky, Journal of Nuclear Materials, 2013, JNM_D_11_00728R3 (in press).
[14] G. Ackland, M. Mendelev, D. Srolovitz, S. Han, A. Barashev, J. Phys.: Condens. Matter. 16 (2004) 1.
[15] Y. Mishin, D. Farkas, M.J. Mehl, D.A. Papaconstantopoulos, Phys. Rev. B 59 (1999) 3393.
[16] G. Bonny, D. Terentyev, R.C. Pasianot, S. Ponce, A. Bakaev, Modell. Simul. Mater. Sci. Eng. 19 (2011).
[17] M. Allen, D. Tildesley, Computer Simulation of Liquids, Clarendon Press, Oxford, 1987.
[18] D. Hull, D.J. Bacon, Introduction to dislocations, Butterworth-Heinemann, Oxford, 2001.
[19] C. Becquart, Report F16O-CT-2003-508840, PERFECT IP Lille, 2005, pp. 22.

E Paper V

Interaction of minor alloying elements of high-Cr ferritic steels with lattice defects: An *ab initio* study

A. Bakaev, D. Terentyev, G. Bonny, T.P.C. Klaver, P. Olsson, D. Van Neck

Journal of Nuclear Materials 444 (2014) 237

Journal of Nuclear Materials 444 (2014) 337–346

Contents lists available at ScienceDirect

Journal of Nuclear Materials

journal homepage: www.elsevier.com/locate/jnucmat

Interaction of minor alloying elements of high-Cr ferritic steels with lattice defects: An *ab initio* study

A. Bakaev [a,b,c], D. Terentyev [a,*], G. Bonny [a], T.P.C. Klaver [d], P. Olsson [e], D. Van Neck [b]

[a] SCK-CEN, Nuclear Materials Science Institute, Boeretang 200, Mol B2400, Belgium
[b] Center for Molecular Modeling, Department of Physics and Astronomy, Ghent University, Technologiepark 903, 9052 Zwijnaarde, Belgium
[c] Department of Experimental Nuclear Physics K-89, Faculty of Physics and Mechanics, St. Petersburg State Polytechnical University, 29 Polytekhnicheskaya str., 195251 St. Petersburg, Russia
[d] Department of Materials Science and Engineering, Faculty of 3mE, TU Delft, Mekelweg 2, 2628 CD Delft, The Netherlands
[e] Department of Neutron Research, Angström Laboratory, Uppsala University, Box 525, SE-75120 Uppsala, Sweden

HIGHLIGHTS

- The interaction of Mo, W, Nb, Ta, V, Mn, Si with point and extended defects is characterized.
- Mn and Si exhibit peculiar interaction with both point and extended lattice defects.
- The results for substitutional atoms of the refractory metals well follow one specific trend.

ARTICLE INFO

Article history:
Received 23 August 2013
Accepted 26 September 2013
Available online 5 October 2013

ABSTRACT

Basic properties of minor alloying elements, namely Mo, W, Nb, Ta, V, Mn, Si entering the conventional and reduced-activation structural Fe–(9–12)Cr steels have been analyzed using *ab initio* calculations. The electronic structure calculations were applied to study the interaction of minor alloying elements with a number of important and well defined lattice structures, such as point defects, the 1/2⟨111⟩ screw dislocation core, high angle symmetric grain boundaries and free surfaces. The studied elements were classified according to their similarities and discrepancies regarding the interaction with the above mentioned defects. The refractory alloying elements are found to follow the same trend whereas Mn and Si exhibit peculiar behavior with respect to the interaction with both point and extended lattice defects. The obtained results are discussed and compared with previously published *ab initio* and available experimental data.

1. Introduction

Because of its low price and superior mechanical properties, Fe-based alloys are one of the most important and widely used metallic materials. One of the fields of application for ferritic steels is the nuclear sector, which due to large safety margins poses special requirements such as good corrosion resistance, low creep rate, high mechanical yield stress and ductility [1,2]. It is important that these properties must be preserved upon exploitation in a radiation environment, which is known to cause the degradation of the desired materials properties [1]. The irradiation-induced degradation originates from out-of-equilibrium atomic rearrangement processes that occur by means of radiation induced defects, whose density is much higher than the thermal equilibrium vacancy concentration. Moreover, some of the lattice defects such as self-interstitial atoms (SIAs) and dislocation loops cannot be generated under thermal ageing conditions due to their very high formation energy.

Interstitial impurities and alloying elements (AEs) play a key role in the development of the materials with designed properties [1]. Consequently, the interaction of the steel's alloying elements with radiation defects, efficiency of their mass transport, affinity of the alloying elements to different microstructural units (e.g. grain boundary, free surface, dislocations, etc.) determine their rearrangement in the course of the irradiation process. For example, non-equilibrium segregation of solutes may lead to the formation of unwanted secondary phases or reduce the strength of grain boundaries [3]. Thus, the preservation of the optimum microstructure during high temperature irradiation is essential for the resistance against the degradation of the material's mechanical properties.

In an effort to study the properties of lattice defects at the atomic scale, a few density functional theory (DFT) works have already been devoted to characterize the interaction of the most important elements of ferritic–martensitic steels, i.e. C and Cr. In particular, DFT methods were applied to investigate the properties of point,

* Corresponding author. Tel.: +32 14333197.
E-mail address: dterentyev@sckcen.be (D. Terentyev).

0022-3115/$ - see front matter © 2013 Elsevier B.V. All rights reserved.
http://dx.doi.org/10.1016/j.jnucmat.2013.09.053

Table 1
The type of periodicity, number of atoms, size of the crystal and k-point mesh of the studied configurations. The column 'additional information' reports the orientation and the type of the GBs and the orientation of free surfaces in the 2D slabs.

Configuration/purpose	Periodicity	Number of atoms	Size of the crystal, $a_0 \times a_0 \times a_0$	k-point mesh	Additional information
Bulk Fe calculations	3D	128	4.0 × 4.0 × 4.0	3 × 3 × 3	
Interaction of solute with GB	3D	72	1.4 × 2.4 × 10.6	9 × 5 × 1	Σ3(110)(111)
		96	2.8 × 1.7 × 9.9	7 × 9 × 1	Σ3(110)(112)
		120	1.0 × 3.2 × 19.2	9 × 5 × 1	Σ5(100)(013)
Interaction of solute with free surfaces	2D	126	3.0 × 3.0 × 10.5	5 × 5 × 1	(100)
		72	12.0 × 2.4 × 1.7	1 × 7 × 9	(110)
		144	4.2 × 4.9 × 7.0	3 × 1 × 1	(111)
		72	2.8 × 8.4 × 2.6	5 × 1 × 6	(112)
Inter-row potential	3D	36	4.2 × 4.9 × 0.9	3 × 2 × 9	
Interaction of solute with a 1/2⟨111⟩ screw dislocation	1D	108	10.0 × 8.8 × 0.9	1 × 1 × 12	

linear and some planar defects in bcc Fe [4–9], FeC [10–13] and FeCr [14–17] systems. However, for the other minor alloying elements typically entering high-Cr commercial steels no extended study has been performed yet.

In this work we perform a DFT study considering the most important minor alloying elements entering the conventional structural (9–12)Cr steels (e.g. T91 and HT9) and reduced activation steels (e.g. E97 and F82H). Besides Cr and C, the minor alloying elements considered are [1]: Mo, W, Nb, Ta, V, Mn and Si. W and Mo act as ferrite stabilizers (as well as Si) and also contribute to solid solution hardening [18–21]. In addition, they may contribute to the formation of Laves phases (if the concentration exceeds ~1%) [20]. V, Nb and Ta are strong carbide formers [20]. Mn on the other hand is an austenite stabilizer used during the production process [22].

In this work, electronic structure calculations are performed to consider the interaction of these minor AEs with a number of important and well defined lattice structures, such as point defects, the core structure of a 1/2⟨111⟩ screw dislocation, high angle symmetric grain boundaries and free surfaces. As the first step we perform calculations in pure Fe matrix and introduce Cr in the dilute limit with the purpose to distinguish and separate contributions of AEs to different radiation-related degradation mechanisms. Additionally, the goal is to provide a full and consistent set of *ab initio* data to be used for the parameterization and validation of upper-scale atomistic cohesive models for large scale simulations. The correspondence between the obtained DFT data and available experimental data is also discussed.

2. Calculation details

2.1. General scheme

In this work, we have performed three types of *ab initio* calculations considering minor AEs in 3D-bulk, 2D-slabs with free surfaces and grain boundaries and 1D-periodic systems containing a 1/2⟨111⟩ screw dislocation. The settings of 3D-bulk calculations are described below, while the description of the model for 2D- and 1D-periodic samples is given in Section 2.3. The DFT calculations were performed using the Vienna *ab initio* Simulation Package VASP [23,24]. We used the projector-augmented wave potentials [25,26] for the calculation of the electronic ground state of the system. The electron exchange–correlation functional was described within the generalized gradient approximation using

Table 2
Ground state properties of the considered AEs. Excess pressure for 3D-periodic bcc Fe cell, containing 127 Fe atoms and one substitutional AE atom is reported in the last column of the table. The abbreviations NM and AFM stand for non-magnetic and antiferromagnetic states, respectively.

Atom	Ground-state structure	Lattice parameter, (Å)	Excess pressure, (kB)
W	Bcc NM	3.176	8.1
Mo	Bcc NM	3.157	7.8
Nb	Bcc NM	3.321	10.6
Ta	Bcc NM	3.312	9.7
V	Bcc NM	2.978	2.7
Mn	58 atoms, AFM	8.544	2.7
Si	Diamond NM	5.470	-0.1
Cr	Bcc AFM	2.849	2.7

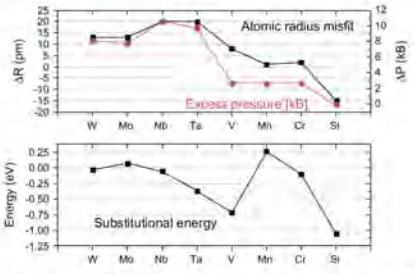

Fig. 1. The upper figure shows the atomic radius misfit (positive misfit means that atom is oversized as compared to equilibrium atomic volume of Fe) and excess pressure computed in the ionically relaxed systems (see text for details) containing a solute atom of the elements indicated. The lower figure shows the substitutional energy.

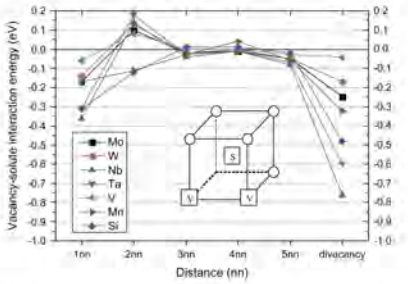

Fig. 2. Vacancy-solute interaction energy as a function of distance. The last value is the total binding energy for the most stable (for all studied alloying elements) di-vacancy – solute complex. The structure of the complex is shown in an inset figure.

PW91 functional [27], with a Vosko–Wilk–Nusair interpolation [28]. For Fe, Cr, Mo, W, Nb, Ta, V, Mn and Si pseudo potentials with 8, 6, 6, 6, 11, 5, 5, 7 and 4 valence electrons were used, respectively. The selected potential for Nb treats the 4p semi-core states as valence states.

Ionic relaxation was performed using the generalized gradient approximation with a force convergence criterion of 0.03 eV/Å. All the calculations were performed keeping the cell shape and volume (equal to the equilibrium volume of bulk iron) constant unless other conditions are specified. The energy cutoff for calculations was 300 eV which was proven to be large enough to provide converged results [29]. A $3 \times 3 \times 3$ k-point mesh was sampled by the Monkhorst and Pack scheme for systems with 128 atoms. The lattice parameter of pure ferromagnetic Fe is taken to be 2.831 Å following previous studies [17,29]. It has been confirmed that this lattice parameter provides the lowest total energy for BCC Fe crystal.

The excess pressure of the single solute atom configurations was calculated as the difference between the external pressure (reported in the VASP output) of the system with and without the substitutional solute.

Given that we perform spin-polarized calculations in the ferromagnetic system and introduce anti-ferromagnetic impurities, one needs to be careful when selecting the initial value of the magnetic moment to ensure that the true minimum energy configuration is obtained after relaxation. In the case of calculations with Mn when its magnetic spin was not anti-ferromagnetic to Fe after the relaxation, we performed additional calculations varying the absolute value of the initial moment as some of the results turned out to be particularly sensitive to the selection of the initial magnetic moment. In the paper we report the results corresponding to the lowest energy configurations only.

2.2. Substitutional and Interaction energy

To assess the substitution and interaction energy we apply standard definitions conventionally used in many similar DFT works [9]. The substitutional energy E_{sub} of a foreign atom F in the bcc Fe matrix is defined as:

$$E_{sub} = E(n\mathrm{Fe} + 1F) - \frac{n}{n+1} \times E((n+1)\mathrm{Fe}) - E(F)_{cryst}, \quad (1)$$

where $E(n\mathrm{Fe} + 1F)$ is the energy of a crystal containing n Fe atoms and one foreign atom, $E((n+1)\mathrm{Fe})$ is the energy of the pure Fe crystal with the same size as the former one, and $E(F)_{cryst}$ is the energy per atom of the element F in its most stable phase.

The interaction energy of n defects $\{A_i\}$ is defined as [9]:

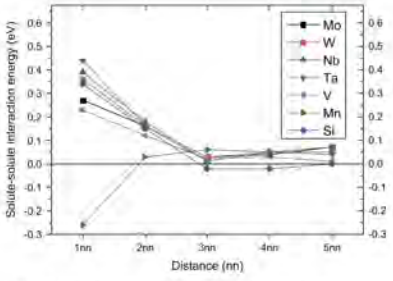

Fig. 3. Solute–solute interaction energy as a function of distance.

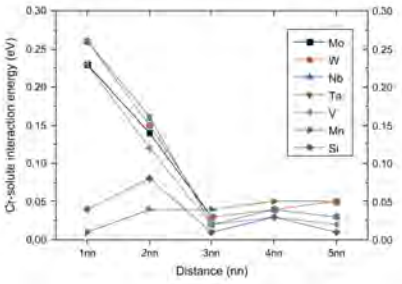

Fig. 4. Cr-solute interaction energy as a function of distance.

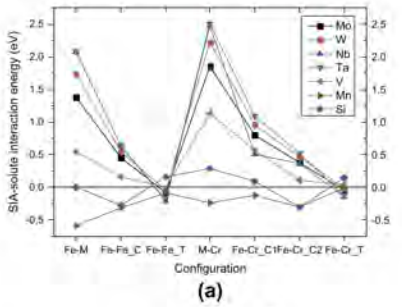

(a)

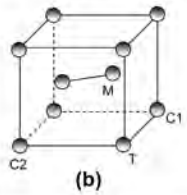

(b)

Fig. 5. (a) SIA-solute interaction energy as a function of local arrangement. (b) Schematic figure explaining the considered configurations. M: Fe-solute mixed dumbbell; C1 and C2 are the sites located in the compressive region of the dumbbell strain field; T is the site located in the tensile region of the dumbbell strain field. Configurations denoted on the figure as Fe–Cr_C/T correspond to the interaction of the mixed Fe–Cr dumbbell with another solute atom placed in either tensile or compressive site. Note that there are two non-equivalent compressive sites, M–Cr configuration corresponds to the case when the dumbbell is formed by Cr and another solute atom. In the case of the configurations involving Cr atom in the dumbbell, the interaction energy between the Fe–Cr dumbbell and another solute atom is calculated.

$$E_i(\{A_i\}) = [E(\{A_i\}) + (n-1)E_0] - \left[\sum_{i=1}^{n} E(A_i)\right], \quad (2)$$

where $E(A_i)$ is the energy of the configuration containing A_i only, $E(\{A_i\})$ is the energy of the configuration with all the n defects, and E_0 refers to a configuration containing no defects or impurities, i.e. bulk bcc iron. Following this notation, a negative value implies an attractive interaction and vice versa.

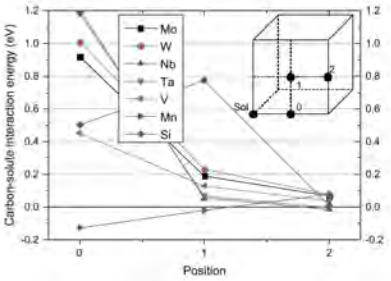

Fig. 6. Interaction energy between an interstitial carbon atom and substitutional solute measured in the positions schematically shown on the inset figure.

2.3. Calculations in 2D- and 1D-periodic cells

2D- and 1D-periodic cells were used to characterize the interaction of minor alloying impurities (as substitutional atoms at the Fe sites) with free surfaces, grain boundaries and the core of a 1/2⟨111⟩ screw dislocation. The specific DFT settings for each considered supercell are provided in Table 1. The reported k-point meshes were tested to provide converged results. In the 2D-periodic cells containing free surfaces, the width of vacuum was set to 10 Å, which was verified to be large enough to avoid interaction between free surfaces through the periodic boundaries. Prior to introducing an impurity, the dimensions of supercells containing grain boundaries were established by optimizing the spacing normal to a grain boundary (GB) interface to ensure the minimum energy.

To compare different grain boundaries we use the following parameters: (a) the GB energy (γ_{GB}) which is defined as [8]:

$$\gamma_{GB} = \frac{E_{GB} - E_{SC}}{2A}, \tag{3}$$

where E_{GB} and E_{SC} are the energies of the GB supercell and its corresponding single total crystal, respectively. A stands for the area of the GB plane. The corresponding single crystal (without GB) was obtained keeping the same basis orientation, k-point mesh and cut-off energy. The free surface energy (γ_{FS}) is defined in a similar way, where E_{GB} is substituted by the total energy of the crystal with free surfaces E_{FS}, and A is the free surface area.

(b). The GB excess free volume (Ω) is defined as [8]:

$$\Omega = \frac{V_{GB} - V_{SC}}{2A}, \tag{4}$$

where V_{GB} and V_{SC} stand for the volumes of the GB supercell and its corresponding single crystal with the same number of atoms, respectively. A is the grain boundary interface area.

Table 3
Characteristics of free surfaces as obtained by DFT calculations.

Surface orientation	Surface area (a_0^2)	Number of atoms on the surface layer	Surface energy (J/m^2)	Magnetic moment of the atoms (Fe/single Mn) on the top layer (μ_B)	Number of non-equivalent planes along Z-direction
100	9.0	9	2.52	2.9/−3.6	7
110	4.2	6	2.44	2.6/−3.2	6
111	20.8	12	2.67	2.8/−3.5	6
112	7.4	6	2.58	2.7/−3.4	6

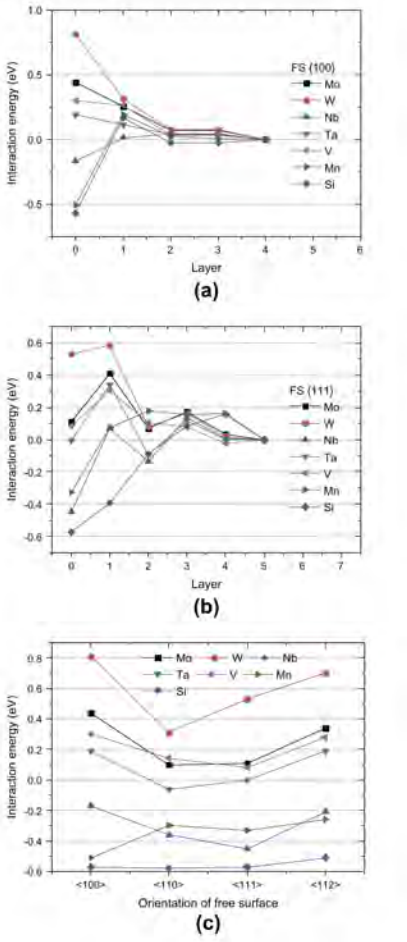

Fig. 7. Interaction energy of substitutional solutes with free surfaces. (a) As a function of depth for the FS with (100) orientation; (b) as a function of depth for the FS with (111) orientation; (c) for all the studied orientations for the case of a solute being placed in the top layer of the surface.

3. Results

3.1. Interaction with point defects

We start with the description of the properties of substitutional atoms. The majority (except for Si) of the calculations of this section had already been performed in the work [9]. We enhance the results of that work by adding excess pressure analysis,

studying interactions with carbon and refining the calculations with Mn. Table 2 reports the used reference structures of the considered AEs. The atomic radius misfit and excess pressure are given in the upper bar of Fig. 1. We see that there is a good correspondence between the calculated excess pressure and atomic size misfit. The largest lattice expansion is realized for the solutes representing refractory metals, i.e. Mo, W, Ta and Nb. It is somewhat smaller for V, Mn and Cr, and is about zero for the semi-conductor Si.

The substitutional energy for each considered AE is presented in the lower part of Fig. 1. The smallest substitutional energy (about zero) is obtained for the refractory metals, except for Ta whose substitution causes an exothermic reaction and the released heat is 0.37 eV. Strongly negative substitutional energies are found for V and Si, −0.71 and −1.06 eV respectively. And finally, Mn has a well pronounced positive substitution energy.

The interaction energy between a vacancy and the solutes is given in Fig. 2 as a function of distance, expressed in nearest neighbor (nn) distance units. Irrespective of the solute type, all the species are attracted to a vacancy in the first nearest neighbor (1nn) position, and the interaction becomes negligible once the objects are placed further than 2nn distance. Considering the short range interaction (i.e. in the 1nn and 2nn), the studied elements can be subdivided into two types. Mn and Si exhibit attractive interaction with a vacancy in both 1nn and 2nn position, and therefore these elements might potentially be dragged by a vacancy [30], although detailed analysis of the migration barriers within five-frequency model is required for a definitive conclusion. All other studied elements exhibit repulsive interaction in 2nn position and attractive in the 1nn. This indicates that these AEs should act as short-range traps for vacancies.

A number of remarks can be made regarding the absolute value of the interaction energy in 1nn position. For the refractory elements and vanadium, the interaction energy rises consistently with the size misfit factor. In contrast, Si and Mn exhibit much stronger binding than expected from the lattice strain induced in perfect bcc Fe. For completeness, we also computed the interaction energy between the di-vacancy and a solute (2nn vacancy–vacancy complex which is the most stable in Fe and solute at 1nn). For all tested elements the interaction is found to be strongly attractive, except for vanadium (see Fig. 2).

Next we proceed to the solute–solute and solute-Cr interactions, which are presented in Figs. 3 and 4, respectively. As in the case of the interaction with a vacancy, the interaction is limited to 1nn and 2nn distance. Among the considered elements, Mn and Si are again the outstanding ones. Indeed, all the solutes exhibit strong mutual repulsion in Fe and repulsion from substitutional Cr, except for the Mn–Mn pair, for which a considerable binding (−0.26 eV) is predicted. This binding, however, changes to weak repulsion in the 2nn and 3nn positions. Why the strong repulsion, found for Cr–Cr pairs in Fe, does not occur for Mn–Mn pair will be discussed later. Although Si and Mn also exhibit weak repulsive interaction with Cr in the immediate neighborhood, its absolute value is much lower than for the other elements.

The interaction energy between $a\langle 110\rangle$ dumbbell (the most stable SIA configuration in Fe) and different solutes is presented in Fig. 5(a) for different local arrangements. The figure caption explains atomic arrangement for the different configurations and Fig. 5(b) schematically shows these arrangements. All the transition metals, except for Mn, exhibit repulsive interaction if placed in the compressive (C) site, attractive interaction in the tensile site (T), and none of them except Mn form stable Fe-solute or Cr-solute dumbbells. The repulsive interaction in the compressive site and the inability to form mixed dumbbell is consistent with the oversized nature of W, Mo, Ta, Nb, V (as substitutes in Fe matrix, see Fig. 1). The attractive interaction in the tensile site is also consistent with expectations from elasticity theory consideration. Finally, given that Cr also behaves as an oversized substitutional, a stable Cr-solute dumbbell does not form with any considered refractory metals nor vanadium atom. Mn shows attractive interaction in

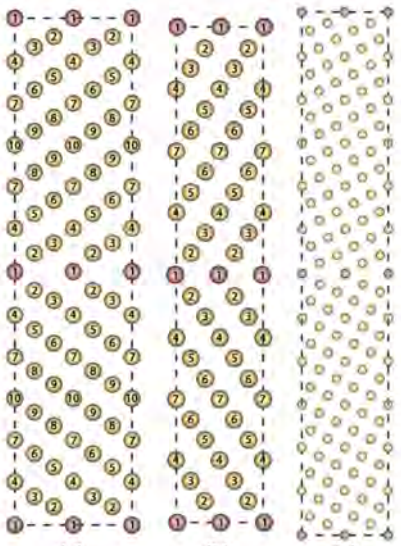

Fig. 8. YZ-plane views of three grain boundaries (a: $\Sigma3(110)(111)$, b: $\Sigma3(110)(112)$, c: $\Sigma5(100)(013)$). In (a) and (b) the equivalent lattice sites are marked with the same numbers. The dark colored atoms represent the grain boundary.

Table 4
Characteristics of grain boundaries as obtained by DFT calculations here.

GB type, XYZ orientation of the crystal	GB area, (a_0^2)	Number of atoms on the GB layer	Number of non-equivalent planes along Z-direction within one grain	GB energy γ_{GB} (J/m^2)	GB excess free volume (Ω), (Å)
$\Sigma3(110)\{111\}$ $[110]\times[111]=[112]$	3.46	2	10	−1.56	0.11
$\Sigma3(110)[112][110]=[\bar{1}12]=[111]$	4.90	4	7	−0.47	0.04
$\Sigma5(100)[013][100]=[013]=[0\bar{3}1]$	3.16	2	10	−1.51	0.11

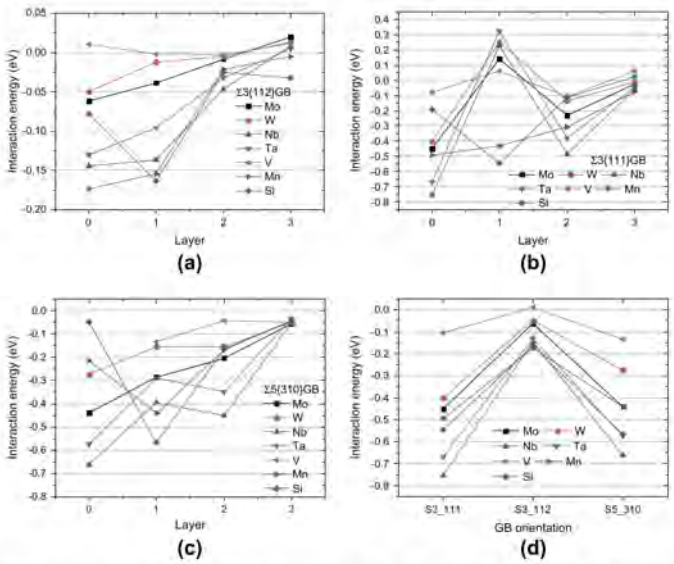

Fig. 9. Interaction energy of substitutional solutes with the three different grain boundaries (a: Σ3(110){112}, b: Σ3(110){111}, c: Σ5(001){310}) computed for the four layers near the grain boundary interface. Figure d presents the maximum interaction energy as a function of GB orientation.

all the studied configurations with dumbbells except for being in tensile sites near to Fe–Fe and Fe–Cr dumbbells where the interaction is very weak or zero, respectively. The reasons for the peculiar behavior of Mn will be discussed later in Section 4. Finally, Si repels or shows negligible interaction in all the configurations except for attraction to Fe–Fe dumbbell in the compressive site as well as to the mixed Fe–Cr dumbbell in the compressive site C2 (see Fig. 5b), i.e. when the distance between Si and Cr is almost as large as 3nn so that their repulsion is negligible (see Fig. 4).

Fig. 6 displays the interaction energy between an interstitial carbon atom in an octahedral position (the most stable configuration [31]) and a substitutional solute atom, calculated in the positions schematically shown in the inset figure. The interaction between an interstitial carbon and all the studied elements is repulsive except for Mn, to which the carbon atom is attracted in the closest octahedral position. The carbon-solute repulsion vanishes at the distance of $a_{0\text{-}Fe}\sqrt{(5/2)}$.

3.2. Interaction with interfaces

Four different open surfaces were considered in this work, namely {100}, {111}, {110} and {112}. The latter two (in addition to {123}) are known to be primary dislocation glide planes in bcc metals, while {100} and {111} are close packed surface planes. The sizes of the supercells used to compute the interaction energy are given in Table 3.

The interaction with the free surface in all the cases was found to last approximately up to the 3rd or 4th interatomic layer. However, the strongest interaction, no matter if it was attractive or repulsive, was seen to take place at the top layer in most of the cases. Only three exceptions were identified for Mo, V and Ta interacting with a {111} surface (see Fig. 7a and b presenting the interaction energy as a function of depth for the FSs with {100} and {111} orientations, respectively). In the following we discuss only the interaction energy for the top layer, see Fig. 7c. Nb, Mn and Si are attracted to all the considered surfaces whereas W, Mo and V exhibit repulsive interaction. Ta exhibits almost no interaction with {110} and {111} surfaces, and weak repulsion from {100} and {112} surfaces is predicted.

The considered grain boundary interfaces have different dimensions, depending on the GB type. To give an idea how close the periodical in-plane images of the alloying atom are, we report the distance in Table 4 together with the interface area and other data for each GB studied such as GB energy and GB excess free volume. The side views (YZ plane) of the studied GB are shown in Fig. 8. The calculated values of the GB energies are in good agreement with the previously published *ab initio* results [8].

As in the case of the free surfaces, the interaction energy was seen to vary only a few (three in most of the cases) interatomic layers, close to the interface plane. This time, however, the variation of the interaction energy is not monotonic and therefore we present the computed interaction energy as a function of location of the solute with respect to the grain boundary plane (GBP), shown in Fig. 9. In all the cases, the considered solutes were found to be attracted to the studied GBs except for vanadium which does not interact with grain boundary Σ3(110){112}. Note that the binding with a Σ3(110){112} GB was much weaker (by about a factor of three) than with the other two GBs, i.e. Σ3(110){111} and Σ5(100){013}. It is also seen from the figures that the profiles of the interaction energy for the refractory metals have similar

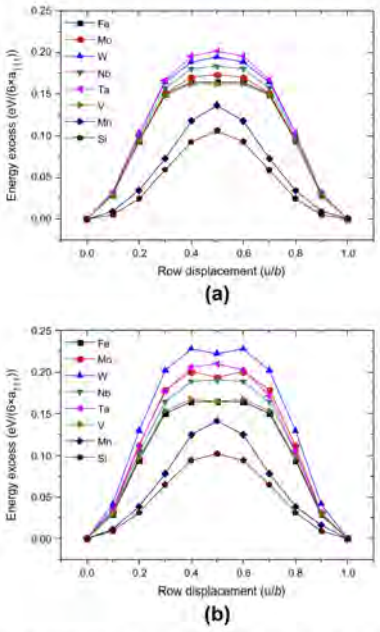

Fig. 10. The variation of the excess energy (normalized over a length of the displaced row and the amount of nearest-neighbor atomic rows (six rows)) versus atomic row displacement ($u/\boldsymbol{b}$) for: (a) a single row of solutes in the Fe matrix; (b) a row of solutes dragged next to another row of solutes (of the same type).

shapes, although their absolute values differ. Si and Mn solutes, on the other hand, exhibit somewhat irregular behavior. For instance, the strongest interaction for Si with all studied GB occurs in the 1st layer away from the GBP, whereas all other elements are mostly attracted to the GB interface itself. Note that in the $\Sigma3\langle110\rangle\{111\}$GB all the solutes except for Mn and Si show repulsive interaction at the 1st layer from the GBP whereas Mn and Si are attracted to the GB.

The maximum binding energy between the considered solutes and GBs is presented in Fig. 9d. We observe that almost irrespective of the GB orientation the order at which the binding energy increases is as follows: V, (W & Mo), (Mn, Si, Ta & Nb). This trend is especially easy to observe in the case of high-energy GBs such as $\Sigma3\langle110\rangle\{111\}$ and $\Sigma5\langle100\rangle\{013\}$. The strongest interaction of Ta and Nb is most likely related to the fact that these solutes produce the largest strain (see Fig. 1), which can be partially relieved at the GB interface. Correspondingly, the smallest binding energy found for vanadium can also be attributed to its small excess pressure generated in bulk bcc Fe (see Fig. 1). The relatively strong binding energy found for Mn and Si (for the $\Sigma3\langle110\rangle\{111\}$ GB) cannot be simply explained by the relief of the lattice strain. Finding the reasons for peculiar behavior of Mn and Si requires in-depth investigation and understanding of the modification of the magnetic state and directional bonding arrangement, which will be a subject of a separate work.

3.3. Interaction with a screw dislocation and lattice friction

As mentioned in the introduction, we also perform calculations to investigate the influence of the solutes on the core structure of a $1/2\langle111\rangle$ screw dislocation and slip-resistance of a $\langle111\rangle$ atomic row (a.k.a. interatomic row potential). The atomic row (AR) method accounts for the relaxation between $\langle111\rangle$ atomic strings and the inter-row potential derived directly from DFT calculations correlates with the type of core structure of a $1/2\langle111\rangle$ screw dislocation [32], which may be isotropic or degenerate [33] depending on the double hump or single hump shape of the interatomic row potential, respectively. In the cases when the flat top-structure is observed, the core configuration can be either degenerate or isotropic [32]. By computing the interatomic row potentials for solutes or pairs of solutes one clarifies the impact of solute-matrix and solute–solute interaction on the lattice friction against the slip involving sliding (re-arrangement) of $\langle111\rangle$ atomic rows. The latter process corresponds to the glide of a $1/2\langle111\rangle$ screw dislocation in bcc metals.

The variation of the energy (normalized over a length of the displaced row and the amount of nearest-neighbor atomic rows (six rows)) versus atomic row displacement ($u/\boldsymbol{b}$) for a single row of solute atoms in the Fe matrix and for a row of solutes standing next to another row of solutes (of the same type) is given in Fig. 10 a and b, respectively. Fig. 10a shows that the addition of an isolated row of oversized refractory metals causes an increase of the amplitude of the energy excess by a factor 1.05–1.25, suggesting that they should suppress the glide of $\langle111\rangle$ rows. The presence of a vanadium row, on the other hand, hardly changes the interatomic potential profile. Mn and Si clearly decrease the atomic row shift resistance and in addition change the shape of the profiles from a double-hump-like or flat-top to a sinusoidal one (single hump). This should be also reflected in the core structure of the screw dislocation, as was validated by separate DFT calculations presented in the following. Fig. 10b, which represents the solute–solute row interatomic potential, essentially shows that only refractory metals cause enhancement of the inter-row friction, while pairs of Mn and Si rows exhibit a weaker friction than between Fe rows and V causes no change of friction.

The differential displacement maps for the studied AEs in different positions relative to the dislocation core structure are presented in Fig. 11. In pure bcc Fe, a $1/2\langle111\rangle$ screw dislocation has a compact non-degenerate core structure. Three $\langle111\rangle$ rows form the core of the screw dislocation. Addition of Mo, Nb, Mn, Ta, V or W in the core position does not disturb the equilibrium structure of the core, which remains symmetric and non-degenerate as shown for Mo in cell Mo-Core in Fig. 11. By displacing Mo (or Nb, Mn, Ta, V, W) away from the core (see cells Mo-1nn and Mo-2nn), its structure remains unchanged, although some limited distortion occurs in the immediate vicinity of an introduced solute. Si clearly modifies the core structure making it extended (split) in a $\{110\}$ plane (see Fig. 11, cell Si-Core). The orientation of the split plane depends on the particular position of Si in the core. The core also remains extended if Si is placed in the 1st nn position (see Fig. 11, cell Si-1nn). Recovery of the symmetric non-degenerate core structure occurs if Si is placed in the 2nd nn position (see Fig. 11 cell Si-2nn).

A similar effect as for Si on the core extension in a $\{110\}$ plane is seen for W, Ta, Nb and weakly for Mo being placed in the 1nn position. Thus, these essentially oversized elements affect the core structure while the dislocation approaches them. Finally, a Mn atom placed at the 1nn position causes heavy relaxation of the dislocation core so that its actual position displaces towards the solute, as shown in cell Mn-1nn of Fig. 11.

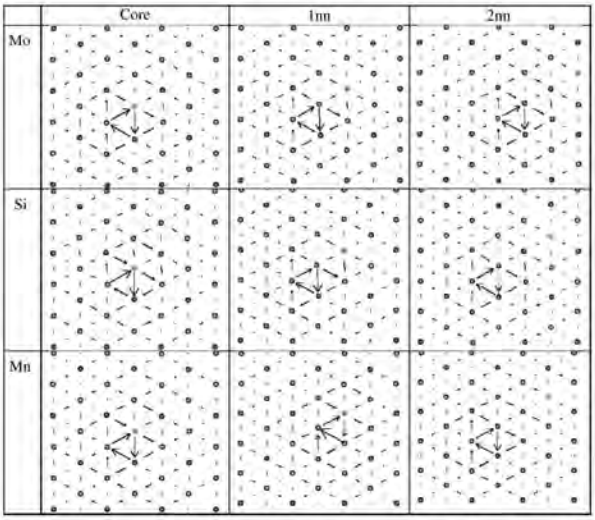

Fig. 11. Differential displacement maps for a 1/2⟨111⟩ screw dislocation interacting with solutes calculated after full relaxation. The alloying element (specified in the left column) is shown by a blue circle. Three different positions for AE are considered, namely: in-core and 1st and 2nd nearest neighbor from the core.

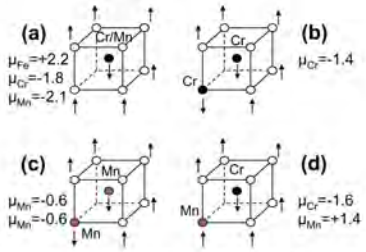

Fig. 12. Magnetic moments obtained for Fe, Cr and Mn atoms for different atomic configurations, namely: (a) one substitutional atom, (b) 1nn pair of Cr atoms, (c) 1nn pair of Mn atoms, (d) 1nn Mn–Cr pair.

4. Summary and conclusions

One of the most striking features of Mn is the absence of Mn–Mn repulsion at the 1nn distance, which is predicted for all the other elements. The reason for this absence could provide an explanation for other deviations from patterns that were observed. Mn behaves as anti-ferromagnetic (its spin is opposite to the spins of Fe atoms) in bcc Fe and the repulsion between Mn atoms would be natural due to the expected 'frustration' of magnetic moments, which was discovered earlier for a pair of Cr atoms in Fe [34]. Yet, it is predicted that two Mn atoms attract each other yielding an interaction energy of −0.26 eV. To rationalize the obtained result we have computed the magnetic moments on Mn and the surrounding Fe atoms in different atomic configurations, see Fig. 12. Given the above mentioned analogy with Cr, we repeated the same calculations for Cr to reveal the difference. For an isolated substitutional Mn/Cr atom its moment is anti-aligned to Fe atoms (see Fig. 12a) as expected. The moments on two Cr atoms placed as 1nn and relaxed (see Fig. 12b) are also anti-aligned with respect to the moments of Fe atoms, but the total value is now reduced to $-1.4\ \mu_B$ compared to $-1.8\ \mu_B$ for the isolated atom. In the case of the Mn–Mn pair, the magnetic moment on each Mn atom is strongly reduced to $-0.6\ \mu_B$, as shown in Fig. 12c. In the case of the Mn–Cr pair, for which the repulsion is also expected, the moment of the Mn atom is flipped to align with Fe atoms and there is apparently no opposition of magnetic moments (unlike in the case of Cr–Cr pair) and consequently no repulsion. Hence, the flexibility of the magnetic moment of the Mn atom and the ability of Mn to modify magnetic moments of the neibourhood Fe atoms are likely to be the key features explaining the absence of Mn–Mn and Mn–Cr repulsion as well as the moderate attraction of Mn to a pure Fe–Fe and mixed Fe–Cr⟨110⟩ dumbbell (see Fig. 5a). As a result, Mn is the only element among the studied ones which exhibits both remarkable attraction to an SIA and vacancy, and forms a stable mixed dumbbell at the same time, following the results obtained here.

For completeness, we bring to the reader's attention DFT and experimental data on Mn–Mn interaction. Mössbauer experiments on Fe5%Mn alloys performed by Chojcan et al. [35] deduced a repulsive interaction of 0.11–0.14 eV for Mn–Mn pairs of solute atoms. These values, however, are obtained assuming a binomial distribution of the Mn atoms which was not certain in that experiment since the solubility of Mn is less than 5% [36] in alpha Fe. Therefore it is unclear if comparison of the latter results with our DFT data is justified.

Vincent et al. [37] performed DFT calculations using ultrasoft pseudopotentials which show a repulsive interaction between

Mn–Mn pairs of 0.28 eV and 0.15 eV for 1nn and 2nn pairs, respectively. Beside the usage of another set of pseudopotentials, the difference with our results might be attributed to the different relaxation conditions.

The interaction of V–V pairs was studied in [35] and a negligible binding of about −0.01 to 0.01 eV was calculated. The DFT results obtained here predict a higher repulsive interaction of 0.23 eV for 1nn and 0.12 eV for 2nn. The later obtained experimental results by Chojcan in Fe–3%V [38] revealed repulsion of about 0.05 eV for V–V pairs. Therefore there is a qualitative agreement between our results and experimental data.

Our next point of the discussion is the correspondence between the predicted interaction nature of the solutes with point defects and available experimental evidence. The predicted strong attractive interaction for the Si-vacancy agrees well with the results of Nagai [39] and Möslang [40], suggesting the formation of stable vacancy-Si pairs. In the same experimental work, Möslang et al. could not reveal strong attractive interaction for a vacancy with Cr and Mn. Cr is indeed known to exhibit a very small positive binding energy with a vacancy (~0.05 eV). Mn, according to the utilized DFT method, is predicted to exhibit a non-negligible positive binding energy ([9] and present work). In addition, according to the resistivity recovery studies of e^- irradiated Fe–Mn alloys, Mn binds vacancies [41].

Considering the interaction with an SIA, the amount of experimental data is also rather limited. Mo is known to suppress the migration of Fe–Fe SIAs and thus acts as a trap for SIAs [42]. The trapping energy was determined to be about 0.06 eV, which is however about the uncertainty of the present calculations due to the limited supercell size. At the same time, Mo does not form the mixed dumbbell [42]. All these features are in line with the currently obtained results, and the binding energy for Mo in the tensile site of an Fe–Fe dumbbell is 0.08 eV in excellent agreement with the experimental result.

Si atoms also show suppression of long-range migration of SIAs (suppression of stage I_E) with increasing Si concentration in isochronal recovery experiments [43]. This has been interpreted as a multiple trapping effect, implying that trapped SIAs, instead of detrapping, may form mixed migrating dumbbells and then be bound to a second Si atom [43]. According to the present calculations Si acts as a relatively strong trap for Fe–Fe dumbbells (0.28 eV) and given the possible formation of mixed Si–Fe dumbbells, multiple trapping by Si is not excluded by our results.

Mn forms a stable mixed dumbbell [41], which agrees with the results of our calculations.

A number of results inconsistent with the trends obtained for refractory metals was obtained for anti-ferromagnetic Mn and diamagnetic Si. Below, we list the observed irregularities for Si and Mn:

1. Attractive interaction with a vacancy in both 1nn and 2nn position.
2. Considerable attractive interaction between two substitutional Mn atoms in the 1nn position.
3. No repulsive interaction with substitutional Cr.
4. Mn is the only element which form a stable mixed$\langle 1\,1\,0\rangle$ Fe–Mn dumbbell, with Si being neutral, while all the other considered elements exhibit strong repulsion.
5. Non-negligible attractive interaction with a $\langle 1\,1\,0\rangle$ Fe–Fe dumbbell in the compressive site.
6. Mn is the only element which exhibits weak attractive interaction with an interstitial carbon.
7. Si, Mn (and Nb) exhibit considerable affinity to a free surface, in contrast to the other elements.
8. Mn and Si are the only elements which are found to facilitate $\langle 1\,1\,1\rangle$ atomic row exchange.
9. Si is the only element that causes strong distortion of the core structure of a $1/2\langle 1\,1\,1\rangle$ screw dislocation.

On other hand, all the considered refractory metals and vanadium, are characterized by the following features:

1. Moderate attraction with a vacancy in the 1nn and non-negligible repulsion in the 2nn.
2. Strong repulsion with Cr and with itself in the 1nn position.
3. Do not form a solute-Fe or solute-Cr$\langle 1\,1\,0\rangle$ dumbbell.
4. Strong repulsion from an isolated interstitial carbon.
5. No affinity to the free surface (except for Nb and Ta).
6. Moderate attraction to the GB interface, correlating with the size misfit factor.
7. Enhancement (except for V where no change is calculated) of the lattice friction that makes $\langle 1\,1\,1\rangle$ atomic row exchange more difficult.
8. Do not alter the screw dislocation core structure if placed in the core, and do create expansion of the core in a $\{1\,1\,0\}$ plane if the solute is placed at the 1nn position from the core.

Rationalization and understanding of the observed systematic trends and some off-trend results (specifically of Mn and Si) require further in-depth analysis.

Acknowledgements

This work was performed in the framework of the EFDA project. We are grateful to the ICT Department of Ghent University for partial support of this work. Part of calculations has been performed at HPC Julich within the 'SORT' project. The research was partly supported by the FWO grant.

References

[1] R.L. Klueh, A.T. Nelson, J. Nucl. Mater. 371 (2007) 37–52.
[2] O. Anderoglu, T. Byun, M. Toloczko, S. Maloy, Metall. Mater. Trans. A 44 (2013) 70–83.
[3] J.P. Wharry, Z. Jiao, V. Shankar, J.T. Busby, G.S. Was, J. Nucl. Mater. 417 (2011) 140–144.
[4] E. Vincent, C.S. Becquart, C. Domain, J. Nucl. Mater. 359 (2006) 227–237.
[5] E. Vincent, C.S. Becquart, C. Domain, Instrum. Methods B 228 (2005) 137–141.
[6] M. Itakura, H. Kaburaki, M. Yamaguchi, Acta Mater. 60 (2012) 3698–3710.
[7] D. Terentyev, T. Klaver, P. Olsson, M. Marinica, F. Willaime, C. Domain, L. Malerba, Phys. Rev. Lett. 100 (2008) 145503.
[8] S.K. Bhattacharya, S. Tanaka, Y. Shiihara, M. Kohyama, J. Phys.: Condens. Matter 25 (2013) 135004.
[9] P. Olsson, T.P.C. Klaver, C. Domain, Phys. Rev. B 81 (2010) 054102.
[10] C.S. Becquart, J.M. Raulot, G. Bencteux, C. Domain, M. Perez, S. Garruchet, H. Nguyen, Comput. Mater. Sci. 40 (2007) 119–129.
[11] C.C. Fu, E. Meslin, A. Barbu, F. Willaime, V. Oison, Effect of C on vacancy migration in alpha-iron symposium on theory, Modeling and Numerical Simulation of Multi-Physics Materials Behavior held at the 2007 MRS Fall Meeting Boston, MA, 2007, pp. 157–164.
[12] C.J. Forst, J. Slycke, K.J. Van Vliet, S. Yip, Phys. Rev. Lett. 96 (2006) 175501.
[13] C. Domain, C. Becquart, J. Foct, Phys. Rev. B 69 (2004) 144112.
[14] P. Olsson, I.A. Abrikosov, L. Vitos, J. Wallenius, J. Nucl. Mater. 321 (2003) 84–90.
[15] D. Nguyen-Manh, M.Y. Lavrentiev, S.L. Dudarev, J. Nucl. Mater. 386–388 (2009) 60–63.
[16] K.O.E. Henriksson, N. Sandberg, J. Wallenius, Appl. Phys. Lett. 93 (2008) 191912.
[17] T. Klaver, P. Olsson, M. Finnis, Phys. Rev. B 76 (2007) 214110.
[18] W.C. Leslie, Metall. Trans. 3 (1972) 5–26.
[19] J. Nutting, The structural stability of low alloy steels for power generation applications, Ion Communications Ltd., London, 1999.
[20] V.Z.K. Foldyna, V. Vodarek, J. Purmensky, 3rd EPRI Conference on Advanced Materials Technology for Fossil Plants, 2001, pp. 89–98.
[21] R.W.K. Honeycomb, Steels: Microstructure and Properties, Edward Arnold, London, 1981.
[22] M. Kutz, Handbook of Materials Selection, Wiley, New York, 2002.
[23] G. Kresse, J. Hafner, Phys. Rev. B 47 (1993) 558–561.
[24] G. Kresse, J. Furthmuller, Phys. Rev. B 54 (1996) 11169–11186.
[25] P.E. Blochl, Phys. Rev. B 50 (1994) 17953–17979.

[26] G. Kresse, D. Joubert, Phys. Rev. B 59 (1999) 1758–1775.
[27] J.P. Perdew, J.A. Chevary, S.H. Vosko, K.A. Jackson, M.R. Pederson, D.J. Singh, C. Fiolhais, Phys. Rev. B 46 (1992) 6671–6687.
[28] S.H. Vosko, L. Wilk, M. Nusair, Can. J. Phys. 58 (1980) 1200–1211.
[29] P. Olsson, C. Domain, J. Wallenius, Phys. Rev. B 75 (2007) 014110.
[30] A.V. Barashev, A.C. Arokiam, Philos. Mag. Lett. 86 (2006) 321–332.
[31] C. Becquart, J. Raulot, G. Bencteux, C. Domain, M. Perez, S. Garruchet, H. Nguyen, Comput. Mater. Sci. 40 (2007) 119–129.
[32] S. Chiesa, M.R. Gilbert, S.L. Dudarev, P.M. Derlet, H. Van Swygenhoven, Philos. Mag. 89 (2009) 3235–3243.
[33] V. Vitek, Cryst. Lattice Defects 5 (1974) 1–34.
[34] T. Klaver, R. Drautz, M. Finnis, Phys. Rev. B 75 (2006) 094435.
[35] J. Chojcan, J. Alloys Compd. 264 (1998) 50–53.
[36] V.T. Witusiewicz, F. Sommer, E.J. Mittemeijer, J. Phase Equilib. Diffus. 25 (2004) 346–354.
[37] E. Vincent, C. Becquart, C. Domain, J. Nucl. Mater. 351 (2006) 88–99.
[38] J. Chojcan, Hyperfine Interact. 156 (2004) 523–529.
[39] Y. Nagai, K. Takadate, Z. Tang, H. Ohkubo, H. Sunaga, H. Takizawa, M. Hasegawa, Phys. Rev. B 67 (2003) 224202.
[40] A. Moslang, E. Albert, E. Recknagel, A. Weidinger, P. Moser, Hyperfine Interact. 15 (1983) 409–412.
[41] F. Maury, A. Lucasson, P. Lucasson, Y. Loreaux, P. Moser, J. Phys.F-Met. Phys. 16 (1986) 523–541.
[42] H. Abe, E. Kuramoto, J. Nucl. Mater. 271–272 (1999) 209–213.
[43] F. Maury, A. Lucasson, P. Lucasson, P. Moser, Y. Loreaux, J. Phys.F-Met. Phys. 15 (1985) 1465–1484.

F Paper VI

Synergetic effects of Mn and Si in the interaction with point defects in bcc Fe

A. Bakaev, D. Terentyev, X. He, D. Van Neck

Journal of Nuclear Materials 455 (2014) 5

Journal of Nuclear Materials 455 (2014) 5–9

Contents lists available at ScienceDirect

Journal of Nuclear Materials

journal homepage: www.elsevier.com/locate/jnucmat

Synergetic effects of Mn and Si in the interaction with point defects in bcc Fe

A. Bakaev [a,b,c,*], D. Terentyev [a], X. He [d], D. Van Neck [b]

[a] SCK•CEN, Nuclear Materials Science Institute, Boeretang 200, Mol B2400, Belgium
[b] Center for Molecular Modeling, Department of Physics and Astronomy, Ghent University, Technologiepark 903, 9052 Zwijnaarde, Belgium
[c] Department of Experimental Nuclear Physics, Institute of Physics, Nanotechnologies and Telecommunications, St. Petersburg State Polytechnical University, 29 Polytekhnicheskaya Str., 195251 St. Petersburg, Russia
[d] China Institute of Atomic Energy, PO Box 275-51, 102413 Beijing, China

ARTICLE INFO

Article history:
Available online 5 March 2014

ABSTRACT

The interaction of Mn, Si and Cr with a vacancy and self-interstitial defects in BCC Fe has been analyzed using *ab initio* calculations. While the interaction of the considered solute clusters with a single vacancy is linearly additive, there is a considerable synergetic effect in the case of self-interstitial atoms, found to bind strongly with Mn–Si pairs. The latter therefore act as deep trapping configurations for self-interstitials. At the same time, the presence of the point defects nearby weakly attractive Mn–Si pairs significantly enhances the solute–solute binding. The revealed effects are rationalized on the basis of charge density and local magnetic moment distributions.

1. Introduction

Fe–Cr-based ferritic steels are considered as candidate materials for Generation IV and fusion installations [1]. Radiation induced degradation of high-Cr ferritic steels is an important factor limiting the temperature window for applications and the operational time span. This is why the significant efforts are dedicated to understand the origin and evolution of radiation induced defects causing the hardening [2,3].

A series of recent works, where the post irradiation experimental analysis of several Fe–Cr model alloys has been performed [4–6], reveal the numerous formation of Cr–Si clusters (also containing Ni and P but in less quantities than Cr and Si) with a number density of 10^{23} m^{-3} and mean radius of ~(1.5–2.5) nm, which cannot be classified as α′ precipitates because of too low Cr content in them. Radiation induced segregation is most likely to be responsible for their formation as the composition of Si in the considered alloys is less than 0.5 at.% i.e. far below its solubility limit in Fe at 300 °C of 10 at.%.

Although the content of Mn (well below the solubility limit in α-Fe [7] at 300 °C) and Si in high-Cr steels is rather low (up to 0.5 wt.%), atom probe studies performed in irradiated commercial ferritic–martensitic steels also revealed the formation of Mn–Si clusters (also containing Ni) [8] with a similar density and size as in [5]. The scenario by which these clusters are formed and how they contribute to hardening in high-Cr steels is so far unclear. Assuming that radiation induced/enhanced segregation is responsible for the occurrence of the above discussed solute-rich clusters, investigation of the interaction of these solutes with point defects (PDs) is the first step.

The interaction of PDs with a single solute atom (Cr, Mn, Si) was extensively studied using *ab initio* techniques in the past [9–14]. The results of these calculations can be summarized as follows:

(i) Mn exhibits attractive interaction with both vacancy and self-interstitial atom (SIA), and it forms a highly stable mixed ⟨1 1 0⟩ split dumbbell. The migration of the mixed Fe–Mn dumbbell via displacement of Mn occurs with the same migration energy [12] as that for an Fe–Fe dumbbell (i.e. 0.34 eV [15]). Hence, Mn can be transferred via SIA defects. The vacancy-Mn exchange (1.03 eV [16]) requires a higher energy barrier than the vacancy migration energy in pure Fe (i.e. 0.65 eV [17]).
(ii) Si is strongly bound to a vacancy and this binding cannot be explained on the basis of lattice-strain compensation so originates from the magnetic relaxation [13]. The migration barrier for Si-vacancy exchange (0.44 eV [16]) is lower than the vacancy migration energy in pure Fe [16]. Si is also attracted to an FeFe and FeCr ⟨1 1 0⟩ split dumbbell (henceforth dumbbell) being placed in the nearest compression site

* Corresponding author at: SCK•CEN, Nuclear Materials Science Institute, Boeretang 200, Mol B2400, Belgium. Tel.: +32 14 33 30 89.
E-mail address: abakaev@sckcen.be (A. Bakaev).

http://dx.doi.org/10.1016/j.jnucmat.2014.02.013
0022-3115/

[14]. The migration barrier for Si in the mixed dumbbell is found to be 0.52 eV [12], which is essentially higher than the SIA migration energy in bcc Fe. Si atoms are therefore expected to be transported by vacancy diffusion mechanism only.

The interaction of multiple solute-PD clusters involving Mn, Si and Cr (the latter being the major alloying element in high-Cr steels) has not been studied so far. Our recent work [14] has clearly shown that Mn and Si are the two outstanding elements entering the composition of high-Cr steels in terms of the interaction with important lattice defects such as: the self-interstitial atom, a high angle grain boundary, a ½⟨1 1 1⟩ screw dislocation core and an interstitial carbon atom. Here, we perform a dedicated *ab initio* study looking for a possible synergy between Mn, Si and Cr simultaneously interacting with PDs attempting to provide some evidence of the enhanced Mn–Si or Cr–Si binding, following the evidence from the above mentioned experiments. Given that in Fe–Cr–Mn–Si alloys the formation of mixed Fe–Cr and Fe–Mn dumbbells is energetically favourable [9,10], the interaction of the mixed SIAs with an isolated Mn or Si atom and with Mn–Si pairs is also addressed to highlight the possible trapping effect originating from the multiple solute-PD interaction.

2. Computational details

The DFT calculations were performed with the Vienna Ab Initio Simulation Package VASP [18,19] using the projector-augmented wave (PAW) potentials [20,21]. The electron exchange–correlation functional was described within the generalized gradient approximation using PW91 functionals [22], with a Vosko–Wilk–Nusair interpolation [23]. For Fe, Cr, Mn and Si pseudo potentials with 8, 6, 7 and 4 valence electrons were used, respectively. Ionic relaxation was performed using the conjugate gradient algorithm with a force convergence criterion of 0.03 eV/Å. By default all the calculations were done keeping the cell shape and volume (equal to the equilibrium volume of bulk iron) constant to provide the results fully compatible with the set of previous DFT works [9–14]. The lowest energy configurations for several PD-solutes structures were re-relaxed performing the cell shape and volume optimization to ensure the convergence of the interaction energies obtained using constant volume calculations. The energy cutoff for calculations was 300 eV which was proven to be enough to provide converged results [24]. A $3 \times 3 \times 3$ *k*-point mesh was sampled by the Monkhorst and Pack scheme for systems with 128 atoms. The lattice parameter of pure ferromagnetic Fe is taken to be 2.831 Å following the previous studies [9,14,24].

Given that we perform spin-polarized calculations in the ferromagnetic system and introduce anti-ferromagnetic impurity (i.e. Mn), one needs to be careful when selecting the initial value of the magnetic moment to ensure that the minimum energy configuration is obtained after the relaxation. In the calculations involving Mn, when its magnetic spin was not anti-ferromagnetic to Fe after the relaxation, we performed additional calculations varying the absolute value of the initial moment as some of the results turned out to be particularly sensitive to the choice of the initial magnetic moment. Below, we report only the results corresponding to the lowest energy configurations found.

To assess the interaction energy we apply the standard definition conventionally used in many similar DFT works [10]. The interaction energy of n defects $\{A_i\}$ is defined as [10]:

$$E_i(\{A_i\}) = |E(\{A_i\}) + (n-1)E_0| - \left[\sum_{i=1}^{n} E(A_i)\right], \quad (1)$$

where $E(\{A_i\})$ is the energy of the configuration containing A_i only, $E(\{A_i\})$ is the energy of the configuration with all the n defects, and E_0 refers to a configuration containing no defects or impurities, i.e. bulk bcc iron. Following this notation, a negative value implies an attractive interaction and vice versa.

To assess a possible synergetic interaction of the solutes with PDs we have applied the following strategy.

Firstly, the energetically stable (in terms of the binding energy) pairs of solute atoms (i.e. Mn–Cr, Mn–Si, Cr–Si) with the distances up to 5th nearest neighbor (nn) were identified. It is worth mentioning that alike solutes were found to strongly repel each other in the 1st and 2nd nearest neighbor positions, and the repulsion vanished in the 3rd coordination shell [10,14]. Mn–Mn is the only exception, as two substitutional Mn atoms were found to attract each other in the 1st position with the interaction energy of −0.26 eV [14]. In this work we considered cross pairs only. Then, once the attracting solute pairs were defined, we have constructed several Mn–Cr–Si clusters searching for the most favourable arrangements. After that, the configurations involving the studied PDs interacting with either a single, pair or triplet cluster were constructed and relaxed.

Using the data on the total energy of the relaxed crystals containing either the solute clusters or solute-PD clusters, we computed the interaction energy of the PDs with a single solute, pair and triplet of solutes, henceforth referred to as E_i(PD-S1), E_i(PD-S1&S2) and E_i(PD-S1&S2&S3). The synergetic effect could therefore be revealed by comparing E_i(PD-S1&S2) and E_i(PD-S1) + E_i(PD-S2) + E_i(S1–S2), where the latter is a linear superposition of the interaction energies. A schematic representation of the explored configurations involving SIAs and vacancies is given in Fig. 1 (see figure caption for detailed explanation).

3. Results

Among the considered solutes cross pairs, only Mn–Si atoms were found to bind with each other in the 1st nn, see Fig. 2. Mn–Mn solute interaction energy is shown for comparison and is taken from [14]. The resulting Mn–Si (1st nn) interaction energy is −0.09 eV. It is worth to mention that in all the studied configuration the magnetic moment of Mn was negative (opposite to the one of Fe) with the only exception of Mn–Si 2nd nn configuration where the magnetic moment of Mn in the lowest energy configuration turned out to be positive $+1.2\mu_B$. However, the difference in the total energy between configurations in which the Mn

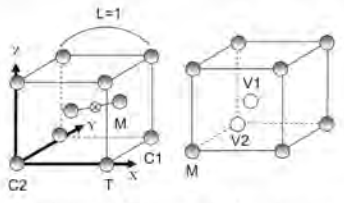

Fig. 1. The studied atomic configurations. The left figure shows non-equivalent sites around a ⟨1 1 0⟩ split dumbbell, namely: M is a position of solute in a mixed dumbbell; C1 and C2 are the sites in the compression region of the dumbbell strain field; T is the site located in the tensile region of the dumbbell strain field. The position of the second solute was defined relative to the center of the box (marked with cross) taking a lattice spacing as unity. The right figure shows the considered configurations with vacancies. M points at a position of the first solute atom. V1 and V2 are the two considered positions for the vacancy. The orientations of *X*, *Y* and *Z* axes are [1 0 0], [0 1 0] and [0 0 1], respectively, for both right and left figures.

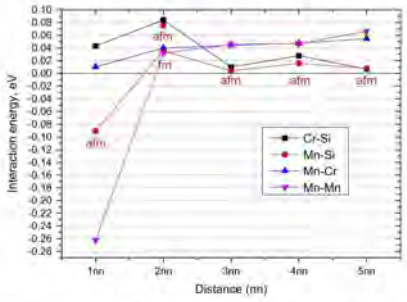

Fig. 2. Interaction energy of the solute pairs. 'fm' points to ferromagnetic (coaligned with Fe atoms) and 'afm' – to antiferromagnetic spin orientation of Mn (in the case of Mn–Si pair), respectively.

magnetic moment was co- and anti-aligned (with $\sim 2.1\mu_B$) is only 0.04 eV.

Note that according to the calculations utilizing the ultrasoft pseudopotential (USPP) method [16], the Mn–Si interaction is practically negligible in the 1st nn (−0.01 eV) and is strongly repulsive in the 2nd nn (0.33 eV) positions. However, the USPP method is believed to be less accurate when the ferromagnetic system is concerned.

Studying the triple solute clusters, we could not find an arrangement having a negative total interaction energy. Out of all studied configurations, the cluster combining Cr, Mn and Si atoms, placed in the 1st nn relative to each other (e.g. in positions Cr = 0.5;0.5;0.5, Mn = 0.0;0.0;0.0 and Si = −0.5;0.5;0.5), corresponds to the lowest energy structure with the interaction energy of +0.06 eV. Hence, the 1st nn Mn–Si and Mn–Mn pairs are the only solute arrangements revealing considerable binding.

The interaction energy for point defects (vacancy, Fe-solute and FeFe dumbbells) associated with either a single or a pair of solutes are reported in Table 1. The difference $\Delta E = E_i(\text{PD-S1\&S2}) - E_i(\text{PD-S1})$ is also reported in the table to indicate the added strength due to the inclusion of the 2nd solute. Since only the Mn–Si cross pair was found to bind in substitutional positions, it is of interest to discuss how the presence of the PDs affects its binding. E_i(PD-S1&S2) varies from −0.09 down to −0.78 eV, implying that the Mn–Si binding is enhanced by the PDs in all the configurations presented in Table 1. Finding E_i(PD-S1&S2) close to zero corresponds to no enhancement of the Mn–Si binding, while a negative value points at the binding increase. A vacancy or FeFe dumbbell inserted nearby the Mn–Si pair increases its interaction energy, respectively, by 0.25–0.34 eV and 0.17–0.39 eV, depending on a specific local arrangement. The strongest effect however is observed in the case of the interaction of Fe–Mn dumbbell with Si solute, which increases the Mn–Si binding energy by 0.78 eV. This strongly bound configuration may occur by either association of the migrating Fe–Mn dumbbell with an isolated substitutional Si, or coalescence of the migrating FeFe dumbbell with the 1st nn Mn–Si pair (resulting in the transformation of FeFe into Fe–Mn dumbbell).

The revealed strong binding of the Mn–Si pair with PDs implies that these solutes can also be considered as traps for mobile PDs. Among the PDs listed in Table 1, only the FeSi dumbbell is immobile, as the dissociation from Si followed by the migration of an FeFe dumbbell is expected [12]. The trapping effect of the Mn–Si pair is the most striking in the case of FeMn dumbbells (see E_i(FeMn + Si) in Table 1), for which the binding energy goes up to −0.78 eV, while FeFe and FeCr dumbbells are bound with an energy up to −0.41 eV. The binding of the Mn–Si pair with a vacancy is even weaker and it reaches −0.34 eV in the lowest energy configuration found.

The addition of the second solute (either Mn or Si) to a PD-S1 configuration increases the total interaction energy i.e. E_i(PD-S1&S2) in all configurations except for FeCr + Mn + Si. However, the added binding energy (ΔE) is of the order of the Mn–Si interaction energy, being ~0.1 eV, which points to the linearly additive interaction character of the PDs with the solutes. Only two

Table 1
Interaction energy of PD-solute configurations. E_i(PD-S1&S2) is the interaction energy of PD with the S1&S2 complex. E_i(PD-S1) is the interaction energy of PD with S1 solute. The interaction energy of a FeSi–S2 configuration was calculated with respect to dissociation to Fe–Fe + Si–S2 clusters. FeFe, FeCr, FeMn, FeSi and MnCr denote ⟨110⟩ dumbbell configurations of different chemistry. The second solute atom (S2) was everywhere added in the 1st nn position to the first solute atom (S1). The coordinates of the S2 are given in the 5th column, the coordinate system is provided in Fig. 1. The energy marked with "*" is obtained using the cell volume/shape relaxation where in all the other configurations cell volume/shape were kept constant.

Configuration: defect + S1 + S2	E_i(PD-S1&S2) (eV)	E_i(PD-S1) (eV)	ΔE (eV)	Equivalent positions of the S2, see Fig. 1.
FeCr + Si(C2) + Mn	−0.41	0.30	−0.11	−1.0;0.0;0.0 0.0;−1.0;0.0
FeCr + Mn(C2) + Si	−0.40	−0.30	−0.10	−1.0;0.0;0.0 0.0; −1.0;0.0
MnCr + Si	−0.29	−0.24	−0.05	−0.5; −0.5;−0.5(C2)
FeCr + Mn(C1) + Si	−0.09	−0.12	0.03	0.0;1.0;0.0 1.0;1.0; −1.0 1.0;0.0;0.0
FeCr + Mn(T) + Si	−0.08	−0.01	−0.07	0.0; −1.0;0.0
Vac + Si(1nn) + Mn	−0.34	0.31	−0.03	−1.0;0.0;0.0 0.0;0.0; −1.0 0.0; −1.0;0.0
Vac + Mn(1nn) + Si	−0.25	−0.17	−0.08	−1.0;0.0;0.0 0.0;0.0;−1.0 0.0; −1.0;0.0
FeMn + Si	−0.78 (−0.77*)	−0.59 (−0.57*)	−0.19	−0.5;−0.5;−0.5 (C2)
FeSi + Mn	−0.42	0.00	−0.42	−0.5;−0.5;−0.5 (C2)
FeFe + Mn(C) + Si	−0.39	−0.32	−0.07	0.0;1.0;0.0 1.0;0.0;0.0
FeFe + Si(C) + Mn	−0.37	−0.28	−0.09	0.0;1.0;0.0 1.0;0.0;0.0
FeFe + Mn(T) + Si	−0.17	−0.09	−0.08	1.0;0.0;0.0 0.0; −1.0;0.0

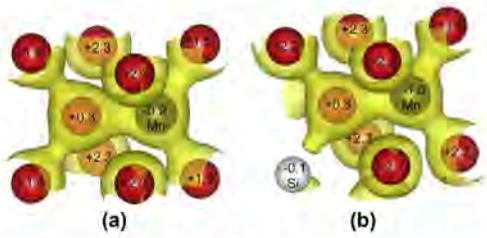

Fig. 3. Distribution of charge density around a ⟨110⟩ split dumbbell in a eight atom bcc cell. Isosurfaces of 0.55 e/Å^3 are shown. The color of the atom refers to its type: red – Fe, black – Mn, white – Si. (a) and (b) figures correspond to FeMn (⟨110⟩ dumbbell) and FeMn (⟨110⟩ dumbbell) + Si(C2) complexes, respectively. (For interpretation of the references to colour in this figure legend, the reader is referred to the web version of this article.)

configurations reveal a remarkable gain in the total energy after the addition of the second solute. These are FeMn and FeSi dumbbells placed in the vicinity of a Si or Mn atom, respectively. In those cases, ΔE is −0.19 eV and −0.42 eV, respectively.

The configuration involving the FeMn dumbbell corresponds to the lowest total energy state, therefore, we focus on its properties to explain the origin of the observed synergetic effect. To do that we have computed the local magnetic moments of all atoms and analyzed the distributions of the charge density in the two configurations, namely: FeMn dumbbell and FeMn dumbbell standing next to Si in the C2 site (see Fig. 1). The change of magnetic moments in FeMn to FeMn + Si (1nn) complexes is shown in Fig. 3 also revealing the charge density distribution. The Fe in the FeMn dumbbell is bonded with two adjacent Fe atoms (see Fig. 3a). The substitution of Fe by Si results in the shift of position of the Fe atom (forming the dumbbell) down by $-0.016 \times a_0$ towards Si atom. That causes a slight on site rotation of the dumbbell axis. At the same time, the introduction of diamagnetic Si instead of ferromagnetic Fe leads to a strong redistribution of the charge density (see Fig. 3b), which apparently causes the recovery of the magnetic moments of the Fe atoms located in the two compression sites (C1 and the site above Si). The corresponding magnetic moments went up from 1.5 and 1.8 to 2.2μ_B. Note that magnetic moments of Mn and other Fe atoms surrounding the defects practically did not change. Hence, the rearrangement of the magnetic states of two Fe atoms, perturbed by the introduction of diamagnetic Si was most likely the reason for the synergetic effect resulting in the strong binding of Mn–Si-dumbbell complex.

Among the configurations listed in Table 1, there is also one in which the synergetic interaction of the FeCr dumbbell and the 1st nn Mn–Si pair resulted in the reduction of the total binding energy. That is the case, when Mn is placed in the compression site next to Cr atom in the dumbbell position. We assign this effect to the antiferromagnetic Cr–Mn repulsion, which is similar to the well known Cr–Cr repulsion in Fe, attributed to the magnetic frustration [25].

The above discussed examples suggest that the interaction of a self-interstitial with the Mn–Si pair is foremost determined by the magnetic contribution rather than strain relaxation. To validate this hypothesis we reveal the effect of cell shape/volume relaxation on the distribution of electronic charge density and magnetic moments in the case of an isolated Mn, Mn–Mn and Mn–Si pairs, and 1st nn Mn–Si pair interacting with the FeFe dumbbell (see Fig. 3a). We took the relaxed (at constant volume) configurations and relaunched a set of calculations optimizing volume and shape of the cell shape but varying the initial magnetic moment on Mn atom(s) from −5 to +5μ_B with an increment of 1μ_B. The reference value of the total energy of the crystal containing a ⟨110⟩ FeFe dumbbell was also computed to calculate the resulting interaction energy. For the studied configurations, the cell shape/volume relaxation has only a virtual effect on the magnetic moment of Mn and surrounding Fe atoms. The strongest deviation of less than 0.03μ_B was observed for the 1st nn Mn–Si pair. The values of E_i(FeMn–Si) and E_i(FeFe–Mn–Si) shifted down by 0.01 and 0.02 eV, respectively, which is a negligible value. This additional calculations prove adequateness of the constant volume/shape relaxation conditions for the selected problem and confirm the robustness of the results given in Table 1.

4. Conclusions

To summarize, we have studied the interaction of point defects in BCC Fe with Mn–Si and Mn–Si–Cr solute clusters using the spin polarized DFT calculations. The goal of the study was to reveal solute–solute cross-pair interaction and possible synergetic effects in the interaction of solute–defect–solute complexes. Based on the obtained results we draw the following conclusions:

(i) Among the studied solutes only Mn and Si form a weakly stable cross pair in the 1st nn position. This pair exhibits attractive interaction with a vacancy, FeFe and different mixed ⟨110⟩ dumbbells.
(ii) Several configurations involving Mn, Si and self-interstitial atoms have been relaxed optimizing volume/cell shape. The re-assessed interaction energies and distribution of magnetic moments near the defected zone revealed negligible deviations, proving appropriateness of the constant volume calculations.
(iii) The interaction energy for a self-interaction with the Mn–Si pair varies from ~0.1–0.8 eV and strongly depends on the local solute arrangement. The strongest binding was observed between an FeFe dumbbell and the 1st Mn–Si pair, which amounted to 0.78 eV. An FeCr dumbbell also exhibits significant binding energy to the Mn–Si pair, which is 0.4 eV. These results suggest that the activation energy for long-range FeFe dumbbell migration in bcc Fe containing Mn and Si, taken as a sum of the migration energy (0.34 eV [15]) and the binding energy, exceeds 1 eV. In the case of the FeCr dumbbell (known to be thermally stable defect), its activation energy for the long-range migration increases up to 0.63 eV (taking 0.23 eV as the migration energy for the FeCr dumbbell [26]).
(iv) The added binding energy due to the insertion of Si next to the FeMn dumbbell is 0.2 eV. Based on the analysis of the charge density maps and local magnetic moments, the origin

of the strong Mn–Si-self interstitial interaction is attributed to the compensation of the magnetic moments of Fe atoms surrounding the dumbbell, occurring due to the perturbation caused by the insertion of diamagnetic Si in ferromagnetic Fe matrix.

(v) The interaction of the Mn–Si pair with a vacancy is less strong than with a self-interstitial atom. The strongest trapping configuration results in the binding energy of 0.34 eV raising the long-range vacancy migration barrier up to 1 eV. This suggests that the trapping of self-interstitials and vacancies at Mn–Si pairs is approximately of the same strength. However, the binding of vacancies to interstitial carbon atoms is even stronger [27].

Following the above conclusions, we would like to put forward that the synergetic interaction of Mn–Si with point defects (not involving Cr), might be responsible for the nucleation of radiation-induced solute-rich complexes associated with growing clusters of point defects. Identification of the role of interstitial carbon and other solutes such as e.g. Ni and P is however needed to complete a complex picture on the elementary interaction of point defects with solutes in Fe-based ferritic steels.

Acknowledgements

This work, supported by the European Commission under the Contract of Association between EURATOM/SCK-CEN, was carried out within the framework of the European Fusion Development Agreement. We are grateful to the ICT Department of Ghent University for partial support of this work. Part of calculations has been performed at HPC Julich within the 'SORT' Project. The research was partly supported by the FWO grant.

References

[1] R.L. Klueh, A.T. Nelson, J. Nucl. Mater. 371 (2007) 37–52.
[2] L. Malerba, G. Bonny, D. Terentyev, E.E. Zhurkin, M. Hou, K. Vörtler, K. Nordlund, J. Nucl. Mater. 442 (2013) 486–498.
[3] L. Malerba, M.C. Marinica, N. Anento, C. Björkas, H. Nguyen, C. Domain, F. Djurabekova, P. Olsson, K. Nordlund, A. Serra, D. Terentyev, F. Willaime, C.S. Becquart, J. Nucl. Mater. 406 (2010) 19–38.
[4] V. Kuksenko, C. Pareige, P. Pareige, J. Nucl. Mater. 432 (2013) 160–165.
[5] V. Kuksenko, C. Pareige, C. Genevois, F. Cuvilly, M. Roussel, P. Pareige, J. Nucl. Mater. 415 (2011) 61–66.
[6] V. Kuksenko, C. Pareige, P. Pareige, J. Nucl. Mater. 425 (2012) 125–129.
[7] V.T. Witusiewicz, F. Sommer, E.J. Mittemeijer, J. Phase Equilib. Diffus. 25 (2004) 346–354.
[8] Z. Jiao, G.S. Was, Acta Mater. 59 (2011) 4467–4481.
[9] T. Klaver, P. Olsson, M. Finnis, Phys. Rev. B 76 (2007) 214110.
[10] P. Olsson, T.P.C. Klaver, C. Domain, Phys. Rev. B 81 (2010) 054102.
[11] E. Vincent, C.S. Becquart, C. Domain, Nucl. Instrum. Methods Phys. Res., Sect. B 228 (2005) 137–141.
[12] E. Vincent, C. Becquart, C. Domain, J. Nucl. Mater. 359 (2006) 227–237.
[13] O.I. Gorbatov, P.A. Korzhavyi, A.V. Ruban, B. Johansson, Y.N. Gornostyrev, J. Nucl. Mater. 419 (2011) 248–255.
[14] A. Bakaev, D. Terentyev, G. Bonny, T.P.C. Klaver, P. Olsson, D. Van Neck, J. Nucl. Mater. 444 (2014) 237–246.
[15] C.-C. Fu, F. Willaime, P. Ordejón, Phys. Rev. Lett. 92 (2004) 175503.
[16] E. Vincent, C. Becquart, C. Domain, J. Nucl. Mater. 351 (2006) 88–99.
[17] C. Domain, C. Becquart, Phys. Rev. B 65 (2002).
[18] G. Kresse, J. Hafner, Phys. Rev. B 47 (1993) 558–561.
[19] G. Kresse, J. Furthmuller, Phys. Rev. B 54 (1996) 11169–11186.
[20] P.E. Blochl, Phys. Rev. B 50 (1994) 17953–17979.
[21] G. Kresse, D. Joubert, Phys. Rev. B 59 (1999) 1758–1775.
[22] J.P. Perdew, J.A. Chevary, S.H. Vosko, K.A. Jackson, M.R. Pederson, D.J. Singh, C. Fiolhais, Phys. Rev. B 46 (1992) 6671–6687.
[23] S.H. Vosko, L. Wilk, M. Nusair, Can. J. Phys. 58 (1980) 1200–1211.
[24] P. Olsson, C. Domain, J. Wallenius, Phys. Rev. B 75 (2007) 014110.
[25] T. Klaver, R. Drautz, M. Finnis, Phys. Rev. B 75 (2006) 094435.
[26] P. Olsson, J. Nucl. Mater. 386–388 (2009) 86–89.
[27] C. Domain, C. Becquart, J. Foct, Phys. Rev. B 69 (2004) 144112.

G Paper VII

Radiation-induced strengthening and absorption of dislocation loops in ferritic Fe-Cr alloys: the role of Cr segregation

D. Terentyev and A. Bakaev

Journal of Physics: Condensed Matter 25 (2013) 265702

IOP PUBLISHING JOURNAL OF PHYSICS: CONDENSED MATTER
J. Phys.: Condens. Matter **25** (2013) 265702 (11pp) doi:10.1088/0953-8984/25/26/265702

Radiation-induced strengthening and absorption of dislocation loops in ferritic Fe–Cr alloys: the role of Cr segregation

D Terentyev[1] and A Bakaev[1,2]

[1] SCK•CEN, Nuclear Material Science Institute, Boeretang 200, B-2400 Mol, Belgium
[2] Centre for Molecular Modelling, Ghent University, Technologiepark 903, B-9052 Zwijnaarde, Belgium

E-mail: dterenty@sckcen.be

Received 17 January 2013, in final form 20 May 2013
Published 12 June 2013
Online at stacks.iop.org/JPhysCM/25/265702

Abstract
The understanding of radiation-induced strengthening in ferritic FeCr-based steels remains an essential issue in the assessment of materials for fusion and fission reactors. Both early and recent experimental works on Fe–Cr alloys reveal Cr segregation on radiation-induced nanostructural features (mainly dislocation loops), whose impact on the modification of the mechanical response of the material might be key for explaining quantitatively the radiation-induced strengthening in these alloys. In this work, we use molecular dynamics to study systematically the interaction of dislocations with $1/2\langle 111\rangle$ and $\langle 100\rangle$ loops in all possible orientations, both enriched by Cr atoms and undecorated, for different temperatures, loop sizes and dislocation velocities. The configurations of the enriched loops have been obtained using a non-rigid lattice Monte Carlo method. The study reveals that Cr segregation influences the interaction mechanisms with both $1/2\langle 111\rangle$ and $\langle 100\rangle$ loops. The overall effect of Cr enrichment is to penalize the mobility of intrinsically glissile $1/2\langle 111\rangle$ loops, modifying the reaction mechanisms as a result. The following three most important effects associated with Cr enrichment have been revealed: (i) absence of dynamic drag; (ii) suppression of complete absorption; (iii) enhanced strength of small dislocation loops (2 nm and smaller). Overall the effect of the Cr enrichment is therefore to increase the unpinning stress, so experimentally 'invisible' nanostructural features may also contribute to radiation-induced strengthening. The reasons for the modification of the mechanisms are explained and the impact of the loading conditions is discussed.

(Some figures may appear in colour only in the online journal)

1. Introduction

Dislocation loops are the primary signature of radiation damage in commercial ferritic–martensitic and austenitic steels and model alloys at temperature $\sim(0.3–0.6)T_M$, where T_M is the melting point [1–3]. These defects cause strengthening by obstructing dislocation motion, if the deformation is mediated by dislocation glide. In turn, the obstruction of dislocation motion (strengthening) leads to embrittlement [4], while the ability of dislocations to absorb dislocation loops when unpinning is believed to be the reason for the formation of clear channels [5–7], as suggested by post-deformation investigations. The presence of clear bands, on the other hand, is known to cause plastic flow localization and non-homogeneous deformation, and lead to loss of ductility as a result.

For the above reasons, the dislocation–loop interaction is being intensively studied both experimentally and theoretically. In particular, recently the numerical modelling of this interaction has become a very active field, where two major complementing techniques are applied, namely the discrete dislocation dynamics (DDD; e.g. [8]) and classical molecular dynamics (MD; e.g. [9]) techniques. The direct dislocation–loop interaction involves the atomic rearrangement of dislocation cores and other atomic-scale processes, like the formation of new junctions, their

movement and their unzipping. MD simulations, being inherently atomistic, are especially efficient to use to study dislocation-core effects and defects of nanometric sizes, which are hardly or not at all resolvable in transmission electron microscopy (TEM).

The MD studies performed so far on pure BCC Fe [10] and on FCC Ni [9] and Cu [11] revealed a number of interaction mechanisms resulting in the complete or partial absorption and transformation of dislocation loops. The properties of junctions, or reaction segments (RS), that are formed in the direct dislocation–loop interaction are especially important because they determine the reaction pathway, the unpinning stress and the outcome product [12, 13]. In turn, environmental variables such as temperature and the loading conditions determining the dislocation velocity affect the mobility of the RS and thus indirectly control the interaction mechanism [14, 15].

Real materials (even pure ones) always contain a certain amount of impurities, while alloys contain alloying elements expressly introduced to provide specific properties. These, under irradiation, *a priori* may segregate to lattice imperfections, e.g. dislocation loops, and form so-called 'decorated' loops. By 'decoration', we mean the presence of high concentrations of interstitial impurities or substitutional solute atoms in the strained region around the loop. Recently, the study of the interaction of carbon-decorated $1/2\langle 111\rangle$ loops with dislocations in BCC Fe revealed that the deposition of atoms of this element at the edge of a loop considerably increases the critical stress required for dislocation unpinning [16]. The reasons for the strengthening effect were attributed to the modification of the dislocation–loop interaction mechanism. Importantly, it has been recognized that the modification of the interaction mechanism also applies for small loops (1 nm size, i.e. unresolvable in TEM), thereby making them non-negligible obstacles for dislocations. In contrast, undecorated loops of 1 nm size and below are athermally absorbed on a dislocation line, via flipping [10]. This points to a possible contribution of 'invisible' damage to the net strengthening, which has been suggested to exist at least in ferritic steels [4].

Unlike for pure metals, for concentrated model alloys as well as ferritic–martensitic and austenitic steels, beside the possible decoration with interstitial impurities like C, the segregation of Cr, Ni and other alloying elements is known to occur under irradiation (see e.g. [17]). In particular, the segregation of Cr on both $\langle 100\rangle$ and $1/2\langle 111\rangle$ dislocation loops is a well-established phenomenon, which has been reported by different independent researchers for different grades of Fe–Cr steels and model alloys [18–21]. Recently, an indisputable proof of the segregation of Cr to dislocation lines and dislocation loops was obtained using tomography atom probe (TAP) techniques applied to examine an irradiated high-Cr ferritic–martensitic steel [22]. Hence, it is important to assess the influence of Cr enrichment on the pinning strength of loops and on their ability to be absorbed by moving dislocations.

Here, we perform an atomistic study to investigate the impact of Cr segregation at loops on the interaction with dislocations. In particular, we consider two kinds of interstitial dislocation loops: $1/2\langle 111\rangle$ and $\langle 100\rangle$, which are typically observed under neutron irradiation at elevated temperature in the high-Cr steels and other Fe–Cr model alloys. We put emphasis on the interaction with edge dislocations, since they are known to be more efficient means for loop absorption and removal as compared to screw dislocations. In addition, the contribution to the plastic flow is comparable for edge and screw dislocations at room temperature and above it. We show that Cr enrichment modifies the interaction mechanism for both $1/2\langle 111\rangle$ and $\langle 100\rangle$ loops. We explain the reasons and explore the effect of loop size, test temperature and dislocation velocity on the extra strengthening caused by solute segregation.

2. Computational details

In order to study the equilibrium arrangement of Cr atoms around $1/2\langle 111\rangle$ and $\langle 100\rangle$ dislocation loops, metropolis Monte Carlo (MMC) simulations were used. The case of Fe–9 at.%Cr at 600 K was considered as representative of the Cr contents and irradiation temperatures of technological interest. Then the MMC crystals were embedded in a large MD sample in which the dislocation had been created and relaxed in advance. The crystal was relaxed again, thermalized at the desired temperature, corresponding to the temperature of the mechanical test, and finally loaded to study the interaction of the moving dislocation with the defect of interest.

To describe the Fe–Fe, Fe–Cr and Cr–Cr interactions, we applied the two-band model potential developed in [23], which was extensively exploited in the past few years to model properties of point defects and dislocations, as well as to describe primary damage and phase separation in the Fe–Cr system. The Fe–Fe part of this potential is the one derived by Ackland *et al* in 2004 [24], which is significantly improved compared to previous Fe–Fe many-body potentials, as far as the description of self-interstitial defects and dislocation properties is concerned. Details on MD and MMC tools and studies are provided below.

2.1. MD simulations

To study dislocation–loop interaction we employed the simulation algorithm developed by Osetsky and Bacon [25]. The principal axes x, y and z of the body-centred cubic (BCC) crystal simulation box were oriented along the $[111]$, $[\bar{1}\bar{1}2]$ and $[1\bar{1}0]$ directions, respectively. The initially straight edge dislocation, with $(1\bar{1}0)$ slip plane x–y, was created along the y direction in pure Fe and had Burgers vector (BV) $1/2[111]$ parallel to the x axis. Periodic boundary conditions were applied along the x and y directions. Along z, the box was divided into three parts: the upper and lower parts consisted of several atomic planes in which atoms were rigidly fixed in their original position relative to each other, whereas atoms in the inner region were free to move during the MD runs. A glide force on the dislocation was generated by displacing the upper rigid block in the x direction, which corresponds to applying simple shear strain e_{xz}. The corresponding

resolved shear stress induced by the applied deformation was calculated as $\sigma_{zx} = F_x/A_{xy}$, where F_x is the total force in the x direction on the lower rigid block due to the atoms in the inner region, and A_{xy} is the xy cross-section area of the box. The size of the inner region of the MD box was 101×3, 30×6 and 25×2 non-equivalent atomic planes along x, y and z (or $25 \times 21 \times 10$ nm^3), respectively. Such crystallites are large enough for considering the interaction of the dislocation with a loop of size up to 5 nm (350 self-interstitial atoms, SIAs), as shown in our previous studies [15, 26, 27]. During an MD run, the dislocation line and dislocation loop were monitored using atomic disregistry analysis, coupled with structural nearest-neighbour analysis (see [12]), as well as by selecting atoms with high potential energy. Statistical averaging was performed over every 250 steps to reveal the atoms belonging to the dislocation core. The latter procedure allowed the identification of the interaction mechanism even at relatively high temperature despite significant thermal noise.

MD simulations were started by initializing the velocity of the relaxed atoms according to Maxwell's distribution for the desired simulation temperature, T, chosen to be in the range of 150–800 K. After thermalization for 10^3 steps, a load was applied at a fixed strain rate. Three different strain rates were applied, resulting in dislocation velocity (v_d) ranging from 4 up to 20 m s^{-1}. Most of the calculations were performed at $v_d = 10$ m s^{-1}. To achieve the desired v_d, the strain rate to be applied, $\dot{\varepsilon}$, was determined according to Orowan's law $\dot{\varepsilon} = \rho b v_d$, where ρ is the dislocation density, equal to $1/(L_X \times L_Z)$, and b is the BV. The integration of Newton's equations was performed using a constant time step (2 fs) in the microcanonical *NVE* ensemble, in which number of particles, system volume and total energy are conserved if the work of external forces is taken into account. No temperature control was applied to limit temperature increase during the simulation, as this was negligible in comparison with the simulated temperature. Every interaction geometry has been simulated ten times at each temperature to account for temperature fluctuation effects. The standard errors are reported everywhere with the average values of the unpinning stress.

2.2. MMC simulations

Following our previous work [31, 32], the MMC simulations were done by sampling within the isobaric–isothermal (*NPT*) statistical ensemble, i.e. with number of particles N, pressure P and temperature T being constant. Three kinds of trials were included in the sampling, namely: (i) random displacement of all atoms from their positions (in this trial, lattice relaxation and vibrational entropy are accounted for); (ii) swapping of atoms of different types; (iii) overall change of the volume of the simulation box to maintain the desired pressure. The calculation is stopped once the total energy of the crystal converges to a constant value (with the tolerance of 10^{-3} eV/atom). The MMC sampling was performed in a cubic box of size $8 \times 8 \times 8$ nm^3 containing ~50 000 atoms arranged in a BCC structure, with the principal axes oriented in the same manner as in the MD simulation (see section 2.1), and with an initial random distribution of Cr atoms. The crystals contained interstitial dislocation loops with BV $1/2\langle 111\rangle$ and $\langle 100\rangle$. The former were of circular shape and the latter had square shape with sides oriented along $\langle 001\rangle$ and $\langle 010\rangle$ directions, as found in experiments [33, 34]. Three different sizes were considered for $1/2\langle 111\rangle$ loops, namely 60, 169 and 350 SIAs, which correspond to loop diameters (D_L) of 2, 3.5 and 5 nm, respectively. Only one size of $\langle 100\rangle$ loops was considered, namely 169 SIAs, i.e. slightly above 3 nm. The interstitial dislocation loops of size D_L with BV $= 1/2\langle 111\rangle$ were created by selecting and cutting three circular non-equivalent $\{111\}$ planes around a desired point in the MMC crystal. Three platelets of $\langle 111\rangle$ crowdions with initial spacing of $0.4 \times a_0$ were introduced there instead and relaxed using the conjugate gradient method.

3. Results

3.1. Local Cr arrangement around dislocation loops

Our previous MMC study, carried out on Fe–10 at.%Cr, showed that both $\langle 100\rangle$ and $1/2\langle 111\rangle$ interstitial dislocation loops of 6 nm diameter exhibit Cr enrichment around their perimeters [31]. The degree of enrichment depends on the simulation temperature and Burgers vector and it appears to be higher for the $\langle 100\rangle$ loop. The degree of enrichment (x_{Cr}) was calculated as the concentration of Cr among the atoms belonging to the edge of the dislocation loop (using structural analysis). It was found that, at 600 K, x_{Cr} is about 25–40 at.%Cr. Here, we considered smaller loops (2–5 nm); however, the results obtained at 600 K for x_{Cr} are close to those in [31], implying that the size of the loop does not significantly influence the enrichment level for the loop density studied. Overall, we could see that x_{Cr} varied from 25 up to 50 at.%Cr. Even though some loose Cr clusters were formed, the composition of Cr in these clusters was too low for considering them as equilibrium α' particles. The Cr decoration was limited to the tensile region of the loop strain field, consistently with the oversized nature of Cr solute atoms in BCC iron. For $1/2\langle 111\rangle$ loops, the enrichment degree was found to increase with loop size. This can be explained by the fact that the sides of relatively small loops do not exhibit fully pronounced dislocation-core structure. Even though, as we already mentioned, there is some variation of x_{Cr} in different loops, we found that statistically (in equivalent MD runs using different initial seeds for velocity distribution) these variations essentially do not affect the average unpinning stress measured in ten runs. Hence, to remain concise we consider only one level of enrichment, 35 at.%Cr.

3.2. Interaction mechanisms with undecorated loops

Before describing the effect of Cr enrichment on the mechanism of interaction between a loop and a moving edge dislocation, it is useful to recall the main features of this mechanism as revealed in pure Fe in our previous studies [10, 12–15, 27]. The average unpinning stress and standard errors are displayed in figures 1(a) and (b) for, respectively, a $\langle 100\rangle$ and a $1/2\langle 111\rangle$ loop interacting with an edge dislocation. All loops

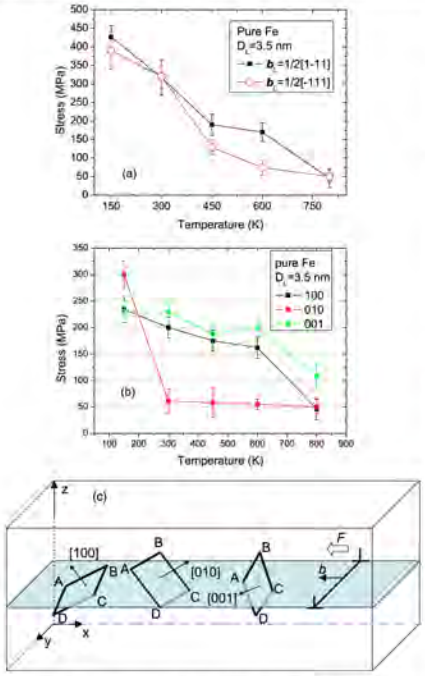

Figure 1. Average unpinning stress calculated in the reactions with (a) $1/2\langle 111\rangle$ and (b) $\langle 100\rangle$ loops, $D_L = 3.5$ nm, undecorated, $v_D = 10$ m s^{-1}. (c) Geometry of interactions considered. The sketch illustrates the orientation and position of the loops before interaction with the positive edge dislocation line moving in a $(\bar{1}10)$ plane in a $[1\bar{1}1]$ direction. The square loops have sides along $\langle 100\rangle$ directions and their centres lie on the glide plane. x, y and z in (c) correspond to $[111]$, $[11\bar{2}]$ and $[\bar{1}10]$ crystallographic directions.

considered contained 169 SIAs and their centres were placed at the dislocation glide plane.

In the case of $1/2\langle 111\rangle$ loops, two out of four possible geometries, namely $\boldsymbol{b}_L = 1/2[\bar{1}11]$ and $\boldsymbol{b}_L = 1/2[1\bar{1}1]$, represent the case where the BV is inclined to the dislocation glide plane (DGP). The other two BVs are parallel to the DGP. If the BV of the loop coincides with the BV of the dislocation, the loop is dragged/pulled by the dislocation and it does not enter any direct dislocation reaction. As a result, such interaction causes very little or no resistance to the dislocation glide, because the migration energy of a $1/2\langle 111\rangle$ loop is very small (0.05 eV) so its glide is practically an athermal process [35]. The case of $\boldsymbol{b}_L = 1/2[111]$ and the loop intersecting the glide plane has not been studied so far and we present results here for the first time. The dynamic drag of the loop placed below the DGP was studied already [35] and it was shown that the interaction process is very similar to that for a $1/2[111]$ loop, i.e. an easy glide of the loop together with a dislocation.

Unlike the case of dynamic drag, the strengthening due to the loops with the BVs inclined to the DGP is significant. Here, we recall the basic steps of the interaction mechanisms for two configurations which have already been thoroughly studied in [10, 14, 36].

(a) *Interaction details for* $\boldsymbol{b}_L = 1/2[1\bar{1}1]$: Under the attractive interaction force, the dislocation makes contact with the loop to form an RS of $[010]$ type; the RS, being sessile in the DGP, pins the dislocation, which bows out under increasing stress. The subsequent reaction path depends on temperature and dislocation velocity. At low temperature and high dislocation velocity, a full screw dipole is drawn first and then closes, so the dislocation unpins leaving the partially absorbed $1/2[\bar{1}11]$ loop behind. High temperature and low dislocation velocity conditions favour the glide of the RS over the loop surface, thereby incorporating the loop onto the dislocation line as a double superjog, according to the reaction $1/2[1\bar{1}1]+[010] = 1/2[111]$. The atom-core visualizations of this interaction processes are given, respectively, in figures 7 and 5 from [10].

(b) *Interaction details for* $\boldsymbol{b}_L = 1/2[\bar{1}11]$: Overcoming the initial repulsive interaction, the dislocation makes contact with the loop and an $[100]$ RS is formed; the latter pins the dislocation and, as in the above-described case, the result can be either the complete absorption of the loop or the dipole closure. Even though the mechanism of complete absorption is more involved in this case (see [14, 36] for details), it activates at approximately the same loading conditions as in the case of the loop with $\boldsymbol{b}_L = 1/2[1\bar{1}1]$. This is why the critical shear stresses are similar for the two loops over a wide temperature range.

The interaction with $\langle 100\rangle$ loops is a more involved process and, as follows from figure 1(b), the dependence of the critical stress, τ_C, on temperature is rather steep for $\boldsymbol{b}_L = [010]$, while there is a smooth descent for the two other geometries. The reason is the different interaction mechanisms and hence different thermal activation behaviours. Below we describe in more detail the interaction mechanism for each of these of loops and its dependence on temperature, following the earlier study [12] where details and MD snapshots are presented. The sketch of the interaction geometries considered is presented in figure 1(c).

(c) *Interaction details for* $\boldsymbol{b}_L = [100]$: The dislocation line is initially attracted by the loop and forms a $1/2[\bar{1}11]$ segment on contact; this RS pins the dislocation. At low temperature the unpinning requires the formation of a screw dipole, cross-slip of the dislocation arms along the two sides of the loop and finally their closure. The so-called 'bi-loop' formed by a set of $[100]$, $1/2[\bar{1}11]$ and $1/2[111]$ segments is left behind. The visualization of this interaction process is given in figure 6 from [12].

With increasing temperature, an upper segment of $[100]$ loop (segment 'AB' on figure 1(c)) is seen to 'flip' on the glide plane. This 'flip' movement can be interpreted as dissociation of a $[100]$ segment into $1/2[\bar{1}\bar{1}\bar{1}]$ and $1/2[\bar{1}11]$ segments. This reaction is unfavourable and therefore a system must

overcome a certain barrier. This is why such a 'flip' is seen only at high temperature. At intermediate temperatures, the flip occurs rarely and at relatively high applied stress. As a result of this dissociation, the $1/2[\bar{1}\bar{1}\bar{1}]$ segment annihilates with the pre-existing $1/2[111]$ segment, while the $1/2[\bar{1}11]$ segment displaces under the dislocation glide plane. Thus, the remaining lower half of the [100] loop pins the dislocation. With increase of the stress, the [100] segment propagates downwards reacting with the $1/2[\bar{1}11]$ segment and forming a glissile superjog on the dislocation line (in exactly the same manner as in the reaction with a $1/2[\bar{1}11]$ loop).

The flip of an upper loop segment is found to enhance with temperature. Important to note for this interaction geometry is that the flip is not favoured due to the elastic repulsion between an upper segment of a dislocation loop and a dislocation line, while in the configuration with $\boldsymbol{b}_L = [010]$, the same flip movement is favourable because the two segments attract each other.

(d) *Interaction details for* $\boldsymbol{b}_L = [010]$: On the contact with the dislocation, the upper half of the loop changes into the $1/2[1\bar{1}1]$ orientation, and this part immediately slips under the DGP. The lower part of the loop now acts as a lock, which glides across the part with $\boldsymbol{b} = 1/2[1\bar{1}1]$, thereby converting the whole loop into a double superjog with $1/2[111]$ orientation. The last step of the reaction is just the same as in the reaction with a $1/2[1\bar{1}1]$ loop. The details of this process are shown in figure 2 in [12]. The critical stress for a [010] loop is, however, much smaller because the actual size of the loop to be swept by the [010] segment is much larger in the case of the $1/2[1\bar{1}1]$ loop. The difference comes from the fact that $1/2\langle 111\rangle$ loops are freely glissile and therefore adjust the optimum interaction geometry to the approaching dislocation, while $\langle 100\rangle$ loops are immobile (at least in the MD timeframe); therefore its position with respect to the DGP will determine the point of the junction. As a result, the high resistance of the [010] loop is observed only at low temperature, at which the [010] segment has low mobility. Once temperature reaches 300 K and above, the absorption proceeds immediately after the flip, and the critical stress of ~50 MPa is needed only to accommodate the absorbed loop into a glissile superjog.

(e) *Interaction details for* $\boldsymbol{b}_L = [001]$: The dislocation approaches the loop, and short $1/2[11\bar{1}]$ segments are created at the two corners (lying in the dislocation glide plane; see figure 1(b) from [12]) so the outer arms of the dislocation are pinned at the corners linked by the $1/2[111]$ segment lying across the loop surface. Further load leads to the formation of a screw dipole. In the reaction at 150 K, the loop is finally sheared. In contrast, at $T = 300$ K one of the screw arms double cross-slips (i.e. up and down along 'AD' and 'DC' sides; see figure 1(c)), thereby converting the lower part of the loop into the $1/2[\bar{1}11]$ orientation. The configuration thereby formed is stable and immobile (because of the upper part with [001] orientation). Even though the interaction mechanism changes with temperature, the unpinning of the dislocation still requires the drawing of the screw dipole, and therefore τ_C stays nearly constant in the temperature range 150–600 K. At $T = 800$ K, however, the complete absorption of the loop is possible, via the flip of the upper part and via sequential interaction with the $1/2[111]$ and $[00\bar{1}]$ segments of the dislocation and the loop, respectively. One can also see the decrease of the critical stress.

Summing up, one can state that the direct interaction between a dislocation and loop involves the process of formation of mixed segments (following Frank's rule and respecting the conservation of the Burgers vector), the formation of a screw dipole, cross-slip/glide of the screw segments and glide of the reaction segments in the loop habit plane. As discussed in [13], the probability for absorption increases with temperature, since the latter activates the movement of the RS over the loop surface, which is the necessary condition for absorption. Correspondingly, the absorption is the alternative interaction mechanism, which allows the unpinning of the dislocation at lower τ_C than in the case of the dipole closure. We now proceed with the detailed description of the interaction of a moving edge dislocation with Cr-enriched loops. In the following subsections, we will consider $\langle 100\rangle$ loops and $1/2\langle 111\rangle$ loops with BVs inclined to DGP and parallel to it.

3.3. The effect of Cr enrichment on the interaction with $\langle 100\rangle$ *loops*

An example of stress–strain loading curves for the [100] loops (both enriched and undecorated) at 150 K and 450 K is shown in figures 2(a) and (b), respectively. We can see that at low temperature the dislocation unpinning from the enriched loop occurs at higher τ_C, while at 450 K, there is almost no difference between the two loading curves. In the following we discuss how the enrichment influences the average value of τ_C (measured over ten runs at each temperature) and the corresponding unpinning mechanisms.

The resulting average critical stress in the case of the interaction with [001] and [100] loops (of 3.5 nm size) with a dislocation moving at a speed of 10 m s^{-1} is presented in figure 3. We do not present here the results for the [010] orientation, because in this orientation the Cr enrichment does not affect the interaction mechanism and the resolved stress is correspondingly the same, just as in the case of the [001] loop (figure 3(a)). In contrast, we observe a pronounced increase of τ_C for the [100] loop when enriched in the temperature range 150–300 K, while at 450 K and higher temperature the strength of the enriched [100] loop is the same as, or lower than, in the undecorated case.

Let us first discuss the reasons for the enhanced strength of the [100] loop seen in the low temperature simulations. The beginning of the interaction occurred in the same manner as in pure Fe, i.e. formation of the RS and screw dipole. However, the cross-slip movement was suppressed on the enriched loop, so that shear occurred at 150 and 300 K. The mechanism becomes identical to that for the undecorated loop at $T = 450$ K and above. This means that, eventually, cross-slip is activated, which is otherwise suppressed due to the enrichment at lower temperature. At high temperature (i.e. above 450 K), undecorated [100] loops flip into the $1/2[\bar{1}11]$ orientation while the pinned dislocation bows out. The flipping is suppressed by Cr decoration, so the enriched

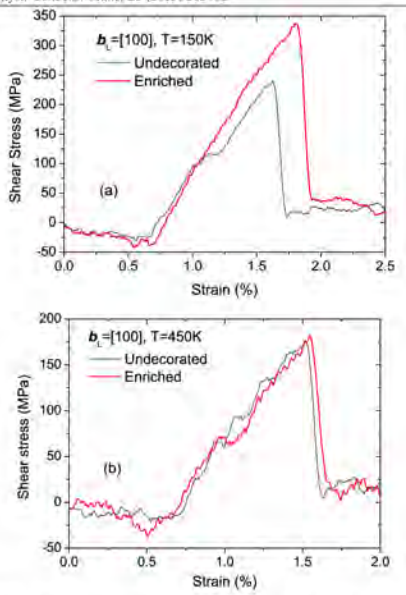

Figure 2. Stress–strain curves computed from MD simulations of the reaction with [100] loops at temperature of (a) 150 and (b) 450 K, $v_D = 10$ m s^{-1}.

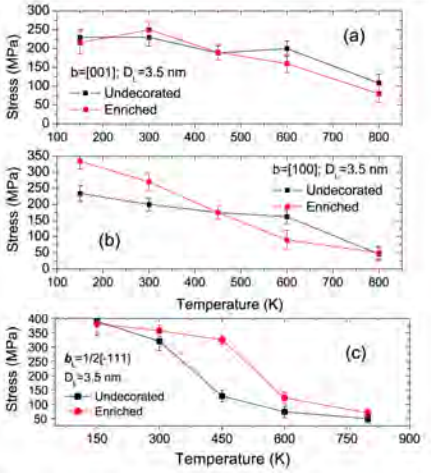

Figure 3. Average unpinning stress calculated in the reactions with (a) [001], (b) [100] and (c) $1/2[\bar{1}11]$ loops, $D_L = 3.5$ nm, $v_D = 10$ m s^{-1}.

loop exhibits the same interaction mechanism as at 450 K, which eventually proceeds at lower stress.

In the case of the [001] loop, there is no effect of Cr enrichment on τ_C; however, the interaction mechanism is affected. As in the case of the [100] loops, Cr enrichment suppresses the cross-slip of the screw dislocation along the loop side in reactions at 150 and 300 K. Yet, since these two mechanisms offer approximately the same loop strength, the $\langle\tau_C\rangle$ values are similar for the decorated and undecorated loops. Above 450 K, thermal activation helped to overcome the resistance of the Cr cloud and the cross-slip mechanism was activated.

The mechanism of interaction with the undecorated [010] loop involved the flip of the upper part into the $1/2[1\bar{1}1]$ orientation on contact with the dislocation line. Apparently, this is energetically a strongly favourable process and it is not suppressed by the enrichment. Once the flip occurs, the upper part slides down leaving the Cr cloud and therefore the enrichment does not play any role in the remaining interaction process.

3.4. The effect of Cr enrichment on the interaction with $\langle\bar{1}11\rangle$ loops with BVs inclined to the dislocation glide plane

The effect of Cr enrichment on the interaction with the 3.5 nm loops with $\boldsymbol{b} = 1/2[\bar{1}11]$ has already been reported in our preliminary study [37]. It was found that the absorption of the loop is suppressed and the corresponding critical stress rises in the temperature range 300–600 K for the dislocation velocity 10 m s^{-1}. The suppression of the absorption reaction by the enrichment was determined to occur due to: (i) freezing of the dislocation loop in its original habit plane, thus delaying the propagation of the [100] reaction segment over the loop surface; and (ii) energetically unfavourable transformation of the $1/2[\bar{1}11]$ into $1/2[111]$ occurring as the [100] RS advances.

The resulting $\langle\tau_C\rangle$ for the $1/2[\bar{1}11]$ is shown in figure 3(c) and the results for the [100] loop containing the same number of defects and loaded in the same conditions are added for comparison. The results for the $1/2[1\bar{1}1]$ and $1/2[\bar{1}11]$ loops are very similar and therefore we do not report or discuss them separately. From figure 3(c), we see that $\langle\tau_C\rangle$ for the enriched loop is substantially higher only at intermediate test temperatures, while it is the same as for the undecorated loop tested at 150 and 800 K. At low temperature this happens because the unpinning proceeds via closure of the screw dipole (for the chosen dislocation velocity) and is therefore not affected by the enrichment. At high temperature, on the other hand, the suppression due to the Cr decoration is overcome with the help of thermal activation.

For the comparison of the effect of the enrichment of $1/2\langle111\rangle$ and $\langle100\rangle$ loops, we selected the [100] loop since this configuration showed the most prominent influence of the enrichment. The comparison given in figure 3 clearly shows that the difference in the interaction mechanisms for the undecorated $1/2[\bar{1}11]$ and [100] loops is also reflected in the case of the enriched loops. In other words: the effect of enrichment appears stronger in the reaction with $1/2\langle111\rangle$ loops than in the case of $\langle100\rangle$ loops. Thus, Cr enrichment

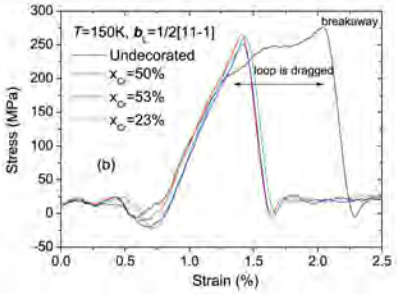

Figure 4. Stress–strain curves computed from MD simulations of the reaction with undecorated and decorated $1/2[111]$ loops, $v_D = 10$ m s^{-1} at $T = 150$ K.

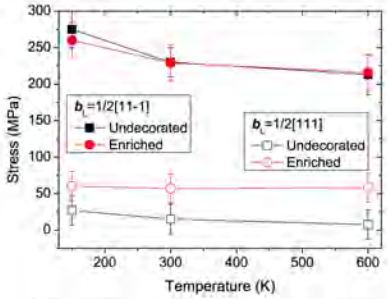

Figure 5. Average unpinning stress calculated in the reactions with $1/2[111]$ and $[111]$ loops, $D_L = 3.5$ nm, $v_D = 10$ m s^{-1}.

is more efficient in the suppression of the propagation of the $\langle 100 \rangle$ reaction segment (occurring in reactions with $1/2\langle 111 \rangle$ loops) than in the suppression of the cross-slip movement of a screw arm (occurring in reactions with $\langle 100 \rangle$ loops).

3.5. The effect of Cr enrichment on the interaction with $\langle 111 \rangle$ loops with BVs parallel to the dislocation glide plane

In the case of an undecorated $1/2[111]$ loop, the dislocation does not enter a direct reaction because the 'easily' glissile loop moves away from the approaching dislocation. The steady state flow stress, which is very low for this interaction process, depends mainly on the linear loop density and dislocation velocity and weakly on temperature. The $1/2[11\bar{1}]$ loop is the second possible configuration in which the loop BV is contained in the dislocation glide plane. If the loop does not intersect the glide plane, the dislocation drags or pushes the glissile loop without contact, as reported earlier [35]. The case where the loop intersects the dislocation glide plane has not been studied so far. The details of the interaction process are given in the appendix. Briefly, it is shown that a quadra-point junction is made on the contact and the loop is dragged along the dislocation line via the mechanism involving break-up and reconstruction of this junction. The latter controls the critical stress at which this configuration glides and remains stable. The higher the temperature, the lower the resolved flow stress at which the loop is dragged along the dislocation line. Prior to considering the effect of the enrichment, we recommend the reader to browse the appendix.

Now we move to the description of the effect of Cr enrichment on the interaction with loops having $\boldsymbol{b}_L = 1/2[111]$ and $1/2[11\bar{1}]$. Irrespective of the specific orientation of the loop, the enrichment immobilized the loops (up to the highest temperature studied), causing modification in the interaction mechanisms for both configurations.

In the case of the $1/2[11\bar{1}]$ loop, no dynamic drag was observed along the dislocation line and the dislocation unpinned as soon as the critical stress reached its critical value. Figure 4 shows the corresponding stress–strain curves for the interaction with the undecorated and enriched loops at $v_d = 10$ m s^{-1}: note that in the case of the undecorated loop a limited drag is clearly seen. Even though there is a clear effect of the enrichment on the ability to drag, the critical shear stress for the unpinning is not changed (figure 5), because the unpinning mechanism is not modified at the dislocation velocity studied. If loading tests were performed at lower dislocation velocity, thereby allowing the drag of undecorated loops, one should see an increase of τ_C for the enriched loops.

In the reaction with the enriched $1/2[111]$ loop, the dislocation approached the immobilized loop and cut it in such a way that the lower part of the loop was absorbed by the dislocation line. The details of the process are displayed in figure 6, whose caption describes the basic reaction steps. The overall effect of the enrichment in this case is the increase of τ_C, as shown in figure 5.

Summing up the results presented in this subsection, we note that the Cr enrichment suppresses the glide of a $1/2\langle 111 \rangle$ loop and thus suppresses the dynamic loop drag, leading to the modification of the interaction mechanism and overall to an increase of the critical stress.

3.6. The influence of strain rate and loop size on the impact of Cr enrichment

The effect of loop size and dislocation velocity has been separately studied in the case of the $1/2[1\bar{1}1]$ loop, since the Cr enrichment has the strongest effect in the case of $1/2\langle 111 \rangle$ loops with the BV inclined to the DGP. Figure 7 displays the added critical stress ($\langle \Delta\tau_C \rangle$) due to the Cr enrichment in the case of dislocation loops containing 60 (1.5 nm), 169 (3.5 nm) and 350 (5 nm) SIAs. For each loop we can see a clearly pronounced maximum corresponding to the temperature at which the influence of the enrichment is the strongest. The temperature corresponding to the maximum $\langle \Delta\tau_C \rangle$ increases with loop size. This originates from the fact that the enrichment enhances τ_C only if the reaction of absorption occurs for the undecorated loop. With increased loop size (and at fixed dislocation velocity), the temperature at which the absorption is triggered also goes up. As a consequence, the peak in figure 7 also shifts towards a higher

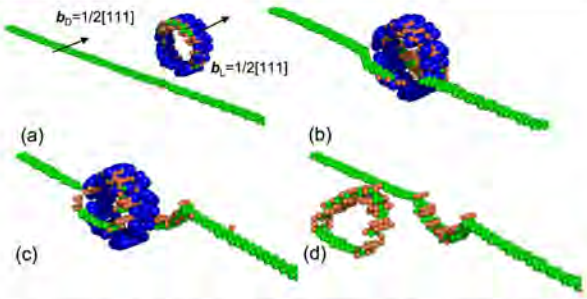

Figure 6. The atom-core visualization of the interaction of the enriched 1/2[111] loop with the dislocation at 150 K and $v_D = 10$ m s^{-1}. Blue balls show Cr atoms which are located in the loop core. (a) The model before load is applied; (b) the dislocation approaches the immobilized loop; (c) the segment substitution has occurred; (d) view of the dislocation-core atoms, showing the half-absorbed loop.

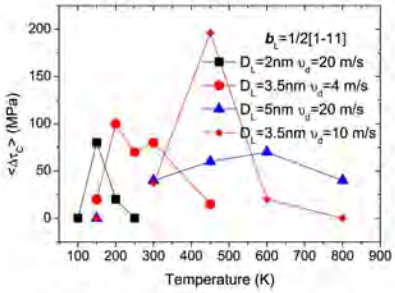

Figure 7. Increase of the average unpinning stress due to the enrichment on the 1/2[111] loop, measured in different loading conditions for different loop sizes as specified in the figure.

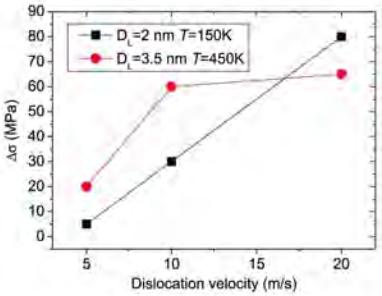

Figure 8. Increase of the average unpinning stress due to the enrichment on the 1/2[111] loop, measured as a function of dislocation velocity for 2 and 3.5 nm loops at two different temperatures, as specified in the figure.

temperature for a larger loop and higher dislocation velocity (see the result for 169-SIA loops in figure 7).

Given that the enhancement of the loop's strength originates from the suppression of the propagation of the RS, one should also expect that the added critical stress $\langle\Delta\tau_C\rangle$ will increase with dislocation velocity (since the RS does not move or moves more slowly, increased dislocation velocity would lead the screw arms to develop more efficiently, so no absorption occurs). To validate this assumption we simulated the interaction process for 60- and 169-SIA loops at 150 K and 450 K respectively, i.e. the temperature at which $\langle\Delta\tau_C\rangle$ is maximum for dislocation velocity of 10 m s^{-1}. The result is presented in figure 8 for dislocation velocity varied from 4 up to 20 m s^{-1}. Indeed, we can see the increase of the loop strength with dislocation velocity confirming our understanding of the mechanism controlling and suppressing the absorption of the loop.

Finally, we note that even small 60-SIA loops now act as non-negligibly strong obstacles at 150 K and above, while in pure Fe the absorption of these and smaller loops is practically athermal in the range of dislocation velocities studied.

3.7. Application of an alternative Fe–Cr interatomic potential

In the present work, we utilized the two-band model Fe–Cr potential developed by Olsson *et al* [23]. An extensive benchmarking of different interatomic potentials for Fe–Cr system, including the one applied here, has been presented recently [28]. The work has shown that the potential applied here provides adequate descriptions of Cr–Cr and Cr–defect interaction. Certainly, the applied potential is no worse than other existing potentials given the problem considered. There is indeed room for further improvement of the potential, as discussed in [29], but at the same time, there is a significant amount of valuable reference data already obtained with the Fe–Fe part of the potential used here [24] regarding the interaction of dislocations with voids, loops and precipitates. Nevertheless, in order to make the statement about the effect of Cr enrichment more robust, we have applied the newly developed Fe–Cr potential [30] for the case of 1/2⟨111⟩ loops. The results are found to be very close to the already presented data showing a strong effect of Cr on the interaction

Table 1. Impact of Cr enrichment on the interaction mechanism and critical resolved shear stress.

Loop orientation	Effect of Cr enrichment	Impact on the reaction outcome	Impact on the critical stress
[001]	Suppression of the cross-slip movement of screw arms of the drawn dipole	Instead of 'bypass' interaction the loop is sheared	Moderate increase
[001]		Shear occurs instead of formation of sessile 'bi-loop'	Minimal
[010]	No change		None
$1/2[\bar{1}11]$	Suppression of the propagation of reaction segment	Reduction of the absorption, delay of complete absorption to higher test temperature	From moderate to strong increase
$1/2[1\bar{1}1]$			
$1/2[11\bar{1}]$	Suppression of dynamic drag	None[a]	Minimal
$1/2[111]$		Half of a loop is absorbed	Strong increase

[a] Here, there is no impact on the reaction outcome only if the loading conditions are such that an undecorated loop is not fast enough to be dragged by the dislocation; see the detailed explanation in section 3.5.

mechanism. Given that the paper is already rather lengthy we did not include them in this work.

4. Discussion

Cr enrichment on dislocation loops (of both ⟨100⟩ and $1/2\langle 111\rangle$ types) in Fe–Cr binaries and high-Cr steels has a long experimental story—at least 20 years. Non-equilibrium segregation of Cr to dislocations and dislocation loops was considered as a possible explanation of 'Cr-reduced' swelling as suggested by Little and Stow in 1980 [38], and 'Cr-increased' strengthening suggested by Suganuma in 1983 [39]. Nowadays, fine scale atomic resolution techniques such as TAP [22] give us a proof of the existence of Cr segregation even on very small loops which may be produced directly in collision cascades initiated by heavy ions or neutrons. On the other hand, according to atomistic simulations in Fe or Fe ∼ 10%Cr [31] the enrichment of dislocation loops by Cr atoms is energetically favourable, as it corresponds to the redistribution of oversized atoms in the tensile region of edge dislocation lines, in this case prismatic loop edges. In this work, we have studied the impact of this type of decoration on the interaction of the interstitial dislocation loops with an edge dislocation.

The analysis of an extensive number of simulated dislocation–loop reactions (almost one thousand) gave a statistical proof that the Cr enrichment does have an impact on the interaction mechanism, leading to different reaction products and unpinning stresses. Depending on loop type, interaction geometry, temperature and dislocation velocity, the effect of the enrichment may appear stronger or weaker. However, it is clear that the interaction with both $1/2\langle 111\rangle$ and ⟨100⟩ loops is subject to modification if enrichment takes place.

To understand why and how strongly the enrichment changes the interaction process, we have performed simulations with undecorated loops under equivalent loading conditions. By comparing the sequence of the interaction mechanisms we saw that Cr enrichment influences a number of modes of the dislocation movement that occur in the case of undecorated loops. The list of specific effects attributed to the decoration is summarized in table 1. In particular, we would like to highlight the impact of the enrichment on $1/2\langle 111\rangle$ loops, which are practically immobilized by Cr clouds. This causes at least three important modifications in the interaction with dislocations in general (not only edge ones): (i) absence of dynamic drag for loops with BV parallel to DGP; (ii) suppression of the absorption for loops with BV inclined to DGP and (iii) suppression of easy flip of small dislocation loops (2 nm diameter and smaller). When undecorated such loops offer no resistance to dislocation glide.

The effect of Cr enrichment appears in different temperature ranges for ⟨100⟩ and $1/2\langle 111\rangle$ loops because principally different modes of dislocation movement (i.e. glide and cross-slip) are involved in the reactions, depending on the loop type. Hence, the impact of Cr enrichment on the loop strength is expected to play a role in different temperature regimes for $1/2\langle 111\rangle$ and ⟨100⟩ loops. On the basis of the simulations performed here, we can conclude that enrichment will enhance the strength of ⟨100⟩ loops in the low temperature range and of $1/2\langle 111\rangle$ loops in the high temperature range (see example in figure 3). Note that here we have considered only edge dislocations, but for screw dislocations we anticipate that the dynamic drag will also be suppressed for the same reasons as above. This prediction will be validated in our upcoming MD study involving screw dislocations.

Another issue to be discussed is the limited timeframe accessible to MD methods. One needs to explore further the effect of strain rate in the reactions involving the emergence and movement of screw dislocations. This problem is, however, relevant for both undecorated and enriched loops. Indeed, the timeframe for the thermal activation of screw dislocations is totally different from that for edge dislocations. To explore the effect of loading rate, it is necessary to transfer the results obtained here to discrete dislocation dynamics (DDD). In addition, the application of DDD should eventually allow one to explore the net effect of Cr enrichment on the movement of several dislocations in an array of loops, given a specific density and fraction of ⟨100⟩ and $1/2\langle 111\rangle$ loops (to be taken from experiments).

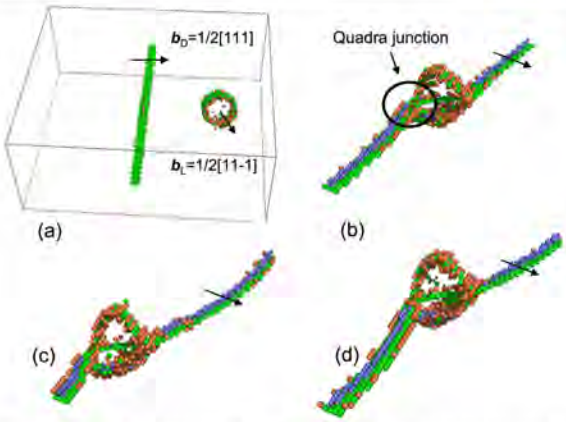

Figure A.1. The atom-core visualization of the interaction of $1/2[11\bar{1}]$ loop ($D_L = 3.5$ nm) with the dislocation at $T = 150$ K and $v_D = 2$ m s^{-1}. (a) The model before the load is applied; (b) formation of two 'quadra-point' junctions, the closest one shown by a circle; (c) the attached loop displaces further along the dislocation line; (d) the attached loop crosses the periodic boundary and keeps moving along the dislocation line.

5. Conclusions

On the basis of the results presented here and accounting for our previously published data [10, 12–15, 27], the following conclusions can be drawn:

(1) The enrichment of Cr on dislocation loops (of both ⟨100⟩ and $1/2\langle 111\rangle$ types) and dislocation lines is experimentally observed in concentrated Fe–Cr alloys and high-Cr ferritic steels. According to our atomistic simulations, this enrichment corresponds to the energetically favourable location of oversized Cr atoms in the tensile region of edge dislocation lines. Hence, the Cr enrichment on interstitial dislocation loops can be seen as the decoration of outer loop edges.

(2) Cr enrichment suppresses several modes of dislocation movements which, depending on loading conditions, may lead to the modification of the interaction mechanism with a corresponding change of the unpinning stress (associated with the loop's strength).

(3) We revealed at least three basic effects of the Cr enrichment leading to a strong impact on the interaction mechanism and the loop's strength, by suppressing: (i) cross-slip, (ii) propagation of the reaction segment on the loop surface and (iii) dynamic drag.

(4) The three suppressed mechanisms would generally trigger the removal and transformation (from $1/2\langle 111\rangle$ to ⟨100⟩ and vice versa) of the dislocation loops in the course of plastic deformation mediated by dislocations (which is the usual case in ferritic steels). Thus, Cr enrichment suppresses the ability of dislocations to absorb radiation-induced dislocation loops. Moreover, the overall effect of the enrichment is the increase of the obstacle strength of loops.

(5) Cr enrichment enhances especially the strength of small $1/2\langle 111\rangle$ loops (with $D_L \sim 2$ nm and less, thus being invisible to TEM), which would exhibit negligible resistance to dislocation glide in pure Fe. Hence, 'invisible' matrix damage in combination with local segregation effects may contribute importantly to the net strengthening.

(6) The impact of Cr enrichment on the interaction of dislocations with loops in general diminishes with increasing test temperature, suggesting that it is of thermal activation nature. Hence, the specific impact of the enrichment will depend on at least three parameters: test temperature, dislocation velocity and obstacle spacing.

Acknowledgments

This research was partially supported by the EURATOM seventh Framework Programme, under Grant Agreement No. 212175 (GetMat Project). This work was also partially supported by the European Commission under the Contract of Association between Euratom and the Belgian State, and carried out within the framework of the European Fusion Development Agreement. The authors acknowledge Dr L Malerba for discussion and proofreading. AB acknowledges an FWO grant for financial support.

Appendix. The interaction of an edge dislocation with $1/2[11\bar{1}]$ loops intersecting the glide plane

Consider a series of snapshots showing the interaction of a $1/2[11\bar{1}]$ loop with the edge dislocation, presented in figure A.1(a). The reaction is simulated at 150 K and the dislocation velocity is 2 m s^{-1}. The corresponding

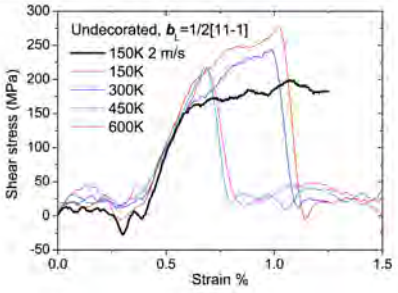

Figure A.2. Stress–strain curves computed from MD simulations of the reaction with $1/2[11\bar{1}]$ loops, $D_L = 3.5$ nm, $v_D = 10$ m s^{-1}, varying temperature, and one curve at 150 K given for $v_D = 2$ m s^{-1}.

stress–strain plot is presented in figure A.2. Initially, there is an attractive interaction and the dislocation approaches the loop. Once the dislocation has reached the loop, it contacts the loop across its surface thus resulting in the formation of a new configuration containing two 'quadra-point' junctions; see figure A.1(b). In principle, this quadra-junction can also be considered as a short [001] segment, which acts as a bridge connecting $1/2[111]$ and $1/2[11\bar{1}]$ segments cutting each other. For some time this complex was stable; however, with increasing stress up to 175–200 MPa it began to move. The configurations of the loop–dislocation complex at strains of 0.75 and 1.25% are shown in figures A.1(c) and (d), respectively. Thus, the loop displaces along the dislocation line while the latter advances. This movement occurs via the mechanism involving break-up and reconstruction of the quadra-point junctions. The latter therefore controls the critical stress at which this configuration glides as a whole. On increasing the dislocation velocity from 2 to 10 m s^{-1}, the loop is not fast enough to follow the dislocation. It starts to curve and, once the critical curvature is reached, the dislocation unpins from the loop at the shear stress of ~275 MPa. On increasing the test temperature the same breakaway occurs, but at a slightly lower stress. Hence, the ability of the loop to be dragged by the dislocation is determined by the dislocation velocity and linear density of loops, given that we simulate a periodic square array of obstacles.

References

[1] Zinkle S J, Maziasz P J and Stoller R E 1992 Dose dependence of the microstructural evolution in neutron-irradiated austenitic stainless-steel *Workshop on Time Dependence of Radiation Damage Accumulation and its Impact on Materials Properties (Montreux, Switzerland)* p 266

[2] Klueh R L and Harries D L 2001 *ASTM Stock Number: MONO3* ISBN 0-8031-2090-7

[3] Gelles D 2004 *J. Nucl. Mater.* **329–333** 304

[4] Schaeublin R, Gelles D and Victoria M 2002 *J. Nucl. Mater.* **307–311** 197

[5] Fukumoto K, Sugiyama M and Matsui H 2007 *J. Nucl. Mater.* **367–370** 829

[6] Victoria M, Baluc N, Bailat C, Dai Y, Luppo M I, Schaublin R and Singh B N 2000 *J. Nucl. Mater.* **276** 114

[7] Gelles D and Schaeublin R 2001 *Mater. Sci. Eng.* **309–310** 82

[8] Yashiro K, Konishi T and Tomita Y 2008 *Comput. Mater. Sci.* **43** 481

[9] Rodney D 2004 *Acta Mater.* **52** 607

[10] Bacon D, Osetsky Y and Rong Z 2006 *Phil. Mag.* **86** 3921

[11] Nogaret T, Robertson C and Rodney D 2007 *Phil. Mag.* **87** 945

[12] Terentyev D, Grammatikopoulos P, Bacon D and Osetsky Y 2008 *Acta Mater.* **56** 5034

[13] Terentyev D, Osetsky Y N and Bacon D J 2010 *Scr. Mater.* **62** 697

[14] Terentyev D A, Osetsky Y N and Bacon D J 2010 *Acta Mater.* **58** 2477

[15] Terentyev D, Malerba L, Bacon D and Osetsky Y 2007 *J. Phys.: Condens. Matter* **19** 456211

[16] Terentyev D, Anento N and Serra A 2012 *J. Phys.: Condens. Matter* **24** 455402

[17] Takahashi H, Ohnuki S and Takeyama T 1981 *J. Nucl. Mater.* **103/104** 1415

[18] Yoshida N, Yamaguchi A, Muroga T, Miyamoto Y and Kitajia K 1988 *J. Nucl. Mater.* **155–157** 1232

[19] Ohnuki S, Takahashi H and Takeyama T 1981 *J. Nucl. Mater.* **103/104** 1121

[20] Wakai E, Hishinuma A, Usami K, Kato Y, Takaki S and Abiko K 2000 *Mater. Trans. JIM* **41** 1180

[21] Terentyev D, Klimenkov M and Malerba L 2009 *J. Nucl. Mater.* **393** 30

[22] Jiao Z and Was G S 2011 *Acta Mater.* **59** 4467

[23] Olsson P, Wallenius J, Domain C, Nordlund K and Malerba L 2005 *Phys. Rev.* B **72** 214119

[24] Ackland G, Mendelev M, Srolovitz D, Han S and Barashev A 2004 *J. Phys.: Condens. Matter* **16** 1

[25] Osetsky Y N and Bacon D J 2003 *Modelling Simul. Mater. Sci. Eng.* **11** 427

[26] Terentyev D, Bacon D and Osetsky Y 2008 *J. Phys.: Condens. Matter* **20** 445007

[27] Terentyev D, Bacon D J and Osetsky Y N 2010 *Phil. Mag.* **90** 1019

[28] Klaver T P C, Bonny G, Olsson P and Terentyev D 2010 *Modelling Simul. Mater. Sci. Eng.* **18** 075004

[29] Terentyev D, Bonny G, Castin N, Domain C, Malerba L, Olsson P, Molodtsov V and Pasianot R C 2011 *J. Nucl. Mater.* **409** 167

[30] Terentyev D, Bonny G, Domain C and Pasianot R C 2010 *Phys. Rev.* B **81** 214106

[31] Zhurkin E E, Terentyev D, Hou M, Malerba L and Bonny G 2011 *J. Nucl. Mater.* **417** 1082

[32] Terentyev D, He X, Zhurkin E and Bakaev A 2011 *J. Nucl. Mater.* **408** 161

[33] Masters B 1965 *Phil. Mag.* **11** 881

[34] Jenkins M L, Yao Z, Hernandez-Mayoral M and Kirk M A 2009 *J. Nucl. Mater.* **389** 197

[35] Rong Z, Osetsky Y N and Bacon D J 2005 *Phil. Mag.* **85** 1473

[36] Nomoto A, Soneda N, Takahashi A and Ishino S 2005 *Mater. Trans.* **46** 463

[37] Terentyev D, Bergner F and Osetsky Y O 2013 *Acta Mater.* **61** 1444

[38] Little E and Stow D 1980 *Met. Sci.* 89

[39] Suganuma K and Kayano H 1983 *J. Nucl. Mater.* **118** 234

H Paper VIII

On the thermal stability of vacancy-carbon complexes in alpha iron

D. Terentyev, G. Bonny, A. Bakaev and D. Van Neck

Journal of Physics: Condensed Matter 24 (2012) 385401

IOP PUBLISHING JOURNAL OF PHYSICS: CONDENSED MATTER
J. Phys.: Condens. Matter **24** (2012) 385401 (12pp) doi:10.1088/0953-8984/24/38/385401

On the thermal stability of vacancy–carbon complexes in alpha iron

D Terentyev[1], G Bonny[1], A Bakaev[1,2] and D Van Neck[2]

[1] SCK-CEN, Nuclear Material Science Institute, Boeretang 200, B-2400 Mol, Belgium
[2] Center for Molecular Modeling, Ghent University, Technologiepark 903, B-9052 Zwijnaarde, Belgium

E-mail: dterenty@sckcen.be

Received 24 January 2012, in final form 8 May 2012
Published 24 August 2012
Online at stacks.iop.org/JPhysCM/24/385401

Abstract
In this work we have summarized the available *ab initio* data addressing the interaction of carbon with vacancy defects in bcc Fe and performed additional calculations to extend the available dataset. Using an *ab initio* based parameterization, we apply object kinetic Monte Carlo (OKMC) simulations to model the process of isochronal annealing in bcc Fe doped with carbon to compare with experimental data. As a result of this work, we clarify that a binding energy of ~0.65 eV for a vacancy–carbon (V–C) pair fits the available experimental data best. It is found that the V_2–C complex is less stable than the V–C pair and its dissociation with activation energy of 0.55 + 0.49 eV also rationalizes a number of experimental data where the breakup of V–C complexes was assumed instead. From the summarized *ab initio* data, the subsequently obtained OKMC results and critical discussion, provided here, we suggest that the twofold interpretation of the V–C binding energy, which is believed to vary between 0.47 and 0.65 eV, depending on the *ab initio* approximation, should be removed. The stability and mobility of small and presumably immobile SIA clusters formed at stage II is also discussed in the view of experimental data.

(Some figures may appear in colour only in the online journal)

1. Introduction

Ferritic iron-based alloys, with body-centered cubic (bcc) structure, have a great technological importance due to their attractive mechanical properties, including their application in the nuclear industry as structural materials. Even an ultrahigh purity Fe contains a certain amount of carbon (of the order of appm), while commercial Fe-based steels contain a considerable amount of carbon (up to a few per cent), needed to form strengthening carbides. It is very well known that the properties of bcc Fe-based alloys are very sensitive to the carbon content dissolved in the matrix, as well as that carbon strongly interacts with lattice point defects [1–4]. One of the most studied examples is the vacancy–carbon interaction. These two species are known to couple with each other thus masking their own properties, which is why a huge amount of theoretical (see old and recent studies [5, 6]) and experimental effort (e.g. [3, 4]) has been devoted to the study of the properties of vacancy–carbon complexes.

High precision atomistic modeling techniques such as density functional theory (DFT) give nowadays the possibility of studying the properties of vacancy–carbon complexes at their origin, i.e. at the atomic scale. DFT techniques allow one to calculate the total formation energy of different vacancy–carbon configurations and hence to derive the corresponding binding energy. Given the binding energy, the conventional way to estimate the dissociation energy for each species (a vacancy or carbon atom) is to calculate the sum of the binding (E_b) and migration energy (E_m) for the corresponding species. Even though this approach has never been fully justified, it is widely used in the community dealing with properties of radiation effects in crystals (see e.g [7–9]). However, depending on the DFT implementation, relaxation conditions and simulation cell size, the results may vary.

Considering the interaction of a vacancy–carbon pair (V–C) studied by DFT techniques [6, 10, 11], there is a considerable deviation of the absolute value of the binding energy (0.47–0.65 eV). At the same time, there are two sets of experimental results suggesting that the dissociation energy

for the V–C pair is ~1.2–1.3 eV [1] or ~1.45–1.55 eV [4]. Taking the migration energy of the vacancy, E_m(V), to be 0.55 eV, which is experimentally well established (see e.g [3, 4]), the binding energy of V–C should be about 0.45 or 0.65 eV. This fork of values is clearly a limit of the accuracy of DFT calculations, depending on the approximation. However, a difference of 0.2 eV is rather large and, due to its importance for the interpretation of many physical phenomena, the actual binding and dissociation energy for a V–C pair certainly deserves further clarification.

The first DFT work performed by Domain *et al* [6] reported E_b(V–C) to be 0.44–0.47 eV (for 54 and 128 atoms), which is close to the lower limit of the experimentally suggested value. However, later DFT studies reported higher values of 0.5 and 0.65 [12], 0.64 [10] and 0.56–0.74 eV [13], which supports the experimental upper limit. The binding energies for V–C and V–C_2 complexes obtained by Domain *et al* [6] have been used to parameterize simple rate theory models applied to reproduce the isochronal annealing experiment by Vehanen *et al* [4] in [14]. The latter work has shown that E_b(V–C) = 0.41 eV satisfactorily reproduces the experimental data up to 450 K. In the experiment by Vehanen *et al*, however, complete annealing of isolated vacancies occurs only at 650 K [4]. The presence of isolated vacancies above 450 K was therefore attributed to the formation of multiple vacancy–carbon complexes. However, it is not clear what these clusters are, as depending on the reference DFT dataset the binding energy for larger V–C clusters deviates as well.

In this work, we compile published DFT data on the vacancy–carbon interaction and formulate a parameterization set for an object kinetic Monte Carlo (OKMC) study. Then, we perform OKMC modeling to reproduce three different experimental isochronal annealing curves in high and low purity Fe, obtained experimentally by Vehanen *et al* [4]. The main purpose of this study is to clarify (i) which binding energy for a V–C pair fits the three sets of experimental data best, (ii) what are the V–C complexes that remain stable up to ~650 K under annealing in carbon-doped iron.

The paper is organized as follows. Section 2 presents an overview and critical discussion of the available DFT and experimental data. Special attention is paid to the interpretation of the experimental data. The section ends with the formulation of the parameterization set and brief explanation of the details of the OKMC simulations. Section 3 contains results and their discussion. Finally, we conclude the paper with a number of remarks.

2. Discussion of available theoretical and experimental data for the parameterization of the OKMC model

2.1. Overview of theoretical data concerning mobility and stability of point-defect clusters

We first discuss the migration energy of point defects in bcc Fe. According to state-of-the-art DFT calculations, the migration energy of the single vacancy, E_m(V), is equal to 0.65–0.67 eV, while for a ⟨110⟩ self-interstitial atom (henceforth, SIA or I) it is equal to 0.34–0.37 eV (see [15] for a review). The scatter is due to the usage of different DFT formalisms and relaxation conditions. However, a scatter of 0.03 eV for the migration energy is not especially large, given its absolute value. Hence, the lower bounds for E_m(I) and E_m(V) can be taken as 0.34 and 0.65 eV. If one assumes that the attempt jump frequency (ν_0) for these point defects is of the order of the Debye frequency (~10^{13}), the experimentally established positions of stage I_E and III, corresponding to the onset of long range migration of I and V, cannot be reproduced [12]. To demonstrate this we have repeated the calculations made in [12] using the same parameterization set as in that work and varying only the vacancy migration energy from 0.55 to 0.65 eV. The results obtained for the highest dose (200 appm) studied by Takaki *et al* [3] are presented in figure 1. Since we are not interested in close pair and correlated recombination stages, the initial concentration of Frenkel pairs (FPs) was taken to be 60% of the as-created number of FPs, following the arguments given in [12]. The evolution of defect population up to stage III and its derivative are presented in figures 1(a) and (b), respectively. The position of stage III measured experimentally [3] is also shown in figure 1(b) by the arrow. The latter figure clearly shows that, if E_m(V) = 0.65 eV and $\nu_0 = 10^{13}$ s^{-1}, the position of stage III occurs 30 K above the experimental data.

Agreement with experimental data requires either a strong increase (at least one order of magnitude) of the attempt frequency pre-factor or a decrease of the migration energy for a vacancy. A number of independent experiments in pure Fe [3, 16] (of different purity) shows that the best fit leads to E_m(I) = 0.27–0.3 eV and E_m(V) = 0.55 eV, keeping the frequency pre-factor 10^{13} s^{-1}. The discrepancy between the migration energy obtained from DFT and experiment is thus rather large and still remains unexplained. In this work, we shall not discuss possible reasons for the discrepancy and simply use the experimental value for V. In addition, the DFT value [12] of the migration energy of the di-vacancy, $E_m(V_2)$, was also set to 0.45, i.e. decreased by 0.1 eV, to keep the correct ranking for the migration of V_1 and V_2.

Secondly, the assumption about the immobility of small SIA clusters with size ≥4 made in [12] contradicts the results of molecular dynamics simulations suggesting that SIA clusters with size ≥7 defects exhibit fast one-dimensional migration along the direction of their Burgers vector (see e.g. [17, 18]). The one-dimensional (1D) mobility of SIA clusters is an essential part of the so-called production bias model, that explains a number of fundamental experimental observations in bcc metals under neutron irradiation [19]. Despite possible inaccuracies of the applied interatomic potentials, the discovery and experimental confirmation of the presence of 1D glissile SIA loops in Fe and other bcc metals should not be neglected. The assumption that I_4, I_5 and I_6 are immobile is, however, vital to reproduce stage III (both position and intensity [12]), as seen in isochronal annealing experiments, e.g. by Takaki *et al* [3]. To demonstrate this, we have performed OKCM simulations (full parameterization details are given in the following section) using E_m(V) =

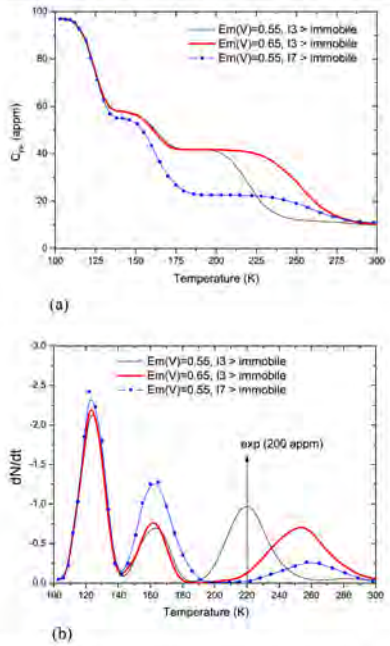

Figure 1. (a) Defect population evolution along isochronal annealing and (b) its derivative. The calculations are performed using three different parameterization sets (see text for details). The arrow shows the position of stage III obtained from experiment after electron irradiation, with 200 appm being the initial concentration of FPs.

0.55 eV and describing I_4 and I_5 clusters as mobile objects, with the migration energy of 0.12 and 0.1 eV, respectively, following [20]. Their migration was considered as a mixture between 1D and 3D dynamics, to be fully consistent with the results of MD studies [20]. These OKMC results are added in figure 1. We see that the intensity of stage II (migration of I_2 and I_3) is now much higher and the position of stage III is shifted by about 30 K. In addition, the height of stage III is lower than that of stage II, opposite to experimental observation (see figure 4 in [3]). The reason for the discrepancy comes from the fact that too many vacancies have been removed during stage II. Hence, it is indeed necessary to assign I_4 and I_5 as immobile objects (at least up to stage III) in order to reproduce the number of vacancies that survived up to stage III, in agreement with experiment, even though it clearly contradicts MD results.

A possible explanation to resolve the dilemma was proposed in [21], where the existence of stable and immobile configurations for SIA clusters of size 3, 4 and 5 was reported. Moreover, these clusters were anticipated to grow and argued to contribute to the nucleation of ⟨100⟩ loops. The fact that I_3 and I_4 exhibit a non-canonical ground state (i.e. consist of non-parallel dumbbells) has been proven by density functional theory calculations as well [21]. Moreover, these clusters are further stabilized by temperature, due to the excess of vibrational entropy. Unfortunately, the activation energy for the transformation into a mobile state has only been determined using high temperature simulations with many-body interatomic potentials, which do not offer an accurate enough description of self-interstitials in ferromagnetic bcc Fe in comparison with DFT techniques. Brute-force MD calculations performed to estimate the lifetime of these so-called 'self-trapped' clusters suggest that their de-trapping energy can exceed E_m(V). Hence, the existence of these configurations explains why the recovery is higher at stage III than at stage II. Recent calculations, performed with the activation relaxation technique [22], show that the de-trapping energy at $T = 0$ K can be as high as 0.5 eV, but at $T > 320$ K it may increase twice as much, due to the vibrational free energy contribution. Thus, the actual energy barrier for the migration of 'non-parallel' clusters might reach 1.3 eV for the I_3 'ring' configuration and 0.8 eV for I_4 [22]. Although these calculations have been done using empirical potentials and await confirmation by DFT, they give an indication of the orders of magnitude involved.

Another possible explanation for the presence of small immobile SIA clusters is their trapping at carbon atoms (C). However, we believe that the trapping of small 3D-mobile SIA clusters by C is unlikely. According to DFT, carbon interacts repulsively with a ⟨110⟩ dumbbell in its immediate vicinity [6], while a weak attractive interaction (~0.19 eV) is present at a considerable distance, due to the overlapping of the strain fields of the two defects. The Fe–C potential recently developed by Hepburn *et al* [23], specifically fitted to the SIA–C interaction taken from DFT, did not reveal any attractive interaction of carbon with parallel and non-parallel SIA clusters of size up to 5 [24]. This is consistent with the general understanding that carbon is not attracted by over-coordinated defects and with the fact that carbon does not influence stage II, attributed to the long range migration of small SIA clusters [3].

Even if we assume that small 3D-migrating SIA clusters might be strongly bound to C (binding energy $\geq$0.3 eV), this still cannot explain stage III in high purity Fe samples (containing $\lesssim$1 appm C), where the concentration of vacancies after stage II still essentially exceeds the content of carbon. On the other hand, assuming that clusters of more than four SIAs exhibit 1D glide and can be captured by carbon with a binding energy of ~0.7 eV [24], one needs to assign an unreasonably high cross-section for the interaction of SIA clusters with carbon, to provide sufficient trapping. Otherwise, SIA clusters will escape to dislocations or grain boundaries and will not provide means for vacancies to recombine, leading to an incorrect reproduction of the height and position of stage III.

We are not aware of any theoretical work explaining what these SIA complexes that allow for the recombination with vacancies at stage III are, and up to what temperature they are

Table 1. Available DFT data for the interactions of C_N–V_M complexes. F = Forst *et al*, D = Domain *et al*, Fu = Fu *et al*; the corresponding references are provided in the text. TW refers to the data obtained in this work. In the OKMC model, all objects are assumed to be immobile. The numbers entering the main parameterization set are given in bold. The dissociation energy for the emission of C_1 or V_1 is equal to $E_b(V) + E_m(V)$ and $E_b(C) + E_m(C)$, depending on which one is lower.

Number of vacancies	Number of C atoms	$E_b(V_1)$	$E_b(C_1)$	E_{2i}	E_{2v}^{opt}
1	1	**0.64**^{F}; 0.47^{D}; 0.51/0.65^{aFu}	**0.64**^{F}; 0.47^{D}; 0.51/0.65^{aFu}	1.2	0.64^{F}; 0.47^{D}; 0.51/0.65^{aFu}
1	2	**2.3**^{F}; 2.15^{D}; 1.09^{Fu}	**1.01**^{F}; 1.03^{D}; 0.66^{Fu}	1.87	1.65^{F}; 1.5^{D}; 1.18^{Fu}
1	3	1.1^{Fu};	0.34^{Fu}; **0.13**^{F}	0.99	1.3^{Fu}; 1.78^{F}
1	4	Spontaneous decay^{b,F,Fu}	Spontaneous decay^{b,F,Fu}		1.31^{F}
2	1	**0.49**^{F}; 0.21^{D}; 0.59^{TW}	**0.92**^{Fu}; 0.39^{D}; 1.06^{TW}	1.04	1.13^{F}; 0.68^{D}; 1.28^{TW}
3	1	**0.34**^{TW}	**0.98**^{TW}	0.89	1.61^{TW}
4	1	**0.53**^{TW}	**0.79**^{TW}	1.08	2.15^{TW}
2	2	**0.49**^{F}	**1.01**^{F}	1.04	2.14^{F}
2	3	**1.09**^{F}	**0.73**^{F}	1.59	2.87^{F}
2	4	**2.62**^{F}	**1.06**^{F}	1.92	3.93^{F}

[a] This value was obtained using the PWSCF code in [11].
[b] Even though the total binding energy of this cluster is positive, the emission of a carbon atom brings the system into a lower energy state.
[c] To estimate this value the binding energy for a di-vacancy (0.29 eV) has been taken from the work of Domain and Becquart [27].

stable. In this work, therefore, we simply perform simulations assuming that SIA clusters of size >3 are immobile.

2.2. *Overview of theoretical data concerning the stability of vacancy–carbon complexes*

The first DFT study on vacancy–carbon interaction was performed by Domain *et al* [6]. In that work, the strength of interaction of V–C, C_2–V, and C_3–V complexes was calculated using the VASP code [25]. In a later work, Forst *et al* [10] explored many more configurations of V_N–C_M clusters by varying N and M, respectively, in the ranges 1–2 and 1–6. The free formation energy (at 160 °C) of the clusters has been calculated using the enthalpies of formation obtained by the VASP code as well. Fu *et al* [11] have also performed DFT calculations using the SIESTA [26] and PWSCF codes to characterize the interaction of V–C and C_2–V complexes. Finally, a very recent work by Ohnuma *et al* reports a DFT study on stability of V–C_N complexes (N = 1–6) performed with VASP using two different parameterization sets [13]. The binding energy for different V–C complexes extracted from these works is summarized in table 1.

All results were obtained in a 128 atom cell, using the GGA approximation and treating Fe as a ferromagnetic material. The only exception is the work of Ohnuma *et al* [13], who also used supercells containing 250 atoms. However, the relaxation conditions were not equivalent in these four works. In [6] the shape of the cell was kept constant during the relaxation, while it was optimized in [11]. In [13], both full and constant volume relaxations were applied. In [10], the free formation energy (i.e. accounting for vibrational entropy at 160 °C) is reported, but we use these data given the absence of another DFT source. In any case, the contribution from the entropy at 160 °C is expected to be rather small, judging from the comparison of the reported free formation energy of a vacancy or di-vacancy cluster with those obtained at 0 K with VASP using a similar parameterization [27]. In order to complete the DFT dataset, we have computed the binding energy for C–V_N (N = 1–4) clusters using the VASP code. Standard VASP potentials were used, with the Perdew–Wang parameterization in the GGA. The perfect supercell consisted of 128 Fe atoms (27 k points were used for the sampling of the Brillouin zone); the atomic relaxation was performed at constant volume. The plane-wave energy cutoff was set to 300 eV. The binding energy is reported for the configurations corresponding to the lowest energy state of each C–V_N cluster.

In table 1 we firstly note that the data obtained by Ohnuma *et al* [13] are coherent with those of Domain *et al* [6]; therefore, we do not henceforth distinguish the data from [6, 13]. Secondly, the V–C binding energy reported in the three cited works varies from 0.47 up to 0.65 eV. We have recalculated the interaction energy for the V–C complex using VASP and applying exactly the same parameterization as in [6], obtaining E_b(V–C) = 0.65 eV, which agrees well with the data provided by Fu *et al* and Forst *et al* The discrepancy of almost 0.2 eV should be attributed to the usage of ultrasoft pseudopotentials in [6]. Note that E_b(V–C) also determines the partial binding energy of a vacancy and carbon in V_2–C and C_2–V clusters, respectively. Given the existing uncertainty, we shall use two datasets for which E_b(V–C) is 0.47 and 0.65 eV. A discussion about the sensitivity of the results obtained with respect to the selected DFT data will be provided later.

Despite the above mentioned discrepancy between DFT results, there is one common trend supported by the three works, namely, the saturation of the binding between V and C. In other words, there exists an optimum ratio for the number of vacancies and carbon atoms resulting in the highest partial binding/dissociation energy. From table 1 it follows that the two most stable complexes are C_2–V and C_4–V_2, with a dissociation energy of ~1.0 + 0.86 eV, due to the emission of a C atom. In principle, one can speculate that larger V–C complexes with optimum composition and structure should also exist. However, the simulation of the experimental data performed by Vehanen *et al* [4] does not require their inclusion in the OKMC model, as will be shown later. In

fact, even the formation of C_4–V_2 complexes is an extremely rare event, because of the very low concentration of vacancies surviving up to the temperature where the stability of the C_4–V_2 complex is important. Hence, it is enough to introduce the reactions leading to the formation and dissociation of V–$C_{1,2,3}$; C–$V_{1,2,3}$ and V_2–$C_{2,3,4}$ complexes, which are all listed in table 1.

The interaction of carbon and SIA defects has been excluded from the present parameterization setup, because of the following two arguments. (i) The weak interaction of carbon with the single SIA, found by DFT, is only important for the correct reproduction of stage I_E and stage II. These low temperature stages are out of the scope of this work. (ii) If one accepts that small SIA clusters of size 4–10 indeed form immobile clusters that are stable at least up to stage III, no clusters larger than ~8 SIAs will be formed, given the concentration of Frenkel pairs surviving up stage I_E in the simulated experiment. So far, we have no evidence from atomistic simulations that carbon could further stabilize ⟨110⟩ parallel or non-parallel SIA clusters (see [24] for a study using the covalent-bonding interatomic potential [23]). Note that earlier interatomic potentials developed for the Fe–C system incorrectly predict a rather high binding energy between single SIA and carbon (see [23] for comparison), which is inconsistent with DFT data and experimental evidence. This is why we do not refer to the data obtained with those potentials. The accurate calculation of the interaction energy between carbon and large SIA clusters (of size larger than five defects) with DFT is challenging, due to the need for a large simulation cell. In the absence of evidence for a strong binding between carbon and small 3D-mobile SIA clusters, we neglect this interaction in our OKMC calculations.

2.3. Analysis of experimental data

Prior to describing our simulation setup, let us list a number of the uncertainties inherent to the experimental determination of the concentration of vacancies and vacancy–carbon complexes in the positron annihilation spectroscopy (PAS) study performed by Vehanen *et al* [4]. We intend to reproduce the isochronal annealing experiments done in pure Fe (i.e. containing ≤5 appm C) and in Fe–50 appm C. The estimation of the concentration of isolated vacancies and clustered vacancies, which is the target experimental data in this work, is given in figures 11 and 14 in [4]. In the following we shall discuss how experimental details were reflected in the parameterization of the OKMC setup.

Pure Fe samples were first cold-rolled and then annealed in a hydrogen atmosphere at 800 °C for 18 h [4]. Carbon-doped samples were also prepared by cutting and annealing at 750 °C [4]. This implies that the dislocation density should be 10^{12}–10^{13} m^{-2}. Note that in the work by Tapasa *et al* [14] it was necessary to assume a much higher dislocation density (10^{14} m^{-2}) in order to reproduce correctly the recovery stage at 350 K with an incorrect V–C binding energy. We shall show that, by applying a more correct parameterization set, the stage at 350 K can be reproduced, in excellent agreement with experiment, without the unjustified assumption of high dislocation density.

In [4], electron irradiation was performed using 3 MeV electrons at 77 K. Here, we shall simulate three experimentally measured isochronal annealing curves, measured in two pure Fe samples, irradiated up to 3×10^{18} and 6×10^{18} e^- cm^{-2}, and in an Fe–50 appm C sample, irradiated up to 10^{18} e^- cm^{-2}. The initial concentration of Frenkel pairs in the first two samples was determined to be 47 (henceforth LD) and 103 (henceforth HD) ppm, respectively, using the value of 30 $\mu\Omega$ cm/at.% as the resistivity of a single Frenkel pair. However, this specific resistivity value, obtained in [28], has been questioned in [29], based on a number of contradictions revealed among existing experimental data. In [29], the specific resistivity for a single Frenkel pair was suggested to be 15 $\mu\Omega$ cm/at.%, i.e. half the value reported in [28]. As a result, the absolute concentration of Frenkel pairs is probably underestimated by a factor of two. Therefore, we shall check how the variation of the initial concentration of Frenkel pairs will influence the results.

Furthermore, the specific trapping rate for small vacancy clusters was assumed to increase linearly with cluster size, based on the early theoretical calculations by Nieminen and Laakkonen [30]. These authors, however, considered small vacancy clusters as first nearest neighbor complexes. According to all existing first principle calculations (see [15] for review), this is not the case for a di-vacancy in bcc Fe, which has its ground state in the configuration where two vacancies are located as second nearest neighbors. Hence, V_2 and stable V_2–C complexes probably contribute to the lifetime attributed to the isolated vacancies. Hence, we shall apply two ways of counting the concentration of single vacancies: with and without di-vacancy clusters.

Finally, we notice that there is an uncertainty concerning the determination of multiple carbon–vacancy complexes by PAS techniques. Density functional theory calculations do suggest that C_3–V complexes are incapable of trapping positrons, while the positron lifetime at C_2–V is significantly reduced as compared with a C–V complex or V_1 [31]. This is another uncertainty addressed in this work, when accounting for the presence of single vacancies attached to carbon atom(s).

As one can see, there are a number of issues related to the interpretation of experimental data, which prohibits an unambiguous comparison of the numerically simulated results with experiment. In addition to the main results presented here, an extra parametric study has been performed to clarify the above summarized issues. For the sake of space we do not present all results, although we shall sometimes refer to them.

3. Object kinetic Monte Carlo parameterization

In the present work we apply the object kinetic Monte Carlo code LAKIMOCA [9], which has been widely used in the past to model accumulation and annealing of radiation damage. In this model, the objects (dislocations, point defects, clusters of point defects, mobile traps, i.e. carbon atoms and complexes containing trap(s)) are treated as center-of-mass positions in

Table 2. Parameterization of SIA clusters. The attempt frequency was set to 6×10^{12} s^{-1} for all migration and dissociation events.

Size	E_m (eV)	Capture radius, (Å)	E_b (I_1)—binding energy for a single SIA
1	0.3	5.151	
2	0.42	6.9	0.8 [12]
3	0.43	7.29	0.92 [12]
>3	Immobile	As in [9]	As in [9], taking $E_f(I_1) = 3.77$; $E_b(I_2) = 0.8$

Table 3. Parameterization of vacancy clusters.

Size	E_m (eV)	Capture radius, (Å)	E_b (V_1)
1	0.55	4.32	
2	0.54	4.68	0.29 [12]
3	0.43	4.94	0.37 [12]
4	0.62	5.15	0.62 [12]
5	0.64	5.32	As in [9]
>5	Immobile	As in [9]	As in [9], taking $E_f(V_1) = 2.07$; $E_b(V_2) = 0.29$

space, corresponding to bcc lattice sites. The objects migrate, dissociate or associate (including recombination) according to the allowed reactions defined by the user. The association of the objects occurs based on the space-overlap and energy gain principle. Each object is treated as a sphere with a given capture radius. The capture radii for I_N and V_N objects are taken from [9]. Time elapses according to the standard residence time algorithm [32].

A general scheme for the description of the interaction between SIA and vacancy defects is described in detail in [9]. The migration energies for SIA and vacancy clusters used in this work are listed in tables 2 and 3, respectively. As discussed, we consider only I_1, I_2 and I_3 as 3D-migrating objects, while larger clusters are considered immobile. Given the range of initial concentration of Frenkel pairs, we note that SIA clusters with size above 10 were not observed to form. Therefore, the introduction of 1D mobility for clusters with size above 10 SIAs does not change the results in any way. Even though we indicate the dissociation energy for I_2 and I_3, in practice these clusters either form larger ones or recombine with vacancies rather than dissociating. The same is true for small vacancy clusters, whose dissociation energy is higher than the migration energy. The parameterization of the binding energy of large vacancy and interstitial clusters is taken from [9].

Carbon atoms are considered here as mobile traps, which can form immobile complexes. The formation of pure carbon clusters is excluded, given that the C–C binding energy (0.16 eV [6]) is significantly smaller than the typical binding energy of V_N–C_M complexes. Multiple V–C complexes cannot dissociate 'all at once' and must decay by sequential emission of vacancies and carbon atoms.

Dislocations are introduced as cylindrical sinks (with capture radius $R_d = 5.0$ Å) of a length corresponding to the required dislocation density (10^{13} m^{-2}). Dislocations can absorb point defects and their clusters, but do not emit them. Carbon atoms are introduced as mobile traps with specific capture radius (R_t, varied from 4 to 10 Å) and migration energy (E^c_m(C) = 0.86 eV). Traps can form immobile complexes with mobile and immobile point defects and their clusters, according to table 1.

Following [12], the initial concentration of Frenkel pairs (FPs) in the simulation is assumed to correspond to the number of defects remaining after the last correlated recombination stage I_{D1} (around 100 K). Indeed, the present OKMC model does not account for the correlated recombination, where the migration barrier of interacting defects is reduced. The fraction of point defects recombined up to stage I_{D1} is known to be ~50% (see table VI in [3]), and slightly increases with the concentration of initially generated FPs. In the simulations, FPs are created at a constant distance of 4×2.87 Å and the I_1–V_1 recombination distance is set to 3.3×2.87 Å [12]. We have used different initial concentrations of Frenkel pairs, in order to obtain the same concentration of vacancies as observed in the target experiment before the onset of stage III, as explained further on. A parallelepiped-like box with sides $100 \times 50 \times 300$ nm^3 was used for all simulations. The simulation corresponding to each target experimental annealing curve has been repeated 20 times to reduce statistical fluctuations. Only averaged curves are shown. Isochronal annealing is performed with the same heating rate as in the target experiment, by increasing temperature every 3 min by 2 K.

4. Isochronal annealing recovery: simulation results

4.1. Initial concentration of Frenkel pairs

Prior to starting the main set of calculations, we have determined the number of FPs to be introduced at 100 K, in order to obtain the same concentration of vacancies as measured in the experiment just before the onset of stage III. As discussed above, according to the experimental measurement the initial concentration of FPs in the two Fe–5 appm C samples was 47 and 103 appm, while the Fe–50 appm C sample was irradiated up to a dose of 10^{18} e$^-$ cm^{-2}, which should give around 16 appm of FPs. Experimentally, the radiation-induced concentration of FPs, C_{FP}, was obtained by measuring the induced resistivity. Our first step is to find an optimal initial C_{FP}, in agreement with the experiment at higher temperature, when the concentration of isolated vacancies is measured directly using PAS.

The parametric study as a function of initial C_{FP}, introduced as described in section 3, has been performed using the parameterization given in the previous section, with 5 appm C in the simulation box. For a pure Fe sample irradiated at low dose (3×10^{18} e$^-$ cm^{-2}), the best agreement is obtained if C_{FP} at 100 K is 22 appm, which provides an estimate for the number of FPs annealed out due to the correlated recombination as high as 54% (assuming the initial concentration to be 47 appm, as reported [4]). For the sample irradiated to higher dose (6×10^{18} e$^-$ cm^{-2}), the best agreement is obtained by placing 45 appm of

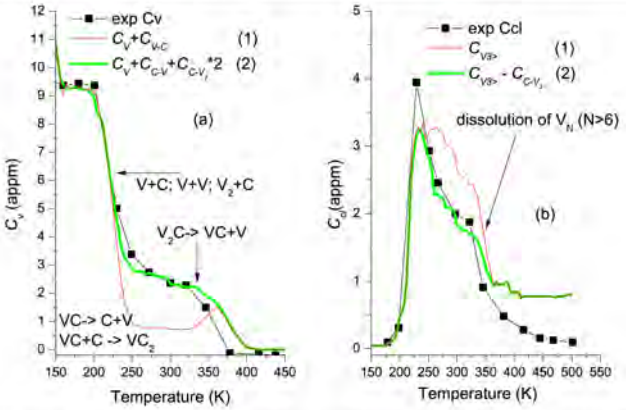

Figure 2. (a) Concentration of isolated vacancies and V–C complexes contributing to the lifetime of single vacancies. (b) Concentration of clustered vacancies, including those decorated by carbon atoms. The experimental data are taken from figure 11 for low dose specimens from [4].

FPs (assuming the initial concentration to be 103 appm, as reported [4]), hence the correlated recombination results in the decrease of the initial concentration of FPs by 56%. These fractions are in reasonable agreement with the data obtained by Takaki *et al* [3], who reported the decrease of the radiation-induced resistivity to be ~50% in pure Fe initially containing 5–125 appm FPs. We therefore conclude that the estimation of the initial concentration of FPs provided using 30 $\mu\Omega$ cm/at.% as the resistivity of a single Frenkel pair is more appropriate than using 15 $\mu\Omega$ cm/at.%. In the latter case, the total fraction of annealed defects would be about 75%, which is well above the estimate of Takaki *et al* [3].

4.2. Pure iron at a low dose

Given the uncertainty about the affinity of positrons to V_2 and V–C_2 clusters, we have counted the number of isolated and clustered vacancies in two ways. The first way to estimate the concentration of vacancies, C_V, is to count all isolated vacancies and C–V complexes together; the alternative is to add also the contribution from C–V_2, knowing that vacancies in this complex are located at second nearest neighbor distance from each other, i.e. they correspond to two open volumes separated by a carbon atom in between. The inclusion or exclusion of V_2 clusters from the count is not important, since these clusters are present in the system only in a very narrow temperature interval, as will be shown later.

The evolution of the concentration of single vacancies, C_{V_1}, in the Fe–5 appm LD specimen is presented in figure 2(a). The first stage starting at ~200 K is due to the long range migration of V_1, which leads to the following three processes: (i) formation of V_2 and larger mobile vacancy clusters; (ii) formation of V–C complexes; (iii) formation

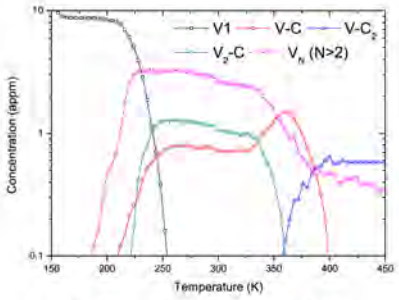

Figure 3. The evolution of the concentration of isolated vacancies, V–C, C_2–V, V_2–C and vacancy clusters containing more than two vacancies modeled in a pure Fe LD specimen (see text for explanations).

of V_2–C complexes. The kinetics of these three reactions is shown in figure 3. The latter shows that at 250 K all isolated vacancies disappear from the system. It is important to note that the concentration of C–V_1 complexes at $T = 250$–325 K is about 1 appm only, while the experimental value is about 3 appm. If one takes into account the contribution from C–V_2 complexes, however, the agreement with experiment is perfect, as clearly follows from figure 2(a). At 325 K, the breakup of C–V_2 complexes ($E_d = 0.49 + 0.55$) starts, resulting in the formation of V–C pairs and isolated vacancies. Some of the vacancies recombine with immobile SIA clusters and dislocations, while some form V–C complexes with the available carbon atoms present in solution. Immediately afterward, at 350 K, the remaining carbon atoms start to move

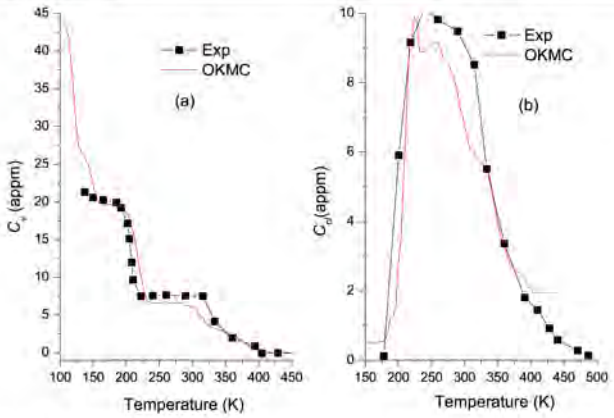

Figure 4. (a) Concentration of isolated vacancies and V–C complexes resulting in a similar lifetime as isolated vacancies. (b) Concentration of clustered vacancies, including those decorated by carbon atoms. The experimental data are taken from figure 11 'high dose' from [4].

and decorate existing V–C complexes to form V–C_2 clusters. The total concentration of V–C_2 complexes at $T > 400$ K remains less than 1 appm.

Other information to be extracted from these simulations is the evolution of the total number of vacancies in clusters (C_{Vcl}), which can also be compared with the experiment. Since C–V_2 complexes indeed seem to contribute to the intensity attributed to the annihilation of positrons at isolated vacancies, it is of interest to compute the total concentration of clustered vacancies (i) by counting all clusters with size equal to and above two and (ii) by excluding vacancies present in C–V_2 complexes. The results and experimental data are presented in figure 2(b), which clearly shows that the second way provides much better agreement with experiment. Thus, there is a good agreement for concentration of both isolated and clustered vacancies at least up to 400 K, assuming that C–V_2 complexes are 'recognized' by positrons as two separate vacancies and not one vacancy cluster.

The details of the evolution of C_{cl} can be described as follows. Clustering starts at 200 K, with the onset of vacancy migration, and the maximum is reached before the breakup of C–V_2 complexes at 250 K. A further decrease of C_{cl} above 350 K occurs due to the dissociation of small vacancy clusters (V_6–V_8) and formation of more stable ones, which dissociate above 500 K (stage V). As a result, some of the vacancy clusters remain stable, although according to experimental results C_{cl} constantly decreases up to 500 K. Probably, the stability of small vacancy clusters is underestimated in the current parameterization.

The only adjusted parameter in this set of simulations was the capture radius of carbon atoms, which varied from 2 to 10 Å to achieve the best agreement with experiment during stage III. The optimal value was found to be 5 Å, which is comparable with the capture radius of I_1.

4.3. Pure iron at high dose

The evolution of C_{V_i} and C_{cl} in the Fe–5 appm HD specimen is presented in figures 4(a) and (b), respectively. There C_{V_i} and C_{cl} were counted by including C–V_2 complexes in C_{V_i} and excluding them from C_{cl}, consistently with the above discussion. We see that C_{V_i} closely follows the experimental curve, even the abrupt decrease at 325 K as seen in experiment.

The concentration of clustered vacancies is also reasonably well predicted, although slightly underestimated in the range 250–350 K. Above 400 K, a considerable number of vacancy clusters still remains in the system, while according to experiment [4] they all disappear at 500 K. In our simulations, the remaining vacancy clusters—as in the case of the low dose sample—start to emit vacancies above 500 K. The stage of dissolution of vacancy clusters obtained by Takaki *et al* [3] is also above 500 K.

At the end of this subsection we shall discuss that the tail of the C_{cl} curve is not well described because of the assumption of immobility of vacancy clusters of size above 5 and because of the very rough estimation of the binding energy of vacancies in clusters using the interpolation formulas. It is well known that the binding energy of small vacancy clusters is dependent on its multiplicity and therefore somewhat less stable vacancy clusters will emit vacancies, thereby contributing to the rearrangement of vacancy clusters and annealing of vacancies in the temperature interval 400–500 K. Thus, a much better agreement in this temperature interval can be obtained by adjusting the properties of vacancy clusters containing 5–15 vacancies. This is, however, out of the scope of the present work.

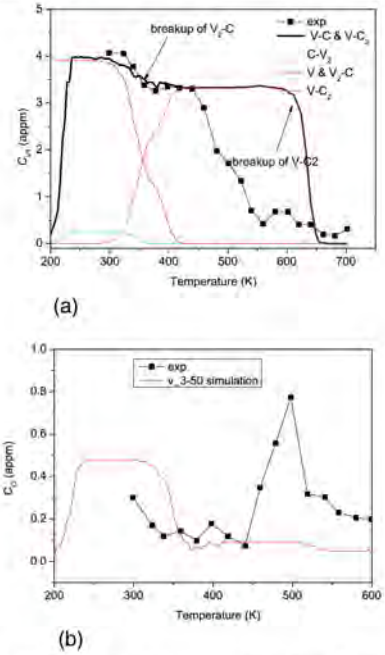

Figure 5. Concentration of isolated vacancies, including C–V and C–V_2 complexes. (b) Concentration of clustered vacancies. The experimental data are taken from figure 14 [4].

4.4. Carbon-doped iron

We now present the results of the simulations in carbon-doped specimens. The evolution of C_{V_1} and C_{cl} in an Fe–50 appm specimen is presented in figures 5(a) and (b), respectively. The total concentration C_{V_1} was counted by including vacancies present in C–V and C–V_2 complexes.

The best fit of the initial concentration of FPs was found to be 10 appm (after I_{D1}), while it is estimated that about 15 appm of FPs were introduced due to irradiation. Hence, only about 30% of the defects have annihilated due to correlated recombination. This fraction is lower than in pure Fe and therefore we conclude that the addition of 50 appm of carbon already influences the correlated recombination, at least for this low dose specimen.

In the work of Tapasa *et al* [14], the V–C binding energy was 0.41 eV; as a consequence, the migration of carbon and breakup of V–C complexes (existing from 200 up to 350 K) coincided. The decrease of C_{V_1} by about 0.5 appm at 350 K, in accordance with experiment, was obtained by introducing an unjustifiably high dislocation sink strength (i.e. dislocation density). In the experiment no such high dislocation density could exist since all specimens were annealed at high temperature [4].

In the present work, the binding energy for the C–V complex is 0.64 eV, for the reasons amply discussed above. Hence, no stage due to the dissociation of C–V can be observed. This stage, however, exists and fits very well the experimental curve, as follows from the results presented in figure 5(a). The stage originates from the dissociation of V_2–C complexes formed in the two-step reaction ($V + V = V_2$, $V_2 + C = C\text{–}V_2$) after the onset of the vacancy migration at about 220 K.

At 350 K, the migration of carbon starts and all V–C pairs become decorated by one and two more carbon atoms. Note that V–C_4 is already an unstable cluster (see table 1). V–C_3 dissociates shortly after its formation ($E_D = 0.99$ eV). Thus, only V–C_2 clusters remain. Here, we assume that V–C_2 complexes are detected by PAS as isolated vacancies. The next stage observed in our simulations is obviously the dissociation of V–C_2 complexes, occurring at ~600 K. This dissociation leads to the formation of a few larger V–C complexes (namely V_2–C_4) but mostly to the annihilation of vacancies on dislocations and remaining SIA clusters, assigned to be immobile. The stage at 600 K predicted here has, however, much higher amplitude in comparison with the experiment. According to the latter, the concentration of vacancies smoothly decreases in the temperature range 450–550 K down to about 1 appm, which is not observed in our simulations. Thus, the agreement with the experiment is very good up to 500 K, while a discrepancy appears above this temperature. The possible origin of this discrepancy is discussed in section 5.

5. Discussion

From the results above we can see that experimental data in pure Fe can be reproduced in good agreement with experiment using the parameterization set with E_b(V–C) = 0.65 eV and low dislocation density, corresponding to annealed Fe. In the considered carbon-doped Fe, however, there is a clear mismatch. No stage at 450 K, as observed in experiment, appears in the simulations. As a consequence, we have disagreement for the evolution of C_{cl} as well (see figure 5(b)). The usage of the binding energy for V–C pairs and V–C_2 complexes taken from Domain *et al* [6] and variation of E_m(V) = 0.55–0.65 eV and E_m(C) = 0.86–0.9 eV in the parameterization set does not allow reproduction of the stage at 450 K either. In the following we discuss possible reasons for the absence of the stage at 450 K.

Firstly, let us mention that the decrease of vacancy concentration starting at 450 K is accompanied by the growth of clustered vacancies. Thus, one of the suitable explanations for this stage is the dissociation of V–C_2 clusters into V–C + C and then the dissociation of V–C pairs. This would allow for the freely moving vacancies to form small (and mobile) clusters. Note that the DFT-predicted binding energy for a V–C pair (0.64 eV) and migration energy of a vacancy (0.55 eV) fits very well the temperature of this stage (~450 K). However, if indeed V–C_2 complexes would

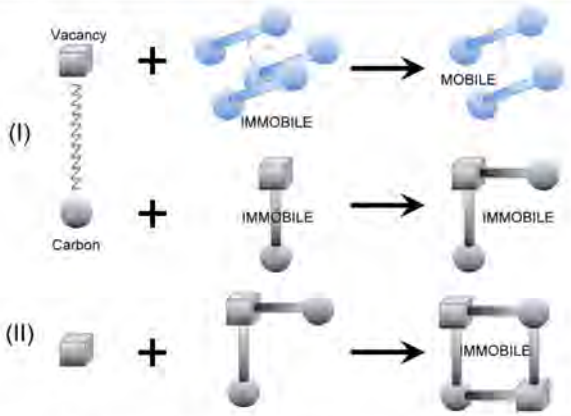

Figure 6. Schematic representation of the formation of C_2–V_2 clusters due to the breakup of the C–V pairs.

dissociate at 450 K one may wonder what stabilizes small undecorated vacancy clusters, which have to survive up to 550–650 K (see figure 14 in [4]). Importantly, the RR study of Takaki *et al* clearly shows that the stage at 600 K is affected by the presence of carbon [3].

We suggest four possible hypotheses to explain the stage at 450 K leading to the disappearance of the lifetime component attributed to single vacancies:

(1) I_3 and some other immobile SIA clusters start their migration at 450 K with ($E_m \approx 1.2$ eV). Some of these clusters interact with V–C_2 clusters and the others grow by coalescence or annihilate at dislocations. Indeed, there are indications that small non-parallel clusters might have such de-trapping energy [22]. This assumption, however, does not explain the increase of C_{e1} observed in the experiment.

(2) There is a fraction of the V–C complexes that remains undecorated by carbon up to 450 K, because carbon is also trapped at the immobile SIA complexes and dislocations. In this case, the stage at 450 K would be due, on the one hand, to the breakup of C–V pairs, which contribute to the growth of vacancy clusters (of C_2–V_2 type) and, on the other, to the recombination with small, immobile SIA clusters. This is illustrated in figure 6 as a two-step reaction: (i) breakup of a C–V pair and (ii) transformation of the C_2–V clusters into C_2–V_2. In this case, the recombination of vacancies with immobile SIA clusters could activate their migration, so that the breakup of one V–C pair in fact would result in the disappearance of at least three vacancies. Thus, it is enough to have about 1 appm or less of V–C complexes to produce such a strong decrease of C_{V_1} at 450–550 K. Since we have no evidence from DFT that carbon could be trapped by SIA clusters, the above proposed mechanism was not included in the parameterization. Yet, one cannot exclude that slowly migrating ⟨100⟩ or non-parallel SIA clusters may attract carbon.

(3) There is an incorrect description of the C–V interaction energy for multiple clusters and the stage that we see at 450 K is the re-arrangement of C–V clusters, resulting in their further decoration, which makes them invisible as 'isolated' vacancies. However, this does not explain the formation of vacancy clusters.

(4) V–C_2 complexes are in fact mobile, with activation energy of about 1.2 eV. While they migrate, they contribute to the growth of larger vacancy clusters (such as V_2–C_4 for instance) decorated by carbon atoms but visible with PAS as vacancy clusters. According to the available DFT data, when a di-vacancy becomes decorated by carbon atoms, two vacancies are taking up the first nearest neighbor positions. This can explain the simultaneous decrease of the signal from isolated vacancies and the appearance of clustered vacancies. One can imagine the migration of the V–C_2 complex to occur in the same way as the well known phenomenon of vacancy–copper drag (e.g. [33]), but this time a vacancy is dragged by a pair of carbon atoms.

Out of these four hypotheses, at least the second and fourth ones do not contradict any available experimental and DFT data.

Another important issue touched on in this work is the thermal stability of C–V clusters enriched with C. Based on the existing DFT results one can conclude that there is an optimum carbon-to-vacancy ratio, which is 2, for which the clusters acquire the highest stability. Such clusters are believed to dissociate via the emission of a carbon atom with dissociation energy ~1.8 eV. It is to be noted, however, that the existence of such strongly bound clusters is only

possible when the concentration of vacancies is lower than, or comparable to, that of carbon dissolved in a matrix. This would not be the case under continuous irradiation conditions, hence the presence of V–C_2 and V_2–C_4 clusters is unlikely, while the presence of V–C and somewhat less stable V_2–C complexes is more likely to occur. However, during the annealing of irradiated specimens the dissolution of V_2–C and V–C and the formation of V–C_2 will occur.

Recently, it has been shown that the presence of stable and immobile V_N–C_M clusters causes the blockage of 1D-migrating dislocation loops of 1/2⟨111⟩ type [24]. Hence, the above discussed variation of the morphology and concentration of V_N–C_M clusters upon annealing of irradiated carbon-doped or even nominally pure Fe may have important consequences on the removal of radiation-induced dislocation loops. One should expect a steep decrease of the density of dislocation loops, accompanied by their rapid growth by coalescence, starting at a temperature of about 600 K, which corresponds to the stability of V–C_2 clusters. This has indeed been observed experimentally for the loops formed under electron and neutron irradiation [34, 35].

Indeed, the DFT-predicted value for the dissociation energy of V–C_2 complexes explains well the stage at 600 K and complete disappearance of isolated vacancies at 700 K in Vehanen's experiment [4], as one can see from figure 5(a). However, this also implies that V–C_2 complexes are seen by PAS as single vacancies, whereas according to [31] the positron lifetime at V–C_2 should be lower than at a vacancy or at a V–C pair. Thus, it is necessary to revise our knowledge about the positron lifetime at different V_N–C_M complexes.

The last subject of the discussion is dedicated to the immobility of small SIA clusters. There is strong experimental evidence since the experiments of Takaki *et al* [3] that these clusters must be present at least up to stage III, i.e., ~220 K. However, nothing is known about the temperature at which these clusters start to anneal. The only work addressing this question uses empirical potentials [22]. The present work suggests that the presence of small, virtually immobile SIA clusters is necessary up to at least 350 K, for the stage due to the dissolution of V_2–C clusters to occur in carbon-doped Fe. If no SIA clusters were present, most of the vacancies would contribute to the formation of V–C and V–C_2 complexes. The binding energy of SIAs in small non-parallel clusters [21] such as I_2, I_3 and I_4 varies from 0.84 up to 1 eV, according to VASP calculations. Thus, if these clusters are indeed immobile, the upper bound energy for the dissociation is ~1.3 eV and the lower bound is ~1.15, i.e. above the stage of carbon migration. Thus, if these clusters are immobile, they are stable enough to explain the stage at 350 K. Moreover, 1.3 eV coincides with the activation energy for stage V, reported by Takaki *et al* [3] and attributed to the dissolution of small vacancy clusters. In the case of Vehanen's experiment [4], the dissociation of small immobile SIA clusters could explain the stage starting at 450 K. Hence, the DFT validation of the migration mechanisms of non-parallel clusters discovered by activation relaxation techniques by Marinica *et al* [22] is essential for the further understanding of radiation defects in bcc Fe.

6. Summary and conclusions

We have performed a set of object kinetic Monte Carlo simulations with the aim to reproduce the evolution of the concentration of isolated and clustered vacancies during isochronal annealing of pre-irradiated pure and carbon-doped iron. The parameterization set was chosen based on available DFT results, and its most important features are the binding and dissociation energies for multiple vacancy–carbon complexes.

The results show that the parameterization set accurately describes the annealing of pure Fe (containing 5 appm of C). In the carbon-doped sample, however, the wide stage at 450 K resulting in the major disappearance of 'isolated' vacancies and formation of vacancy clusters could not be reproduced. Two possible reasons for the absence of this stage have been suggested, namely (i) migration or dissolution of immobile SIA clusters and (ii) the possibility of migration of V–C_2 complexes and their coalescence into larger C–V complexes.

The compiled DFT data and currently used parameterization set can support and help to rationalize a number of independent experimental data obtained in low purity Fe, as follows.

(i) E_b(V–C) = 0.64 eV and E_m(V) = 0.55 eV explains the effective migration energy for a vacancy extracted to be ~1.2 eV by Kiritani *et al* [36] from the observation of the shrinkage and growth of dislocation loops. It also explains the temperature of ~500 K corresponding to the onset of carbon precipitation while vacancies are present in Fe–C, as obtained by Takeyama and Takahashi [37]. Furthermore, it supports the interpretation of the threshold temperature for void swelling, suggested to be reduced due to the formation of stable V–C complexes by Little [38]. Finally, it explains the activation energy for the vacancy migration in low purity Fe measured by Diehl *et al* [39] to be 1.28 eV.

(ii) The presence of more stable V–C_2 clusters explains why some isolated vacancies can still be detected up to 700 K in the PAS experiment of Vehanen *et al* [4]. In addition, the existence of these highly stable V_N–C_M clusters, capable of trapping 1D-migrating 1/2⟨111⟩ dislocation loops [24], may explain why these loops are observed up to and start to decrease in number and coalesce at ~600 K [34].

(iii) E_b(C–V_2) = 0.49 eV and E_m(V) = 0.55 eV explains well the stage at 350 K observed in the experiment by Vehanen *et al* [4], as well as 410 K as the temperature assigned by Takamura [40] for the vacancy migration, in the annealing experiments after neutron irradiation.

(iv) Given that the parameterization set with E_b(V–C) = 0.65 eV explains not only the experiment by Vehanen *et al* [4], but also a number of other experiments in low purity iron, we conclude that the value for the V–C binding energy of 0.47 eV reported in [6] is an unreliable result.

(v) Simulations performed in carbon-doped Fe strongly suggest that small immobile SIA clusters formed at stage

II ($T = 150$–200 K) must be thermally stable not just up to stage III (around 220 K), but up to 350 K, giving rise to the recovery due to the breakup of V_2–C.

Acknowledgments

This work, supported by the European Commission under the Contract of Association between EURATOM/SCK-CEN, was carried out within the framework of the European Fusion Development Agreement. Partial support was also received from the EURATOM Seventh Framework Programme, under the Perform60 project. DT thanks his colleagues Dr L Malerba and Dr A L Nikolaev for useful remarks, discussions and proofreading.

References

[1] Arndt R A and Damask A C 1964 *Acta Metall.* **12** 341
[2] Little E A and Harries D R 1970 *Met. Sci. J.* **4** 188
[3] Takaki S, Fuss J, Kugler H, Dedek U and Schultz H 1983 *Radiat. Eff.* **79** 87
[4] Vehanen A, Hautojärvi P, Johansson J and Yli-Kauppila J 1982 *Phys. Rev.* B **25** 762
[5] Johnson R 1965 *Acta Metall.* **13** 1259
[6] Domain C, Becquart C and Foct J 2004 *Phys. Rev.* B **69** 144112
[7] Soneda N and Diaz de la Rubia T 1998 *Phil. Mag.* A **78** 995
[8] Caturla M, Diaz de la Rubia T and Fluss M 2003 *J. Nucl. Mater.* **323** 163
[9] Domain C, Becquart C and Malerba L 2004 *J. Nucl. Mater.* **335** 121
[10] Forst C J, Slycke J, van Vliet K J and Yip S 2006 *Phys. Rev. Lett.* **96** 175501
[11] Fu C C, Meslin E, Barbu A, Willaime F and Oison V 2008 *Solid State Phenom.* **139** 157
[12] Fu C, Dalla Torre J, Willaime F, Bocquet J and Barbu A 2005 *Nature Mater.* **4** 68
[13] Ohnuma T, Soneda N and Iwasawa M 2009 *Acta Mater.* **57** 5947
[14] Tapasa K, Barashev A, Bacon D and Osetsky Y 2007 *Acta Mater.* **55** 1
[15] Malerba L *et al* 2010 *J. Nucl. Mater.* **406** 7
[16] Maury F, Lucasson P, Lucasson A, Faudot F and Bigot J 1987 *J. Phys. F: Met. Phys.* **17** 1143
[17] Osetsky Y, Bacon D, Serra A, Singh B and Golubov S 2003 *Phil. Mag.* **83** 61
[18] Terentyev D, Malerba L and Hou M 2007 *Phys. Rev.* B **74** 104108
[19] Singh B, Woo C and Foreman A 1992 *Mater. Sci. Forum* **97–99** 75
[20] Terentyev D A, Malerba L and Hou M 2007 *Phys. Rev.* B **75** 104108
[21] Terentyev D, Klaver T, Olsson P, Marinica M, Willaime F, Domain C and Malerba L 2008 *Phys. Rev. Lett.* **100** 145503
[22] Marinica M-C, Willaime F and Mousseau N 2011 *Phys. Rev.* B **83** 094119
[23] Hepburn D and Ackland G 2008 *Phys. Rev.* B **78** 165115
[24] Terentyev D, Anento N, Serra A, Jansson V, Khater H and Bonny G 2011 *J. Nucl. Mater.* **408** 272
[25] Kresse G and Hafner J 1993 *Phys. Rev.* B **47** 558
[26] Soler J M, Artacho E, Gale J D, Garcia A, Junquera J, Ordejon P and Sanchez-Portal D 2002 *J. Phys.: Condens. Matter* **14** 2745
[27] Domain C and Becquart C 2002 *Phys. Rev.* B **65** 024103
[28] Maury F, Biget M, Vajda P, Lucasson A and Lucasson P 1976 *Phys. Rev.* B **14** 5303
[29] Nikolaev A 2007 *Phil. Mag.* **87** 4847
[30] Nieminen R M and Laakkonen J 1979 *Appl. Phys.* **20** 181
[31] Pushka M J and Nieminen R M 1982 *J. Phys. F: Met. Phys.* **12** L211
[32] Young W M and Elcock E W 1966 *Proc. Phys. Soc.* **89** 735
[33] Arokiam A, Barashev A, Bacon D and Osetsky Y 2005 *Phys. Rev.* B **71** 174205
[34] Arakawa K, Hatanaka M, Mori H and Ono K 2004 *J. Nucl. Mater.* **329–333** 1194
[35] Eyre B and Bartlett A 1965 *Phil. Mag.* **12** 261
[36] Kiritani M, Takata H, Moriyama K and Fujita F 1979 *Phil. Mag.* A **40** 779
[37] Takeyama T and Takahashi H 1973 *J. Phys. Soc. Japan* **35** 939
[38] Little E 1979 *J. Nucl. Mater.* **87** 11
[39] Diehl J, Merbold U and Weller M 1977 *Scr. Metall.* **11** 811
[40] Takamura S 1979 *Radiat. Eff. Lett.* **43** 69

I Paper IX

Interaction of carbon-vacancy complex with minor alloying elemnets of ferritic steels

A. Bakaev, D. Terentyev, X. He, E.E. Zhurkin, D. Van Neck

Journal of Nuclear Materials 451 (2014) 82

Journal of Nuclear Materials 451 (2014) 82–87

Contents lists available at SciencesDirect

Journal of Nuclear Materials

journal homepage: www.elsevier.com/locate/jnucmat

Interaction of carbon–vacancy complex with minor alloying elements of ferritic steels

A. Bakaev [a,b,c,*], D. Terentyev [a], X. He [d], E.E. Zhurkin [c], D. Van Neck [b]

[a] SCK•CEN, Nuclear Materials Science Institute, Boeretang 200, Mol B2400, Belgium
[b] Center for Molecular Modeling, Department of Physics and Astronomy, Ghent University, Technologiepark 903, 9052 Zwijnaarde, Belgium
[c] Department of Experimental Nuclear Physics K-89, Institute of Physics, Nanotechnology and Telecommunications, St. Petersburg State Polytechnical University, 29 Polytekhnicheskaya Str., 195251 St. Petersburg, Russia
[d] China Institute of Atomic Energy, P.O. Box 275-51, 102413 Beijing, China

ARTICLE INFO

Article history:
Received 24 January 2014
Accepted 19 March 2014
Available online 26 March 2014

ABSTRACT

Interstitial carbon, dissolved in bcc matrix of ferritic steels, plays an important role in the evolution of radiation-induced microstructure since it exhibits strong interaction with vacancies. Frequent formation and break-up of carbon–vacancy pairs, occurring in the course of irradiation, affect both kinetics of the accumulation of point defect clusters and carbon spatial distribution. The interaction of typical alloying elements (Mn, Ni, Cu, Si, Cr and P) in ferritic steels *used* as structural materials in *nuclear* reactors with a carbon–vacancy complex is analyzed using *ab initio* techniques. It is found that all the considered solutes form stable triple clusters resulting in the increase of the total binding energy by 0.2–0.3 eV. As a result of the formation of energetically favourable solute–carbon–vacancy triplets, the dissociation energy for vacancy/carbon emission is also increased by ~0.2–0.3 eV, suggesting that the solutes enhance thermal stability of carbon–vacancy complex. Association of carbon–vacancy pairs with multiple solute clusters is found to be favorable for Ni, Cu and P. The energetic stability of solute(s)–carbon–vacancy complexes was rationalized on the basis of pairwise interaction data and by analyzing the variation of local magnetic moments on atoms constituting the clusters.

1. Introduction

Fe-based steels with body centered cubic (BCC) structure such as bainitic or high-Cr ferritic–martensitic ones are the common structural materials for nuclear applications [1]. During operation the steels undergo degradation due to the harsh exploitation conditions. Radiation-induced embrittlement is one of the limiting factors determining safety and effective exploitation of a nuclear setup (see e.g. [1,2]). The embrittlement is conventionally attributed to the obstruction of dislocation movement by nanometric lattice defects formed as a result of radiation-induced/enhanced segregation and accumulation of point defect clusters growing to the dislocation loops and nano-voids [2].

Recent experimental studies involving several high resolution techniques including atom probe tomography (APT) emphasize the presence of solute-rich clusters (SRC), composed of major alloying elements, revealed in different types of commercial steels [3–8]. Remarkably, all the mentioned experimental works report extremely high density of SRC (up to 10^{24} m^{-3}). Due to their small size, these clusters are invisible to transmission electron microscopy (TEM).

The APT techniques, however, cannot determine the full structure of the SRCs and therefore their possible association with radiation-induced lattice defects remains unknown. Specially dedicated atomistic study addressing segregation in Fe–Mn–Ni–Cu alloys – a model for reactor pressure vessels (RPV) steel, has suggested that non-equilibrium formation of SRCs can be explained by their association with in-cascade created dislocation loops [9]. In line with that, the association of Mn and Si (important solutes entering RPV steels) with self-interstitial atoms resulting in highly stable configurations was also recently proven by *ab initio* calculations [10]. However, a combination of APT and positron annihilation spectroscopy (PAS) analysis also revealed the presence of vacancy-rich SRC complexes [11,12] in both western and Russian types of RPV steels. Hence, the mechanism of nucleation of SRCs on vacancies also needs to be clarified.

Investigation of vacancy-type defects in Fe-based steels cannot be carried without consideration of carbon, which has a great impact on the stability and mobility of vacancies in BCC Fe matrix [13,14]. Carbon atoms are dissolved in BCC iron matrix as

* Corresponding author at: SCK•CEN, Nuclear Materials Science Institute, Boeretang 200, Mol B2400, Belgium. Tel.: +32 486685042.
E-mail address: abakaev@sckcen.be (A. Bakaev).

http://dx.doi.org/10.1016/j.jnucmat.2014.03.031
0022-3115/

interstitial impurities and occupy octahedral sites in the equilibrium lattice [15]. Rigorous *ab initio* calculations have confirmed experimental observations that interstitial carbon (C) is strongly bound to a single vacancy [15] and multiple highly stable carbon–vacancy (C–V) complexes can grow further [16]. Although different *ab initio* codes and methods exhibit some discrepancies in terms of the absolute values of the C–V interaction energies (see analysis in [17,18]), qualitatively they all convey to the same message: mobility and stability of vacancies and small vacancy clusters are defined by the amount of interstitial carbon dissolved in a matrix.

Earlier *ab initio* works dedicated to study of solute alloying elements in bcc Fe also reveal the positive binding energy (i.e. attractive interaction) for several elements with vacancies [19–21], which is especially strong for Cu, Si and P. An interstitial carbon, however, repels most of the studied solutes (Mo, W, Nb, Ta, V, Si, Cr) except for Mn. But in the case of Cu–vacancy–carbon cluster it has been demonstrated that a single vacancy may act as bounding chain for carbon–solute complex, so that the simultaneous presence of Cu–C pair enhances thermal stability of Cu–C–vacancy complex [22]. This result might provide a hint for the nucleation of thermally stable solute–carbon–vacancy (S–C–V) clusters observed in the afore mentioned APT studies.

In this work we therefore perform a parametric *ab initio* study to investigate thermal stability of S–C–V complexes and consider a main set of alloying elements entering the composition of RPV steels, namely: Mn, Ni, Cu, Si, Cr and P. The density functional theory (DFT) method offers an efficient way to consider the energetic stability of small SRC clusters and to validate possible synergetic effects of vacancy–carbon and vacancy–solute binding. Correspondingly, we apply this tool and use exactly the same parameterization (except for the higher cut-off plane wave energy which is necessary for a system with a carbon atom) as in the earlier studies [19,21] to have fully compatible results with the already published data. The main purpose of the work is therefore to identify S–C–V structures with the lowest energy, compute the corresponding binding and dissociation energy of such complexes, and examine evolution of the incremental binding energy by addition of extra solutes to stable S–C–V clusters.

2. Computational details

The DFT calculations were performed with the Vienna Ab Initio Simulation Package VASP [23,24] using the projector-augmented wave (PAW) potentials [25,26]. The electron exchange–correlation functional was described within the generalized gradient approximation using PW91 functionals [27], with a Vosko–Wilk–Nusair interpolation [28]. For Fe, Cr, Mn, Si, Ni, Cu, P and C pseudo potentials with 8, 6, 7, 4, 10, 11, 5 and 4 valence electrons were used, respectively. Ionic relaxation was performed using the conjugate gradient algorithm with a force convergence criterion of 0.03 eV/Å. All the calculations were done keeping the cell shape and volume (equal to the equilibrium volume of bulk iron) constant. The energy cutoff for calculations was 450 eV which was checked to be enough to provide converged results. A $3 \times 3 \times 3$ k-point mesh was sampled by the Monkhorst and Pack scheme for systems with 128 atoms. The lattice parameter of pure ferromagnetic Fe is taken to be 2.831 Å following the previous studies [19,21].

Given that we perform spin-polarized calculations in the ferromagnetic system and introduce an anti-ferromagnetic impurity (i.e. Mn), one needs to be careful when selecting the initial value of the magnetic moment to ensure that the true minimum energy configuration is obtained after the relaxation. For the configurations involving Mn, we performed additional calculations varying the absolute value and sign of the initial magnetic moment of Mn as some of the results turned out to be particularly sensitive to this choice. Below, we report the results corresponding to the lowest energy configurations only.

To assess the binding energy we apply standard definition conventionally used in many similar DFT works [19]. The binding energy of n defects $\{A_i\}$ is defined as [19]:

$$E_b(\{A_i\}) = \sum_{i=1}^{n} E(A_i) - [E(\{A_i\}) + (n-1)E_0], \quad (1)$$

where $E(A_i)$ is the energy of the configuration containing A_i only, $E(\{A_i\})$ is the energy of the configuration with all the n defects and E_0 refers to a configuration containing no defects or impurities, i.e. bulk bcc iron. Following this notation, a positive value implies an attractive interaction and vice versa.

Considering defect clusters the term 'total interaction energy' refers to the energy which is necessary to separate all the defects away from a cluster. In practice, the dissolution of a complex cluster takes place by consecutive emission of its constitutes and characterization of the energy barrier for that process requires introduction of another term. The energy to remove one entity forming a cluster consisting of N objects will be called *the incremental binding energy* of an object #1 to $N-1$ cluster and will be referred to as E_b^1. If the removal of a single entity (e.g. object #1) from a cluster (containing e.g. three objects) results in the formation of a repulsive configuration (e.g. object #2 repels object #3), the incremental binding energy for object #1 is considered to be equal to the total binding energy of the cluster 1–3.

3. Results and discussion

Characterization of a possible synergetic effect of solute–carbon–vacancy interaction requires subdivision of the interaction energy between different entities and its estimation as a function of mutual spacing. This section therefore contains five subsections dedicated to the study of carbon–vacancy, solute–solute, solute–vacancy, solute–carbon and solute–carbon–vacancy in one cluster. For the sake of briefness, we shall use the notations S, C and V for the considered constitutes.

3.1. Carbon–vacancy interaction

Using the above described DFT parameterization set, we have recalculated the vacancy–carbon interaction energy which was found to be 0.70 eV, being the maximum value at the distance of $a_0/2$ between C and vacancy. This value is close to 0.64 eV, which was deduced using the formation energies reported by Forst et al. in [16]. In that work, a larger supercell was used, which eventually explains the deviation of 0.06 eV [16]. Note that the earlier study of Domain et al. reports rather low value of the C–V binding energy, namely 0.47 eV [15]. The reason for the discrepancy with our calculations and results of Forst et al. is discussed in [17].

In the discussion below, we will refer to the migration energy for carbon which is taken to be 0.92 eV as estimated by Domain et al. [15], being very close to the experimental values of 0.88 eV [29] and 0.85 eV [30]. We will use the value for the vacancy migration energy of 0.65 eV [31], which was obtained by VASP with a similar parameterization as here. Thus, the dissociation of the vacancy–carbon pair is to occur via emission of a vacancy (for details see [17]) and the corresponding dissociation energy is $E_d = 1.35$ eV, conventionally calculated as a sum of the binding energy and the migration energy (of the emitting specie).

3.2. Solute–solute interaction

The S–S interaction at the distance of 1nn (first nearest neighbour) and 2nn (second nearest neighbour) is shown in Fig. 1. As calculated in [19,21] there is an attractive binding energy between a pair of Mn or Cu atoms at the 1nn position which vanishes at the 2nn distance. The pairs of P atoms, for which we performed additional calculations, repel each other at 1nn distance and the repulsion is negligible at the 2nn distance. Si–Si or Cr–Cr form strongly repelling configurations in the both 1nn and 2nn positions. Ni shows negligible interaction with another Ni atom added in either 1nn or 2nn position.

3.3. Solute–vacancy interaction

The S–V binding energy as a function of distance is presented in Fig. 2. All the considered solutes exhibit attractive interaction with the vacancy which vanishes at the 3nn distance. Ni is, however, the only element showing non-monotonic binding energy, with the maximum in the 2nn position. P and Si reveal the strongest interaction energy to a vacancy (0.38 eV and 0.29 eV, respectively), which are 3p elements and therefore have strong contribution to the magnetic disorder. While, Cr and Ni show the weakest interaction (binding up to 0.1 eV), although Ni binds stronger in the 2nn position. Mn and Cu exhibit moderate binding energy in the range 0.16–0.26 eV.

3.4. Solute–carbon interaction

The solute–carbon interaction, presented in Fig. 3a, was inspected by placing a carbon atom in each octahedral position within the 5th nearest neighbour distance from the solute. The interaction vanishes to zero at the distance of $3/2a_0$ and is strongly repulsive for all the solutes except for Mn. Previously, the attractive interaction for Mn–carbon was also reported in [32]. It is also important to mention that Si and P exhibit outstandingly strong repulsive interaction with carbon being initially placed at a distance of $0.75–0.90a_0$. The interaction energy for all the other elements monotonically descents with the S–C distance.

In the calculations involving Mn atom, we have attempted several initial guesses for the Mn spin (both co- and anti-aligned with Fe atoms). The lowest energy configuration, revealing weak but attractive interaction, was obtained for the ferromagnetic spin orientation. The displacement of carbon atom from its perfect octahedral position after the complete relaxation of Mn–C pair (see Fig. 3b) was practically negligible, while we observed a significant shift of the magnetic moment on Mn atom (by +2.75 μ_B, see Fig. 3(d)). The observed effect might therefore be related to the peculiar magnetic relaxation of anti-ferromagnetic manganese inside the ferromagnetic iron matrix in the vicinity of carbon, which introduces certain magnetic disturbance/disorder on magnetic behaviour of Fe atoms.

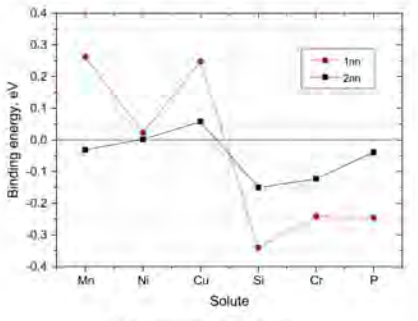

Fig. 1. Solute–solute binding energy.

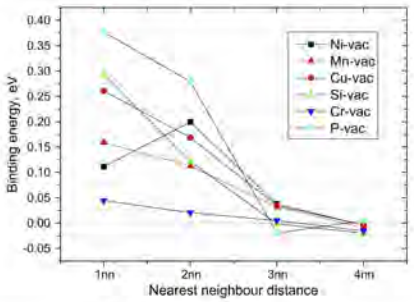

Fig. 2. Solute–vacancy binding energy.

The relaxation-induced displacement of the carbon and other solute atoms as well as the change of their magnetic moments are shown in Fig. 3(b)–(e). One can see that the solute displacement for the interaction with carbon in the 1nn is practically similar for all the solutes, except for P atom, and the displacement essentially drops in the 2nn position (and for larger distances). The displacement of carbon atom, on the other hand, depends greatly on the solute type and in the case of P, Si, Cr, Mn and Cu it is higher for the 2nn position than for the 1nn one. Consistently, Si–C and P–C interaction is found to be stronger in the 2nn pair. The strong repulsion for Si–C and P–C pairs should therefore be attributed to the elastic interaction.

3.5. Solute–vacancy–carbon complexes

Following the above presented data for the pair interaction of different constitutes, one can anticipate the structure of the most favourable S–C–V clusters. As the carbon–vacancy interaction is expected to provide the highest binding, the nuclei should involve this pair as shown in Fig. 4. Then, all the possible neighbourhood positions for a solute were considered accounting for the crystal symmetry. The complex with the lowest formation energy is shown in Fig. 4 and this configuration provides the lowest energy state for all the studied solutes. The cluster structure represents itself a triangle, where the vacancy stands as 1nn to a solute, while the S–C distance is $\sqrt{6}/2a_0 \approx 1.2a_0$.

The total and incremental binding energies for S–C–V clusters as well as the dissociation energies are shown in Fig. 5. The two straight solid lines reveal the V–C binding and dissociation energy to provide the reference and underline the synergetic effect of the solute addition. Following the energy balance, one reveals that the emission of a vacancy from all the complexes (except for Mn–V–C) results in the formation of the repulsive carbon–solute pair. For those cases the incremental binding energy $E_b^I(CS + V)$ is considered to be equal to the total binding energy $E_b(S + V + C)$. In the case of Mn solute the incremental binding energy $E_b^I(CMn + V)$ is equal to 0.80 eV. From Fig. 5 it clearly follows that the total binding energy $E_b(S + V + C)$ is essentially higher than solute–vacancy binding energy $E_b(S + V)$ and lays above the vacancy–carbon binding

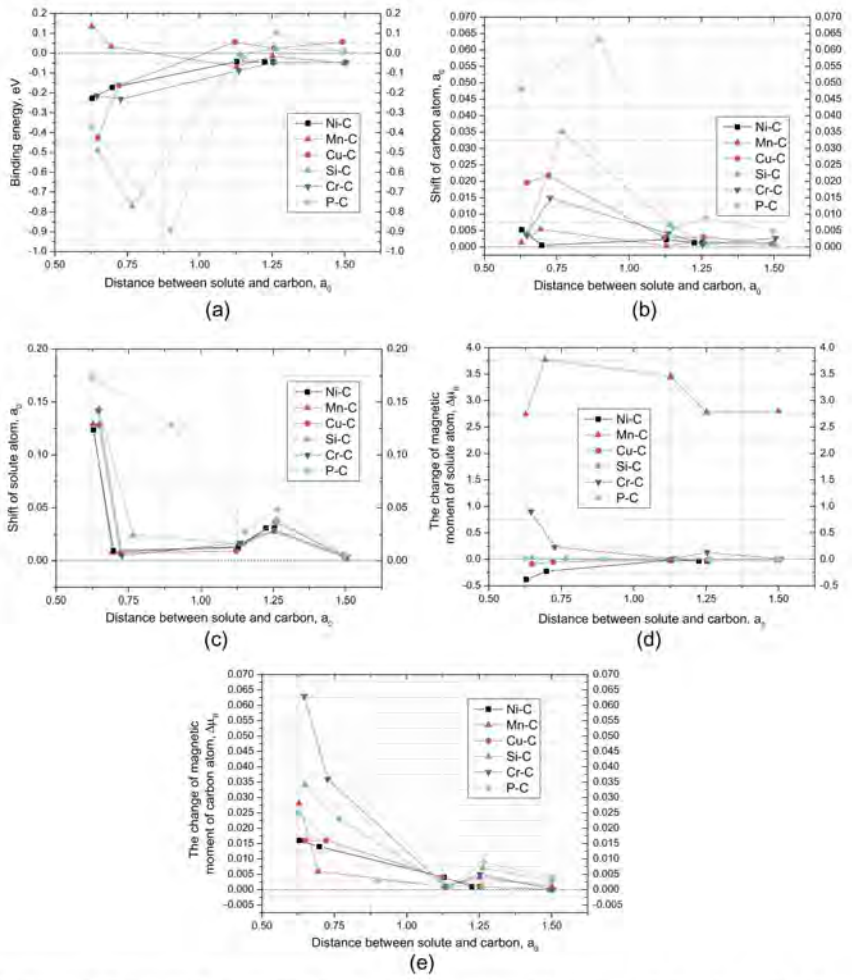

Fig. 3. (a) Solute–carbon binding energy. Displacement of (b) carbon atom and (c) solute atom obtained after the relaxation of solute–carbon pair. Change of magnetic moments of (d) solute and (e) carbon atoms obtained after the relaxation of solute–carbon pair.

energy $E_b(V+C)$ value. The incremental binding energy of carbon in the triple complex $E_b^I(VS+C)$ is approximately the same as its binding with vacancy $E_b(V+C)$.

Due to the increase of the binding of a vacancy in the triple complex (as compared to V–C) by approximately 0.2–0.3 eV the dissociating specie in the triple complex (either carbon or vacancy) will be defined by the type of the solute constituting the cluster. The dissociation energies for a vacancy and carbon from each of the considered S–V–C complexes are compared in Fig. 5.

The dissociation by the emission of an interstitial carbon requires a lower energy barrier than for a vacancy in the case of phosphorus–V–C complex. While for Ni-, Cr- and Mn-containing clusters the dissociation is more likely to occur by the emission of a vacancy, leading to subsequent breakup of the S–C pair. The dissociation by either of the species is equally probable in the case

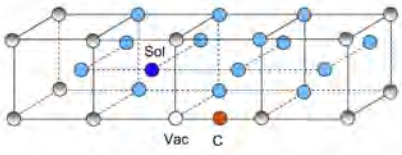

Fig. 4. Considered configurations of solute–vacancy–carbon complexes. Light blue atoms refer to the studied positions of a solute. The dark-blue-coloured atom refers to the lowest energy configuration. Non-filled circle refers to the position of a vacancy. The carbon atom is shown by an orange circle. (For interpretation of the references to colour in this figure legend, the reader is referred to the web version of this article.)

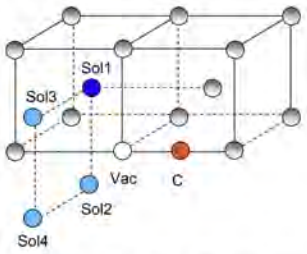

Fig. 6. The schematic picture of larger solute–vacancy–clusters considered.

of Cu and Si. Overall, we see that the dissociation barrier for the S–C–V clusters is by about 0.3 eV higher than E_d(V–C). Hence, the association of vacancies and carbon with any of the studied solutes leads to a higher thermal stability of V–C pairs.

3.6. Addition of extra solutes (up to three) to vacancy–solute–carbon complex

To explore a mechanism of growth of an elementary S–C–V complex and possibility for a multiple trapping, we have considered the addition of extra solutes (up to three) in the equivalent positions and have verified if the inclusion results in a deeper trapping of the mobile species (i.e. C and V). The structures of the inspected clusters are presented in Fig. 6, where all three additional positions are equivalent to the position 'Sol1' with respect to the orientation of the C–V complex.

Firstly, we consider the interaction energy for the extra solutes added to the S–C–V complex. Fig. 7 presents the binding energy of the nth solute to S_{n-1}–C–V complex. So far, we have considered S_n–C–V complexes containing solutes of the same kind. Clearly, all the considered clusters will gain energy by absorbing at least one more solute. However, Mn-, Si- and Cr- containing clusters are not expected to accept the third solute. This can be explained by the solute–solute repulsive interaction taking place for the Cr–Cr and Si–Si pairs. The explanation for the repulsion of 3rd and 4th Mn atom from Mn_2–V–C cluster requires further investigation. It is very likely that the energetic stability of larger Mn-, Cr- and Si- rich clusters could be realized by further addition of vacancies and carbon atoms.

Ni-, Cu- and P-made clusters on the contrary keep gaining the energy as more solutes are added. In the case of Cu, the attractive interaction is consistent with its extremely low solubility limit (in the calculations involving 1–4 Cu atoms its concentration is about 0.8 at.%, 1.6 at.%, 2.3 at.% and 3.1 at.%, respectively, while the solubility limit is below 0.2 at.% at the temperatures below 800 K [33,34]). P atom exhibits very strong positive binding energy to a vacancy, which eventually overwhelms a weaker P–P repulsive interaction, resulting in the energetically stable $P_{2,3,4}$–C–V complexes.

4. Summary and conclusions

In this work we have considered the stability of different solute–carbon–vacancy complexes exploring the solute atoms (Mn, Ni, Cu, Si, Cr and P) entering a composition of typical commercial ferritic steels used as structural nuclear components (such as reactor pressure vessels or high-Cr ferritic/martensitic steels). The purpose of these calculations was to explore whether the formation of

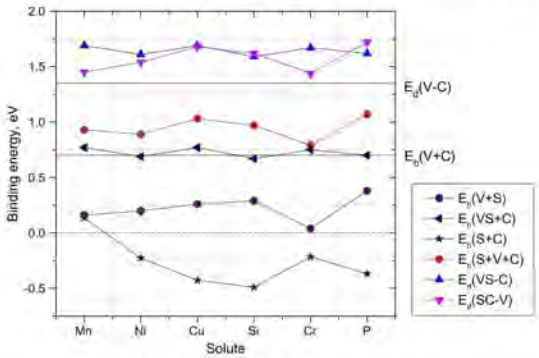

Fig. 5. Comparison of binding and dissociation energies. The following notations are used for: E_b(V + S) solute–vacancy binding energy, E_b(S + C) solute–carbon binding energy; E_b^1[VS + C] incremental binding energy of carbon to vacancy–solute pair; E_b(S + C + V) total binding energy of vacancy–solute–carbon complex; E_d(VS–C) and E_d(SC–V) dissociation energy of vacancy–solute–carbon cluster via the emission of carbon or vacancy, respectively. Black solid lines reveal the vacancy–carbon binding and dissociation energy in the absence of the interaction with solutes.

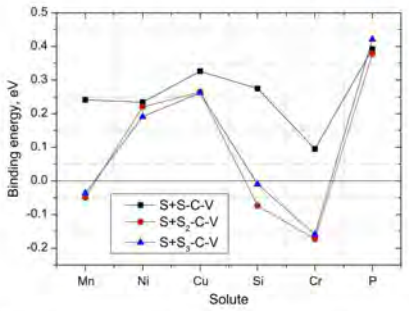

Fig. 7. The incremental binding energy of the nth solute to $S_{(n-1)}$–C–V cluster.

solute–carbon–vacancy complexes is energetically favourable process and to identify the optimal structures corresponding to the lowest energy using the DFT method. We found that all the considered solutes form stable S–C–V clusters, which have the same unique structure irrespective of the solute type. Based on the DFT results, the corresponding binding and dissociation energy for S–C–V triplets and the larger S_n–C–V (n = 2–4) complexes are calculated to examine the effect of the solutes on thermal stability of vacancies and carbon atoms.

The growth of the S–C–V complexes to S_2–C–V (with the same kind of solute) was found to be favourable for all the studied solutes, and Ni-, Cu- and P-containing clusters can accommodate up to three additional solutes. The growth of the Mn-, Cr- and Si-rich clusters is eliminated due to S–S or S–C repulsive interaction. However, the formation of thermally stable S_n–V–C containing mixed types of solutes cannot be ruled out and needs to be further explored.

The binding energy of an interstitial carbon to different S–V complexes is approximately the same as the V–C binding energy. However, the total binding energy is raised by about 0.2–0.3 eV for all the elements except for Cr. The presence of Mn, Cu and Cr slightly increases (by 0.1 eV) the binding energy of carbon to V–S complex, as compared to its binding to a vacancy in the C–V complex.

The dissociation of S–C–V clusters by the emission of an interstitial carbon requires a lower energy barrier than the one of a vacancy only in the case of P. While for Ni-, Cr-, Mn-containing clusters the dissociation is expected to happen by the detachment of a vacancy (leading to immediate breakup of the S–C pair in the case of Ni and Cr). The dissociation by either of the specie is equally probable in the case of Cu and Si. Overall, we see that the dissociation barrier for the S–C–V clusters is by about 0.2–0.3 eV higher than E_d(V–C), therefore the association of vacancies with any of the studied solutes leads to a stronger pinning of both freely migrating interstitial carbon and vacancies.

Acknowledgements

This work, supported by the European Commission under the Contract of Association between EURATOM/SCK-CEN, was carried out within the framework of the European Fusion Development Agreement. The computational resources (Stevin Supercomputer Infrastructure) and services used in this work were provided by the VSC (Flemish Supercomputer Center), funded by Ghent University, the Hercules Foundation and the Flemish Government – department EWI. Part of calculations has been performed at HPC Julich within the 'SORT' project. The research was partly supported by the FWO grant.

References

[1] R.L. Klueh, A.T. Nelson, J. Nucl. Mater. 371 (2007) 37–52.
[2] G.R. Odette, G.E. Lucas, Jom – J. Miner. Met. Mater. Soc. 53 (2001) 18–22.
[3] M.K. Miller, K.F. Russell, J. Nucl. Mater. 371 (2007) 145–160.
[4] Z. Jiao, G.S. Was, Acta Mater. 59 (2011) 1220–1238.
[5] G.S. Was, J.P. Wharry, B. Frisbie, B.D. Wirth, J. Nucl. Mater. 411 (2011) 41–50.
[6] E. Meslin, M. Lambrecht, M. Hernández-Mayoral, F. Bergner, L. Malerba, P. Pareige, B. Radiguet, A. Barbu, D. Gómez-Briceño, A. Ulbricht, A. Almazouzi, J. Nucl. Mater. 406 (2010) 73–83.
[7] V. Kuksenko, C. Pareige, P. Pareige, J. Nucl. Mater. 432 (2013) 160–165.
[8] Z. Jiao, G.S. Was, Acta Mater. 59 (2011) 4467–4481.
[9] G. Bonny, D. Terentyev, A. Bakaev, E.E. Zhurkin, M. Hou, D. Van Neck, L. Malerba, J. Nucl. Mater. 442 (2013) 282–291.
[10] A. Bakaev, D. Terentyev, X. He, D. Van Neck, J. Nucl. Mater. http://dx.doi.org/10.1016/j.jnucmat.2014.02.033.
[11] A. Kuramoto, T. Toyama, T. Takeuchi, Y. Nagai, M. Hasegawa, T. Yoshiie, Y. Nishiyama, J. Nucl. Mater. 425 (2012) 65–70.
[12] A. Kuramoto, T. Toyama, Y. Nagai, K. Inoue, Y. Nozawa, M. Hasegawa, M. Valo, Acta Mater. 61 (2013) 5236–5246.
[13] P. Hautojärvi, J. Johansson, A. Vehanen, J. Yli-Kauppila, Phys. Rev. Lett. 44 (1980) 1326–1329.
[14] P. Hautojarvi, L. Pollanen, A. Vehanen, J. Ylikauppila, J. Nucl. Mater. 114 (1983) 250–259.
[15] C. Domain, C. Becquart, J. Foct, Phys. Rev. B 69 (2004) 144112.
[16] C.J. Forst, J. Slycke, K.J. Van Vliet, S. Yip, Phys. Rev. Lett. 96 (2006) 175501.
[17] D. Terentyev, G. Bonny, A. Bakaev, D.V. Neck, J. Phys.: Condens. Matter. 24 (2012) 385401.
[18] 1998 Microstructural stability of creep resistant alloys for high temperature plant applications, IOM Communications, London.
[19] P. Olsson, T.P.C. Klaver, C. Domain, Phys. Rev. B 81 (2010) 054102.
[20] O.I. Gorbatov, P.A. Korzhavyi, A.V. Ruban, B. Johansson, Y.N. Gornostyrev, J. Nucl. Mater. 419 (2011) 248–255.
[21] A. Bakaev, D. Terentyev, G. Bonny, T.P.C. Klaver, P. Olsson, D. Van Neck, J. Nucl. Mater. 444 (2014) 237–246.
[22] B. Minov, M. Lambrecht, D. Terentyev, C. Domain, M.J. Konstantinovic, Phys. Rev. B 85 (2012).
[23] G. Kresse, J. Hafner, Phys. Rev. B 47 (1993) 558–561.
[24] G. Kresse, J. Furthmuller, Phys. Rev. B 54 (1996) 11169–11186.
[25] P.E. Blochl, Phys. Rev. B 50 (1994) 17953–17979.
[26] G. Kresse, D. Joubert, Phys. Rev. B 59 (1999) 1758–1775.
[27] J.P. Perdew, J.A. Chevary, S.H. Vosko, K.A. Jackson, M.R. Pederson, D.J. Singh, C. Fiolhais, Phys. Rev. B 46 (1992) 6671–6687.
[28] S.H. Vosko, L. Wilk, M. Nusair, Can. J. Phys. 58 (1980) 1200–1211.
[29] S. Takaki, J. Fuss, H. Kuglers, U. Dedek, H. Schultz, Radiat. Effects 79 (1983) 87–122.
[30] A. Vehanen, P. Hautojärvi, J. Johansson, J. Yli-Kauppila, P. Moser, Phys. Rev. B 25 (1982) 762–780.
[31] C. Domain, C. Becquart, Phys. Rev. B 65 (2002) 024103.
[32] N.I. Medvedeva, D.C.V. Aken, J.E. Medvedeva, J. Phys.: Condens. Matter. 23 (2011) 326003.
[33] G. Salje, M. Feller-Kniepmeier, J. Appl. Phys. 48 (1977) 1833–1839.
[34] M. Perez, F. Perrard, V. Massardier, X. Kleber, A. Deschamps, H. de Monestrol, P. Pareige, G. Covarel, Philos. Magn. 85 (2005) 2197–2210.

J Paper X

On the thermal stability of late blooming phases in reactor pressure vessel steels: An atomistic study

G. Bonny, D. Terentyev, A. Bakaev, E.E. Zhurkin, M. Hou, D. Van Neck, L. Malerba

Journal of Nuclear Materials 442 (2013) 282

Journal of Nuclear Materials 442 (2013) 282–291

Contents lists available at SciVerse ScienceDirect

Journal of Nuclear Materials

journal homepage: www.elsevier.com/locate/jnucmat

On the thermal stability of late blooming phases in reactor pressure vessel steels: An atomistic study

G. Bonny [a,*], D. Terentyev [a], A. Bakaev [a,b,c], E.E. Zhurkin [c], M. Hou [d], D. Van Neck [b], L. Malerba [a]

[a] SCK•CEN, Nuclear Materials Science Institute, Boeretang 200, B-2400 Mol, Belgium
[b] Ghent University, Center for Molecular Modeling, Technologiepark 903, B-9052 Zwijnaarde, Belgium
[c] Saint-Petersburg State Polytechnical University, Experimental Nuclear Physics Department, K-89, Faculty of Physics and Mechanics, 29 Polytekhnicheskaya Str., 195252 St. Petersburg, Russia
[d] Université Libre de Bruxelles, CP223, Faculté des Sciences, Bd du Triomphe, B-1050 Bruxelles, Belgium

ARTICLE INFO

Article history:
Received 1 June 2013
Accepted 12 August 2013
Available online 3 September 2013

ABSTRACT

Radiation-induced embrittlement of bainitic steels is the lifetime limiting factor of reactor pressure vessels in existing nuclear light water reactors. The primary mechanism of embrittlement is the obstruction of dislocation motion produced by nanometric defect structures that develop in the bulk of the material due to irradiation. In view of improving the predictive capability of existing models it is necessary to understand better the mechanisms leading to the formation of these defects, amongst which the so-called "late blooming phases". In this work we study the stability of the latter by means of density functional theory (DFT) calculations and Monte Carlo simulations based on a here developed quaternary FeCuNiMn interatomic potential. The potential is based on extensive DFT and experimental data. The reference DFT data on solute–solute interaction reveal that, while Mn–Ni pairs and triplets are unstable, larger clusters are kept together by attractive binding energy. The NiMnCu synergy is found to increase the temperature range of stability of solute atom precipitates in Fe significantly as compared to binary FeNi and FeMn alloys. This allows for thermodynamically stable phases close to reactor temperature, the range of stability being, however, very sensitive to composition.

1. Introduction

Radiation-induced embrittlement of bainitic steels is the lifetime limiting factor of the irreplaceable reactor pressure vessels (RPV) in existing nuclear light water reactors (LWR). The primary mechanism of embrittlement is the obstruction of dislocation motion produced by nanometric defect structures that develop in the bulk of the material due to irradiation. Two classes of nano-structural features are considered as the main contributors to the embrittlement of RPV steels, both hardly visible in the electron microscope: (a) clusters of solute atoms such as Cu, Ni, and Mn, generally catalogued as precipitates; and (b) the so-called 'matrix damage', generally interpreted in terms of clusters of point-defects [1–3].

In the first class of features, one can further distinguish between Cu-rich precipitates (CRPs) [2] and Mn–Ni-rich precipitates (MNPs) [4]. The formation of the latter, which might also not contain Cu, is favoured by low(er) temperature and high Ni (and Mn and Si) content [3]. MNPs without Cu are detected only at sufficiently high neutron fluence, not only in (low-Cu) RPV steels [5,6], but also in FeMnNi model alloys [6,7]. Moreover, based on simplified thermo-dynamic-kinetic models briefly recalled below, there is a belief that precipitates rich in Mn and Ni, once nucleated, will rapidly grow to large volume fractions [3]. For these reasons, they are more commonly denoted as *late blooming phases* (LBP), or confused with them. Their appearance has been associated with the possibility of a sudden and unexpected increase of embrittlement above a certain dose, that cannot be predicted by current commonly used empirical correlations [2,3], thereby posing a question mark on the possibility of extending the lifetime of existing LWR.

In view of improving the predictive capability of existing models it is necessary to understand better the mechanisms leading to the formation of these so-called LBPs, to investigate their stability and to assess their strength as obstacles to dislocation motion. The possibility of forming Cu free MNPs was put forward for the first time in [8], based on regular solution theory calculations and equilibrium lattice Monte Carlo simulations, parameterized purely on the basis of thermodynamic considerations [2–4,9]. These early simulations led to the conclusion that it is thermodynamically favourable for Mn, Ni and Si to precipitate and form clusters at the interface around a core of Cu. Moreover, the results of the simulations suggested that lower temperature and lower Cu content, or higher Mn, Ni and Si content, would favour Mn, Ni and Si

* Corresponding author.
E-mail address: gbonny@sckcen.be (G. Bonny).

0022-3115/$ - see front matter © 2013 Elsevier B.V. All rights reserved.
http://dx.doi.org/10.1016/j.jnucmat.2013.08.038

enrichment of these clusters. The model did not include, however, any description of the mechanisms of precipitation by diffusion, nor any detail about solute/point-defect interaction. It was indeed explicitly assumed that MNPs, as well as CRPs, are stable thermodynamic phases, the formation of which is enhanced under irradiation, and would be more frequently found in low-Cu steels, especially if temperature is low (265 °C versus the usual 288 °C) and dose is fairly high [2,4,8,9].

In a recent study [10], a more advanced simulation methodology was used to investigate the physical mechanism of formation of LBPs. Namely, an atomistic kinetic Monte Carlo model parameterized on electronic structure calculations data was used to study the formation and evolution under irradiation of solute clusters in FeMnNi ternary and FeCuMnNi quaternary alloys. Two populations of clusters were observed to form, which can be discriminated by whether or not the solute atoms are associated with self-interstitials and their clusters. MnNi-rich clusters, that invariably contained a large majority of self-interstitials, were observed to form at a very early stage of the irradiation in both modelled alloys; the quaternary alloys contained also self-interstitial-free, Cu-containing clusters. MnNi-rich clusters nucleated very early via a self-interstitial-driven mechanism, earlier than Cu-rich clusters; the latter, however, grew in number much faster than the former, helped by the strong thermodynamic driving force to Cu precipitation in Fe, thereby becoming dominant in the low dose regime. The kinetics of the number density increase of the two populations was thus significantly different. The somewhat provocative conclusion of that work was that the so-called *late blooming phases* might well be neither *late*, nor *phases*. Indeed, a specific feature of the model used in [10] was that the precipitation of Ni and Mn due to thermodynamic driving forces was implicitly excluded, as a consequence of the fact that the density functional theory (DFT) calculations used to parameterize the model predicted repulsion between Ni and Mn pairs in Fe. Even so, Ni and Mn clusters did form, at very low doses, catalysed by the presence of self-interstitials, thereby showing that the thermodynamic stability of these clusters as phases is *not a necessary condition* for their appearance under irradiation. The intimate relationship between solutes and self-interstitials also casts some doubts on the physical justification of distinguishing between "precipitates" and "matrix damage" as two separate classes of embrittling features.

Nonetheless, the work in [10] left open the question of whether or not NiMn(Si) clusters may or not be regarded as thermodynamic phases and, if so, under which conditions and with which range of stability. As a matter of fact, considering the FeMn and FeNi binary alloys separately, the respective phase diagrams indicate that the solubility limits of Mn and Ni in α-Fe at 300 °C are approximately 3 and 4 wt% respectively [11–14], i.e., significantly higher than the typical Ni and Mn content in RPV steels. Nonetheless, the solubility limit provided for the *ternary* FeMnNi alloy (TCFE5 database) by the *Thermocalc* software [15] (0.64 at.% and 0.2 at.% at 300 °C for Mn and Ni, respectively [7]) is significantly lower, denoting a strong synergy between Ni and Mn in Fe. *Thermocalc* uses an experimental database of thermodynamic functions, extrapolated whenever the available data are insufficient, to calculate the phase diagram of most alloys, based on free energy functions of temperature and concentration and common tangent construction (Computer Coupling of Phase Diagrams and Thermochemistry: Calphad database and formalism). Quite clearly, extrapolation to temperatures for which it is difficult to obtain experimental calorimetric data is always uncertain. In particular, the data for the MnNi interaction used in Calphad originate from an extrapolation of experiments realized by Dinsdale at temperatures ~400 °C [16]. The difference between the results of the DFT-informed model in [10] and the *Thermocalc* results arises from the nature of the MnNi interaction, which is attractive in the Calphad database, while it is repulsive according to so far available DFT calculations [17]. Thus, there seems to be a discrepancy between DFT and Calphad and a good part of the present work is devoted to investigating whether this discrepancy is real or not and whether it can be removed and, if so, how.

This is done by performing new DFT calculations to be used, together with experimental phase diagram indications, to develop a thermodynamically consistent interatomic potential for the FeCuNiMn system. We show that, even though DFT calculations predict instability of Ni–Mn pairs and triplets, Ni–Mn clusters become stable above a certain size. By informing the interatomic potential to this new insight, as well as to other experimental reference data, it becomes possible to use it as a reliable tool to study phase stability in the FeCuNiMn system. The use of appropriate Metropolis Monte Carlo techniques to build the phase diagram of the quaternary alloy from the potential allows us in this work, therefore, to give a reasonable *ab initio*, rather than experimental, estimate of the range of temperature and concentration in which MnNi(Cu) precipitates in Fe can be considered as thermodynamically stable phases, as well as the expected equilibrium concentration of Ni and Mn in those phases.

The advantage of fitting an interatomic potential over building a purely thermodynamic model is that the former can also be fitted, up to a certain extent, to reproduce the interaction of solute atoms with point-defects and their clusters. This is done and partly tested in the present work, opening the way to the study of complexes composed of both point-defects and solute atoms. The ultimate objective is that the interaction of these nanofeatures with dislocations can be investigated quantitatively. As a matter of fact, irrespective of whether solute clusters in RPV steels are or are not thermodynamically stable phases, their association (or not) with point-defect clusters, especially self-interstitial clusters, will influence not only their kinetics of formation and stability, but also, and more importantly, the strength that they oppose as obstacles to dislocation motion.

2. Methods and formalisms

2.1. Density functional theory calculations

The DFT calculations were performed using the Vienna *ab initio* simulation package (VASP) [18,19]. VASP is a plane-wave DFT code that implements the Projector Augmented Wave (PAW) method [20,21]. Standard PAW potentials supplied with VASP were used, with exchange and correlation functional described by the Perdew–Wang parameterization [22] in the Generalised Gradient Approximation (GGA), with a Vosko–Wilk–Nusair interpolation [23]. For Fe, Cu, Ni and Mn pseudo potentials with 8, 11, 10 and 7 valence electrons were used, respectively.

Finite temperature smearing was obtained following the Methfessel–Paxton method with a smearing width of 0.3 eV. The plane-wave cut-off energy was set to 300 eV, which proved sufficient for convergence of the binding and migration energy of the selected configurations. Brillouin zone sampling was performed using the Monkhorst–Pack scheme, where meshes of $3 \times 3 \times 3$ k-points proved sufficient for convergence. The total energy was calculated in periodic bcc supercells containing 128 atoms in a fixed volume set to the equilibrium volume of Fe.

For the defect-solute and solute–solute interactions the total binding energy of a configuration containing n objects ($i = 1...n$) X_i is defined as,

$$E_b(X_1,\ldots,X_n) = \sum_i E(X_i) - \left[E\left(\sum_i X_i\right) + (n-1)E_{ref}\right], \quad (1)$$

where E_{ref} is the energy of the supercell without any objects (pure bcc Fe), $E(X_i)$ is the energy of the supercell containing the single

object X_i, and $E(\sum_i X_i)$ is the energy of the supercell containing all interacting objects. Within this definition positive values of E_b denote attraction.

We note that for spin-polarized calculations concerning antiferromagnetic solutes we took special care in selecting the initial value of the magnetic moments, so as to ensure that the true minimum energy configuration was obtained. In the paper we report the results corresponding to the lowest energy configurations only.

2.2. Interatomic potential

The atomic interactions are described here using the embedded atom method (EAM) [24], which is widely used to describe metals and their alloys. In addition to pair interactions, V, this approach includes an embedding energy, F, that depends on the local electron density, ρ. The latter term approximates the many-body contribution of all nearby atoms. The total energy within the EAM is given as,

$$E = \frac{1}{2}\sum_{\substack{i,j=1 \\ j\neq i}}^{N} V_{t_i t_j}(r_{ij}) + \sum_{i=1}^{N} F_{t_i}(\rho_i), \tag{2}$$

Here N represents the total number of atoms in the system, r_{ij} is the distance between atoms i and j, and t_i denotes chemical species (Fe, Ni, Cu or Mn in our case). The local electron density around atom i, contributed from its neighbours, is given as,

$$\rho_i = \sum_{\substack{j=1 \\ j\neq i}}^{N} \varphi_{t_j}(r_{ij}), \tag{3}$$

where φ denotes the electron density function of the considered element. Thus, for the FeNiCuMn quaternary system 18 functions need to be defined: φ_{Fe}, φ_{Ni}, φ_{Cu}, φ_{Mn}, F_{Fe}, F_{Ni}, F_{Cu}, F_{Mn}, V_{FeFe}, V_{NiNi}, V_{CuCu}, V_{MnMn}, V_{FeNi}, V_{FeCu}, V_{FeMn}, V_{NiCu}, V_{NiMn}, and V_{CuMn}.

In this work we use as starting point the state-of-the-art ternary FeNiCu potential [25]. In this potential, the Fe part is taken from Mendelev et al. [26] ('potential 2'), the Cu part from Mishin et al. [27] ('EAM 1') and the Ni part from Voter and Chen [28]. The Fe potential has been widely used, tested and has demonstrated so far to be the one that succeeds at best in reproducing the properties of iron that are of interest for radiation damage studies [29], including dislocation properties [30]. The Cu and Ni potentials, though not specifically developed to model radiation damage, represent state-of-the-art potentials that are suitable for our purposes. The Fe–Cu, Fe–Ni and Ni–Cu interactions in this potential were fitted using the experimental phase diagram as direct reference, while following DFT indications to fit the point-defect/solute-atom interaction and vacancy migration barriers, as described in [25,31,32].

In the literature we found two modified embedded atom method (MEAM) potentials to describe Mn, developed by Torelli et al. [33] and Kim et al. [34]. However, for reasons of compatibility with the ternary EAM type FeNiCu potential a Mn potential of EAM type is desirable. Thus, six functions remain to be fitted in the present work: φ_{Mn}, F_{Mn}, V_{MnMn}, V_{FeMn}, V_{NiMn}, and V_{CuMn}. Similarly to the FeNiCu potential, we target for the fitting the experimental phase diagram, as well as both experimental and DFT indications concerning point-defect/solute-atom interaction and vacancy migration barriers. The methodology used to do so is detailed in [35] and the parameterization of the fitted functions is given in Appendix A. In Sections 3 and 4 the data selected for the fitting are discussed.

As DFT indication we used three different data sets: our own calculations (detailed in Section 2.1), another PAW-based data set and a data set obtained using ultra soft pseudo potentials (USPP). The references to the latter two data sets are given in the caption text of the tables with initial ab initio fitting data. As a general rule, priority was given to the USPP data set for reasons of consistency, as the FeNiCu potential was also fitted to that data set. In the absence of USPP data or in the necessity of a trade-off, other data were used.

2.3. Monte Carlo calculations

In this work the phase boundaries were estimated by means of Metropolis Monte Carlo (MC) sampling [36] within the isobaric semi-grand canonical ensemble (N, P, T, $\Delta\mu$) for binaries and isobaric grand canonical ensemble (N, P, T) for ternary and quaternary, respectively. Both MC methods include three types of trials of which two are common to both methods: (i) a random displacement of all atoms from their current positions (by this trial lattice relaxation and vibrational entropy are accounted for); (ii) the overall volume change of the simulation box (this trial allows the desired pressure to be maintained, even if a structural transition was to occur). In the semi-grand canonical ensemble the third trial consists of the change of species of a randomly picked atom (by this trial the equilibrium composition is sampled), while in the grand canonical ensemble the latter consists of the random exchange of two atoms of different species (by this trial the equilibrium configurations are sampled). The decision on the acceptance of the new configuration is based on the standard Metropolis algorithm [36] and one set of these trials is termed an "MC step".

The phase boundaries are obtained by scanning the chemical potential difference, $\Delta\mu$ versus composition. A plot of such a curve is obtained at every desired temperature and any discontinuity in the latter is interpreted as a phase transition (see [37] and references therein for more details). In order to identify the solubility limit at a given temperature, the average composition of the last three points (which show statistical scatter) is taken before the phase transition occurs, the maximum spread in the latter serving as error bar.

The ternary and quaternary phase boundaries are obtained by scanning the temperature (50 K temperature grid) for different compositions (0.5–2% Ni or Mn and 0–0.5% Cu). In this way the phase boundary was established by visual inspection of precipitation. The disadvantage of such simulations compared to the ones for the binaries is that they are lengthy (typically 5×10^6 MC steps after thermalization by molecular dynamics) and large box sizes are necessary (containing 21,296 atoms) to minimize surface effects. On the other hand, the advantage is that these simulations are simple and provide precise information on the precipitate morphology and composition.

3. Manganese: DFT data and interatomic potential

Pure manganese undergoes the following allotropic transformations: (i) the ground state is non-collinear anti-ferromagnetic α-Mn (Strukturbericht A12) with Néel temperature $T_N \approx 98$ K, (ii) at 1000 K paramagnetic β-Mn is stabilized (Strukturbericht A13), (iii) in the range 1368–1406 K γ-Mn appears (fcc – Strukturbericht A1), (iv) from 1406 K up to melting point, $T_M = 1517$ K, δ-Mn is the stable structure (bcc – Strukturbericht A2). The three independent elastic constants obtained from experiment (on polycrystals) for α-Mn are $C_{11} = 203$ GPa, $C_{12} = 33$ GPa and $C_{44} = 85$ GPa (values are for the anti-ferromagnetic phase at 4 K and are similar to the ones observed in the paramagnetic phase [38]). This yields a bulk modulus, $B = \frac{1}{3}(C_{11} + 2C_{12})$, of 90 GPa, which is compatible within the range of values found in other experiments, namely: 60 GPa [39], 93 GPa [40], 131 GPa [41], 137 GPa [42] and 158 GPa [43].

The experimental elastic constants reveal a negative Cauchy pressure, $\frac{1}{2}(C_{12}-C_{44})$, of −26 GPa. As reported in [44], this fact points towards angularity in the bonding which cannot be captured within a many-body central framework such as the EAM formalism [45–47]. Since the development of an angular dependent Mn potential is outside the scope of this work (the potential is not meant to describe pure Mn, but Mn as alloying element in Fe: the Mn content in Western-type LWR pressure vessel steels is at most a few per cents) and is incompatible with our EAM type FeNiCu potential, we tried to stabilize α-Mn with modified elastic constants to give a slightly positive Cauchy pressure but conservation of bulk modulus. All such trials, however, met with failure. Either α-Mn was not the ground state structure, or the embedding function had a negative curvature, which is physically unacceptable. It is interesting to note, from an EAM fitting viewpoint, that the stabilization of α-Mn seemed to be closely correlated to a negative Cauchy pressure.

Given the failure to produce an EAM type potential that stabilizes α-Mn as the ground state, we alternatively chose γ-Mn as the ground state. This choice can be justified as in metallurgy Mn is known to be an austenizer when added as solute in iron [48]. To obtain the target cohesive energy for γ-Mn and the competing δ-Mn and ε-Mn (hcp – Strukturbericht A3) we used DFT calculated energy differences reported in [49,50] (see Table 1) with as reference the experimentally measured cohesive energy for α-Mn, $E_c = 2.92$ eV [51]. However, from these values ε-Mn is stabilized over γ-Mn, which in reality is only expected to stabilize under high pressure [43]. To avoid this complexity, we opted to fit a short range EAM potential such that both hcp and fcc structures are degenerate. We also mention here that the γ-δ energy difference predicted by DFT was chosen as reference instead of the Calphad data, because the latter gave rise to a potential with fcc/bcc transition temperature below 300 K.

No experimental value is available for the elastic constants of γ-Mn. Therefore we performed DFT calculations on antiferromagnetic (AFM) crystals ($L1_0$ ordered ground state [50]) and non-magnetic (NM) crystals (emulating the paramagnetic state – experimentally an anti-ferromagnetic – paramagnetic transition is observed in quenched γ-Mn crystals at ~500 K [53,54]). The DFT results obtained for the three independent elastic constants are summarized in Table 1. We observe a large discrepancy between AFM and NM calculations, especially for the bulk modulus. This is consistent with similar calculations performed on α-Mn [49] and β-Mn [50]. Given the softness of Mn and the small discrepancy between the elastic constants measured in anti-ferromagnetic and paramagnetic α-Mn crystals, we believe that our anti-ferromagnetic results seem the most reasonable input. It must be noted, however, that the AFM results yield a negative Cauchy pressure of −52 GPa. For the sake of fitting an EAM-type Mn potential, however, we have (artificially) chosen a small but positive Cauchy pressure of 10 GPa as target value. The bulk modulus B and C', on the other hand, were kept as obtained from the DFT calculations (see Table 1). The latter modifications should have little or no influence when studying Fe-rich alloys.

The fcc/bcc transition and melting temperature of the potential were obtained by means of thermodynamic integrations [55,56]. By performing the latter we obtained the Helmholtz free energy of the fcc and bcc phase as well as the Gibbs free energy of the liquid phase as a function of temperature. We note that for the solid phases we constrained the volume to avoid allotropic transformations during the thermodynamic integration. As a result, the transition from fcc to bcc and bcc to liquid were estimated from the intersections of the respective free energy curves. The results of this procedure are summarized in Table 1.

Having discussed all desired properties of the Mn potential, its actual properties are summarized and compared to DFT, Calphad and experimental data in Table 1. Given the above discussed constraints and the expected use of the potential, we consider its performance adequate for our purposes.

Table 1
Comparison of basic properties of Mn with predictions by the potential.

Property	Experiment or calculation	Potential
$E_c(\gamma\text{-Mn})$ (eV/atom)	2.888[a]/2.853[c]	2.889
$\Delta E_c(\gamma-\delta)$ (eV/atom)	0.008[a]/0.079[c]	0.081
$\Delta E_c(\gamma-\alpha)$ (eV/atom)	−0.010[a]/−0.006[c]	0.000
$a_0(\gamma\text{-Mn})$ (Å)	3.750[a]/3.547[c]/3.551[d]/3.496[e]	3.496
$a_0(\delta\text{-Mn})$ (Å)	2.812[c]	2.812
$a_0(\varepsilon\text{-Mn})$ (Å)	–	Ideal a/c ratio
B(GPa)	99[f]/251[g]	99
C'(GPa)	35[f]/84[g]	35
$\frac{1}{2}(C_{12}-C_{44})$ (GPa)	−52[f]/3[g]	10
$T_{bcc\to liq}$ (K)	1406	1127 ± 40
$T_{bcc\to liq}$ (K)	1517/1411[c]	1353 ± 40

[a] Based on experiment and Calphad assessment, Refs. [12,51].
[b] Based on experiment and DFT calculations, Refs. [49–51].
[c] Calphad assessment, Ref. [12].
[d] DFT calculations, Refs. [49,50].
[e] Experiment, Ref. [52].
[f] DFT, this work, calculations in anti-ferromagnetic ground state (Li_0 magnetic ordering).
[g] DFT, this work, calculations in non-magnetic ground state.

4. The quaternary alloy: DFT data and interatomic potentials

4.1. Iron-manganese

In Table 2 point-defect properties of Mn in a bcc Fe matrix calculated by both DFT and the potential are summarized. Properties that were explicitly targeted during the fit of the potential are indicated with the symbol *.

In general, the USPP data set predicts less binding or more repulsion than the PAW data set. Although they generally predict the same trend, there are some striking qualitative differences: repulsion (USPP) versus attraction (PAW) of Mn–Mn pairs and repulsion versus neutral interaction for Mn in the tensile region of a ⟨1 1 0⟩ self-interstitial atom (SIA). Given the quantitative uncertainty and qualitative indefiniteness in the binding energy for

Table 2
Comparison of point-defect Mn-solute properties in the bcc Fe matrix between DFT and the potential.

Property	DFT (eV)	Potential (eV)
E_b Mn–Mn (1nn)*	−0.28[a]/0.08[b]	0.02
E_b Mn–Mn (2nn)*	−0.20[a]/0.04[b]	0.01
E_b Mn–Vac (1nn)	0.12[a]/0.21[b]	−0.02
E_b Mn–Vac (2nn)	0.07[a]/0.14[b]	0.00
$E_f(1\,1\,0)$ (Mn)	3.70[c]	4.69
$E_f(1\,1\,1)$–$E_f(1\,1\,0)$ (Mn)	0.63[c]	0.37
$E_f(1\,0\,0)$–$E_f(1\,1\,0)$ (Mn)	1.15[c]	0.72
E_f(Octa)–$E_f(1\,1\,0)$ (Mn)	1.26[c]	0.77
E_f(Tetra)–$E_f(1\,1\,0)$ (Mn)	0.42[c]	0.79
$E_{sp}(1\,1\,0)$ Fe–Mn*	0.37[a]/0.57[b]	0.37
E_b SIA Mn in tension	−0.36[a]/0.03[b]	0.01
E_b SIA Mn in compression	0.10[a]/0.35[b]	0.07
$E_b(1\,1\,0)$ Fe–Mn. Mn in compression	0.29[c]	0.31
$E_b(1\,1\,0)$ Mn–Mn	0.47[c]	0.33
E_b Fe–Mn crowdion	0.66[c]	0.49
E_{mf}(Vac → Mn)*	1.03[a]/0.93[b]	1.06
$E_{mf}(1\,1\,0) \to (0\,1\,1))$ (Mn)	0.34[d]	0.34

[a] DFT, USPP, Ref. [58].
[b] DFT, PAW, Ref. [59].
[c] DFT, PAW, this work.
[d] DFT, USPP, Ref. [60].

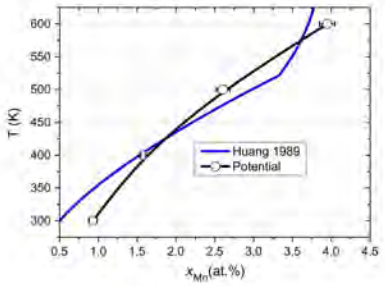

Fig. 1. Comparison between experimental Mn solubility and the one obtained from the potential.

Mn–Mn pairs, we decided to keep its value small and make a close fit to the FeMn experimental solubility limit (see Fig. 1). We note that, given this constraint, it proved impossible to fit a significant Mn-vacancy binding. Any effort to try to do so resulted in a strong underestimation of Mn solubility, and given the study at hand we opted for reproducing the latter correctly.

From the DFT calculated formation energy of the different interstitial Mn configurations, summarized in Table 2, it is clear that the ⟨110⟩ mixed dumbbell is the most favourable configuration. In addition, the latter configuration gives a strong binding energy, as well as the Mn crowdion. All these important effects are well reproduced by the potential. From the other interstitial configurations summarized in Table 2 we learn that Mn essentially behaves as an undersized atom as it exhibits binding in compressed zones and even allows for a stable ⟨110⟩ MnMn mixed dumbbell. Again, all these effects are well reproduced by the potential.

Finally, we mention that the Mn-vacancy exchange barrier and Mn Johnson jump [57] are in excellent agreement with the DFT values.

The Fe-rich phase boundary obtained with the potential is compared with the Calphad calculated one [12] in Fig. 1. The kink in the Calphad curve observed around ~520 K is of magnetic origin and cannot be reproduced within an EAM framework. Nevertheless, the agreement between potential and Calphad calculations is satisfactory.

4.2. Iron–manganese–nickel

In Table 3 properties of small NiMn clusters in a bcc Fe matrix calculated by both DFT and the potential are summarized. Properties that were explicitly targeted during the fitting of the potential are indicated with the symbol *.

Considering the DFT data first, we observe that pure Mn and Ni clusters in Fe are binding, Mn clusters being the most stable ones. Mixed NiMn clusters, on the other hand, are repulsive for clusters up to size 3 and stable starting from size 4. Thus the apparent contradiction between DFT and Calphad, discussed in the introduction, is resolved if large enough clusters (>size 4) are taken.

However, when fitting a potential with repulsive NiMn pairs, it is impossible to stabilize mixed clusters, irrespective of the size. Therefore we opted for fitting a small but binding value also for NiMn pairs, even though this is at variance with DFT, and use the experimental NiMn phase diagram as additional fitting input. Given this constraint and as shown in Table 3, we observe that the potential does allow for the formation of mixed NiMn clusters.

Table 3
Comparison of the binding energy of MnNi clusters in the bcc Fe matrix between DFT and the potential.

Property	DFT (eV)	Potential (eV)
E_b Ni–Mn (1nn)[c]	−0.06[b]/0.00[c]	0.01
E_b Ni–Mn (2nn)[c]	−0.06[b]/−0.08[c]	0.00
E_b triangle Mn_2	0.11[b]	0.05
E_b triangle $NiMn_2$	−0.05[b]	0.03
E_b triangle Ni_2Mn	−0.01[b]	0.13
E_b triangle Ni_3	0.05[b]	0.06
E_b tetrahedron Mn_4	0.20[b]	0.10
E_b tetrahedron $NiMn_3$	0.08[b]	0.08
E_b tetrahedron Ni_2Mn_2 (Ni 1nn)	0.00[b]	0.02
E_b tetrahedron Ni_2Mn_2 (Ni 2nn)	0.02[b]	0.16
E_b tetrahedron Ni_3Mn	0.05[b]	0.08
E_b tetrahedron Ni_4	0.10[b]	0.09
E_b⟨110⟩ Ni–Mn[c]	0.12[c]	0.12

[a] DFT, USPP, Ref. [58].
[b] DFT, PAW, this work.
[c] DFT, USPP, Ref. [60].

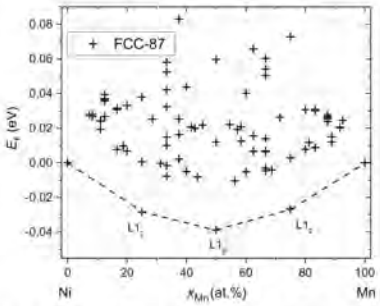

Fig. 2. Possible ground state intermetallics of the NiMn system at zero Kelvin as obtained by the potential.

Finally, we mention that the ⟨110⟩ NiMn dumbbell is stable with the potential and reproduces the DFT value.

In Fig. 2 the zero Kelvin phase diagram is presented in the form of a superposition of possible ground state intermetallics, i.e., FCC-87 ground state structures (see [35] for more details). Briefly, for the desired intermetallics to be true ground states of the system, all other candidate states should lie above the convex hull of the latter. As shown in Fig. 2, the potential only stabilizes experimentally observed intermetallic phases, which are: the $L1_2$ Ni_3Mn, $NiMn_3$ and $L1_0$ NiMn phases [61–63].

4.3. Iron–manganese–copper

In Table 4 properties of small CuMn clusters in a bcc Fe matrix calculated by both DFT and the potential are summarized. Properties that were explicitly targeted during the fitting of the potential are indicated with the symbol *.

The DFT data on the CuMn pairs predict weak attraction at 1nn and weak repulsion at 2nn distance. Given the uncertainty in the DFT data we gave priority to a close reproduction of the Mn solubility limit in Cu. With respect to clusters, both DFT and the potential predict binding for all configurations, with the binding energy monotonically increasing as Mn atoms are replaced by Cu ones. This trend is supported by experiments, where a small Cu

Table 4
Comparison of the binding energy of MnCu clusters in the bcc Fe matrix between DFT and the potential.

Property	DFT (eV)	Potential (eV)
E_b Cu–Mn (1nn)[a]	0.04[a]/0.13[b]	0.04
E_b Cu–Mn (2nn)[a]	−0.07[a]/−0.02[b]	0.02
E_b triangle Mn_2	0.11[b]	0.05
E_b triangle $CuMn_2$	0.18[b]	0.08
E_b triangle Cu_2Mn	0.34[b]	0.16
E_b triangle Cu_3	0.51[b]	0.24
E_b tetrahedron Mn_4	0.20[b]	0.10
E_b tetrahedron $CuMn_3$	0.32[b]	0.15
E_b tetrahedron Cu_1Mn_2 (Cu 1nn)	0.35[b]	0.22
E_b tetrahedron Cu_1Mn_2 (Cu 2nn)	0.41[b]	0.26
E_b tetrahedron Cu_2Mn	0.66[b]	0.35
E_b tetrahedron Cu_4	0.92[b]	0.48
E_b(110) Cu–Mn[c]	−0.06[c]	0.06

[a] DFT, USPP, Ref. [58].
[b] DFT, PAW, this work.
[c] DFT, USPP, Ref. [60].

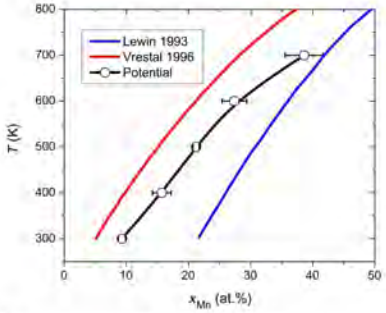

Fig. 3. Comparison between CuMn phase diagrams resulting from thermodynamic models and the potential.

solubility in Fe [64,65] is observed compared to Mn in Fe [12]. It is worth to notice that the total binding energy of CuMn clusters is higher than that of NiMn clusters; an effect that is also reproduced by the potential.

Finally, we mention that the ⟨110⟩ CuMn is unstable both according to DFT and potential.

In Fig. 3 the Mn solubility limit in Cu obtained from Calphad calculations [66,67] and the potential are compared. We notice that the uncertainty on the Calphad calculations is large and the chosen parameterizations represent the limiting cases. The solubility limit predicted by the potential lays between the limiting cases.

5. Thermal stability of nickel-manganese-copper clusters

In this section we present the results from exchange Monte Carlo in isobaric grand canonical ensemble using the above developed potential. We thus provide an estimate of the solubility of NiMn and NiMnCu clusters in a bcc Fe matrix.

In Fig. 4 the NiMn solubility limit for the FeNiMn alloy is presented. Clearly there exists a synergy between Ni and Mn, as the addition of either element elevates the solvus by up to 150 K compared to the binary FeNi and FeMn solubility limits; or, alternatively, at any given temperature in the range considered the solubility limit moves towards smaller concentrations. The latter is consistent with the thermodynamic calculations in [6].

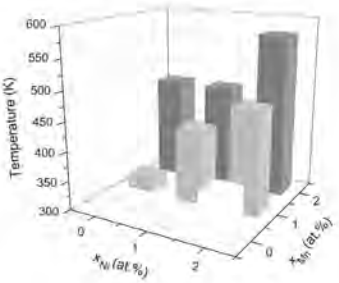

Fig. 4. The NiMn solubility limit in the ternary FeNiMn alloy resulting from the MMC simulations.

For the ternary alloys exhibiting phase separation with concentrations $x_{Ni} \geqslant x_{Mn}$ we found the coexistence of two phases in the form of the Fe-rich matrix and a single NiMn precipitate. The latter precipitates are nearly spherical and composed of an equimolar Ni and Mn fraction with a negligible amount of Fe. In fact, closer inspection reveals that the B2 intermetallic is formed, as shown in Fig. 5a. The formation of this intermetallic can be rationalized from the NiMn phase diagrams where an intermetallic at 50%Mn (Ni) occurs. The excess amounts of Ni are soluble in the Fe-rich matrix.

For the ternary alloys exhibiting phase separation with concentrations $x_{Ni} < x_{Mn}$ we found the coexistence of three phases in the form of the Fe-rich matrix, a single B2 ordered NiMn precipitate and an additional Mn-rich precipitate. Both precipitates are nearly spherical (containing a negligible amount of Fe) and the latter contains ~20% of Ni homogeneously distributed in the Mn-rich precipitate, as visualized in Fig. 5b.

The addition of 0.5% Cu (well beyond the Cu solubility in Fe) to the ternary FeNiMn alloy has a significant impact on the phase diagram. Two situations are identified: (i) the Cu precipitates together with Ni and Mn forming a ternary phase (see Fig. 6a) and (ii) the Cu precipitates without active involvement of Ni and Mn (see Fig. 6b). In the first situation, a nearly spherical precipitate is formed consisting of a mixture of ~20% Cu, ~40% Ni and ~40% Mn, as visualized in Fig. 6a. The second situation involves a nearly spherical Cu precipitate with a dilute shell of Ni and Mn atoms attached to it, similar to the observation of Cu-rich precipitates with a dilute Ni shell in supersaturated FeNiCu alloys [25].

It is interesting to note that similar type of NiMn and CuNiMn clusters were found in the work of Odette and Wirth [4]. In particular, for quaternary alloys containing 0.4% Cu, 1.4% Mn and various amounts of Ni ($x_{Ni} < x_{Mn}$) in the temperature range 533–566 K they observed nearly pure Cu clusters surrounded by a patchy Mn and Ni shell. For the highest Ni contents (>1.12% Ni), the NiMn shell was ordered or grown as an appendage epitaxial to a nearly pure Cu region. Judging from our results, the latter observation probably indicates a three phase region: (i) Fe-rich matrix, (ii) NiMn ordered phase (see Fig. 5a) and (iii) Cu precipitate with NiMn shell (see Fig. 6b). As shown below (see Fig. 7), the selected temperature and composition ranges probably prohibit the formation of the ternary CuNiMn phase. We conclude that the present results are not in contradiction with the findings in [4].

In Fig. 7 we compare the solubility limit for the FeNiMn (for equal Ni and Mn content) with the one containing an additional 0.5% Cu. For clarity, we identified situation (i) as phase separation while situation (ii) was identified as full solubility of Ni and Mn.

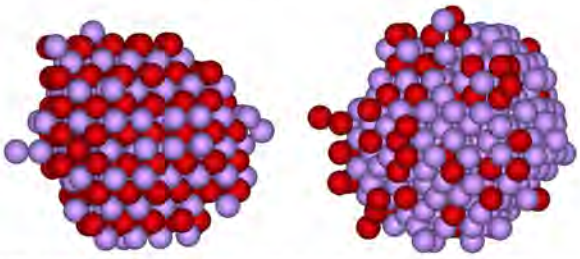

Fig. 5. Precipitate (a) B2 and (b) Mn-rich precipitates. The red (dark) atoms denote Ni while the purple (light) atoms denote Mn. (For interpretation of the references to colour in this figure legend, the reader is referred to the web version of this article.)

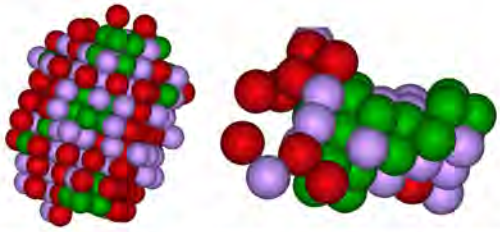

Fig. 6. Precipitate (a) ternary CuMnNi rich precipitate. The red (dark) atoms denote Ni, the purple (light) atoms denote Mn and the green (grey) atoms denote Cu. (For interpretation of the references to colour in this figure legend, the reader is referred to the web version of this article.)

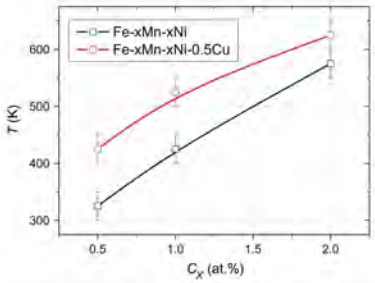

Fig. 7. Comparison of MnNi solubility with or without addition of 0.5% Cu.

We observe a clear synergistic effect of Cu on the solubility limit, raising the latter by 50 K up to 100 K. This means that ternary CuNiMn precipitates may become thermodynamically stable at reactor temperature (~600 K) with sufficiently high Cu and Ni levels.

6. Discussion

We fitted a quaternary interatomic potential to DFT and experimental data of relevance for the study of irradiation effects in the FeNiMnCu alloy. DFT calculations predict instability of NiMn pairs and triplets. However, additional DFT calculations show that NiMn clusters are stable above a certain size. This suggests that it is possible to stabilize NiMn clusters in Fe.

We used the developed potential to study the thermal stability of NiMn(Cu) clusters and verified that the synergy of both or all three elements may indeed lead to stable precipitation at reactor temperature (~600 K), especially if Cu is present in relatively high concentration. Compared to the solubility limit of the binaries, in general we can say that the synergy between Ni and Mn raises the solubility limit by ~100–150 K, while an additional 0.5% Cu raises it by another ~50–100 K. Thus the synergy of Ni, Mn and Cu can raise the solubility limit by up to ~200 K, correspondingly pushing the solvus towards progressively lower concentrations at a given temperature. From the results of Fig. 7, we observe that, in Fe–2%Mn–%2Ni, precipitates would form up to 575 K and the addition of 0.5% Cu would raise this temperature further up to 625 K. This is about 60–70 K higher than the typical reactor's operating temperatures, although of course such a large amount of these solutes is never found in RPV steels. From Fig. 4 we can say that, for a realistic composition of about 1%Ni and 1%Mn, the solvus will be at 450–500 K, so ~50–100 K below the reactor's operating temperature, but the addition of enough Cu might raise the solvus enough to make precipitation thermodynamically possible, although probably the amount of Cu required would exceed the typical Cu content of RPV steels.

As a matter of fact the above analysis is conservative, due to a shortcoming in the FeNi part of the potential. While both FeMn and FeCu were especially fitted to the experimental solubility limit, the FeNi potential was not. Emphasis was put on reproducing the experimentally observed intermetallic phases [32]. As a consequence, the FeNi potential overestimates the experimental Ni solubility in bcc Fe [14] by about a factor five, as shown in Fig. 8. In

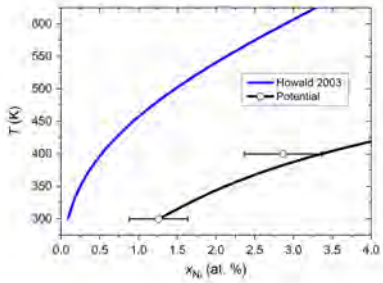

Fig. 8. Comparison between FeNi phase diagrams resulting from thermodynamic models and the potential.

turn, this means that, although all presented results are qualitatively meaningful, the lowest temperature here reported at which precipitates are observed is only a lower boundary. Given the overestimation of the Ni solubility in the binary alloy, the synergy of Ni and Mn might raise the solvus by up to 300 K, resulting in precipitation up to ~725 K and higher for high Ni and Mn content (~2%), when accounting also for the effect of 0.5% Cu. This is more than 150 K above the reactor's operating temperature. It is therefore not impossible that, at the reactor's operating temperature, NiMn and especially NiMnCu precipitates are thermodynamically stable phases.

Nonetheless, the present study does not elucidate whether the operating conditions (temperature and fluence) would allow the thermodynamic equilibrium state to be actually reached. When considering the reactor's operating temperature, for typical solute contents, one sees that it is very close to the solubility limit, i.e., the system under reactor conditions will generally be only barely inside the miscibility gap. Thus, the thermodynamic driving force (i.e. chemical potential) for the formation of MNP will be limited compared to e.g. the one for CRP in high Cu RPV steels and very little variations in composition or temperature might determine whether or not the system is actually inside or outside the miscibility gap. Much will depend on the efficiency of the kinetics leading to precipitation. This might explain why the actual observation of "late-blooming" effects, and especially their effect on mechanical properties, are often elusive and requires relatively low irradiation temperature [69]. At the same time, the fact that even in the best case the composition would be very close to the solvus suggests that it is very unlikely that large volume fractions of MNPs can ppear all of a sudden.

Let us consider now the energy barriers for the different mechanisms that can realize mass transfer. Under thermal annealing condition these are vacancies. The vacancy solute migration barriers are [58], 0.56 eV for Cu, 0.65 eV for Fe, 0.70 eV for Ni and 1.03 eV for Mn. Therefore Cu atoms will re-distribute faster than the Ni ones and Mn will be almost immobile at reactor operating temperature, compared to Cu, Ni and Fe. In other words, under thermal ageing conditions it might prove impossible or very difficult to form MnNi clusters, especially without, or in presence of very little, Cu, even if they were thermodynamically stable.

When considering irradiation, however, the vacancy fluxes drastically increase. Moreover, another mechanism for mass transfer is activated, i.e., self-interstitial diffusion. As only Mn and Fe form stable interstitials, they are the only elements that can be transported in this way. Given their migration barriers of 0.34 eV [68], they diffuse equally fast as self-interstitials in Fe and considerably faster than vacancy mediated diffusion, although their steady-state concentration is likely to be considerably lower than the vacancy concentration, depending on the sink population. Thus, while the rearrangement of Cu and Ni is expected to be mainly driven by vacancy diffusion, the rearrangement of Mn (and Fe) is expected to be mainly driven by self-interstitial diffusion. The higher efficiency of Mn transport over Ni and Cu transport is likely to explain why Mn is observed to precipitate first [6,7,10]. Moreover, transport via self-interstitials would be the origin of the presence of these point-defects in MNPs, and might also be catalysing precipitation, consistently with the prediction of the model proposed in [10]. Yet another effect that would only appear under irradiation and possibly lead to faster nucleation of precipitates than under thermal ageing, even irrespective of their thermodynamic stability, is the segregation at point-defect clusters of solutes transported by point-defects.

The question of whether the above mechanisms form an additional driving force towards the formation of stable NiMn and NiMnCu precipitates, however, together with the actual role of nucleation on point-defect clusters as a mechanism to catalyse precipitation, is at present the subject of speculation. Yet these details are important, because the thermodynamic stability of the precipitates or their association with point-defects might influence significantly the strength of their interaction with dislocations. To clarify this question the development of nanostructure and microchemical evolution models that treat simultaneously point-defect cluster formation and solute transport is necessary. The present potential can contribute to the parameterization of such models. It can equally be used in molecular dynamics simulations to estimate the dislocation obstacle strength of the outcome of the process of precipitation, whichever the mechanism. These are the objectives of future work.

7. Conclusion

We developed an interatomic potential for the FeCuNiMn quaternary alloy based on extensive DFT data on solute–solute and solute-point defect interaction, as well as on experimental data, always privileging experimental consistency within the unavoidable series of compromises that have to be made in the fitting process.

The reference DFT data on solute–solute interaction reveal that, while Mn–Ni pairs and triplets are unstable, larger clusters are actually kept together by attractive binding energy. Thus, the formation of thermodynamically stable Mn–Ni-rich phases in Fe is actually possible and this fact is accounted for by the potential, in agreement with Calphad predictions, thereby removing the apparent discrepancy of the latter with DFT, if only pairs and triplets are considered.

The Ni–Mn synergy increases significantly the temperature range of stability of solute atom precipitates in Fe as compared to binary alloys. Cu is found to extend the range of thermodynamic stability of the precipitates even further, thereby explaining the observations of MNPs, and making their appearance possible in RPV steels, even under thermal ageing and in the absence of Si. Nevertheless, under reactor conditions (temperature, composition...), the system will be barely inside the miscibility gap: small variations in temperature and composition will determine significantly different thermodynamic conditions in terms of precipitate stability, making the production of sufficient volume fractions of these phases to observe a late blooming effect rather elusive. It is therefore speculated that the appearance of Mn–Ni-rich precipitates under irradiation, irrespective of their thermodynamic stability, is actually made kinetically possible by the massive fluxes of point-defects and by point-defect cluster formation, that are strictly the consequence of irradiation.

The mechanism leading to the formation of the so-called late blooming phases, or more correctly Mn–Ni-rich clusters (with

inclusion or not of point-defects), as well as their actual thermodynamic stability under reactor conditions, are assumed to influence their strength as obstacles to dislocation motion, thereby determining (or not) a visible change in the mechanical response of the material after their appearance. The interatomic potential presently developed is expected to contribute significantly to unravel these still open issues.

Acknowledgements

This work was performed in the framework of the EC-funded FP7/PERFORM60 project, under grant agreement 232612. A part of this work was carried out using the HELIOS supercomputer system at Computational Simulation Centre of International Fusion Energy Research Centre (IFERC-CSC), Aomori, Japan, under the Broader Approach collaboration between Euratom and Japan, implemented by Fusion for Energy and JAEA. GB is grateful to N. Baetens for useful discussions.

Appendix A:. potential parameterization

Given the ternary FeNiCu potential [25], the pair potentials V are parameterized as,

Table A1
The optimized parameter set for the present potential.

MnMn			
k	r_k (Å)	a_k (eV Å^{-3})	
1	2.00000000E + 00	1.00000000E + 02	A = −1.82507983E + 00 eV
2	2.50000000E + 00	4.08563703E + 00	B = 9.12539918E-01 eV
3	2.68750000E + 00	−9.53987268E-02	C_0 = 2.29590248E-02
4	2.87500000E + 00	−3.61659426E + 00	r_0 = 4.00000000E + 00 Å
5	3.06250000E + 00	5.80612286E + 00	
6	3.25000000E + 00	−3.92221726E + 00	
7	3.43750000E + 00	3.15773891E + 00	
8	3.62500000E + 00	−5.40379206E + 00	
9	3.81250000E + 00	5.73167705E + 00	
10	4.00000000E + 00	−2.17285477E + 00	
FeMn			
k	r_k (Å)	a_k (eV Å^{-3})	
1	2.00000000E + 00	1.94252170E + 02	
2	2.32857143E + 00	−9.30366408E + 00	
3	2.40000000E + 00	2.50000000E-01	
4	2.65714286E + 00	3.91455751E + 00	
5	2.98571429E + 00	−4.60199252E + 00	
6	3.31428571E + 00	6.24436003E + 00	
7	3.64285714E + 00	−3.79624807E + 00	
8	3.97142857E + 00	1.20087815E + 00	
9	4.30000000E + 00	−2.17700581E-01	
NiMn			
k	r_k (Å)	a_k (eV Å^{-3})	
1	2.00000000E + 00	6.25441631E + 01	
2	2.23142857E + 00	5.09238791E + 00	
3	2.30000000E + 00	2.50000000E + 00	
4	2.46285714E + 00	2.56431281E + 00	
5	2.69428571E + 00	−9.63005933E + 00	
6	2.92571429E + 00	2.02436170E + 01	
7	3.15714286E + 00	−2.20193779E + 01	
8	3.38857143E + 00	1.38210959E + 01	
9	3.62000000E + 00	−3.71026389E + 00	
CuMn			
k	r_k (Å)	a_k (eV Å^{-3})	
1	2.00000000E + 00	6.24913195E + 01	
2	2.30000000E + 00	3.55000000E + 01	
3	2.31428571E + 00	3.44649496E + 00	
4	2.62857143E + 00	−2.91539938E-01	
5	2.94285714E + 00	1.58453589E + 00	
6	3.25714286E + 00	−8.34895346E-01	
7	3.57142857E + 00	−1.07164946E-01	
8	3.88571429E + 00	7.17045029E-01	
9	4.20000000E + 00	−3.62350526E-01	

$$V(r) = \sum_{k=1}^{N_p} \left[a_k (r_k - r)^3 \Theta(r_k - r)\right] \tag{A1}$$

with a_k the spline coefficients, r_k the knots and Θ is the Heaviside function. The density function φ is parameterized as,

$$\varphi(r) = C_0 (r_0 - r)^3 \Theta(r_0 - r), \tag{A2}$$

with r_0 the cut-off knot and C_0 a normalization factor. The embedding function F is parameterized as,

$$F = A\sqrt{\rho} + B\rho \tag{A3}$$

with A and B fitting parameters. The optimized parameter set for the present potential is summarized in Table A1.

References

[1] C.A. English, W.J. Phythian, R.J. McElroy, Mater. Res. Soc. Symp. Proc. 439 (1997) 471.
[2] G.R. Odette, G.E. Lucas, Rad. Eff. Def. Sol. 144 (1998) 189.
[3] G.R. Odette, R.K. Nanstad, JOM 61 (2009) 17.
[4] G.R. Odette, B.D. Wirth, J. Nucl. Mater. 251 (1997) 157.
[5] P. Pareige, J.C. Van Duysen, P. Auger, App. Surf. Sci. 67 (1993) 342.
[6] E. Meslin, B. Radiguet, P. Pareige, A. Barbu, J. Nucl. Mater. 399 (2010) 137.
[7] E. Meslin, B. Radiguet, P. Pareige, C. Toffolon, A. Barbu, Exp. Mech. 51 (2011) 1453.
[8] G.R. Odette, Mater. Res. Soc. Symp. Proc. 373 (1995) 137.
[9] C.L. Liu, G.R. Odette, B.D. Wirth, G.E. Lucas, Mater. Sci. Eng. A 238 (1997) 215.
[10] R. Ngayam-Happy, C.S. Becquart, C. Domain, L. Malerba, J. Nucl. Mater. 426 (2012) 198.
[11] M. Hansen, K. Anderko, Constitution of Binary Alloys, McGraw-Hill Book Co., 1958.
[12] W. Huang, Calphad 13 (1989) 243.
[13] R.A. Howald, Metall. Mater. Trans. A 34 (2003) 1759.
[14] T.B. Massalski, H. Okamoto, Binary Alloys Phase Diagrams, 2nd ed., Plenum, New York, 1996.
[15] J.O. Andersson, T. Helander, L. Höglund, P.F. Shi, B. Sundman, Calphad 26 (2002) 273.
[16] A.T. Dinsdale, Calphad 15 (1989) 317.
[17] E. Vincent, C.S. Becquart, C. Domain, J. Nucl. Mater. 382 (2008) 154.
[18] G. Kresse, J. Hafner, Phys. Rev. B 47 (1993) RC558.
[19] G. Kresse, J. Furthmuller, Phys. Rev. B 54 (1996) 11169.
[20] P.E. Blöchl, Phys. Rev. B 50 (1994) 17953.
[21] G. Kresse, D. Joubert, Phys. Rev. B 59 (1999) 1758.
[22] J.P. Perdew, J.A. Chevary, S.H. Vosko, K.A. Jackson, M.R. Pederson, D.J. Singh, C. Fiolhais, Phys. Rev. B 46 (1992) 6671.
[23] S.H. Vosko, L. Wilk, M. Nusair, Can. J. Phys. 58 (1980) 1200.
[24] M.S. Daw, M.I. Baskes, Phys. Rev. B 29 (1984) 6443.
[25] G. Bonny, R.C. Pasianot, N. Castin, L. Malerba, Philos. Mag. 89 (2009) 3531.
[26] M.I. Mendelev, S. Han, D.J. Srolovitz, G.J. Ackland, D.Y. Sun, M. Asta, Philos. Mag. 83 (2003) 3977.
[27] Y. Mishin, M.J. Mehl, D.A. Papaconstantopoulos, A.F. Voter, J.D. Kress, Phys. Rev. B 63 (2001) 224106.
[28] A.F. Voter, S.P. Chen, Mater. Res. Soc. Symp. Proc. 82 (1987) 175.
[29] L. Malerba, M.C. Marinica, N. Anento, C. Björkas, H. Nguyen, C. Domain, et al., J. Nucl. Mater. 406 (2010) 19.
[30] C. Domain, G. Monnet, Phys. Rev. Lett. 95 (2005) 215506.
[31] R.C. Pasianot, L. Malerba, J. Nucl. Mater. 360 (2007) 118.
[32] G. Bonny, R.C. Pasianot, L. Malerba, Modelling Simul. Mater. Sci. Eng. 17 (2009) 025010.
[33] P. Torelli, F. Sirotti, P. Ballone, Phys. Rev. B 68 (2003) 205413.
[34] Y.-M. Kim, Y.-H. Shin, B.-J. Lee, Acta Mater. 57 (2009) 474.
[35] G. Bonny, R.C. Pasianot, L. Malerba, Philos. Mag. 89 (2009) 3451.
[36] M.P. Allen, D. Tildesley, Computer Simulation of Liquids, Clarendon Press, Oxford, 1987.
[37] G. Bonny, R.C. Pasianot, E.E. Zhurkin, M. Hou, Comp. Mater. Sci. 50 (2011) 2216.
[38] R. Tarumi, Y. Kawasaki, Y. Tabe, H. Ogi, M. Hirao, T. Kagayama, Jap. J. Appl. Phys. 45 (2006) 4487.
[39] P.W. Bridgman, E.A. Mason, Collected experimental papers of P.W. Bridgman 33 (1965) 516.
[40] M. Rosen, Phys. Rev. 166 (1968) 561.
[41] K. Takemura, O. Shimomura, K. Hase, T. Kikegawa, J. Phys. F Met. Phys. 18 (1988) 197.
[42] N. Mori, M. Takahashi, G. Oomi, J. Magn. Magn. Mater. 31 (1983) 135.
[43] H. Fujihisa, K. Takemura, Phys. Rev. B 52 (1995) 13257.
[44] N. Miao, B. Sa, J. Zhou, Z. Sun, Comp. Mater. Sci. 50 (2011) 1559.
[45] R. Pasianot, D. Farkas, E.J. Savino, Phys. Rev. B 43 (1991) 6952.
[46] O. Yifang, Z. Bangwei, L. Shuzhi, J. Zhanpeng, Z. Phys. B 101 (1996) 161.
[47] Z. Bangwei, O. Yifang, L. Shuzhi, J. Zhanpeng, Phys. Rev. B 262 (1999) 218.
[48] P. Marshall, Austenitic Stainless Steels: Microstructure and Mechanical Properties, Elsevier Applied Sciences, 1984.
[49] D. Hobbs, J. Hafner, D. Spisak, Phys. Rev. B 68 (2003) 014407.

[50] J. Hafner, D. Hobbs, Phys. Rev. B 68 (2003) 014408.
[51] C. Kittel, Introduction to Solid State Physics, John Wiley & Sons, New York, 1996.
[52] H. Okamoto, Phase Diagrams of Binary Iron Alloys, ASM International, Materials Park, OH, 1993.
[53] T. Jo, K. Hirai, J. Phys. Soc. Jpn. 55 (1986) 2017.
[54] H. Uchishiba, J. Phys. Soc. Jpn. 31 (1971) 436.
[55] M. de Koning, A. Antonelli, Phys. Rev. E 53 (1996) 465.
[56] M. de Koning, A. Antonelli, S. Yip, J. Chem. Phys. 115 (2001) 11025.
[57] R.A. Johnson, Phys. Rev. 134 (1964) A1329.
[58] E. Vincent, C.S. Becquart, C. Domain, J. Nucl. Mater. 351 (2006) 88.
[59] P. Olsson, T.P.C. Klaver, C. Domain, Phys. Rev. B 81 (2010) 054102.
[60] E. Vincent, C.S. Becquart, C. Domain, Nucl. Instr. Meth. Phys. Res. B 255 (2007) 78.
[61] B.R. Coles, W. Hume-Rothery, J. Inst. Met. 80 (1951) 85.
[62] A. Lasserre, F. Reynaud, P. Coulomb, Scr. Metall. 12 (1978) 715.
[63] N.A. Gokcen, J. Phase Equil. 12 (1991) 313.
[64] G. Salje, M. Feller-Kniepmeier, J. Appl. Phys. 48 (1977) 1833.
[65] M. Perez, F. Perrard, V. Massardier, X. Kleber, A. Deschamps, H. de Monestrol, P. Pareige, G. Covarel, Philos. Mag. 85 (2005) 2197.
[66] K. Lewin, D. Sichen, S. Seetlaraman, Scand. J. Metall. 22 (1993) 310.
[67] J. Vrestal, J. Stepankova, P. Broz, Scand. J. Metall. 25 (1996) 224. Data were modified by A.T. Dinsdale (7/3/2000) to avoid bcc phase being stable in regions where it should not be stable.
[68] E. Vincent, C.S. Becquart, C. Domain, J. Nucl. Mater. 359 (2006) 227.
[69] F. Bergner, A. Ulbricht, H.W. Viehrig, Philos. Mag. Lett. 89 (2009) 795.

K Paper XI

Effects of carbon decoration on the absoption of <100> dislocation loops by dislocations in iron

D. Terentyev, A. Bakaev and E.E. Zhurkin

Journal of Physics: Condensed Matter 26 (2014) 165402

IOP Publishing Journal of Physics: Condensed Matter
J. Phys.: Condens. Matter **26** (2014) 165402 (10pp) doi:10.1088/0953-8984/26/16/165402

Effect of carbon decoration on the absorption of ⟨100⟩ dislocation loops by dislocations in iron

D Terentyev[1], A Bakaev[1,2,3] and E E Zhurkin[3]

[1] SCK•CEN, Nuclear Materials Science Institute, Boeretang 200, Mol, B2400, Belgium
[2] Center for Molecular Modeling, Department of Physics and Astronomy, Ghent University, Technologiepark 903, 9052 Zwijnaarde, Belgium
[3] Department of Experimental Nuclear Physics, Institute of Physics, Nanotechnologies and Telecommunications, St Petersburg State Polytechnical University, 29 Polytekhnicheskaya str., 195251, St Petersburg, Russia

E-mail: dterenty@sckcen.be

Received 27 October 2013, revised 6 February 2014
Accepted for publication 7 February 2014
Published 1 April 2014

Abstract
This work closes a series of molecular dynamics studies addressing how solute/interstitial segregation at dislocation loops affects their interaction with moving dislocations in body-centred cubic Fe-based alloys. We consider the interaction of ⟨100⟩ interstitial dislocation loops decorated by different numbers of carbon atoms in a wide temperature range. The results reveal clearly that the decoration affects the reaction mechanism and increases the unpinning stress, in general. The most pronounced and reproducible increase of the unpinning stress is found in the intermediate temperature range from 300 up to 600 K. The carbon-decoration effect is related to the modification of the loop–dislocation reaction and its importance at the technologically relevant neutron irradiation conditions is discussed.

Keywords: dislocation, carbon, iron, segregation

Online supplementary data available from stacks.iop.org/JPhysCM/26/165402/mmedia

(Some figures may appear in colour only in the online journal)

1. Introduction

Body-centred cubic iron (bcc Fe) is one of the most important technological metals especially for structural applications, including nuclear sector. Fe–chromium–carbon-based ferritic and ferritic/martensitic (F/M) steels are promising candidate structural materials for Fusion and GEN IV nuclear reactors [1]. Nevertheless they suffer from severe degradation of mechanical properties when exposed to neutron irradiation at reactor operation temperature in terms of hardening, loss of ductility and finally embrittlement [1]. Moreover, once a relatively high level of radiation-induced hardening is reached, the work hardening measured in uniaxial tensile tests becomes either strongly reduced or even inexistent [2–4]. The latter phenomenon is called plastic-induced softening or instability and it is considered as a potentially serious problem in the assessment of the integrity of components made with steels and subjected to high neutron dose.

The physical origin of the hardening and change of plastic behaviour of neutron irradiated Fe (and metals in general) lays in the formation of nano-scale agglomerates being clusters of point defects which obstruct dislocation movement [5]. Agglomeration of vacancies results in the formation of nano-voids, while gathering of self-interstitial atoms (SIAs) leads to the formation of platelet clusters known as dislocation loops [6]. Self-interstitials and vacancies are produced in neutron-induced collision cascades in equal amounts. However, the growth of voids and SIA clusters occurs at different rates, depending on irradiation conditions and material. In the case of bcc Fe and Fe-based ferritic steels, the dislocation loops are recognized as the primary neutron-induced nano-structural defects. Hence, the degradation of the mechanical response is

primarily related to the accumulation and growth of dislocation loops [7–11]. This is why the complete understanding of the interaction of dislocations with dislocation loops, i.e. reaction mechanism and unpinning stress, is an important subject. Moreover, the plastic instability phenomenon, mentioned earlier, is currently understood to be a consequence of the removal of the dislocation loops by moving dislocation lines. This process can explain the formation of clear bands or dislocation channels, seen by transmission electron microscopy, that make the material locally inhomogeneous and unstable upon load [12]. Clear bands in pure Fe [8] and modifications of loop pattern in Fe–9Cr [7] have been experimentally observed.

To rationalize the formation of clear bands in bcc Fe, molecular dynamics (MD) modelling was applied to address the interaction of moving dislocations with dislocation loops [13–18]. The absorption of dislocation loops was explained on the basis of reactions between different dislocation segments observed using dislocation-core analysis in atomistic simulations. The principal mechanisms ensuring loop absorption were determined to be same for both screw and edge dislocations, irrespective of the interaction occurring with $\frac{1}{2}\langle 1\,1\,1\rangle$ or $\langle 1\,0\,0\rangle$ loops. Importantly, the absorption process was found to be enhanced by increasing temperature. The role of thermal activation and the competition between different reaction pathways (leading to loop absorption or structural transformation) was also identified with the aid of MD simulations [19, 20]. By transferring the MD results to a dislocation dynamics approach, it became possible to assess simultaneously the role of thermal activation in hardening and, if needed, to introduce a numerical criterion for loop absorption or structural transformation implicitly treating loops as stochastic obstacles [21]. The good agreement between experiment and modelling for the strengthening due to $\frac{1}{2}\langle 1\,1\,1\rangle$ loops in bcc Fe has shown the adequacy and usefulness of such MD simulations. The formation of dislocation channels upon plastic deformation of Fe containing $\frac{1}{2}\langle 1\,1\,1\rangle$ loops has been also explained on the basis of rigorous dislocation dynamics simulations treating loops as dislocation segments [22].

Real F/M steels, however, contain a set of alloying elements among which the most important are substitutional chromium (Cr) and interstitial carbon (C). Two types of interstitial dislocation loops with Burgers vector (BV) $\frac{1}{2}\langle 1\,1\,1\rangle$ and $\langle 1\,0\,0\rangle$ are known to form in high Cr steels, with the fraction being dependent on Cr content [23, 24] and irradiation temperature [25]. More recently, fine atom probe and transmission electron microscopy (TEM) experiments unambiguously revealed Cr and C segregation to dislocation loops in model Fe–Cr alloys as well as in commercial F/M steels [26, 27]. Taking into account this evidence, recent MD studies have addressed the effect of Cr and C segregation on $\frac{1}{2}\langle 1\,1\,1\rangle$ loops and $\langle 1\,0\,0\rangle$ loops [28–30]. In the case of $\frac{1}{2}\langle 1\,1\,1\rangle$ loops, it was demonstrated that Cr or C segregation modifies the interaction mechanism and increases the unpinning stress depending on ambient temperature and loop size. However, the effect of carbon decoration on the resistance of $\langle 1\,0\,0\rangle$ loops, observed in bcc Fe, Fe–C and Fe–Cr alloys, as well as in F/M steels, upon irradiation at elevated temperature, has not been studied so far, while there is evidence of strong interaction of C with $\langle 1\,0\,0\rangle$ loops [31].

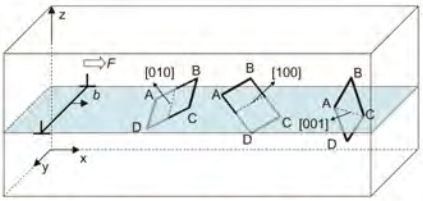

Figure 1. Interaction geometry for three possible orientations of $\langle 1\,0\,0\rangle$ loops interacting with a $\frac{1}{2}\langle 1\,1\,1\rangle\langle 1\,1\,0\rangle$ edge dislocation.

This work closes therefore a series of MD studies dedicated to the effect of Cr–C segregation on the interaction with gliding dislocations [28–30]. Since the previous works addressing the interaction of dislocation defects in Fe considered a $\frac{1}{2}\langle 1\,1\,1\rangle\langle 1\,1\,0\rangle$ edge dislocation, we continue the investigation using the same type of dislocation. Here, we consider the interaction of $\langle 1\,0\,0\rangle$ interstitial dislocation loops with size 3.5 nm being decorated by different amount of C atoms. The paper is organized as follows. First we present the background in terms of the analysis of loop–dislocation interactions in the absence of C decoration. Then, the MD computational details are briefly described. The results are subdivided into two sections separately addressing the effect of C decoration on the reaction mechanisms and unpinning stress. The paper closes with discussion and conclusions.

2. Background: interaction mechanisms in pure Fe

Prior to describing the computational methodology and results, we summarize the interaction mechanisms operating for $\langle 1\,0\,0\rangle$ loops in Fe. For each interaction geometry we provide a schematic picture that shows the elementary steps constituting the interaction processes, which will be useful for describing the effects of C decoration.

There are three possible orientations of a $\langle 1\,0\,0\rangle$ dislocation loop with respect to a $\frac{1}{2}[1\,1\,1]$ $(\bar{1}\,1\,0)$ edge dislocation, which are shown in figure 1. In this work, we consider square loops with sides oriented along $\langle 1\,0\,0\rangle$ directions, as observed in experiments in pure Fe under ion irradiation [25]. The dashed lines crossing the loop's surfaces in figure 1 indicate the intersection with the dislocation glide plane (DGP). The corners of the loops are labelled by letters to facilitate description of the reactions. x, y and z axes on the figure correspond to $[1\,1\,1]$, $[1\,1\,\bar{2}]$ and $[\bar{1}\,1\,0]$ directions, respectively. In the following we list the typical interaction mechanisms observed for the undecorated loops, previously presented in [17].

(a) We shall start the description of the mechanisms from the case of $\boldsymbol{b}_L = [1\,0\,0]$. The interaction details are shown schematically in figure 2 (see also animated gif figure 2 attached as online supplementary materials (stacks.iop.org/JPhysCM/26/165402/mmedia). The dislocation line glides towards the loop and forms a reaction segment (RS) of $\frac{1}{2}[1\,1\,1]$ type on contact (see figure 2(*b*)). The RS, which is not glissile in the DGP, pins the dislocation.

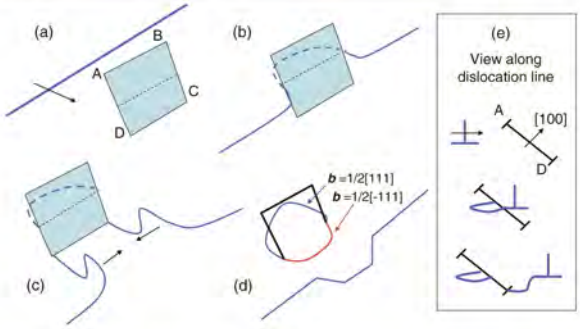

Figure 2. Schematic representation of the interaction mechanism for a loop with $\boldsymbol{b}_L = [1\,0\,0]$ at low temperature, $T \leq 150$ K.

At 150 K and below, the loop is simply sheared by the dislocation. At 300 K, the unpinning proceeds with the formation of a screw dipole, cross-slip of dislocation arms along sides AB and BC (see figures 2(*c*) and (*e*)) and their closure. The so called 'bi-loop' formed by a set of [1 0 0]; ½ [$\bar{1}$ 1 1] and ½ [1 1 1] segments is left behind (see figure 2(*d*)).

In high temperature (300–600 K) simulations, the upper segment 'AB' (see figure 1) is always seen to 'flip' on the glide plane. The interaction details are presented schematically in figure 3 (figures 3(*a*) and (*b*); see also animated gif figure 3 stacks.iop.org/JPhysCM/26/165402/mmedia). This movement can be also interpreted as dissociation of [1 0 0] into two segments: ½[$\bar{1}\bar{1}\bar{1}$] and ½[$\bar{1}$ 1 1]. This reaction is unfavourable and therefore for it to occur the system must overcome a certain barrier. This is why such 'flip' is seen only at high enough temperature. As a result of the dissociation, the ½[$\bar{1}\bar{1}\bar{1}$] segment annihilates with the pre-existing ½[1 1 1] segment, while the ½[$\bar{1}$ 1 1] segment displaces underneath the DGP (see figure 3(*c*)). Thus, the remaining lower half of the [1 0 0] loop pins the dislocation. With increase of stress, the [1 0 0] segment DC propagates downwards reacting with the ½[$\bar{1}$ 1 1] segment and forming a superjog of ½[1 1 1] type on the dislocation line (see figures 3(*d*) and (*e*)). This configuration is glissile and the jogged dislocation advances under the action of shear stress.

The flipping of the upper part of the loop is found to be enhanced by increasing temperature. It is important to note that, in this configuration, the flip is not favoured due to the repulsion between upper dislocation loop segment and dislocation line. While in the configuration with $\boldsymbol{b}_L = [0\,1\,0]$, the upper side BC (see figure 1) is attracted to the dislocation line and the flipping movement is therefore favoured.

(b) The interaction details for the loop with $\boldsymbol{b}_L = [0\,1\,0]$ are given in figure 4 (see also animated gif figure 4 stacks.iop.org/JPhysCM/26/165402/mmedia). Upon contact with the dislocation line (figure 4(*b*)), the upper half of the loop flips on the DGP (see figure 4(*c*)) and is converted into ½[1 $\bar{1}$ 1] orientation. The latter segment immediately slips underneath the DGP and the lower [1 0 0] AD segment now acts as a lock (see figure 4(*d*)). The unpinning occurs by the glide of the AD segment across the part with BV ½[1 1 1], thereby converting the whole loop into a double superjog segment with $\boldsymbol{b}$ = ½[1 1 1] (see figure 4(*e*)). The last step of the reaction is just the same as in the reaction with a ½ [1 $\bar{1}$ 1] loop. The details of this process are shown in figure 2 in [17]. τ_C for the [0 1 0] loop is, however, much smaller than in the case of the ½ [1 1 1] loop, because the actual size of the loop to be swept by the [0 1 0] segment is much larger in that case. The difference comes from the fact that the ½⟨1 1 1⟩ loop is freely glissile (within MD timeframe) and therefore it adjusts the optimum interaction geometry with the approaching dislocation, while a ⟨1 0 0⟩ loop is immobile (at least at the MD timescale), therefore its initial position with respect to the DGP determines the junction configuration. As a result, the high resistance of the [0 1 0] loop is observed only at low temperature. Above 300 K, the flip of the upper part occurs spontaneously resulting in the absorption reaction. A critical stress of ~50 MPa is needed to accommodate the absorbed loop into a superjog and reform its shape to become glissile.

(c) The interaction details for the [0 0 1] loop are presented in figure 5 (see also animated gif figure 5 stacks.iop.org/JPhysCM/26/165402/mmedia). The dislocation approaches the loop (see figure 5(*a*)), makes a short ½ [1 1 $\bar{1}$] segment at the closest corner A (see figure 5(*b*)) and then at the corner C (see figure 5(*c*)). Thus, the dislocation arms pinned at the corners are linked by the ½[1 1 1] segment laying across the loop surface. Further load leads to the formation of a screw dipole. In the reaction at 150 K, the loop is simply sheared without cross-slip movement of the dipole arms. While at T = 300 K, one of the screw arms double cross-slips (i.e. up and down along 'AD' and 'DC' sides of the loop, see figure 5(*c*)), thereby converting the lower part of the loop into ½ [$\bar{1}$ $\bar{1}$ 1] orientation. The formed configuration is stable and immobile (because the upper part has [0 0 1] orientation), while the jogged dislocation glides away. Even though the interaction mechanism changes with temperature, the unpinning of the dislocation always requires the formation of the screw dipole, and therefore τ_C stays nearly constant in the

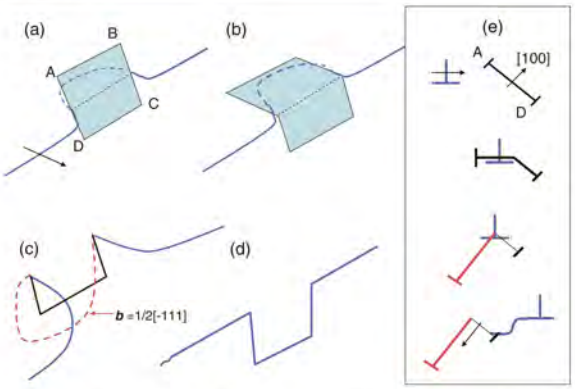

Figure 3. Schematic representation of the interaction mechanism for a loop with $\boldsymbol{b}_L$ = [1 0 0] at intermediate temperature, T = 300–600 K.

temperature range 150–600 K. At T = 800 K, the complete absorption of the loop occurs by the flip of the upper part and sequential interaction with the ½[1 1 1] and [0 0 1] segments of the dislocation and loop, respectively.

Based on the compilation of reactions presented above, one can note the intimate relation between the interaction geometry and absorption mechanism. The loops with $\mathbf{b}_L$ inclined to the DGP are absorbed by the 'flip' of their upper half, which is equivalent to the dissociation reaction: [100] = ½[111] + ½[$\bar{1}$11]. Apparently, the dissociation is induced by the external stress imposed from the approaching dislocation line. Another possibility is the direct propagation of a ⟨100⟩ segment along the loop surface. In the reactions involving loops with BV belonging to the DGP, the loop absorption requires first the emergence of a screw dipole and is completed by the cross-slip movement of screw arms. We can therefore reveal the following three principal mechanisms triggering the absorption: (1) dissociation of a ⟨100⟩ segment; (2) glide of a ⟨100⟩ segment across the loop surface; (3) cross-slip movement of a ½⟨111⟩ screw segment along ⟨100⟩ sides of the loop.

In the absence of C atoms, three basic reaction mechanisms (RM) can be distinguished, depending on the interaction geometry and simulation temperature:

(RM#1) Loop shear without cross-slip, which occurs for loops with BV = [1 0 0] and [0 0 1] at the lowest temperature studied (i.e. 150 K).

(RM#2) Formation of a screw dipole, local cross-slip around a loop, unpinning resulting in the formation of a 'bi-loop'. This RM operates in the intermediate temperature range (300–600 K) for loops with BV = [1 0 0] and [0 0 1].

(RM#3) Flip of the upper part and complete absorption on dislocation line, taking place for the [0 1 0] loop in the intermediate temperature range, and for all loops at 800 K and above.

Having these mechanisms and temperature limits in mind, we have studied the effect of carbon decoration. Carbon atoms are expected to segregate in the tensile regions of the dislocations, as has been revealed in our early study, particularly for ⟨1 0 0⟩ edge dislocations and loops [31]. The presence of carbon atoms directly in the loop core imposes a certain disturbance of its equilibrium structure and therefore may modify or suppress any of the three above listed principal mechanisms involved in the absorption process, and as a result may change the whole reaction mechanism.

3. Brief summary of computational details

As in our preceding works [28–30], the simulation scheme of a periodic array of dislocations developed in [32] is employed. The principal axes x, y and z of the simulated bcc crystal, as shown in figure 1, are oriented along the [1 1 1], [1 1 $\bar{2}$] and [$\bar{1}$ 1 0] directions, respectively. The edge dislocation with BV= 1/2[1 1 1] and slip plane x–y is created along the y direction with periodic boundary conditions applied along the x and y axes. The box is divided into three parts along z, so that the upper and lower parts (consisting of several atomic planes) contain rigidly fixed atoms. A glide force in the x direction on the dislocation is generated by the relative displacement of the rigid blocks in the x direction, which corresponds to simple shear strain e_{xz}. The resolved shear stress is calculated as $\tau = F_x/A_{xy}$, where F_x is the total force in the x direction on the lower outer block from all atoms in the inner region and A_{xy} is the x–y cross-section area of the box.

The inner region of the MD box was contained 101×3 non-equivalent atomic planes along x, 30×6 along y and 25×2 along z (corresponding to 25×21×10 nm^3). Five different temperatures were simulated, namely: 150, 300, 450, 600 and 800 K. The lattice parameter was adjusted for each temperature to respect zero pressure condition. MD simulations were started by initializing the velocity of the relaxed atoms according to Maxwell's distribution for the desired simulation temperature. After thermalization, shear was applied

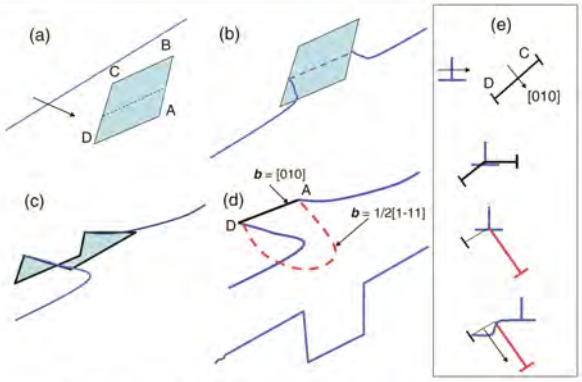

Figure 4. Schematic representation of the interaction mechanism for a loop with $\boldsymbol{b}_L = [0\,1\,0]$ occurring at $T \geqslant 150\,\mathrm{K}$.

at fixed strain rate, resulting in the dislocation velocity of $10\,\mathrm{m\,s^{-1}}$ determined using Orowan's law [6]. The integration of Newton's equations was performed using a constant time step (2 fs) in the microcanonical NVE ensemble, in which a number of particles, system volume and total energy are conserved if the work of external forces is taken into account. No temperature control was applied, as the temperature increase within a typical simulation run was negligible.

All simulations used a recently developed covalent bond many-body interatomic potential for the Fe–C system [33]. This potential removes most of the shortcomings of previously developed Fe–C potentials and provides a correct (i.e. in line with *ab initio* data) trend for the energetics of vacancy–carbon (covalent directional bonding), C–$\langle 1\,1\,0\rangle$ self-interstitial and C–C complexes in a bcc Fe matrix. Another reason to apply this potential is that it is the only available Finnis–Sinclair-type potential that includes the C–C interaction. The Fe–Fe part of this potential, derived by Ackland *et al* [34] predicts the compact core structure for a $\frac{1}{2}\langle 1\,1\,1\rangle$ screw dislocation in agreement with *ab initio* calculations.

Visual inspection of dislocation configurations formed during the simulated reactions was performed by identifying atoms belonging to dislocation cores. We used the analysis specially developed for high temperature simulations in [17, 18], that combines different properties of core atoms, namely: atomic disregistry, coordination number, common neighbours and potential energy.

An interstitial dislocation loop of square shape with sides oriented along $\langle 1\,0\,0\rangle$ directions was placed so that its centre coincided with the DGP. The loop had a size of ~3.5 nm. Three possible orientations for the loop BV ([1 0 0], [0 1 0] and [0 0 1]) were introduced. To study the effect of different level of carbon segregation, we have studied four possible carbon arrangements, including from one to four C atoms. In all cases, these were placed in the middle of the loop's sides, in the most favourable position (tensile dislocation core region), as defined in our earlier study [31]. Pairs of C atoms were placed on opposite (up–down or left–right) and adjacent (up–right or left–down) sides. Two configurations were generated for a triplet of C atoms, placing the impurities on left–up–right and left–down–right sides. Correspondingly, four configurations were inspected for an isolated C atom. For each interaction geometry (3 variants) and each simulation temperature (5 variants) 11 different C atom arrangements were inspected, which sums up to a total of 165 reactions.

When inspecting the RMs, we found that it was the same for configurations containing three and four C atoms, hence we did not distinguish the results. In the other cases, the RMs differ for the configurations where C atoms were placed on the sides below or above the glide plane. The reasons for these effects will be discussed later. To reduce the number of plots and figures presented, we subdivided the results by grouping configurations leading to the qualitatively (and very often quantitatively) same results. For a single C atom, we distinguish configurations in which the atom is below and above the DGP and refer to them as 'DN' and 'UP', respectively. For pairs of C atoms, we distinguish configurations in which C atoms are placed on the upper and lower sides (referred to as 'UD') and left and right sides (referred to as 'LR'). The same notation will be used to report the unpinning stress (averaged over the total number of configurations of that type).

4. Results

The results have shown that carbon decoration changes the interaction mechanism mostly in the reactions modelled in the intermediate temperature range, and mainly involving loops with BV [1 0 0] and [0 0 1]. The absorption reaction is always observed for the [0 1 0] loop irrespective of temperature and number of decorating C atoms. As the interaction mechanism modifies, the unpinning stress changes as well and usually increases. Generally, the unpinning stress increases with the number of decorating C atoms. To rationalize the interrelation

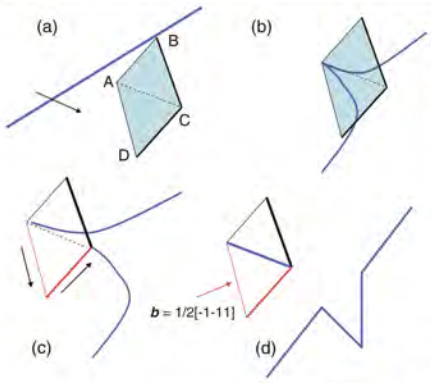

Figure 5. Schematic representation of the interaction mechanism for a loop with $\boldsymbol{b}_L$= [0 0 1] in the intermediate temperature range T=300–600 K.

between the unpinning stress increase and carbon decoration, we first discuss its impact on the interaction mechanisms.

4.1 Effect of carbon decoration on the interaction mechanisms

In addition to the three mechanisms revealed in pure Fe, two more types of reactions were observed for the decorated loops. The fourth RM (henceforth referred to as RM#4) was found to operate for the loops with BV [1 0 0] and [0 0 1]. A sequence of snapshots is given in figure 6 (see also animated gif figure 6. in the online supplementary material stacks.iop.org/JPhysCM/26/165402/mmedia) for the reaction involving the [1 0 0] loop decorated by four C atoms. The interaction proceeds in the same way as in pure Fe (see figure 3 and its description in section 2) up to the point when the upper part of the loop flips on the DGP (see figure 6(*c*)). After that the propagation of the [1 0 0] segment downwards across the loop surface does not occur and the screw dipole closes instead. As a result, a ½[$\bar{1}$ 1 1] loop is left behind (see figure 6(*d*)). Since the upper part was partially absorbed on the dislocation line, the reformed ½[$\bar{1}$ 1 1] loop has a size of ~2 nm (i.e. 1.5 times smaller than the original [1 0 0] loop). Two out of four C atoms remain attached to the core of the reformed loop, while the other two (previously attached to the dissociated segments) are free to migrate in the matrix.

As a demonstration of the effect of carbon decoration on the stress–strain relationship (τ–ε), we present the corresponding curve in figure 7, compared with that for the undecorated loop (which was completely absorbed), simulated under the same conditions. Clearly, the suppression of the absorption reaction leads to a higher unpinning stress (more than double), as expected since the closure of a screw dipole requires the highest stress. In principle, the above described mechanism can be considered as a subtype of RM#3, in which the last stage (propagation of the RS across loop surface) was suppressed. Once the resolved shear stress reached a critical value screw dipole closure naturally took place.

The second additional mechanism (henceforth referred to as RM#5) revealed for the decorated loops was seen only for the [0 0 1] loops in simulations at T = 450 and 600 K. The visualization snapshots in figure 8 show the reaction at T = 450 K for the loop decorated by two C atoms placed on sides AD and DC. The latter two are the sides along which the cross-slip movement takes place if the temperature regime corresponds to RM#2 (see its description in section 2). The initial stage of the interaction is the same as in RM#2, but the reaction ceases at the step involving the cross-slip movement (see figure 8(*b*)). Applying sufficiently high shear stress the cross-slip activates, but unlike in the absence of the decoration both arms encircle the loop. The closest arm goes from the corner A to C via D, while the furthest arm cross-slips up to the corner B and then down to C. The configuration at the end of the cross-slip movement is shown in figure 8(*c*). As a result, the loop is converted into ½[1 1 $\bar{1}$] orientation and partially absorbed by the dislocation line (see figure 8(*d*)). Importantly, the two C atoms are displaced during the cross-slip movement and the reformed ½[1 1 $\bar{1}$] loop is free to migrate. The critical stress in the case of the above described RM (curve not shown) was about 25% higher than that obtained for the undecorated loop.

To provide a general picture about the effect of carbon decoration on the interaction mechanism, we have constructed histograms for the [1 0 0] and [0 0 1] loops showing the number of RM as a function of temperature. The height of the columns in figure 9 corresponds to the number of RM introduced in sections 2.1 and 4.1. It is clear that RM are not affected at the highest temperature, as thermal activation eventually compensates for the C-added resistance.

The main modifications occur in the temperature range 300–600 K. In the case of the [1 0 0] loop, decorating C atoms suppress the complete absorption and change mechanism to the formation ½[$\bar{1}$ 1 1] loop, which emerges after the unpinning.

In the case of the [0 0 1] loops, C atoms, placed on the loop sides subject to the interaction with the cross-slipping screw arms, eventually increase the critical stress for the propagation of the screw segments. At a higher level of stress, the activation of the cross-slip movement of both dislocation arms becomes possible (which was never seen for undecorated loops). As a result, the whole loop can be converted into ½[1 1 $\bar{1}$] orientation. Hence, the C decoration biases the interaction mechanism towards the transformation from ⟨1 0 0⟩ into ½⟨1 1 1⟩ type, instead of leading to the complete absorption into a glissile superjog. Notably, the decoration of at least two sides of the loops is necessary to modify the reaction mechanism.

We also stress that in reactions modelled at elevated temperature, C atoms were regularly detached from the loops after the interaction. By tracing the coordinates of the C atoms, it appeared that their movement took place simultaneously with the reformation of the loop's segments entering the reactions with the gliding dislocation. The limited C migration (and release from the loops) could therefore serve as indication of irreversible dislocation–loop interaction, modifying the original structure of the loops.

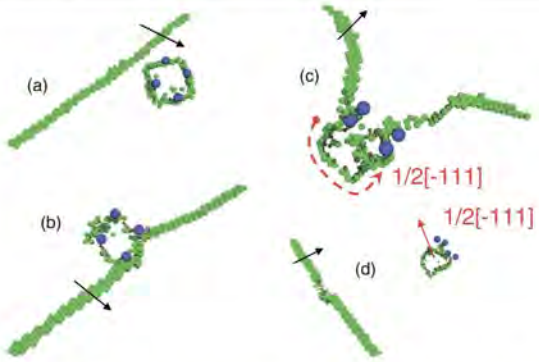

Figure 6. Visualization of different stages of the reaction involving a [1 0 0] loop decorated by four C atoms (blue spheres) at $T = 300$ K. A black arrow shows the direction of dislocation movement. On (*d*), the dislocation got unpinned and transmitted to the left part of simulation box via periodic boundary conditions. A red dashed line shows the position of the ½[$\bar{1}$ 1 1] segment formed after the flip of the upper part of the pre-existing [1 0 0] loop.

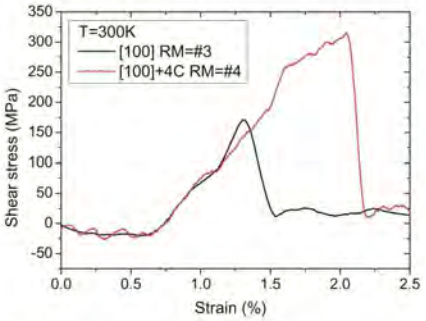

Figure 7. τ–ε plots for reactions with undecorated and decorated (by 4 C atoms) [1 0 0] loop simulated at $T = 300$ K.

4.2 Effect of carbon decoration on unpinning stress

The values of the unpinning stress measured in all the simulated reactions are summarized in figure 10, and the results for undecorated loops (obtained in [17, 30]) are also added. The error bars on the curves for undecorated loops were obtained from the five runs for each interaction geometry and temperature. In the calculations involving C atoms each point is averaged over two runs, which brings a considerable scattering and makes the comparison somewhat ambiguous. Despite that, it is possible to reveal at least two effects of carbon decoration on τ_C:

(i) even though carbon decoration does not affect the RM for the [0 1 0] loops, the unpinning stress is regularly higher for the decorated loops (see figure 10(*b*)) in the temperature range 300–600 K.

(ii) There is considerable (and reproducible for different carbon arrangements) increase of τ_C for the [1 0 0] and [0 0 1] loops at $T = 300$–450 K, at which the decoration modifies the interaction mechanisms, suppressing loop absorption.

Thus, carbon decoration leads to the increase of the loop strength, at least in the intermediate temperature interval. In simulations at the lowest and highest temperatures (i.e. 150 and 800 K), the effect of carbon on the unpinning stress is unclear, due to a large scatter of the results. Clearly, a better statistic is necessary to establish more robust and meaningful comparison.

5. Discussion

The results for the ⟨1 0 0⟩ interstitial loops decorated by C atoms presented here reveal clearly that the decoration affects the RM and increases the unpinning stress. Even though we have studied the interaction with the gliding ½[1 1 1]($\bar{1}$ 1 0) edge dislocation only, the mechanisms due to which the modification of the RM and unpinning stress takes place will also operate for ½⟨1 1 1⟩ screw dislocations, and edge dislocations gliding in ⟨1 1 2⟩ planes. Hence, the decoration is expected to affect the interaction of loops with moving dislocations of different characters in both ⟨1 1 0⟩ and ⟨1 1 2⟩ slip planes.

The most pronounced and reproducible increase of the unpinning stress for the decorated loops was found in the intermediate temperature range from 300 up to 600 K. In the case of the [1 0 0] and [0 1 0] loops, the increase of τ_C clearly correlates with the modification of the interaction mechanism, which explains its origin. In the case of the [1 0 0] loops, at a certain stage of the interaction, the C atoms suppress the propagation of the [1 0 0] segment across the loop surface, which otherwise

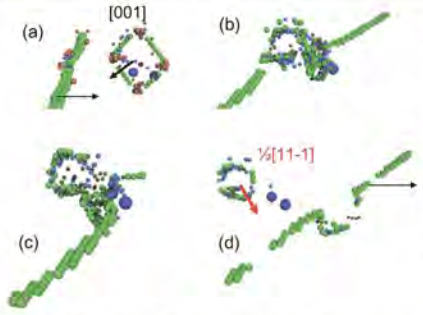

Figure 8. Visualization of different stages of the reaction involving a [0 0 1] loop decorated by 2 C atoms (blue spheres) simulated at 450 K. On (*d*), the jogged dislocation got unpinned, leaving behind a ½[1 1 $\bar{1}$] loop.

occurs in reactions with undecorated loops (see figure 4(*d*)). This prevents complete loop absorption and simultaneously changes the unpinning reaction pathway, resulting in the emergence and closure of a screw dipole. Since the propagation of the [1 0 0] segment completing the reaction is to occur downwards, the effect is therefore seen in configurations with C atoms placed below the DGP.

In the case of the [0 0 1] loop, the presence of C atoms on the loop's segments enhances their resistance against propagation of screw arms (i.e. step 'c' in figure 5) and therefore delays the unpinning. It is important, for this to happen, that a C atom should be encountered by the propagating screw segments. If a sufficient number of C atoms is placed on the relevant loop sides, the resolved shear stress may reach a critical value at which an alternative mechanism, not observed without decoration, activates. That situation realizes in the case of 3C and 4C decoration of the [0 0 1] loop at 450–600 K (see description of RM#5 in section 4.1) which leads to the modification of the reaction outcome.

Finally, in the case of the 'weak' [0 1 0] loops, the addition of an increasing number of C atoms in the loop core led to the reproducible increase of the unpinning stress. In that configuration, it was essential that C atoms should be placed on the 'left' and 'right' sides (i.e. AB and CD in figure 1), across which the [0 1 0] segment has to propagate to complete the reaction. The retention of its movement due to the extra resistance offered by decorating C atoms explains the added strengthening. Correspondingly, strong effect was observed for the 'LR' pair and configurations involving three and four C atoms.

One can therefore conclude that the actual level of carbon segregation is an important parameter defining both the loop's strength (i.e. hardening) and RM (i.e. plastically induced modification of microstructure). The results presented here, together with our previous studies [28–30] that address the effect of chromium and carbon decoration, have clearly demonstrated that the disturbance of the loop core by impurity inclusion suppresses certain dislocation-mediated mechanisms that determine the whole reaction process. As a result, it may lead to increase of τ_C, may modify the reaction outcome, or provoke both effects. These parametric and self-consistent studies involving both ½⟨1 1 1⟩ and ⟨1 0 0⟩ loops therefore confirm unambiguously that impurity/solute segregation on radiation defects is another variable (in addition to deformation temperature and rate) that influences local deformation mechanisms and in turn causes global changes of microstructure under plastic deformation. It therefore implies that not only the density and the size distribution of defects, but also their microchemical morphology can be a valuable input from microstructural predictive models embedded in the multi-scale chain of computational tools [35]. At the same time, whether or not the specific mechanisms described here will be of relevance in real situations will depend on the frequency of ⟨1 0 0⟩ loops and carbon decoration. Since the appearance of these loops is favoured at higher temperature (at least upon ion irradiation), it is possible that the enhancement of their strength as dislocation obstacles is not practically measurable, but the main message is that the increase of obstacle strength as a consequence of solute segregation on loops is a general phenomenon, independent of loop type.

The so far identified effects of Cr and C segregation have very similar qualitative consequences: (i) suppression of loop absorption and (ii) increase of τ_C. However, these two experimentally observed segregating atoms [26, 27] exhibit significantly different features. Cr atoms are substitutional solutes. The spatial rearrangement of Cr atoms on a loop in the course of interaction with dislocations is therefore naturally not possible in the case of standard mechanical tests (and of course in MD simulations) as it requires defects offering the possibility of mass transport (e.g. vacancies). Carbon atoms, on the other hand, are interstitial impurities, which perform in-core diffusion at sufficiently high temperature. In the high temperature simulations carried out here, we have regularly observed limited, but non-negligible, carbon migration. This is a very important feature and should be regarded as a fundamental difference in the way Cr and C atoms influence loops' strength. The decorating C atoms are often detached from the loops after dislocation unpinning, in most of the reactions, especially in simulations at $T \geq 450$ K. In agreement with the present observations, previous works addressing the mobility of carbon decorating dislocations loops also reported limited carbon migration occurring within a relatively short MD-timescale frame [29]. This implies that local carbon in-core rearrangement is certainly expected to take place in the reactions involving slowly moving dislocations (for velocities much lower than metres per second, unachievable for MD techniques) in the technologically important temperature range. How strongly the 'pipe migration' of carbon would influence RM and unpinning stress remains to be investigated. It is obvious, however, that standard MD techniques are not applicable for this problem: the further development of large-scale accelerated dynamics or hybrid MD–Monte Carlo approaches is necessary.

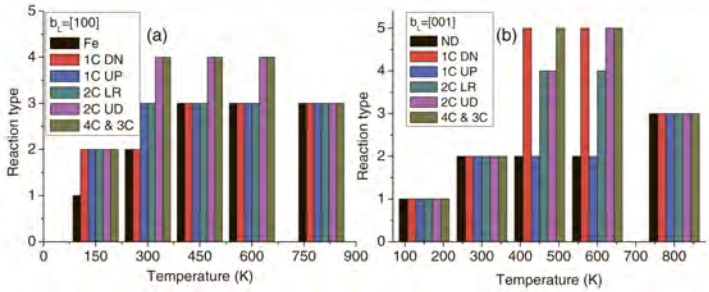

Figure 9. Classification of reaction mechanisms as a function of temperature and level of carbon enrichment.

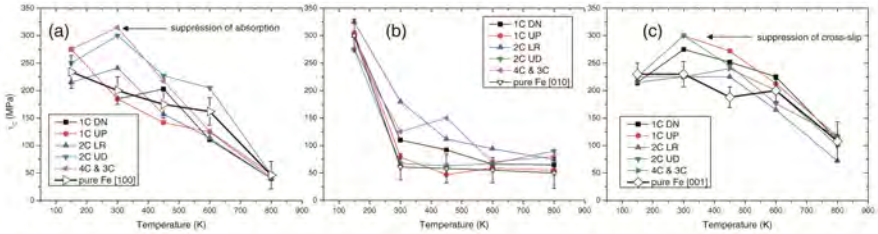

Figure 10. The unpinning stress as a function of temperature calculated for (*a*) [1 0 0], (*b*) [0 1 0] and (*c*) [0 0 1] loops with and without carbon decoration.

6. Conclusions

Based on the above presented results and their discussion the following conclusions are drawn:

(i) Carbon decoration leads to the modification of the reaction mechanism in the intermediate temperature range (300–600 K), and it is expressed in the suppression of complete absorption of ⟨1 0 0⟩ loops in favour of transformation into ½⟨1 1 1⟩ loops. The effect of carbon decoration on the interaction mechanism enhances with increasing number of C atoms residing on the core of the dislocation loop.

(ii) There is a reproducible increase of the unpinning stress for the decorated loops in the temperature interval T=300–600 K. The reasons for the higher loop resistance are rationalized in terms of the modification and suppression of several elementary dislocation reactions contributing to the [1 0 0] loop–dislocation interaction process.

(iii) The strongest effect of carbon decoration on the loop resistance is seen for the 'weak' [0 1 0] loops, which otherwise are athermally absorbed on dislocation lines at T = 300 K and above.

(iv) Non-negligible carbon migration was regularly observed in reactions at $T \geq 450$ K. This implies that carbon rearrangement is expected to take place in the course of the loop–dislocation interaction at elevated temperature and low deformation rates. The effect of in-pipe carbon diffusion on the reaction mechanism and unpinning stress should therefore be investigated.

Acknowledgments

This work, supported by the European Commission under the Contract of Association between EURATOM/SCK-CEN, was carried out within the framework of the European Fusion Development Agreement. Partial support was also received from the EURATOM 7th framework programme, under Perform 60 project. DT thanks his colleague Dr. L. Malerba for the useful remarks and proofreading.

References

[1] Klueh R L and Nelson A T 2007 *J. Nucl. Mater.* **371** 37
[2] Lucon E and Vandermeulen W 2009 *J. Nucl. Mater.* **386–388** 254
[3] Lucon E, Leenaers A and Vandermeulen W 2008 *Fusion Eng. Design* **83** 620
[4] Tong Z and Dai Y 2009 *J. Nucl. Mater.* **385** 258
[5] Bacon D, Gao F and Osetsky Y 2000 *J. Nucl. Mater.* **276** 1
[6] Hull D and Bacon D J 2001 *Introduction to Dislocations* (Oxford: Butterworth-Heinemann)
[7] Gelles D and Schaeublin R 2001 *Mater. Sci. Eng.* **309–310** 82
[8] Zinkle S J and Singh B N 2006 *J. Nucl. Mater.* **351** 269
[9] Gaganidze E, Schneider H, Dafferner B and Aktaa J 2006 *J. Nucl. Mater.* **355** 83

[10] Matijasevic M and Almazouzi A 2008 *J. Nucl. Mater.* **377** 147
[11] Matijasevic M, Lucon E and Almazouzi A 2008 *J. Nucl. Mater.* **377** 101
[12] Was G S 2007 *Fundamentals of Radiation Materials Science* (New York: Springer)
[13] Nomoto A, Soneda N, Takahashi A and Ishino S 2005 *Mater. Trans.* **46** 463
[14] Bacon D, Osetsky Y and Rong Z 2006 *Phil. Mag.* **86** 3921
[15] Terentyev D, Malerba L, Bacon D and Osetsky Y 2007 *J. Phys.: Condens. Matter* **19** 456211
[16] Liu X Y and Biner S B 2008 *Scr. Mater.* **59** 51
[17] Terentyev D, Grammatikopoulos P, Bacon D and Osetsky Y 2008 *Acta Mater.* **56** 5034
[18] Terentyev D, Bacon D J and Osetsky Y N 2010 *Phil. Mag.* **90** 1019
[19] Terentyev D, Osetsky Y N and Bacon D J 2010 *Scr. Mater.* **62** 697
[20] Terentyev D A, Osetsky Y N and Bacon D J 2010 *Acta Mater.* **58** 2477
[21] Terentyev D, Monnet G and Grigorev P 2013 *Scr. Mater.* **69** 578
[22] Arsenlis A, Rhee M, Hommes G, Cook R and Marian J 2012 *Acta Mater.* **60** 3748
[23] Porollo S, Dvoriashin A, Vorobyev A and Konobeev Y 1998 *J. Nucl. Mater.* **256** 247
[24] Katoh Y, Kohyama A and Gelles D 1995 *J. Nucl. Mater.* **225** 154
[25] Jenkins M L, Yao Z, Hernandez-Mayoral M and Kirk M A 2009 *J. Nucl. Mater.* **389** 197
[26] Terentyev D, Klimenkov M and Malerba L 2009 *J. Nucl. Mater.* **393** 30
[27] Jiao Z and Was G S 2011 *Acta Mater.* **59** 4467
[28] Terentyev D, Bergner F and Osetsky Y O 2012 *Acta Mater.* **61** 1444
[29] Terentyev D, Anento N and Serra A 2012 *J. Phys.: Condens. Matter* **24** 455402
[30] Terentyev D and Bakaev A 2013 *J. Phys.: Condens. Matter* **25** 265702
[31] Terentyev D, Anento N and Serra A 2012 *J. Nucl. Mater.* **420** 9
[32] Osetsky Y N and Bacon D J 2003 *Modelling Simul. Mater. Sci. Eng.* **11** 427
[33] Hepburn D and Ackland G 2008 *Phys. Rev.* B **78** 165115
[34] Ackland G, Mendelev M, Srolovitz D, Han S and Barashev A 2004 *J. Phys.: Condens. Matter* **16** 1
[35] Wirth B, Odette G, Marian J, Ventelon L, Young-Vandersall J and Zepeda-Ruiz L 2004 *J. Nucl. Mater.* **329–333** 103

L Paper XII

Hardening due to dislocation loop damage in RPV model alloys: role of Mn segregation

D. Terentyev, X. He, G. Bonny, A. Bakaev, E. Zhurkin, L. Malerba

Submitted to Journal of Nuclear Materials as of June 2014

Hardening due to dislocation loop damage in RPV model alloys: role of Mn segregation

D. Terentyev[1], X. He[2], G. Bonny[1], A. Bakaev[1,3,4], E. Zhurkin[4], L. Malerba[1]

[1]SCK•CEN, Nuclear Materials Science Institute, Boeretang 200, B-2400 Mol, Belgium
[2] China Institute of Atomic Energy, P.O.Box:275-51, 102413, Beijing, China
[3] Center for Molecular Modeling, Department of Physics and Astronomy, Ghent University, Technologiepark 903, 9052 Zwijnaarde, Belgium
[4] Department of Experimental Nuclear Physics K-89, Faculty of Physics and Mechanics, St.Petersburg State Polytechnical University, 29 Polytekhnicheskaya str., 195251, St.Petersburg, Russia

Abstract

Hardening of reactor vessel pressure steels is generally attributed to precipitates and point defects clusters - matrix damage. Recent experiments and atomistic simulations suggest that Mn-Ni-Cu-rich clusters are the result of the segregation to small dislocation loops, making the distinction between precipitates and matrix damage blur. Here, we study the interaction of $a_0/2<111>$ dislocation loops with moving dislocations addressing the effect of Mn-Ni-Cu segregation at loops on their strength and interaction mechanism. It is found that Mn-enrichment significantly increases the unpinning stress, especially for small, invisible dislocation loops; and the solute segregation enhances loop resistance against absorption by moving dislocations.

PACS : 61.80.Az, 61.82.Bg
Keywords: Iron, ferritic steel, precipitation, dislocation, molecular dynamics
*Author for correspondence. Email: dterenty@sckcen.be, Tel.: +32-14-333197; fax: +32-14-321216

1. Introduction

Radiation-induced embrittlement of bainitic steels is the lifetime limiting factor of the reactor pressure vessels (RPV) in currently operating nuclear light water reactors (LWR). The

primary mechanism of embrittlement is the obstruction of dislocation motion produced by nanometric defect structures that develop inside the material due to irradiation at the RPV operating temperature. Two classes of nano-structural features are considered to contribute to the embrittlement of RPV steels, both hardly detectable by means of transmission electron microscopy (TEM). These are (i) clusters of Cu, Ni, Mn and other solutes, generally catalogued as *precipitates*; and (ii) the so-called *matrix damage*, interpreted as clustering of point-defects [1; 2; 3; 4]. The former features are further subdivided into Cu-rich precipitates (CRP), which have been long identified as an important source of hardening [1], and Mn-Ni-rich precipitates (MNP). The latter are expected to appear more clearly at high enough fluence especially in low-Cu/high-Ni steels and for relatively low irradiation temperatures [2]. They are therefore proposed to explain the increase of hardening at high dose (i.e. beyond 0.1 dpa) [5]. Due to the 'late' appearance of these nano-features, and assuming they are stable thermodynamic phases that might suddenly develop in large volume fractions, they are often called 'late blooming phases' (LBP) [2; 5]. Based on a combination of experimental observations and atomistic studies, they are currently understood as radiation-induced agglomerations of Mn-Ni-rich clusters on point-defect clusters [6; 7; 8], thereby making the distinction between precipitates and matrix damage somewhat ambiguous.

Nanovoids and vacancy-solute clusters, together with Cu precipitates, were initially identified as the main source of hardening in RPV steels [1]. However, positron annihilation spectroscopy (PAS) studies do not reveal the formation of nanovoids in RPV steels irradiated under conditions of technological relevance: only small clusters containing a few vacancies are found [7; 9; 10]. In Fe-Cu model alloys these are deduced by PAS to be associated with Cu-rich precipitates [10; 11]. Dedicated atomistic molecular dynamics (MD) studies of the interaction of dislocations with Cu-vacancy-rich precipitates suggest, however, that, while full Cu precipitates may partially contribute to RPV steel hardening, the contribution of solute-vacancy-type defects to hardening is doubtful [12; 13].

Nanometric dislocation loops (DL), typically observed in bcc Fe and Fe-based RPV-model alloys at relevant irradiation conditions [7], offer an alternative explanation for the hardening. TEM observation of fairly small (< 5 nm in diameter) DLs has been reported in Russian-type VVER steels [14; 15; 16; 17], although generally not in "Western-type" pressurized water reactor (PWR) steels [7; 18; 19]. However, higher irradiation doses with ions or electrons make interstitial-type dislocation loops visible also in typical PWR steels [20; 21]. Moreover, recent accurate studies revealed the presence of low densities (~10^{20} m^{-3}) of small DL, often decorating dislocations and grain boundaries, also in neutron-irradiated

RPV steels from surveillance specimens of European nuclear power plants. It is therefore reasonable to assume that DLs are indeed always present in irradiated RPV steels, but remain too small to be easily detected by TEM up to irradiation doses typical for RPV end of life. The recent indications that these small loops might be decorated by solute atoms (Mn, Ni, Cu, …) which would find there the appropriate location to precipitate even outside the range of thermodynamic stability of phase separation [6], suggest that small loops and especially solute-decorated small loops should be studied as possible source of radiation hardening in RPV steels.

In this work, we perform MD simulations to investigate the interaction of DLs with moving dislocations using the configurations of the interstitial loops decorated by Mn, Ni and Cu atoms obtained from a preceding simulation study, using Metropolis Monte Carlo (MMC) techniques with an appropriate interatomic potential [6]. While in pure Fe the majority of loops are of <100> type [19], both types of loops with Burgers vector (BV) $a_0/2$<111> and a_0<100> are present in RPV steels [21] and model Fe-based based alloys containing Mn, Ni and Cu [7; 22; 23]. Since $a_0/2$<111> loops are primarily seen in displacement cascades in bcc Fe [24; 25] irrespective of the applied interatomic potentials [26], we begin our investigation considering these DLs. Given that the DLs of concern in RPV steels are believed to be at the limit of the TEM resolution, we consider relatively small defects, 1.5, 3.5 and 5 nm in diameter, interacting with an edge dislocation at room temperature (test temperature). The effect of solute enrichment on the strength with which the obstacle opposes to dislocation movement is studied in the binary Fe-Mn, ternary Fe-Mn-Ni and quaternary Fe-Mn-Ni-Cu systems. As a first step, the main accent is put on the effect of Mn as this element is known to exhibit strong interaction with both vacancies and self-interstitial atoms [27], so its segregation to dislocation loops is primarily expected.

2. Computational Details

To perform MMC and molecular dynamics (MD) simulations we describe the atomic interaction in the Fe-Mn-Ni-Cu system applying the interatomic potential developed by Bonny *et al.* in [6].The potential was developed accounting for point-defect solute interactions as well as thermodynamic consistency with experimental phase diagrams. The pure elements: Fe, Mn, Ni and Cu were taken from Refs. [28], [6], [29] and [30], respectively. The cross potentials for FeMn, NiMn and CuMn were fitted in [6], NiCu [31], FeNi in [32] and FeCu in [33].

2.1 DL configurations for MD simulations

The equilibrium arrangements of Mn, Ni and Cu atoms around $a_0/2<111>$ circular DLs are obtained by using MMC sampling [34] within the isobaric grand canonical ensemble (*N*, *P*, *T*). The method includes three types of trials to make the system evolve from a given initial condition to equilibrium: (i) a random displacement of all atoms from their current positions (by this trial lattice relaxation and vibrational entropy are accounted for); (ii) the overall volume change of the simulation box (this trial allows the desired pressure to be maintained, even if a structural transition were to occur); (iii) the third trial consists in the random exchange of two atoms of different species (by this trial the equilibrium configurations are sampled). The decision on the acceptance of the new configuration is based on the standard MMC algorithm [34] and one set of these trials is termed an "MC step". The convergence of the total energy usually required about 5×10^6 MC steps (starting from the random crystals pre-thermalized by MD simulations) for crystals containing $\sim22\cdot10^3$atoms, i.e. sufficiently large to avoid loop self-interaction via periodic boundary conditions.

As mentioned in the introduction is focus here is made on the effect of Mn, we therefore consider the following alloys at 600 K: Fe-0.5%Mn, Fe-1%Mn, Fe-2%Mn, Fe-1%Ni-1%Mn, Fe-2%Mn-2%Ni and Fe-0.8%Mn-0.8%Ni-0.5%Cu. As an example of the results of MMC simulations, Fig.1 provides a visualization of the MnNiCu precipitate formed near a 3.5 nm hexagonal $a_0/2<111>$ interstitial loop in the Fe-0.8%Mn-0.8%Ni-0.5%Cu system equilibrated at 600 K. The equilibrated MMC crystals were then embedded in a large MD sample that contained a pre-relaxed dislocation. The MD crystal was relaxed again, thermalised at the desired test temperature (e.g. 300 K) and finally loaded to induce the DL-dislocation interaction. Details of the MD simulations are provided in the following subsection.

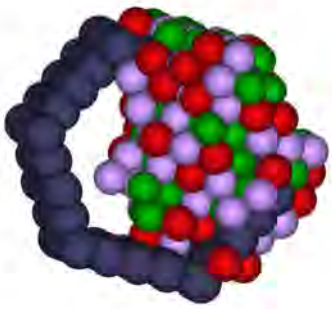

Fig.1. Arrangement of Mn, Ni and Cu atoms in a MnNiCu precipitate formed on a $a_0/2<111>$ DL. Mn, Ni and Cu are shown by purple, red and green spheres, respectively, while dark blue spheres indicate atoms constituting the core of the DL.

In this work, we investigate how the equilbrium solute re-arrangement in the core of DLs (obtained via MMC simulations similar to [8] but analysed in a different way) affects the DL-dislocation interaction mechanism and critical unpinning stress. As a measure of the solute re-arrangement we analyse chemical types of atoms constituting the loop core and those present in the immeadiate vicinity i.e. in the nearest compressed and tensile shells (see [35] for a more detailed description). Even though some solute clusters (precipitates) whose size exceeds these regions of the loop might form after MMC simulations, depending on initial alloy composition and loop size, we neglect their presence, as here we exclusively investigate the effects attributed to the solute enrichment in the core of DLs. The present approximation is supported by the fact that only the core atoms of a DL contribute to the interaction with a dislocation and its obstacle strength with respect to the dislocation passage. The impact of solute precipitatation on dislocation loops will be the subject of a separate study.

2.2 MD simulations

To study dislocation-loop interaction we employed the simulation algorithm developed by Osetsky and Bacon [36]. The principal axes x, y and z of MD crystal, shown in Fig. 2, were oriented along the [111], [$\bar{1}\bar{1}$2] and [1$\bar{1}$0] directions, respectively. The edge dislocation with BV=$a_0/2<111>$ in the ($1\bar{1}0$) slip was created along the y direction. Periodic boundary

conditions were applied along the x and y directions. Along z, the box was divided into three parts: the upper and lower parts consisted of several atomic planes in which atoms were rigidly fixed in their original position relative to each other, whereas atoms in the inner region were free to move during the MD runs. A glide force on the dislocation was generated by displacing the upper rigid block in the x direction, which corresponds to applying simple shear strain e_{xz}. The corresponding resolved shear stress induced by the applied deformation was calculated as $\sigma_{zx} = F_x/A_{xy}$, where F_x is the total force in the x direction on the lower rigid block due to the atoms in the inner region, and A_{xy} is the xy cross-section area of the box. The size of the inner region of the MD box was 101×3, 30×6 and 25×2 non-equivalent atomic planes along x, y and z (or 25×21×10 nm^3), respectively. Such crystallite is large enough to consider the interaction of the dislocation with a loop of diameter up to 5 nm (350 self-interstitial atoms, SIAs), as shown in our previous studies [37; 38; 39]. During an MD run, the dislocation line and loop were monitored using atomic disregistry analysis, coupled with structural nearest-neighbour analysis (see [40]), as well as by selecting atoms with high potential energy. Statistical averaging was performed over every 250 steps to reveal the atoms belonging to the dislocation core. The latter procedure allowed the identification of the interaction mechanism even at relatively high temperature, despite the significant thermal noise.

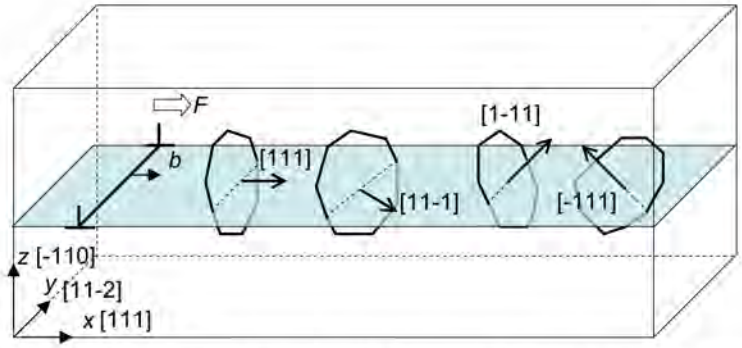

Fig.2. Interaction geometry for four possible orientations of $a_0/2<111>$ loops interacting with an edge dislocation with BV = $a_0/2[111]$. F denotes the direction of the shear force that acts on the dislocation.

MD simulations were started by initializing the velocity of the relaxed atoms according to the Maxwell's distribution for the desired simulation (mechanical test) temperature, T, chosen to be in the range of 150 to 800 K. After thermalization for 10^3 steps, load was applied at a fixed strain rate, resulting in dislocation velocity (v_d) of 10 m/s. To achieve the desired v_d, the strain rate to be applied, $\dot{\varepsilon}$, was determined according to Orowan's law $\dot{\varepsilon} = pbv_d$, where p is the dislocation density, equal to $1/(L_X \times L_Z)$ and b is the BV. The integration of Newton's equations was performed using a constant time-step (2.5 fs) in the microcanonical NVE ensemble, in which number of particles, system volume and total energy are conserved if the work of external forces is taken into account. No temperature control was applied to limit temperature increase during the simulation, but the latter was always negligible.

3. Results

3.1 Reference interaction mechanisms and loop's strength

Prior to describing the effect of solute segregation, we recall the interaction mechanism and strengthening of $a_0/2<111>$ loops in pure Fe, under the loading conditions applied here. Two out of four possible interaction geometries, shown in Fig.2, namely: $\boldsymbol{b}_L = a_0/2[\bar{1}11]$ and $a_0/2[1\bar{1}1]$, represent the case when the BV is inclined to the dislocation glide plane (DGP). In the other two cases the BVs of the loops are parallel to the DGP and these can therefore be dynamically dragged or pulled by the approaching dislocations. The latter interaction causes very little or no resistance to the dislocation glide, because the migration energy of $a_0/2\langle 111\rangle$ loops is very small (0.05 eV) so its glide is practically an athermal process [41]. The case of the loop with BV $=1/2[11\bar{1}]$ intersecting the glide plane has been recently studied in [42]. It was shown that the loop can also be dragged by the dislocation although at significantly lower dislocation velocity. The dislocation and loop enter the reaction forming a configuration that contains two 'quadra-point' junctions, see Fig.A1(b) in Ref. [42]. This junction is hardly mobile and therefore its stability determines the critical breakaway stress, while its mobility defines the condition for dynamic drag. Given the applied loading conditions and for the loop sizes studied here, the dynamic drag does not occur and the loop is eventually sheared by the

dislocation once a significant shear stress is reached (which ~250 MPa at 300 K for a 3.5 nm loop).

The resistance of the loops with the BV inclined to the DGP is much higher than in the case of dynamic drag. The interaction mechanism requires the formation and propagation of a reaction segment of <100> type. Both inclined configurations have already been thoroughly studied in bcc Fe in [43; 44; 45] and, for the loading conditions applied here, the expected critical stress for 1.5, 3.5 and 5 nm loops at 300 K is 50, 300 and 360 MPa, respectively.

3.2 Local solute arrangement around dislocation loops

In the alloys studied here, the decoration of solutes was seen on both compression (CS) and tensile sites (TS) of the loop core in approximately equal amounts. Here, as in our previous MMC study carried out in Fe-Cr alloys [45], the enrichment (x_{sol}) is quantified as concentration of solutes among the atoms belonging to the dislocation loop core, defined using the structural analysis. In the Fe-Mn binary alloys, $x_{sol\,(CS)}$ was always about 10% lower than $x_{sol\,(TS)}$. Both values grow approximately linearly with increasing Mn content in the matrix. With addition of Ni, some Mn atoms were replaced by Ni and Fe atoms, so the solute content in the loop core in Fe-1%Mn-1%Ni became lower than $x_{sol\,(CS\ or\ TS)}$ in Fe-2%Mn. The content of Ni decorating the loop was about three times lower than that of Mn in Fe-1%Mn-1%Ni, and four times lower in Fe-2%Mn-2%Ni. In the quaternary alloy, the Mn content in the core was 0.2%, with 0.1% Ni and 0.01% Cu. Despite very weak Cu segregation, the addition of Cu recovers Mn segregation and enhances segregation of Ni, as compared to the local atomic arrangement found in the ternary Fe-Mn-Ni system. The solute decoration is not spread over the whole loop perimeter homogeneously in all the cases and sometimes is seen to be localized.

The average concentration of the solutes in the compression and tensile sites of the 3.5 nm DL core is reported in Table 1. The trends observed in the enrichments computed for 1.5 and 5 nm loops were similar to those discussed above. More details about the deposition of Mn, Ni and Cu in binary, ternary and quaternary alloys can be found in [8].

Table 1. Solute composition in the 3.5 nm DL core after MMC calculations.

Alloy's composition	$x_{sol\ (CS)}$	$x_{sol\ (TS)}$	x_{sol}
0.5%Mn	Mn=7%	Mn=9%	Mn=8%
1%Mn	Mn=18%	Mn=20%	Mn=19%
2%Mn	Mn=32%	Mn=37%	Mn=34%
1%Mn – 1%Ni	Mn=15% Ni =7%	Mn= 19% Ni = 8%	Mn= 17% Ni = 7.5%
2%Mn – 2%Ni	Mn= 22% Ni = 6%	Mn=26 % Ni = 6%	Mn= 24% Ni = 6%
0.8%Mn – 0.8%Ni – 0.5%Cr	Mn=19% Ni =10% Cu = 1%	Mn=22% Ni =10% Cu =1 %	Mn= 21% Ni = 10% Cu = 1%

3.3 Interaction of enriched loops with dislocations

In the simulations employing MMC-obtained DL configurations, four different reaction mechanisms (RM) were distinguished. Their brief description is as follows:

(i) complete removal of the loop, which occurs by its incorporation on the dislocation line or by dynamic drag;

(ii) partial absorption i.e. reduction of the loop size without modification of its orientation, which occurs when the absorption reaction started but did not get to completion (see examples of the interaction with inclined loops at low temperature [39]). Another reaction pathway was identified in the reactions involving loops with BV=a_0/2[111] immobilized by the solute decoration, the examples will follow;

(iii) loops shear, which was seen only for DLs with BV=a_0/2[11-1] loops. While in the case of undecorated loops <001> type junctions with limited mobility formed on contact, the loops remain completely immobilized by the solute decoration.

(iv) Orowan type reaction, which corresponds to the case when the loop opposes strong resistance to the dislocation. At sufficiently high shear stress, the emergence of a screw dipole and its closure occurs at resolved stress close to the Orowan limit (i.e. $\mu \boldsymbol{b}/L$, where μ and L is the shear modulus and free dislocation passage distance, respectively).

Strong impact of the solute segregation on the critical stress is found only for 1.5 nm DLs. The suppression of loop absorption, especially promoted by the segregation of Mn, was observed for larger loops, as will be shown in the following examples.

Our first example refers to the interaction of solute-enriched loops with BVs contained in the DGP. Consider the stress-strain relationship shown in Fig.3(a) corresponding to the interaction of the dislocation with a 3.5 nm $a_0/2[111]$ loop, whose equilibrium configuration was obtained in the Fe-1%Mn alloy (so, it contains ~20% Mn atoms in the core region). In this interaction geometry, the undecorated loop (pure Fe in the figure) simply glides in front of the approaching dislocation, under the action of the repulsive force. The steady-state stress for the applied loading conditions (i.e. loop size and temperature) is only ~20 MPa, i.e. very low. The visualization of the interaction process for the decorated loop is given in Fig.4. One sees that the loop does not glide at all, the resolved shear stress (RSS) keeps increasing and, as the dislocation approaches, a local backward bending of the dislocation line is clearly produced (see Fig.4(b)). Once the RSS reaches 70 MPa, the dislocation overcomes the repulsive interaction and makes contact with the loop (see Fig.4(c)), determining a drop in the RSS which, in fact, becomes negative as a consequence of the reaction. The result (see Fig.4(d)) is that the lower part of the loop is absorbed on the dislocation line as a superjog, while the upper part remains attached to the decorating Mn atoms, which remain in their original positions.

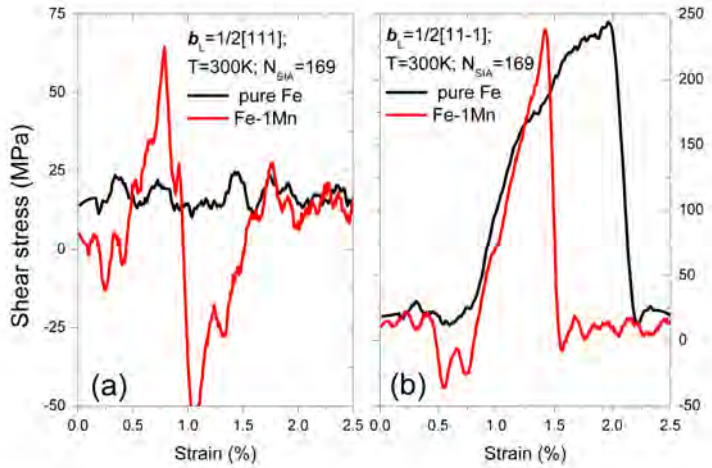

Fig.3. Stress-strain relationship corresponding to the interaction of 3.5nm DLs with (a) BV=a_0/2[111] and (b) BV=a_0/2[11-1].

The stress-strain curve for another interaction geometry with BV contained in the DGP is shown in Fig.3(b). In this case, we see that the profiles of the stress rapidly increase with strain both for the decorated and undecorated loop. However, for the former the growth is practically linear, which implies that almost no plastic deformation occurs before the dislocation unpins from the loop. This is the main effect of solute segregation in this case which, for the rest, hardly influences the RSS maximum value. However, in terms of the details of the interaction mechanism the difference is important. Let us recall the process for the undecorated loop, illustrated graphically in Ref. [42]. As the dislocation contacts the loop, there is the formation of a new configuration containing two [001] nodes. These act as a bridge connecting ½[111] and ½[111] segments cutting each other. For some time the whole complex is stable, but once the RSS reaches ~175 MPa, the loop-dislocation configuration begins to move. The loop displaces along the dislocation line (in the [11-1] direction) while the latter advances. This movement occurs via a mechanism that involves break-up and reconstruction of the [001] junctions. The latter therefore controls the critical stress at which this configuration glides as a whole. Break-up or stable drag are therefore determined by

deformation speed and temperature (needed to activate break-up of [001] junctions). In the applied conditions, the deformation speed is too high to see stable glide and the loop is finally sheared at the critical stress of ~250 MPa. The evidence for the limited drag (and plastic deformation) is seen on the stress-strain curve as an increase from the straight line, which is not observed for the decorated loop (loaded in the same conditions). Visual inspection has proven that the decorated loop was completely immobilized by the solutes and no displacement along the dislocation line was observed in this case.

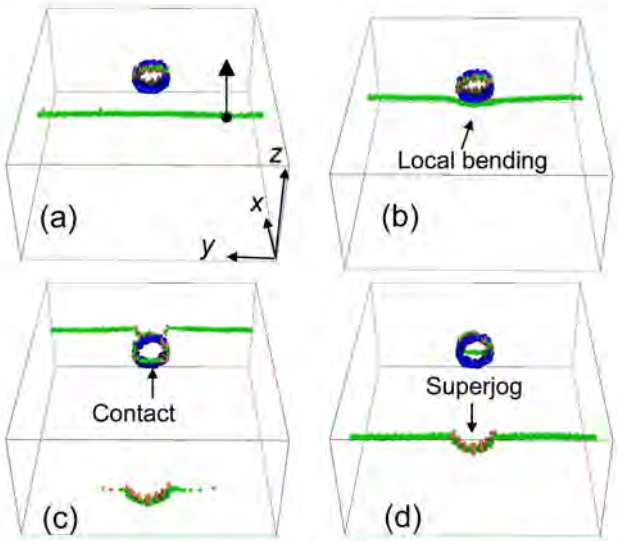

Fig.4. Visualization of the interaction of an edge dislocation with $a_0/2$[-111] DL of size 3.5nm modelled at 300 K. The equilibrium arrangement of Mn solutes (shown by blue balls) is obtained after MMC simulations in Fe-1%Mn alloy.

Our next example demonstrates the strong effect that enrichment may have also on the unpinning stress, while the reaction mechanism proceeds in the same way. Consider the stress-strain relationship shown in Fig.5(a), that corresponds to the interaction of a 1.5 nm loop with BV=$a_0/2$[-111]. This is the case of the inclined configuration, previously studied by several independent researches [44]. It is well established that, for loops with size below 2 nm, the inclined interaction in pure Fe results in the complete absorption of the loop by its flip and incorporation on the dislocation line in the form of a superjog. The critical stress of 50 MPa

(see Fig.5(a)) is only needed to reform the superjog into a glissile configuration. The decorated loop opposes much stronger resistance to this process, even though eventually it is completely absorbed by the dislocation. Note that the RSS does not become negative as the dislocation approaches the decorated loop. This occurs because the loop was completely immobilized by Mn atoms, so that it did not glide in its prism to establish the optimum interaction geometry. Overcoming the initially repulsive interaction, the dislocation makes eventually contact also with the decorated loop and forms the mixed [100] reaction segment, which propagates along the loop surface once the RSS reaches 275 MPa. So, the solute enrichment turns out to change the interaction mechanism (though not the reaction outcome), leading to a major increase of the unpinning stress, by approximately a factor five. As will be shown later, the effect of the enrichment is inherently dependent on the Mn content in the loop core, specifically for this interaction geometry and loop size.

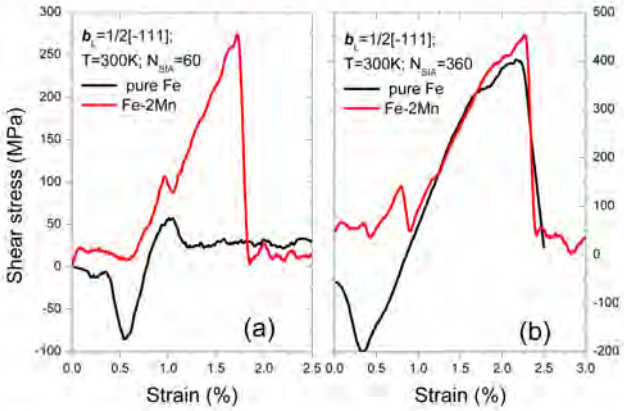

Fig.5. Stress-strain relationship corresponding to the interaction of $a_0/2[-111]$ DLs of size (a) 1.5nm and (b) 5nm.

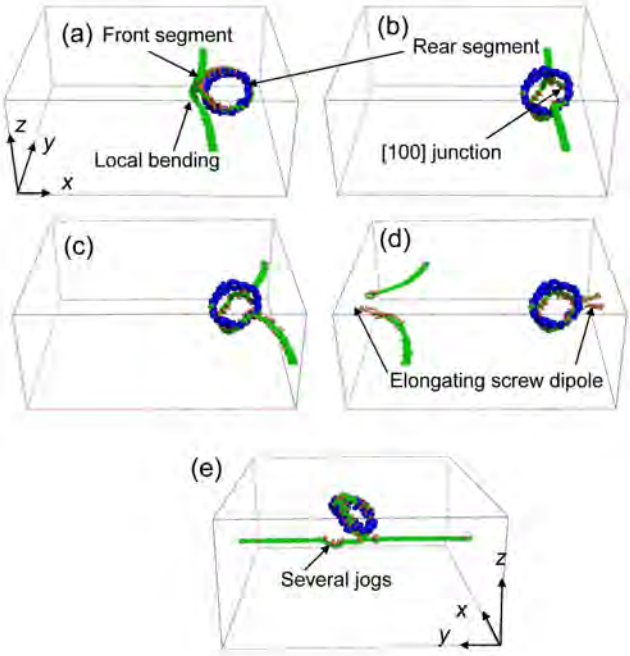

Fig.6. Visualization of the interaction of an edge dislocation with $a_0/2$[-111] DL of size 5nm modelled at 300 K. The equilibrium arrangement of Mn solutes (shown by blue balls) is obtained after MMC simulations in Fe-1%Mn alloy.

The evolution of stress-strain relationships for a larger, 3.5 nm size, loop in the same interaction geometry is presented in Fig.5(b). In this case the unpinning stress is close to 400 MPa for both undecorated and enriched loops. Nevertheless, there is an important effect of solute enrichment on the reaction outcome. While the undecorated loop is completely absorbed (see section 3.1), the enrichment almost totally suppresses the absorption. Let us consider the details of the interaction mechanism, presented in Fig. 6. The dislocation approaches the loop and bends backwards due to the repulsion from the front loop segment (Fig. 6a). The repulsive interaction displaces the front loop segment above the dislocation glide plane and the dislocation comes into contact with the rear loop segment to form the reaction segment with <001> orientation (Fig. 6b). The latter pins the dislocation (Fig. 6c)

and eventually a screw dipole emerges (Fig. 6d). The dipole closes by the glide of the two arms (with a couple of cross-slip events), resulting in the breakaway of the dislocation and restoration of the loop in its original position (Fig. 6e). This effect points to a very important implication with respect to the transfer of these results to DD techniques, as local chemical arrangement becomes another variable defining the reaction outcome. Another implication is that by suppressing absorption the damaged matrix remains hard to the passage of new dislocations and the formation of defect-free channels is prevented or, at least, delayed.

3.4. Summary and discussion

Fig. 7 summarizes the main results of this work. Fig. 7(a) shows graphically the types of interaction mechanisms as functions of loop size and configuration. One can see that a systematic change in the interaction mechanism takes place for the loops with BV=a_0/2[-111], irrespective of the loop size. The interaction mechanism is also different for the loops with BVs contained in the DGP, irrespective of the type of solute enrichment. Finally, the interaction mechanism remains unchanged in the two interaction geometries involving the a_0/2[1-1] loops with size 1.5 and 3.5 nm.

The unpinning stress for the undecorated and enriched loops is compared in Fig. 7(b). In the case of the decorated loops, we consider the mean value defined by averaging over the six considered configurations. One can see that the unpinning stress for the enriched loops is higher or similar to the one in pure Fe. The increase of the unpinning stress is superimposed in Fig. 7(a), showing some correlation with the modification of the interaction mechanism in the case of a_0/2[-111] loop. However, it is to be mentioned that the relative increase of the stress (i.e. $\tau_{enriched}/\tau_{undecorated}$) depends strongly on loop size. In the case of the a_0/2[-111] loop, it is 5 and 1.2, respectively for 1.5 and 3.5 nm.

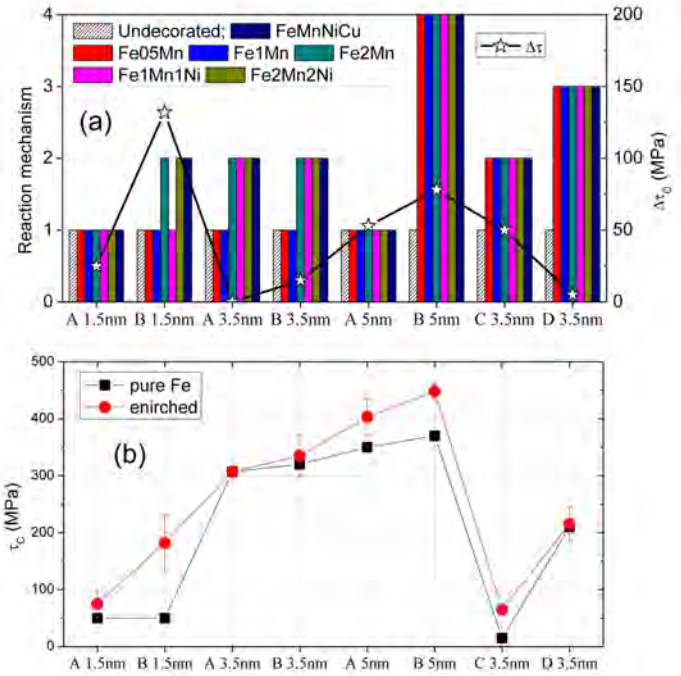

Fig.7. (a) Interaction mechanism (left Y axis) and added critical resolved shear stress (right Y axis) as functions of loop size and its Burgers vector. (b) Unpinning stress for the undecorated and enriched loops. Letters 'A', 'B', 'C', and 'D' on X axes refer to the orientation of Burgers vector of the DLs as [1-11], [-111], [111] and [11-1], respectively. The numbers on Y axis in fig.(a) refers to the following interaction mechanisms: (1) – absorption/drag; (2) – partial absorption/replacement; (3) – shear, (4) – Orowan-like reaction, see description of the mechanisms in text.

One must also note the relatively large spread of the mean value of the unpinning stress for the 1.5 nm loop, see Fig. 7(b). A detailed comparison of the loading curves in all inspected configurations is presented in Fig. 8(a). The unpinning stress clearly correlates with the Mn content in the loop core, thereby demonstrating the importance of the segregation of Mn specifically. It is worth noticing that Mn exhibits very strong attractive interaction with a

<111> crowdion i.e. -0.75 eV, while Ni and Cu are nearly neutral [27]. Cr atoms are also attracted to the <111> crowdion with the interaction of -0.4 eV, which is almost twice as low. Since the DL-dislocation reaction involves the re-orientation of crowdions forming the loop core, the strong solute-crowdion interaction suppresses the dislocation reaction. The significant affinity of Mn to <111> crowdions (adequately captured by the interatomic potential used) may explain why the content of Mn in the loop core defines its resistance to the dislocation passage. The segregation-induced suppression of the loop re-orientation may also take place for solutes segregating to the tensile core region, which would translate to the compressed region after the loop reorientation. In this case, the repulsive interaction with <111> crowdions would be equivalent resisting force suppressing DL-dislocation reaction. Hence, the ability of segregating solutes to suppress the reaction with dislocations should depend not on the sign of the interaction but on its absolute strength.

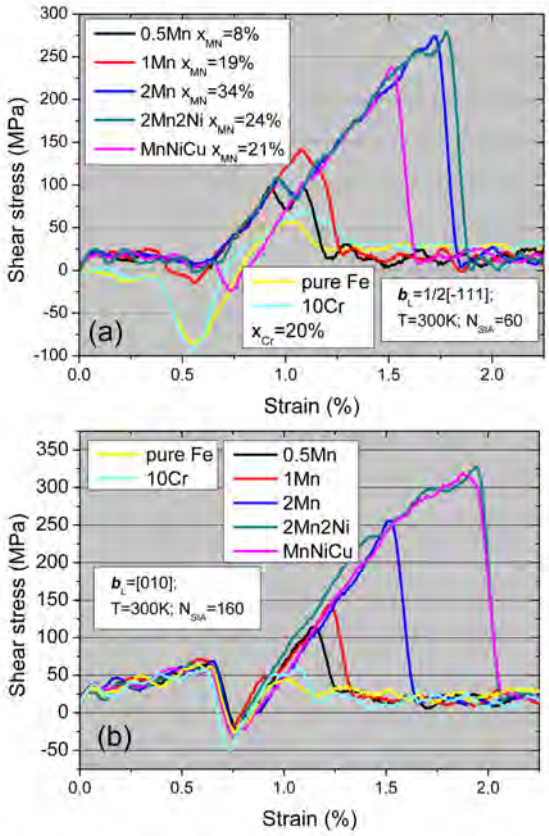

Fig.8. Stress-strain relationship corresponding to the interaction of (a) $a_0/2[-111]$ DLs of size 1.5nm and (b) $a_0[010]$ DLs of size 3.5nm, whose configurations were obtained by MMC simulations in several alloys. The composition of the alloys is reported in the figure inset, as well the concentration of Mn in the loop core.

To demonstrate that let us compare the effect of segregation of Mn and Cr. For the latter, we consider the results obtained for the 1.5 nm loop equilibrated by MMC in Fe-10%Cr at 600 K from [41] (x_{sol}~0.2 i.e. comparable to the enrichment obtained in the Fe-1%Mn alloy). Clearly, the Cr enrichment of small loops has much weaker effect on the unpinning stress as

compared to the Mn enrichment, which is consistent with the much stronger affinity of Mn to the ⟨111⟩ crowdion. To make this statement even more robust, we provide in Fig.8(b) the results preliminarily obtained for 3 nm size a_0<010> loops, whose configurations were prepared by equivalent MMC runs as for $a_0/2$<111> loops. We obtained essentially the same trends as in the case of $a_0/2$<111> loops, namely: (i) Mn enrichment enhances loop's strength; (ii) Mn decoration has much stronger effect than Cr; however, in this case the presence of Ni seems to be more determinant than the presence of Mn, possibly because of the type of interaction between Ni and ⟨100⟩ crowdions. Detailed investigation of the enrichment on <100> loops will be given in our upcoming work.

The observations discussed above bring us to the important conclusion that loop-dislocation interaction depends not only on the degree of segregation (i.e. content of solutes in the loop core), but also on the strength of the specific solute-loop interaction. The segregation of Cu or Ni or Mn on a given loop is not equivalent. Among Mn, Ni and Cu, the first element has the strongest effect, although the effect of Ni in the binary alloy still needs to be investigated. At the same time, the analysis of the MMC data discussed in section 3.2, suggests competitive interaction between Mn, Ni and Cu. The addition of Ni to a ternary Fe-Mn-Ni alloy weakens Mn segregation, while the addition of Cu in the quaternary Fe-Mn-Ni-Cu alloy reduces Ni segregation at loops and consequently enhances Mn content in the loop core. Thus, small variations of Mn, Ni, Cu concentrations dissolved in the matrix may lead to a strong change in the chemical potential for Mn segregation at loops, thereby influencing also the degree of radiation hardening. Another issue not to be forgotten is the complementary decoration of loops by carbon atoms. Even though dissolved in small amounts, carbon has enormous influence on the loop mobility and on the interaction with dislocations [35; 46]. Given that Mn is known to enter carbides and substitutional Mn exhibits attractive interaction with interstitial carbon in bcc Fe [47], the synergic Mn-C interaction on the dislocation loop core should have strong contribution to the establishment of the local chemistry and even further on the resulting hardening.

In RPV steels, the decoration of dislocation loops by solutes occurs under continuous neutron irradiation at ~300°C. On the one hand, the solutes will be transported by radiation induced defects, which obviously have different mass transport efficiency. The latter will depend on the concentration of solutes dissolved in the matrix, on temperature, and also on local solute-defect interactions. Depending on the efficiency of each transport mechanism, the fluxes of solutes and defects reaching dislocation loops will change: these are kinetic factors that will influence the local chemistry around loops. On the other hand, thermodynamics will

also play a role to determine the type of phase that should eventually precipitate on the loops at steady state, if not equilibrium. This will also be influenced by the competition with other stable phases. For example the concentration of solutes dissolved in matrix will be influenced also by the formation of CRP that will likely contain also vacancies, the presence of which has been undoubtedly confirmed by several experimental techniques. Hence, the precise determination of the local chemistry around small dislocation loops that are barely visible by TEM and not recognizable by other techniques remains a difficult task both for atomistic simulations and experiments. It seems therefore reasonable to envisage limiting cases for solute segregation at dislocation loops, to be validated using refined advanced experimental techniques (e.g. atom probe), and apply atomistic simulations to evaluate the consequences with regard to plastic deformation.

4. Conclusions

Based on the above results and discussion, we can summarize as follows our conclusions:

1. In Fe-Mn binary, Fe-Mn-Ni ternary and Fe-Mn-Ni-Cu quaternary alloys the segregation of Mn to the core of $a_0/2<111>$ dislocation loops occurs at equilibrium at 600 K. When analyzing the regions close to the dislocation loop core, Mn appears to be the most strongly segregating element, while Cu is the weakest one. Mn and Ni occupy competing positions in the loop core, so the segregation level of Mn in the ternary alloy is lower than in the binary. At the same time, the addition of Cu suppresses the segregation of Ni, so that Mn concentration in the loop core recovers back, as a result. Hence, the interplay between all three chemical elements will contribute to the final chemical arrangement (without accounting for kinetic effects). In any case, Mn seems to always prevail, its content being about 2-3 and 5 times higher than that of Ni and Cu, respectively. Mn is therefore expected to play the major role on the properties of loops upon plastic deformation in the quaternary Fe-Mn-Ni-Cu alloys. The separate effect of the other elements, however, still needs to be assessed.

2. The study of the interaction with edge dislocations of small, 1.5 nm diameter $a_0/2\langle 111\rangle$ dislocation loops enriched with Mn, Mn-Ni and Mn-Ni-Cu reveals that the main effect of the enrichment is the significant increase of the unpinning stress. By increasing Mn content in the

core of the loops, the unpinning stress increases too. This effect has obviously direct consequences on increasing the radiation hardening attributed to the so-called matrix damage.

3. The study of the interaction with edge dislocation of larger (3.5 and 5 nm diameter) $a_0/2\langle 111\rangle$ loops reveals that the enrichment suppresses mainly the absorption and dynamic drag of loops i.e. reactions involving instantaneous removal of loops by the dislocation front. Instead of being absorbed, the loops remain essentially intact after interaction with the dislocation, except being partially absorbed and sheared. This effect, too, may have consequences regarding the strain hardening evolution and in particular, the formation of defect-free channels, expected to be prevented or at least delayed.

5. Acknowledgements:

Part of calculations has been performed at HPC Julich. Partial support was also received from the EURATOM Seventh Framework Programme, under the Perform60 project.

References:

[1]G.R. Odette, Scripta Metallurgica 17 (1983) 1183.
[2]G.R. Odette, G.E. Lucas, Journal of the Minerals Metals & Materials Society 53 (2001) 18.
[3]G.R. Odette, C.L. Liu, B.D. Wirth, Microstructure Evolution during Irradiation 439 (1997) 457.
[4]C.A. English, W.J. Phythian, R.J. McElroy, Microstructure Evolution during Irradiation 439 (1997) 471.
[5]G.R. Odette, R.K. Nanstad, Jom 61 (2009) 17.
[6]G. Bonny, D. Terentyev, A. Bakaev, E.E. Zhurkin, M. Hou, D. Van Neck, L. Malerba, Journal of Nuclear Materials 442 (2013) 282.
[7]E. Meslin, et al., Journal of Nuclear Materials 406 (2010) 73.
[8]G. Bonny, D. Terentyev, L. Malerba, Journal of Nuclear Materials submitted (2014).
[9]S.C. Glade, B.D. Wirht, G.R. Odettes, P. Asoka-Kumar, P.A. Sterne, R.H. Howell, Philosofical Magazine 85 (2003) 629.
[10]M. Lambrecht, L. Malerba, A. Almazouzi, Journal of Nuclear Materials 378 (2008) 282.

[11]Y. Nagai, K. Takadate, Z. Tang, H. Ohkubo, H. Sunaga, H. Takizawa, M. Hasegawa, Physical Review B 67 (2003) 224202.
[12]D. Terentyev, L. Malerba, G. Bonny, A.T. Al-Motasem, M. Posselt, Journal of Nuclear Materials 419 (2011) 134.
[13]D. Terentyev, L. Malerba, Journal of Nuclear Materials 421 (2012) 32.
[14]J. Kocik, E. Kielova, J. Cizek, I. Prochazka, Journal of Nuclear Materials 303 (2002) 52.
[15]G. Maussner, L. Scharf, R. Langer, B. Gurovich, Nuclear Engineering and Design 193 (1999) 359.
[16]E.A. Kuleshova, B.A. Gurovich, Y.I. Shtrombakh, D.Y. Erak, O.V. Lavrenchuk, Journal of Nuclear Materials 300 (2002) 127.
[17]B.A. Gurovich, E.A. Kuleshova, Y.I. Shtrombakh, D.Y. Erak, A.A. Chernobaeva, O.O. Zabusov, Journal of Nuclear Materials 389 (2009) 490.
[18]K. Fukuya, K. Ohno, H. Nakata, S. Dumbill, J.M. Hyde, Journal of Nuclear Materials 312 (2003) 163.
[19]M. Hernandez-Mayoral, D. Gomez-Briceno, Journal of Nuclear Materials 399 (2010) 146.
[20]K. Fujii, K. Fukuya, N. Nakata, K. Hono, Y. Nagai, M. Hasegawa, Journal of Nuclear Materials 340 (2005) 247.
[21]T. Hamaoka, Y. Satoh, H. Matsui, Journal of Nuclear Materials 399 (2010) 26.
[22]D.T. Hoelzer, F. Ebrahimi, Mat. Res. Soc. Symp. Proc. 373 (1995) 57.
[23]A. Okada, H. Maeda, K. Hamada, I. Ishida, Journal of Nuclear Materials 271&272 (1999) 133.
[24]A. Calder, D. Bacon, Journal of Nuclear Materials 207 (1993) 25.
[25]L. Malerba, Journal of Nuclear Materials 351 (2006) 28.
[26]D. Terentyev, C. Lagerstedt, P. Olsson, K. Nordlund, J. Wallenius, C. Becquart, L. Malerba, Journal of Nuclear Materials 351 (2006) 65.
[27]P. Olsson, T.P.C. Klaver, C. Domain, Physical Review B 81 (2010) 054102.
[28]M. Mendelev, S. Han, D. Srolovitz, Philosophical Magazine 83 (2003) 3977.
[29]A. Voter, S. Chen, Materials Research Society Symp. Proc. 82 (1987) 175.
[30]Y. Mishin, M. Mehl, D. Papaconstantapoulos, physical Review B 63 (2001).
[31]G. Bonny, R.C. Pasianot, N. Castin, L. Malerba, Philosophical Magazine 89 (2009) 3531.
[32]G. Bonny, R.C. Pasianot, L. Malerba, Modelling and Simulation in Materials Science and Engineering 17 (2009) 025010.
[33]R. Pasianot, L. Malerba, Journal of Nuclear Materials 360 (2007) 118.
[34]M. Allen, D. Tildesley, Computer Simulation of Liquids, Clarendon Press, Oxford, 1987.

[35]D. Terentyev, N. Anento, A. Serra, Journal of Physics-Condensed Matter 24 (2012) 455402.

[36]Y.N. Osetsky, D.J. Bacon, Modelling and Simulation in Materials Science and Engineering 11 (2003) 427.

[37]D. Terentyev, D. Bacon, Y. Osetsky, Journal of Physics: Condensed Matter 20 (2008) 445007.

[38]D. Terentyev, D.J. Bacon, Y.N. Osetsky, Philosophical Magazine 90 (2010) 1019.

[39]D. Terentyev, L. Malerba, D. Bacon, Y. Osetsky, Journal of Physics: Condensed Matter 19 (2007) 456211.

[40]D. Terentyev, P. Grammatikopoulos, D. Bacon, Y. Osetsky, Acta Materialia 56 (2008) 5034.

[41]Z. Rong, Y.N. Osetsky, D.J. Bacon, Philosophical Magazine 85 (2005) 1473.

[42]D. Terentyev, A. Bakaev, Journal of Physics-Condensed Matter 25 (2013) 265702.

[43]A. Nomoto, N. Soneda, A. Takahashi, S. Ishino, Materials Transactions 46 (2005) 463.

[44]D. Bacon, Y. Osetsky, Z. Rong, Philosophical Magazine 86 (2006) 3921.

[45]D.A. Terentyev, Y.N. Osetsky, D.J. Bacon, Acta Materialia 58 (2010) 2477.

[46]D. Terentyev, N. Anento, A. Serra, Journal of Nuclear Materials 420 (2012) 9.

[47]A. Bakaev, D. Terentyev, G. Bonny, T.P.C. Klaver, P. Olsson, D. Van Neck, Journal of Nuclear Materials 444 (2014) 237.

List of publications

Journal papers

1. A. Bakaev, D. Terentyev, G. Bonny, T.P.C. Klaver, P. Olsson and D. Van Neck, *Basic Properties of Minor Alloying Elements in High-Cr Ferritic Steels: An Ab Initio Study*, Journal of Nuclear Materials, 444 (2014) 237.

2. A. Bakaev, D. Terentyev, X. He and D. Van Neck, *Synergetic Effects of Mn and Si in the Interaction with Point Defects in bcc Fe*, Journal of Nuclear Materials, 455 (2014) 5.

3. A. Bakaev, D. Terentyev, X. He, E.E. Zhurkin and D. Van Neck, *Interaction of carbon-vacancy complex with minor alloying elements of ferritic steels*, Journal of Nuclear Materials, 451 (2014) 82.

4. A. Bakaev, D. Terentyev, X. He, E.E. Zhurkin and D. Van Neck, *Energetic stability of solute-vacancy-carbon complexes in bcc iron*, submitted to Journal of Nuclear Materials, 2014.

5. D. Terentyev, A. Bakaev and E.E. Zhurkin, *Effect of carbon decoration on the absorption of <100> dislocation loops by dislocations in iron*, J. Phys.: Condens. Matter, 26 (2014) 165402.

6. D. Terentyev, A. Bakaev, X.J. Shi and D. Van Neck, *Glide of dislocations in <111>{321} slip system: an atomistic study*, submitted to Modelling and Simulation in Materials Science and Engineering, 2014.

7. D. Terentyev, V. Dubinko, A. Bakaev, Y. Zayachuk, W. Van Renterghem and P. Grigorev, *Dislocations mediate hydrogen retention in tungsten*, Nuclear Fusion, 54 (2014) 042004.

8. D. Terentyev, K. Heinola, A. Bakaev and E.E. Zhurkin, *Carbon–vacancy interaction controls lattice damage recovery in iron*, Scripta Materialia, 86 (2014) 9—12.

9. G. Bonny, D. Terentyev, A. Bakaev, P. Grigoriev and D. Van Neck, *Many-body central force potentials for tungsten*, Modelling Simul. Mater. Sci. Eng. 22 (2014) 053001.

10. D. Terentyev, X. He, G. Bonny, A. Bakaev, E. Zhurkin and L. Malerba, *Hardening due to dislocation loop damage in RPV modelalloys: role of Mn segregation*, submitted to Journal of Nuclear Materials, 2014.

11. V.I. Dubinko, D. Terentyev, P. Grigorev, A. Bakaev, G. Van Oost, F. Gao, Fei; D. Van Neck and E.E. Zhurkin, *Dislocation mechanism of deuterium retention in tungsten under plasma implantation*, J.Phys.: Condens. Matter, 26 (2014) 395001.

12. A. Bakaev, D. Terentyev, X. He and E.E. Zhurkin, *Energetics of radiation defects in Fe-based austenitic alloys: Atomic scale study*, Nuclear Instruments and Methods in Physics Research Section B: Beam Interactions with Materials and Atoms, 303 (2013) 33.

13. D. Terentyev, A. Bakaev and Yu.N. Osetsky, *Interaction of dislocations with Frank loops in Fe–Ni alloys and pure Ni: An MD study*, Journal of Nuclear Materials, 442 (2013) S628.

14. D. Terentyev and A. Bakaev, *Interaction of a screw dislocation with frank loops in Fe-10Ni-20Cr alloy*, Journal of Nuclear Materials, 442 (2013) 208.

15. D. Terentyev and A. Bakaev, *Radiation-induced strengthening and absorption of dislocation loops in ferritic Fe–Cr alloys: the role of Cr segregation*, J.Phys.: Condens. Matter 25 (2013) 265702.

16. G. Bonny, D. Terentyev, A. Bakaev, E.E. Zhurkin, M. Hou and L. Malerba, *On the thermal stability of late blooming phases in reactor pressure vessel steels: An atomistic study*, Journal of Nuclear Materials, 442 (2013) 282.

17. G. Bonny, N. Castin, J. Bullens, A. Bakaev, T.C.P. Klaver and D. Terentyev, *On the Mobility of Vacancy Clusters in Activation Reduced Steels: An Atomistic Study in the FeCrW Model Alloy*, J.Phys.: Condens. Matter 25 (2013) 315401.

18. D. Terentyev, G. Bonny, A. Bakaev and D. Van Neck, *On the thermal stability of vacancy-carbon complexes in alpha iron*, J.Phys.: Condens. Matter 24 (2012) 385401.

19. D. Terentyev, X. He, E. Zhurkin and A. Bakaev, *Segregation of Cr at tilt grain boundaries in Fe–Cr alloys: A Metropolis Monte Carlo study*, Journal of Nuclear Materials, 408 (2011) 161.

20. G. Bonny, D. Terentyev, R. C. Pasianot, S. Ponce and A. Bakaev, *Interatomic potential to study plasticity in stainless steels: the FeNiCr model alloy*, Model. Simul. Mater. Sci. Eng. 19 (2011) 085008.

Oral presentations at international conferences & workshops

1. *Segregation-induced embrittlement in RPV steels: assessment by atomistic simulations*, 8th ENEN PhD Event, Burgos, Spain, 9–10 July 2014.
   → **Prize for the best presentation**

2. *Ab initio study of synergetic effects of Mn and Si in the interaction with point defects in bcc Fe*, 5th Workshop on Nuclear Fe Alloys: modeling and experiments, Rome, Italy, 28–29 November 2013.

3. *Interaction of dislocations with radiation defects in FeNiCr austenitic alloy*, Perform-60 seminar in SCK-CEN, Mol, Belgium, 29 August 2013.

4. *Ab initio study of basic properties of minor alloying elements in high-Cr ferritic steels*, 4th n-FAME and 22nd Fe-Cr alloys workshop, Edinburgh, Scotland, 4–5 June 2013.

5. *Atomistic modelling of interaction of edge dislocations with radiation defects in austenitic alloys FeNiCr*, XXXXIII Tulinov conference. Physics of interaction of charged particles with crystals, Moscow, Russia, 28–30 May 2013.

6. *Microchemistry of dislocations loops in Fe-based ferritic alloys studied by atomistic Metropolis Monte Carlo techniques*, EMR2012 — the Energy and Materials Research Conference, Torremolinos, Spain, 20–22 June 2012.

7. *Microchemistry of dislocation loops in ferritic Fe-Cr and Fe-Cu-Ni-Mn alloys studied by atomistic Metropolis Monte Carlo*, COSIRES 2012: Computer Simulation of Radiation Effects in Solids, Santa Fe, New Maxico, USA, 25–29 June 2012.

8. *Interaction of W and Mo with vacancy defects in bcc Fe studied by ab initio methods*, EMR2011 — the Energy and Materials Research Conference, Nice, France, 9–13 May 2011.

9. *DFT calculations in Fe(-Cr) system with addition of W and Mo: towards development of Fe- Cr-W/Mo interatomic potential*, 18th Workshop on Multiscale

Modelling and Basic Experiments of Iron-Chromium Alloys for Nuclear Applications, Dresden, Germany, 4–5 May 2011.

Poster presentations

1. *Synergy of interaction between point defects, carbon and typical alloying elements of Fe-based steels*, COSIRES 2014: Computer Simulation of Radiation Effects in Solids, Alicante, Spain, 8–13 June 2014.
2. *Synergetic effects of Mn and Si in the interaction with point defects in bcc Fe*, International Conference: Towards Reality in Nanoscale Materials VII, Levi, Finland, 10–12 February 2014.
3. *Ab initio modeling of fusion reactor materials: Unravelling the hydrogen retention mechanisms*, International Conference on Scientific Computing 2013, Paphos, Cyprus, 3–6 December, 2013.
4. *Interaction of minor alloying elements with lattice defects in ferritic high-Cr steels: ab initio study*, 16th International Conference On Fusion Reactor Materials, Beijing, China, 20–26 October 2013.
5. *Modelling the interaction of radiation defects with dislocation in Fe-10Ni-20Cr alloys*, 16th International Conference On Fusion Reactor Materials, Beijing, China, 20–26 October 2013.
6. *Trapping of H on dislocations and grain boundaries in W alloys: an atomistic study*, 14th International Conference on Plasma-Facing Materials and Components for Fusion Applications, Jülich, Germany, 13–17 May 2013.
7. *Interaction of dislocations with Frank loops in FeNiCr austenitic alloys*, MMM 2012 — 6th International Conference on Multiscale materials modeling. Biopolis, Singapore, 15–19 October 2012.
8. *Characterization of radiation defects in Fe-based austenitic alloys*, COSIRES 2012: Computer Simulation of Radiation Effects in Solids, Santa Fe, New Maxico, USA, 25–29 June 2012.